Heterogeen geïntegreerde III-V-microlasers op silicium gebaseerd op resonante roosterspiegels

Heterogeneously Integrated III-V on Silicon Microlasers Based on Resonant Grating Mirrors

Yannick De Koninck

Promotoren: prof. dr. ir. R. Baets, prof. dr. ir. G. Roelkens
Proefschrift ingediend tot het behalen van de graad van
Doctor in de Ingenieurswetenschappen: Fotonica

Vakgroep Informatietechnologie
Voorzitter: prof. dr. ir. D. De Zutter
Faculteit Ingenieurswetenschappen en Architectuur
Academiejaar 2014 - 2015

UNIVERSITEIT GENT

ISBN 978-90-8578-769-3
NUR 950, 959
Wettelijk depot: D/2015/10.500/13

Universiteit Gent
Faculteit Ingenieurswetenschappen en Architectuur
Vakgroep Informatietechnologie

Promotoren: Prof. Dr. Ir. Roel Baets
Prof. Dr. Ir. Gunther Roelkens

Universiteit Gent
Faculteit Ingenieurswetenschappen en Architectuur

Vakgroep Informatietechnologie
Sint Pietersnieuwstraat 41, B-9000 Gent, België

Tel.: +32-9-331.49.00
Fax.: +32-9-331.48.99

Dit werk kwam tot stand in het kader van een specialisatiebeurs van het FWO-Vlaanderen (Fonds voor Wetenschappelijk Onderzoek Vlaanderen).

Proefschrift tot het behalen van de graad van
Doctor in de Ingenieurswetenschappen:
Fotonica
Academiejaar 2014-2015

Dankwoord

De bestseller in spe die voor uw neus ligt en waar u ongetwijfeld nog jarenlang plezier aan zal beleven is niet enkel het werk van ondergetekende. Sta mij toe u in de volgende paragrafen kennis te laten maken met de protagonisten van de tragi-komische queeste waarvan de resultaten in onderliggend schrift worden beschreven.

Roel Baets heeft op verschillende momenten in mijn, al niet meer zo korte, leven een beslissende rol gespeeld. Een van de meest frappante voorbeelden daarvan speelde zich af in het voorjaar van het gezegende jaar 2007. Na 2.5 jaar eerder mijn studies te zijn begonnen met het idee computerwetenschapper te worden had ik na enkele maanden een beter idee: ik ging elektrotechnieker worden. Dat was namelijk veel cooler. Dat ging over chips. En chips, dat weet iedereen, dat is de toekomst. Dus ik draai mijn kar en ga voor een Bachelor in de Elektrotechniek. De keuzemogelijkheden voor een Master opleiding aansluitend op zo een bachelor zijn beperkt tot drie opties: iets meer software, iets meer hardware of fotonica. Moeilijke keuze. Software of hardware? Fotonica zeker, niet, dat is met lenzen en lenzen is niets voor mij. Lenzen dat is het verleden. Chips dat is de toekomst. Dat weet iedereen. Enter Roel Baets. Roel doceert het vak fotonica in het tweede semester van de derde bachelor Elektrotechniek. 6 studiepunten? Serieus? Over lenzen? Nu goed, als het moet, moet het. Les 1: Roel vertelt dat hij enkele dagen voordien de Koning over de vloer heeft gekregen. Nu hadden we daar al veel gehoord op de banken van de auditoria aan de Jozef Plateaustraat maar dat was toch iets nieuw. De Koning is geïnteresseerd in lenzen? Serieus? Wat bleek nu: niet zo heel lang geleden had iemand iets nieuws uitgevonden: een chip die werkte met optische signalen in plaats van met elektrische signalen. Dus toch chips? En de Koning, die tenslotte op de hoogte moet blijven van alles wat er zich in zijn rijk afspeelt, was polshoogte komen nemen van hoe die chips werken en hoe die gemaakt worden. Roel maakte tijdens die eerste les van de gelegenheid gebruik om ons in te leiden tot die wondere wereld van de fotonica. Met dezelfde powerpoint presentatie die hij aan de Koning had gegeven. De daaropvolgende weken zijn slechts een wazige herinnering. Maar halverwege dat tweede semester van de derde Bachelor Elektrotechniek in het gezegende jaar 2007 wist ik kristalhelder wat ik zou gaan aanvangen met mijn leven: een Master in de Fotonica. Want Fo-

tonica dat was dus blijkbaar ook met chips. En chips dat is de toekomst. Dat weet iedereen. Nu gebiedt de eerlijkheid mij ook te zeggen dat, eens je wat meer weet waaraan en waaraf, lenzen nog wel interessant zijn.

Na twee zomers vakantiewerk te mogen doen bij de onderzoeksgroep, een heel erg interessante masterthesis en omzwervingen naar de uithoeken van onze planeet was het in April 2010 zo ver: ik begin als onderzoeker bij de fotonica groep. Ik mag mij vier jaar bezig houden met lasers en chips en wat niet al. En wie worden mijn promotoren (verschiet niet): Roel Baets en Gunther Roelkens.

Roel Baets kennen we ondertussen al maar Gunther Roelkens is nieuw. De naam van Gunther Roelkens laat zich niet toevallig afkorten tot Gu Roe. Gunther is namelijk een guru in alles wat te maken heeft met lasers, chips, III-V materialen, processing en alles daartussenin. Ik had dus een soort van dream-team achter mij staan. Roel is een meester-motivator, weet altijd perfect hoe hij je in de juiste richting moet sturen en kan doormiddel van een stel welgemikte vragen razendsnel doordringen tot de essentie van de zaak. Gunther is dan weer een wandelende encyclopedie die schijnbaar uit elke hopeloze situatie een uitweg weet te vinden. Socrates meets McGiver zeg maar. Ik kon mij geen beter duo wensen.

En ja, zoals dat dan gaat, krijg ik een bureau toegewezen. Einde van de gang links, de bureau links achteraan. En dan komt er iemand zeer belangrijk ten tonele in de gedaante van: Bart Kuyken. Bart heeft uiteraard ook een eigen bureau: einde van de gang links, de bureau links vooraan. Recht tegenover de mijne dus. Bart en ik delen een paar cruciale eigenschappen: we houden graag de actualiteit in het oog, we bespreken graag het reilen en zeilen van onze omgeving, we luisteren allebei graag naar iets oudere muziek en we zijn altijd geïnteresseerd als het over de Tweede Wereldoorlog gaat. We hebben ook een idee voor een 3D tv, met perspectief, maar dat is misschien iets voor later. Maar bovenal heb ik zelden zo veel en zo hard gelachen en mij zo goed geamuseerd als met Bart Kuyken. BFFs dus.

Aan de overkant van onze bureau, einde van de gang rechts dus, zat jaren lang mijn compagnon de route Peter De Heyn. De Heyn en De Koninck zaten in dezelfde groep tijdens de computeroefeningen van de eerste Bachelor en zijn elkaar sinds dien niet meer uit het oog verloren. De Heyn en De Koninck losten samen oefeningen op, maakten samen muziek, brachten samen het forum op de website van VTK in kaart, fietsten samen traditiegetrouw van Antwerpen naar bijna elke proclamatie, fietsten samen gezakt en gepakt naar de Ardennen en trokken samen met de fiets door Nederland op zoek naar het pittoreske Lelystad. Enfin, compagnon de route first class dus.

En over het einde van de gang rechts en Nederland gesproken. Tegenover Peter De Heyn zat Thijs Spuesens. Thijs Spuesens is altijd goed gezind. Maar dat is niet zijn enige talent. Thijs Spuesens kan enorm hard met een fiets rijden. En ik fiets graag. En Thijs Spuesens is gezegend met een aantal vrienden die we kunnen

catalogeren als knotsgek. Maar absoluut in de goeie zin van het woord. Dus gingen Thijs Spuesens, enkele van die knotsgekke vrienden en ikzelf af en toe eens fietsen. En als we dat deden pakten we het meestal groots aan. Zo beklommen we met zijn allen menig Franse bergpas: de Mont Ventoux, de Col du Galibier en onlangs reden we ook nog een tochtje in de Vogezen. Na elke reis was Thijs Spuesens een kleine week verkouden omdat hij te lang boven op de berg op mij had staan wachten. Waarom bleef die man en zijn Nederlandse aanhang dan keer op keer mee gaan met mij vraagt u? Omdat ik, al zeg ik het zelf, het talent bezit om tegen bodemprijzen reizen te organiseren naar de Franse gebergtestreken. In diezelfde bureau, einde van de gang rechts, zat ook lange tijd Diedrik Vermeulen. Zelden heb ik iemand gekend die, als hij een doel voor ogen heeft, er zo voor gaat. Een doorzetter dus. Inspirerende kerel zonder meer.

En nu we toch over de edelmoedige sport van het fietsen bezig zijn zou ik u willen voorstellen aan Sam Werquin. Net als Thijs Spuesens kan Sam Werquin verschrikkelijk hard met een fiets rijden. Ik heb het genoegen gehad om doorheen de jaren vele malen met Sam Werquin de Vlaamse, Waalse, Franse en Tsjechische wegen onveilig te maken. Er zijn 2 ritten in het bijzonder die voor de eeuwigheid in mijn geheugen gegrift staan: die keer toen we de Reuzen van Ardennen te lijf zijn gegaan aan een gemiddelde snelheid van 27.4 km per uur en de eerste keer dat we de Mont Ventoux beklommen. Als ik me niet vergis was dat voor ons beiden de eerste keer dat we een echte col buiten categorie beklommen. Op die beklimming hadden we ook het gezelschap van Geert Morthier. Geert Morthier was tevens de man achter - en promotor van - mijn eerder vernoemde razend interessante master thesis.

En het blijft wielertoeristen regenen op de eerste verdieping van de Sint Pietersnieuwstraat nummer 41. We blijven achteraan de gang en verhuizen terug naar de bureau aan de linker kant. Inderdaad, de ruimte alwaar ikzelf ook meer dan 4 mooie jaren heb gesleten. Want daar hield ook Pieter Wuytens kantoor. Pieter Wuytens is een natuurtalent. Niet alleen achter zijn bureau maar ook op zijn fiets. Zelden heb ik iemand gekend die zich een koersfiets aanschaft en binnen het tijdsbestek van 30 dagen fietstochten maakt aan een gemiddelde snelheid van 30 kilometer per uur. Waanzinnig is zoiets. Topkerel.

Ik hoop dat u nog niet zeeziek bent want we verhuizen terug naar de overkant van de gang. U hebt goed de tel bijgehouden dus u weet dat we nu terug in het territorium van Thijs Spuesens en Peter De Heyn zijn. In datzelfde kantoor was de praktijk van Meester Raphael Van Laer gevestigd. Meester Van Laer is gespecialiseerd in erg complexe zaken waarover hij dan publiceert in gerenommeerde tijdschriften met een schwung die u zelden gezien heeft bij een man van zulk kaliber. Maar laat u niet bedriegen door looks van Raphael Van Laer. Raphael Van Laer beschikt ook over een stel gouden benen waarmee hij probleemloos binnen de 40 minuten 10 kilometer afhaspelt. Maar als het heel snel moet gaan dan moet u bij Eva Ryckeboer zijn. Eva Ryckeboer behaalde een medaille op de Olympi-

sche Spelen (voor bedrijven, maar dat is een detail). Eerder diezelfde week had ze moeten afrekenen met een valpartij waardoor ze haar kansen op een ander sprintnummer niet had kunnen verdedigen. Maar opgeven staat niet in het woordenboek van Eva Ryckeboer. Bovendien is Eva Ryckeboer altijd vrolijk.

Schuin tegenover Eva Ryckeboer had de heer Thomas Van Vaerenberg zijn kamp opgezet. Thomas Van Vaerenbergh is een intrigerend individu. Thomas Van Vaerenberg is een wereldreiziger. Maar Thomas Van Vaerenbergh zal in de geschiedenisboeken vooral onthouden worden omwille van zijn onnavolgbare cool en geduld. Thomas Van Vaerenbergh was namelijk in de volgende penibele situatie gesukkeld: zijn bureau stond quasi onder onze basketbalring. Iemand, ik weet niet wie, had op een gegeven moment het lumineuse idee om een mini-basketbalring op te hangen in het bureau einde van de gang rechts. Bij een mini-basketbalring hoort een mini-basketbal. En een mini-basketbalspeler. Vaak was ik dat zelf. Hoewel ik een ontelbaar keer de ring mistte, waarna de mini-basketbal op het bureau (soms zelfs de computer) van Thomas Van Vaerenbergh terecht kwam is het mij 1 maal gelukt: vanop een slordige 4 meter afstand met mijn rug naar de ring de mini-basketbal doorheen de mini-basketbalring gooien. Het wordt niet veel beter dan dat.

Ondertussen hebt u wel begrepen dat de Fotonica groep eerder een verdoken sportclub is dan een onderzoeksgroep. Maar gelukkig werd er ook aan onderzoek gedaan. Dames en Heren mag ik u voorstellen aan Karel Van Acoleyen. Karel Van Acoleyen en ikzelf vormden jarenlang een van de meest beruchte recherche teams van Oost-Vlaanderen. Hoewel onze reputatie na verloop van tijd bijna Hollywoodiaanse proporties aan nam waren we spijtig genoeg niet in staat alle misdaad een halt toe te roepen. Al zal dat niet aan de het gewiekste brein van Karel Van Acoleyen gelegen hebben.

Maar de Sint-Pietersnieuwstraat en haar nabije omgeving was allerminst een politiestaat. Vrijheid en liberale ideeën vierden hoogtij. Start-ups schoten er als paddenstoelen uit de grond. Een van de moedigste ondernemers die ooit voet zette in fotonica-land was de heer Elewout Hallynck. Volgens de legende werd Elewout Hallynck op een warme novemberochtend wakker met een idee dat de wereld voor goed zou veranderen. Die dag verklaarde hij de oorlog aan losse papieren en begon hij zijn ondertussen legendarische handel in nietjesmachines. Maar ondanks zijn drukke leven als marchant van bureauartikelen maakte Elewout Hallynck ook graag tijd om zijn medemens te entertainen. Elewout Hallynck was namelijk het brein achter de clandestiene piraatradioshow ePIXradio - best effort radio met Hallynck en De Koninck. Mede door zijn talent om jingles te assembleren, playlists samen te stellen en uitdagende spelconcepten te bedenken gleed ePIXradio in een mum van tijd de radio hall-of-fame binnen.

Op dinsdag namiddag en om de twee weken op donderdag deden we ook aan wetenschappelijk onderzoek. Het laatste kwart van mijn vierjarig parcours als

doctoraatstudent had ik het genoegen om die momenten in de clean-room door te brengen. Als u niet weet wat een clean-room is gaat u naar uw computer en googlet u ”clean room”. De clean room, gevestigd in het mondaine Zwijnaarde, wordt bij elkaar gehouden door Steven Verstuyft. Steven Verstuyft heeft wat men in het Duits fingerspitzengefühl noemt. Als u ooit de onweerstaanbare drang voelt om een halfgeleidercomponent te processen raad ik u ten stelligste aan om uw aanpak eerst met Steven Verstuyft te overleggen. Steven Verstuyft heeft mij veel geleerd. Een van de meest pragmatische levenslessen die Steven Verstuyft mij meegaf is de volgende: als er iets van groot-elektro kapot is los je dat best op door dat toestel te vervloeken naar de donkerste kerkers van de Hel. Of door het terug op te starten.

Maar Steven Verstuyft is niet de enige die er voor zorgt dat de clean-room op wieltjes loopt. Er is ook nog Liesbet Van Landschoot. Liesbet Van Landschoot is altijd goed gezind. En dat straalt ze af op andere mensen. Liesbet Van Landschoot is ook een van de aller strafste FIB operatoren die ik ooit gekend heb. En Liestbet Van Landschoot was er bij toen ik van vreugde bijna in tranen uitbarstte toen op 11 maart 2014 tussen 14 uur en 14 uur 30 bleek dat mijn ondergeëtste multi-quantum wells opgevuld waren met BCB. En terwijl ik met een vlag aan het zwaaien was en champagne uitdeelde aan iedereen die die dag aanwezig was in de clean-room liet Liesbet Van Landschoot zich niet meeslepen door de emoties en legde de SEM beelden vlijmscherp vast op de gevoelige plaat.

Tijdens de eerste maanden van mijn tijd in de clean-room had ik het genoegen lief en leed daar te delen met Martijn Tassaert. Martijn Tassaert deed dingen die gelijkaardig waren aan de mijne. Zelden heb ik iemand gekend die zo efficiënt en op voorhand werkte als Martijn Tassaert.

Laat u mij toe om de volgende personages in het Engels toe te spreken. Let me introduce you to my friends from the Orient. Let’s start with Amin Abbasi, Ashim Dhakal, Yingtao Hu, Yanlu Li, Muhammad Muneeb, Aditya Malik, Pijush Kumar Pal, Kumar Saurav, Ruijun Wang, Zhechao Wang and Jing Zhang. These brave men brought ancient Asian crafts and secrets to our premises that almost allowed us to produce an elixir for eternal life and turn lead into gold. Also they reminded us that some Dutch words, such as *gezond* are virtually impossible to pronounce in English. Another extraordinary man is my Chinese language tutor Weiqiang Xie. To this day I enjoy your performance as a casino owner in the 2014 photonics short movie. You nailed that part big time.

Chen Hu is one of the sweetest people I have ever met. Xin Fu was the inspiration for my 2014 top-hit song *Xin Little Fu*. Lianyan Li and Sulakshna Kumari are some of the bravest laser-makers in the Northern hemisphere.

To characterize the very first prototype of our resonant mirror laser we went abroad. To the Laboratoy for Photonics and Nanostructures in Marcoussis, France. Marcoussis is situated south of Paris. During that time I learned a valuable lesson:

the Paris Peripherique is a nightmare. And French researchers are awesome. Fabrice, Rama, Alex and Paul: thank you so very much for all the effort you put into helping me and allowing me to use your setup up to 3 times. I have to admit that up until that point I myself didn't really believe this would ever work. So being at your lab was a key moment in this story. Thanks a lot!

En over Frankrijk gesproken. Jarenlang hadden we een echte Francaise in onze rangen: Pauline Mechet. Pauline Mechet is een duizendpoot. Ze is: professioneel micro-disk bouwer, aspirant manager van opkomende bands en badminton kampioen. Bovenal was ze een frequent bezocht tussenstation langs de drukke verkeersader begin-van-de-gang / einde-van-de-gang. Een mens moet af en toe eens kunnen vertellen wat er op zijn lever licht niet waar?

Tijdens het academiejaar 2011-2012 had ik het genoegen om begeleider te zijn van maar liefst 2 master-thesissen: die van Tanbir Hassan en die van Andreas De Groote. Andreas De Groote zou later onze onderzoeksgroep vervoegen. Onthoudt u deze naam goed dames en heren. Ik heb een voorgevoel dat deze man vroeg of laat een wereldrijk zal stichten. Hij heeft er alleszins een passende naam voor.

Een jaar later, gedurende het academiejaar 2012-2013 mocht ik dan weer Haolan Zhao onder mijn vleugels nemen. Ook Haolan zou zich later bij onze clan aansluiten. Het was mij zoals eerder gezegd een genoegen.

Over de jaren heen heb ik het bureau mogen delen met een aantal uitzonderlijke persoonlijkheden. Zo was er Martijn Fiers. Fiers - fear - no fear. Martijn kende geen angst. Stel: je bent op uitstap in Temse, er ligt een groot schip aangemeerd aan de kaai doormiddel van een dik touw. Wat doe je dan: uiteraard klim je op dat touw, ga je ondersteboven hangen. No fear dus. Dan was er ook Marie Verbist die mij de televisieserie How I met your mother leerde kennen. Waar ik haar niet dankbaar genoeg voor kan zijn. Er waren de stille krachten Herbert D'heer, Nebiyu Yebo en Utsav Dave die zich waarschijnlijk meer dan eens geërgerd hebben aan de chitchat van Bart Kuyken en mezelf. Sorry boys.

En dan waren er nog een hele batterij topkerels en topvrouwen die de Sint-Pietersnieuwstraat 41 en het Technologiepark in Zwijnaarde zonder twijfel de aangenaamste werkplaats van het land en ver daarbuiten maakten. Met het risico per ongeluk iemand te vergeten noem ik ze graag allemaal bij naam: Peter Bienstman, Wim Bogaerts, Nicolas Le Thomas, Dries Van Thourhout, Pieter Dumon, Rodica Morarescu. Ananth Subramanian, Jeroen Allaert, Bert Coryn, Youssef Drissi, Ilse Meersman, Michael Vanslembrouck, Danae Delbeke, de fantastische dames begin van de gang rechts: Kristien De Meulder en Ilse Van Royen, Leila Abdollahi, Koen Alexander, de fantastische actrice Suzanne Bisschop, Hongtao Chen, Soren Dhoore, Sarvagya Dwivedi, Pieter Geiregat, the ever friendly John George, Jesper Hakansson, het duo dat kerstbomen plant rond de clean-room: J-doggydog Jan-Willem Hoste en Alfonso Ruocco, Ang Li, de goeie Daan Martens, De

man met de gouden strik: Frederic Peyskens, Sanja Radosavljevic, Antonio Ribeiro, Bendix Schneider, Ashwyn Srinivasan, Bin Tian, Monsieur Paul Tiebot, Sarah Uvin, Kasper Van Gasse, Anton Vasiliev, wie anders dan Gunay Yurtsever, Yunpeng Zhu, De meester zelf Ronnnnyyyy Bockstaele, Tom Claes, Wout De Cort, Bram De Geyter, Katrien De Vos, Alban Gassenq, Joris Geessels, Samir Ghosh, Kristinn Gylfason, Nannicha Hattasan, Anthony Hope, Koen Huybrechts, Amit Khanna, Kasia Komorowska, Rajesh Kumar, Emmanuel Lambert, Francois Leo, Cristina Lerma Arce, Adil Masood, Abdoulghafar Omari, Shibnath Pathak, Parastesh Pirasteh, Khai Quang Le, Joris Roels, Sukumar Rudra, Dorian Sanchez, Shankar Kumar Selvaraja, Stevan Stankovic, Andrea Trita en last maar zeker en vast not least: Kristof Krikri Vandoorne.

U ziet, dat is een uit de kluiten gewassen onderzoeksgroep.

Laten we het even oven een andere boeg gooien. Want de boog kan niet altijd gespannen staan. En dus zoek je af en toe contact met mensen die niet zo geïnteresseerd zijn in chips. Staat u mij toe om in willekeurige volgorde nog enkele mensen te bedanken.

- Glenn Potums: mijn compadre for life. De man die schijnt te begrijpen wat ik grappig vind en niet zal twijfelen om die kennis te gebruiken.
- Eva Chaubet: al 20 jaar best friends
- Louis Franckx: top-top-topkereltje en met het risico te klinken als een bejaard man: mijn oogappel
- Kris Franckx: de vader van een top-top-topkereltje en zelf een top-top-topkerel
- Boris Kuijpers: nog zo'n compadre for life en de man waarmee ik nog vele avonturen hoop te beleven
- Ruth Mellaerts: de lovebird van Boris Kuijpers en van hetzelfde kaliber. Kan niet beter.
- De familie van Boris Kuijpers: Bart Kuijpers, Anne-Marie Buyle en Arno Kuijpers. Als er 1 plaats is ter wereld die ik mijn tweede thuis zou noemen is het jullie tipi aan de private weg.
- De overige semi-boys nighters: Hans Vandenbroeck en Kevin Put. We hebben afgesproken om hier niks over te zeggen.
- De gezellige vierhoek: Melissa Put, Jozef Tytgat, Kathy Sels, Ben Van den Bergh en Nathalie De Smet. Gezelliger dan dit wordt het niet.

- De Malinas Machinas: Glenn Potums, Melissa Put, Hans Fromthepants, Eva Chaubet, Dimmitry Van Vaerenbergh, Yana Deluster, Nickolas Ronsse, Anneleen Teck, Kathy Sels, Dennis Collen, Silke Vinckx, Charlotte Roggemans, Giuseppe Gap Temporale, Angie Baijens, Anne-Roos Vandezande, Christopher Franckx, Tommy Teck, Daniela Cocco, Thomas the thunder of the Ardennes - Aerts en Ben Van den Bergh: Jullie zijn stuk voor stuk, van kop tot teen fantastisch.
- Perumal Dharanipathy: I am patiently waiting for your first novel that you talked about on the shores of the Lac Leman. You are an inspiration.
- Henkie De Koninck en Martinie Somers: met deze twee kornuiten is het allemaal begonnen. Bedankt voor alles!! In het licht van dit werk misschien vooral voor de talloze dozen Lego die jullie voor mij gekocht hebben.
- Celine De Koninck, Claire De Koninck en Charlotte De Koninck: ik heb de 3 beste zussen ter wereld. Daar is geen discussie over. Sinds 11 juni 1988 zijn wij 1 team.
- Ruben Bruynooghe: de man van Charlotte De Koninck en een topkerel pur sang.
- Nancy Verhoft, Bert Crockaerts, Elien Bruyndonckx, Rik Crockaerts en Rebecca Meeuwes: De gezelligste (stief)familie die ik me kan wensen.
- Mijn fantastische schoonfamilie: Koen Wabbes, Karin Vansteenwegen, Charlotte Wabbes en Kobe Wabbes: ik had het niet beter kunnen treffen!
- Jozeffa Theresia Sladts: sinds 8 oktober 1986 in de vroege ochtend mijn aller beste vriendin. En de vrouw op wiens schoot ik groot geworden ben. Om u te bedanken heb ik een apart boek nodig.
- Charles Somers: de held uit mijn jonge jaren en de man aan wie ik het liefst dit boek zou willen laten zien.
- Tante Maria en Tante Jeanne: de twee stamhoofden van de Somers Clan en de warmhartigste jongedames van Grobbendonk, Koningshooikt en ver, ver daarbuiten.
- Alex Verlinden: de man die mij op 12 jarige leeftijd aan het mondaine strand van de Lilse Bergen introduceerde tot het beroep van ingenieur. En mij Delphi 3 leerde kennen. Dat was het begin.

En dan is er nog 1 iemand. Iemand heel speciaal: Lynn Wabbes. Lynn Wabbes is de vrouw die altijd, *altijd* klaar staat als het iets minder vlot gaat dan voorop gesteld. Lynn Wabbes is de vrouw die u kan doen lachen als het moet en zelfs als het niet moet. Lynn Wabbes is de eerste aan wie ik wil vertellen dat iets gelukt is. Lynn Wabbes doet dan zelfs de moeite om te begrijpen wat er juist gelukt is. Lynn Wabbes is mijn ultieme Compagnon de route (met een hoofdletter) en zonder haar

zou het hierna volgende verhaal er nooit gekomen zijn. Al de rest zeg ik wel tegen haar apart.

Ok, we kunnen er aan beginnen. Sit back and relax want het gaat een flitsend avontuur worden.

Februari 2015
Yannick De Koninck

Table of Contents

List of Figures

List of Tables

List of Acronyms

B

BE	Band-edge
DBR	Distributed Bragg Reflector
BCB	Benzocyclobutene
DFB	Distributed Feedback

C

CMOS	Complementary Metal-Oxide Semiconductor
CW	Continuous Wave

D

DC	Duty Cycle

E

eDBR	evanescent Distributed Bragg Reflector

F

FDTD	Finite Difference Time Domain
FIB	Focused Ion Beam

FP	Fabry-Perot
FT	Fourier Transform
FWHM	Full-Width at Half Maximum

H

HBED	Hybrid Band-Edge Defect
HEMT	High-Electron Mobility Transistors

I

ICP	Inductively Coupled Plasma
IPA	Iso-Propyl Alcohol
IV	Current / Voltage
IVBA	Inter Valence Band Absorption

J

IR	Infra Red

M

MPW	Multi Project Wafer
MQW	Multi-Quantum Well

O

OSA	Optical Spectrum Analyser

P

PECVD	Plasma-Enhanced Chemical Vapour Deposition

PIC	Photonic Integrated Circuit
PR	Photoresist

R

RIE	Reactive Ion Etcher
RPM	Revolutions per minute
R/T spectrum	Reflection / Transmission spectrum

S

SCH	Separate Confinement Heterostructure
SEM	Scanning Electron Microscope
SMSR	Side-Mode Suppression Ratio
SOI	Silicon on Insulator
SRH	Shockley Read Hall

T

TE	Transverse Electric
TLM	Transmission Line Measurement
TM	Transverse Magnetic

Nederlandse samenvatting –Summary in Dutch–

Gedurende de laatste 20 jaar is het veld van de geïntegreerde fotonica, en dan in het bijzonder de silicium-fotonica, uitgegroeid tot een belangrijke technologie die een brede waaier aan nieuwe toepassingen mogelijk maakt, zoals toekomstige hogesnelheids, korte-afstands-interconnecties [1]. Een van de belangrijkste componenten in zulke geïntegreerde systemen is de laser-bron. Om laser-functionaliteit naar het silicium fotonica plaftorm te brengen lijkt de meest realistische aanpak op korte termijn de heterogene integratie van III-V materialen [2]. Sinds de eerste experimentele demonstraties van deze technologie ongeveer 10 jaar geleden [3], probeert men steeds vaker de drempelstroom en totale energieconsumptie van zulke lasers te verlagen. Microschijflaser [1] halen een drempelstroom onder het mA-niveau maar hebben geen sterk golflengte selectie mechanisme waardoor zulke lasers een lage zij-mode onderdrukking hebben. Recent werk rond korte-caviteits gedistribueerde Bragg reflectie hybride silicium lasers levert drempelstromen van 8.8 mA [4] voor lasers met een hoge zijmode onderdrukking.

Het doel van dit werk is om een nieuw type heterogeen geïntegreerde III-V op silicium laser voor te stellen, te ontwerpen, te fabriceren en experimenteel te demonstreren. Deze laser zal zich onderscheiden van de meest recente resultaten te vinden in de wetenschappelijke literatuur door de unieke combinatie van de volgende eigenschappen:

- Lage drempel stroom (mA niveau)
- Enkelvoudige lasermode (hoge zijmode onderdrukking $>$ 30dB zonder te verspringen tussen zijmodi)
- De definitie van de III-V golfgeleider zo eenvoudig mogelijk: geen adiabatische tapers, geen roosters. De golfgeleider moet met contactlithografie worden gedefinieerd, wat wil zeggen met gelimiteerde resolutie en handmatige alignatie.
- Zo veel mogelijk gebruik maken van de beschikbare productiefaciliteiten uit de electronica-industrie (CMOS): ontwerp de laser op een dusdanige manier dat het golflengte selectiemechanisme vooral in de silicium laag wordt gedefineerd.

Om aan deze lijst voorwaarden te voldoen, stellen we een nieuwe aanpak voor gebaseerd op resonante spiegels. Twee identieke passieve silicium roostercaviteiten zijn evanescent gekoppeld met eenzelfde III-V golfgeleider. De III-V golfgeleider ligt boven de silicium caviteiten en samen vormen zij een lineaire structuur, zoals afgebeeld op figuur 1a. Als een eigenmode met de resonantiegolflengte van de silicium caviteit door de III-V golfgeleider propageert zal deze de silicium caviteit exciteren. De energie die zich opbouwt binnenin de silicium caviteit zal op haar beurt terugkoppelen in de III-V golfgeleider en dat zowel co-directioneel met het invallend licht als contra-directioneel. Het co-directioneel terugkoppelende licht zal destructief interfereren met de propagerende eigenmode in de III-V golfgeleider terwijl het contra-directioneel terugkoppelend licht terug in de III-V golfgeleider koppelt richting de andere silicium caviteit. Daar zal het vervolgens weer worden gereflecteerd zodat binnenin de III-V golfgeleider een resonantie ontstaat.

Moderne CMOS fabricagetechnieken laten toe om compacte silicium caviteiten te maken met een hoge kwaliteitsfactor. Met andere woorden, deze aanpak laat toe om spiegels te ontwerpen die een hoge reflectiviteit bezitten binnen een smalle bandbreedte en dat over een korte interactielengte. Door de aard van het ontwerp van deze spiegels kan het gegenereerde laser licht makkelijk in een externe silicium golfgeleider worden gekoppeld zonder gebruik te maken van taper structuren. Een externe silicium golfgeleider kan simpelweg gekoppeld worden aan een (of beide) silicium caviteiten om zo een kleine fractie van de energie die zit opgeslagen in de silicium caviteit te extraheren en richting het SOI circuit te leiden.

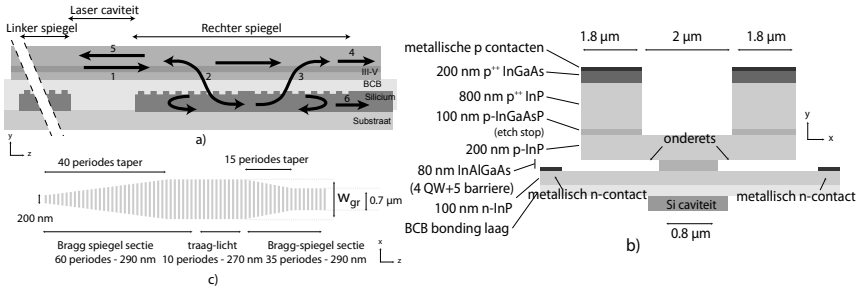

Figuur 1: Schematische representatie van: a) de laser layout behandeld in dit werk b) de III-V golfgeleider dwarsdoorsnede c) de geoptimaliseerde silicium caviteit

Door verstrooingstheorie toe te passen, een wiskundig raamwerk geleend uit de kwantummechanica en bruikbaar om lineaire bi-directionele optische caviteiten, langs de zijkant gekoppeld aan een golfgeleider, te bestuderen, kunnen de maximale reflectiviteit R_{max} en bandbreedte $\Delta\lambda$ door middel van twee opmerke-

lijk eenvoudige vergelijkingen worden beschreven:

$$R_{max} = \frac{1}{1 + Q_\kappa/Q_i} \tag{1}$$

$$\frac{\Delta\lambda}{\lambda_c} = \frac{1}{Q_i} + \frac{1}{Q_\kappa} \tag{2}$$

waarbij Q_i de intrinsieke kwaliteitsfactor (Q-factor) van de de caviteit is en Q_κ een pseudo-Q-factor die gerelateerd is aan de koppelsterkte tussen de III-V golfgeleider en de silicium caviteit. λ_c is de resonantiegolflengte van de caviteit. Hoewel deze twee vergelijkingen niet makkelijk betrouwbare numerieke resultaten opleveren geven ze wel een goed inzicht in de afwegingen die gemaakt moeten worden bij het ontwerpen van resonante spiegels: hoge reflectiviteit kan worden bekomen als de verliezen in de cavitiet veel lager zijn dan de koppelsterkte tussen de III-V golfgeleider en de caviteit. In dit geval wordt de reflectorbandbreedte bepaald door de koppeling: $\Delta\lambda = \lambda_c/Q_\kappa$. Deze twee eenvoudige vergelijkingen dienen als gids bij het bestuderen van de eigenschappen van resonante spiegels. Hoge reflectiviteit ($> \ 90\%$) kan worden behaald binnen een bandbreedte van slechts enkele nanometers met een silicium caviteit die niet langer is dan $25\,\mu m$.

Eerst wordt een optisch gepompte structuur voorgesteld om de potentiële voordelen van resonante spiegels als reflectoren in III-V op silicium lasers te bevestigen. Deze laser meet slechts $55\,\mu m$ lang en $2\,\mu m$ breed. Het drempelpompvermogen van dit experimenteel aangetoonde ontwerp bedroeg enkele miliWatts en de laser opereerde in een enkelvoudige mode met een zijmode onderdrukking tot 39 dB.

Desalniettemin is de praktische toepasbaarheid van een optisch gepompte laser eerder gering en is de Heilige Graal van dit werk een elektrisch geïnjecteerde laser. Om elektrische injectie te bekomen dienen metallische contacten te worden geplaatst op de III-V golfgeleider om de injectie van elektrische ladingsdragers mogelijk te maken. Deze metalen structuren moeten ver genoeg van de optische mode worden geplaatst om hoge absorptieverliezen te vermeiden. Bijgevolg is de III-V golfgeleider traditioneel een dikke structuur ($\sim 1 - 2\mu m$) met typisch een hoge effectieve brekingsindex van ongeveer 3.4. Bovendien ondersteunt zo'n III-V golfgeleider verschillende geleide optische modi.

De effectieve brekingsindex van een $220\,nm$ hoge, oneindig brede silicium golfgeleider bedraagt ongeveer 2.8 bij een golflengte van $1550\,nm$. Met andere woorden, door gebruik te maken van een traditionele III-V golfgeleider is er een significant verschil tussen de effectieve brekingsindex van die golfgeleider en de silicium caviteit. Zo'n aanzienlijk verschil leidt tot een lage koppelsterkte en bijgevolg een lage maximale reflectiviteit van de resonante spiegels. Bovendien heeft de silicium caviteit een extra verliesmechanisme: licht lekt naar de hogere-orde modi van de III-V golfgeleider die een lagere effectieve brekingsindex hebben dan de fundamentele mode.

Om dit probleem op te lossen moet de effectieve brekingsindex van de III-V golfgeleider verlaagd worden om beter overeen te komen met de effectieve brekingsindex van de silicium caviteit. Er moet wel voor worden gezorgd dat er steeds een pad beschikbaar is voor de elektrische ladingsdragers om zich van de metallische contacten naar de actieve laag te begeven. Dit kan door middel van 2 ingrepen:

- het etsen van een sleuf in de toplagen van de III-V golfgeleider om de optische mode naar beneden te down
- het onder-etsen van de multi-kwantum put laag (MQW - eng. : *multi-quantum well*) om de afmeting van de optische mode ook lateraal te beperken.

Het voorgestelde ontwerp wordt weergegeven in figuur 1. De sleuf in de p-gedopeerde lagen is $2\,\mu m$ breed en de MQW laag wordt ondergeetst tot een totale breedte van slechts $800\,nm$. Door deze aanpassingen daalt de effectieve brekingsindex van de III-V golfgeleider tot een waarde van ongeveer 2.85. Bovendien is het aantal geleide modi die deze structuur ondersteunt vele malen verkleind.

Zoals eerder gezegd is optische koppelsterkte tussen de III-V golfgeleider en de silicium caviteit niet de enige factor die de reflectie van de spiegels bepaalt. Ook de intrinsieke Q-factor speelt een belangrijke rol. In de optische gepompte laser bestond de silicium caviteit uit een 1-dimensionaal rooster met een kwart-golflengte defect in het midden. Door verstrooiing ten gevolge van zo een abrupt defect stagneert de intrinsieke Q-factor van zulke caviteiten bij een waarde van ongeveer 4000. Om de intrinsieke kwaliteitsfactor verder te verhogen kan het abrupte kwart-golflengte defect vervangen worden door een meer adiabatische overgang door middel van een 10-perioden lang rooster met een kortere periode dan de omsluitende spiegel-roosters. Hierdoor verhoogt de kwaliteitsfactor van 4000 naar meer dan 60000.

Figuur 2 toont de reflectie en transmissie spectra van de resonante spiegel die bestaat uit de III-V golfgeleider geometrie zoals getoond in figuur 1b en de caviteit zoals in figuur 1c. Deze spectra werden uitgerekend doormiddel van 3D eindige differentie - tijdsdomein simulaties [5]. De silicium caviteit is $1.5\,\mu m$ breed en de afstand tussen de onderkant van de III-V golfgeleider en de top van de silicium caviteit bedraagt $200\,nm$. Bij de resonantiegolflengte reflecteert de spiegel 88% van het invallend licht binnen een $1.27nm$ brede golflengte band. Met een afstand van $100\,\mu m$ tussen de caviteiten bedraagt de totale lengte van de laser $160\,\mu m$. Een eenvoudig lasermodel voorspelt een drempelstroom tussen $1.5\,mA$ en $10\,mA$. Deze grote spreiding wordt veroorzaakt door de grote onzekerheid op de Auger-recombinatiecoefficient en de de oppervlakterecombinatiecoefficient.

Buiten de drempelstroom is ook de serie-weerstand een belangrijke eigenschap van halfgeleider-lasers . Vooral de dunne p-gedopeerde regio die de twee pilaren

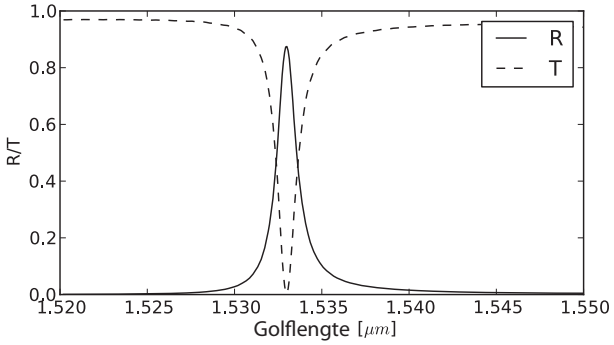

Figuur 2: Gesimuleerd reflectie en transmissie spectrum van de elektrisch genjecteerde resonante spiegel

verbindt met de actieve laag kan voor problemen zorgen. De doperingsniveaus werden gekozen door hoge optische verliezen af te wegen met een hoge serie-weerstand. De totale serie-weerstand wordt geraamd op $37.4\,\Omega$. Ongeveer de helft hiervan kan worden toegeschreven aan de p-gedopeerde regio tussen de actieve laag en de p-gedopeerde pilaren. De andere helft wordt verdeeld over de dunne n-gedopeerde laag en de p-pilaren (inclusief contactweerstanden).

Tenslotte is ook de thermische weerstand tussen de actieve laag en het substraat van groot belang omdat deze bepaalt in welke mate de laserjunctie zal opwarmen als functie van het verbruikte vermogen. Verhoogde temperaturen zorgen meestal voor een verlaagde performantie van halfgeleiderlasers. Door gebruik te maken van een commercieel eindige-elementen computerprogramma kan de thermische weerstand geschat worden op $1.58K/mW$. Deze hoge thermische weerstand wordt vooral veroorzaakt door de $2\,\mu m$ dikke siliciumoxide buffer laag tussen de optische silicium laag en het substraat. Deze oxide laag verhindert efficiënte afvoer van warmte naar het substraat.

Om de III-V golfgeleiderstructuur afgebeeld in figuur 1b te fabriceren werd een toegewijd technologisch proces ontwikkeld. De passieve SOI wafers die de silicium rooster-caviteiten reeds bevatten worden gefabriceerd in een CMOS productielijn bij IMEC georganiseerd door ePIXfab [6]. Na zorgvuldig het oppervlak van de silicium chip schoon te maken wordt een dunne laag benzocyclobuteen (BCB) aangebracht. Een 4mm bij 8mm niet-bewerkte InP chip, met haar bruikbare lagen bovenaan, wordt na zorgvuldig schoonmaken en het aanbrengen van een $150\,nm$ dikke oxide laag (die de adhesie met BCB versterkt) ondersteboven op de silicium chip geplaatst. De temperatuur wordt verhoogd en er wordt druk aangebracht op de chip-combinatie. Nadat de BCB laag gebakken en gepolymeriseerd is wordt het InP substraat verwijderd door middel van waterstof-chloride. Enkel een dunne laag ($\sim 1.5\mu m$) III-V materiaal blijft over. Zoals afgebeeld op

figuur 1b bestaat deze laag uit: 200 nm sterk p-gedopeerd InGaAs, 800 nm sterk p-gedopeerd InP, 100 nm p-gedopeerd InGaAsP, 200 nm p-gedopeerd InP, een 80 nm MQW laag uit InAlGaAs en een 100 nm n-gedopeerde InP laag.

Een siliciumoxide laag wordt aangebracht waarop eerst de patronen van de III-V golfgeleiderstructuur kan worden aangebracht die dan wordt getransfereerd naar de III-V laag door middel van een natte ets. Na elke ets van ternair of quaternair materiaal wordt een conforme laag siliciumnitride gedeponeerd en onmiddellijk weer anisotroop weggeëtst zodat de zijwanden van de structuur beschermd blijven van andere natte etsstappen verder in het proces. Dit is vooral belangrijk bij het onder-etsen van de MQW regio omdat dan de chip een lange tijd ondergedompeld wordt in een citroenzuur etsmengsel dat ook de InGaAs en InGaAsP lagen wegetst.

Er moet tijdens de fabricage ook aandacht besteed worden aan de mechanische stabiliteit van de InP structuur. Onmiddellijk na het onderetsen van de MQW regio worden de pilaren enkel ondersteund door de dunne p-gedopeerde InP regio die hen verbindt met de actieve laag. Hoewel de zwaartekracht slechts een beperkte rol speelt op zulke kleine schaal, kunnen thermische effecten en interne spanning de structuur alsnog instabiel maken. Om de stabiliteit te verhogen wordt de regio tussen de pilaren versterkt met een 200 nm dikke silicium nitride laag. Op die manier kunnen de MQWs veilig worden onder-geëtst. Nadien wordt een dunne laag BCB aangebracht die het ondergeëtste volume opvult. Eens deze BCB gebakken is is de structuur mechanisch stabiel en kan de versterkende silicium nitride laag worden weggehaald. Na het etsen van de III-V structuur kunnen metaalcontacten worden aangebracht. De structuur wordt geplanariseerd met BCB en nadat er openingen zijn gemaakt naar het n-InP kunnen de gouden pads worden gedeponeerd waarmee de structuren via probe naalden zullen kunnen worden uitgemeten.

Figuur 3 toont een scanning-elektronen microscoop (SEM) beeld van een doorsnede van de laser gemaakt door met een gefocuste ionenbundel een snede in de laser te maken. De afbeelding toont de structuur zoals die werd ontworpen in figuur 1b. De BCB laag is slechts 40 nm dik. Opgeteld bij de 150 nm dikke silicium oxidelaag die op de III-V laag werd gedeponeerd voor het bondingsproces komt dit op een totale afstand van 190 nm tussen de onderkant van de III-V golfgeleider en de bovenkant van de silicium caviteit. Zoals eerder gezegd meet de laser in totaal $160\,\mu m$ lang. De lasers werden uitgemeten door probe-naalden aan te verbinden met de gouden pads op de chip en vervolgens 100ns lange stroompulsen met een herhalingsinterval van $5\,\mu s$ doorheen de laser te pompen. De laser koppelt het gegenereerde licht vervolgens in een silicium golfgeleider die via een roosterkoppelaar in een glasvezel koppelt. Deze glasvezel splitst in twee waarbij de helft van het licht naar een vermogenmeter gaat en de andere helft naar een optisch spectrum analysetoestel.

Figuur 4(linkse as) toont het opgevangen piekvermogen in de glasvezel als functie van de piekstroom bij een gestabiliseerde substraattemperatuur van $20°C$.

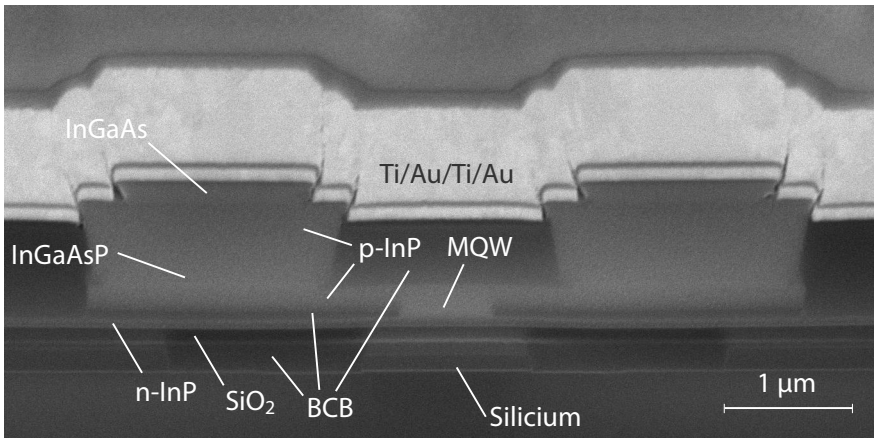

Figuur 3: SEM beeld van de dwarsdoorsnede van de gefabriceerde laser. De III-V golfgeleider en onderliggende silicium caviteit kunnen worden onderscheiden

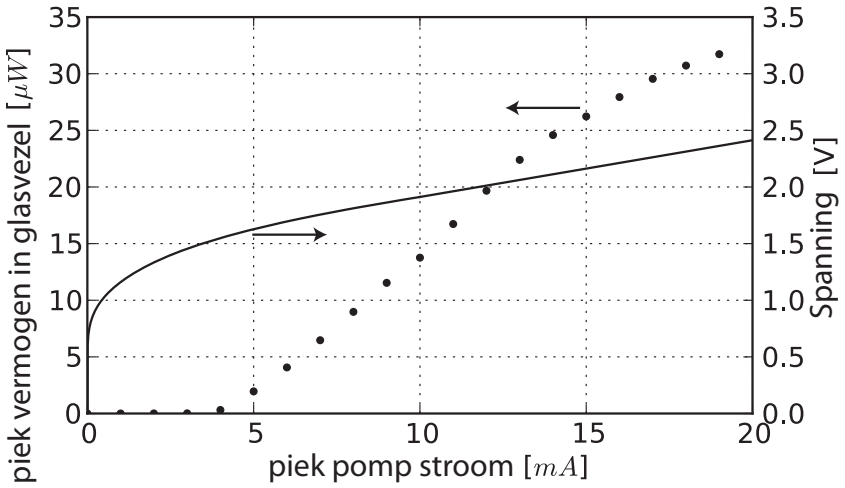

Figuur 4: Optisch vermogen zoals gemeten in de glasvezel en spanning tussen de elektroden van de laser als functie van de stroom die door de structuur vloeit

Deze grafiek toont duidelijk de laserdrempel bij $4\,mA$. Door rekening te houden met de opgemeten verliezen van de roosterkoppelaar (7 dB) en het feit dat de laser aan beide zijden licht uitstraalt (3 dB) kan worden aangenomen dat het piekvermogen dat door de laser wordt uitgestraald in de silicium golfgeleiders nog 10

maal groter is dan de opgemeten waarden. Dit leidt dan tot een differentiële efficiëntie van $30\,\mu W/mA$. De rechter as van figuur 4 toont de opgemeten spanning tussen de metallische contacten als functie van de injectiestroom. Uit deze informatie kan een serie-weerstand van $50\,\Omega$ worden afgeleid.

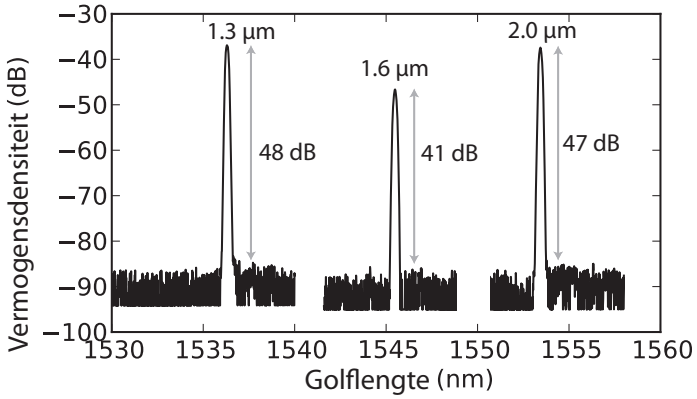

Figuur 5: Spectra van drie verschillende laser, elk met een verschillende silicium caviteits-breedte

Figuur 5 op haar beurt toont dan weer de spectra van 3 verschillende lasers. Deze hebben hetzelfde III-V golfgeleiderontwerp en lengte, maar hebben elk een verschillende silicium caviteitsbreedte. Door de breedte van de silicium caviteit te variëren verandert de resonantiegolflengte en bijgevolg ook de golflengte waarop de laser licht uitzendt. De drie lasers emitteren in 1 enkele longitudinale mode met een zijmode onderdrukking tot 48 dB.

Het was echter niet mogelijk om de laser in continu bedrijf aan te sturen. De reden daarvoor is hoogst waarschijnlijk de hoge thermische weerstand. Uit opgemeten data kan deze ook experimenteel geschat worden op 1.6 K/mW. Simulaties tonen echter aan dat een eenvoudige ingreep, zoals een gouden hitte-verspreider bovenop de pilaren deze thermische weerstand met een factor 3 kan verlagen waardoor aansturing in continu bedrijf mogelijk zou kunnen worden.

Referenties

[1] Thijs Spuesens, Johan Bauwelinck, Philippe Regreny, and Dries Van Thourhout. *Realization of a Compact Optical Interconnect on Silicon by Heterogeneous Integration of IIIV*. IEEE Photonics Technology Letters, 25(14):1332–1335, July 2013.

[2] Gunther Roelkens, Liu Liu, Di Liang, Richard Jones, Alexander Fang, Brian Koch, and John Bowers. *III-V/silicon photonics for on-chip and inter-chip optical interconnects*. Laser & Photonics Reviews, 4(6):751–779, November 2010.

[3] A W Fang, H Park, R Jones, O Cohen, M J Paniccia, and J E Bowers. *A continuous-wave hybrid AlGaInAs-silicon evanescent laser*. IEEE Photonics Technology Letters, 18(9-12):1143–1145, 2006.

[4] Chong Zhang, Sudharsanan Srinivasan, Yongbo Tang, Martijn J. R. Heck, Michael L. Davenport, and John E. Bowers. *Low threshold and high speed short cavity distributed feedback hybrid silicon lasers*. Optics Express, 22(9):10202, April 2014.

[5] Lumerical Solutions http://www.lumerical.com. *Lumerical FDTD*.

[6] The Silicon Photonics Platform-ePIXfab http://www.epixfab.eu. *ePIXfab*, 2012.

English summary

Over the past two decades, integrated photonics, and silicon photonics in particular, has gained importance as a technological enabler for a wide range of exciting new applications such as future high-speed short distance interconnects [1]. One of the key components in such densely integrated systems is the laser source. To bring laser functionality to the silicon platform, the most promising short-therm approach is the heterogeneous integration of III-V materials [2]. Ever since the first experimental demonstrations of this technology in the second half of the previous decade [3], there has been a trend to reduce the laser threshold and to lower the overall power consumption. Microdisk lasers [1] can reach sub-mA threshold currents but suffer from the absence of a strong wavelength selection mechanism which results in a low side-mode suppression ratio. Recent work on short-cavity DFB hybrid silicon lasers shows that excellent continuous wave (CW), single mode laser performance can be accomplished with threshold currents as low as 8.8mA [4].

The aim of this work is to propose, design, fabricate and demonstrate a new type of heterogeneously integrated III-V on silicon laser that distinguishes itself from the current state of the art due to the unique combination of the following properties:

- Low threshold current (mA level)
- Single mode (high side-mode suppression ratio $>$ 30dB + no mode hops)
- III-V waveguide patterning as simple as possible: no tapers, no gratings. Contact lithography (limited resolution + manual alignment accuracy) should be sufficient to pattern the laser's III-V layer.
- Harness the power of CMOS processing: design the laser in such a way that the wavelength selective mechanism is mainly defined in the silicon layer.

To accomplish this, a novel approach, based on resonant mirrors is presented. Two identical passive silicon grating cavities are coupled to the same III-V waveguide above to form a linear device as shown schematically in figure 6a. Each silicon cavity is evanescently coupled to the InP waveguide. If the optical mode in the InP waveguide is of the silicon cavity's resonance wavelength, the silicon cavity will be excited. The energy built-up inside the silicon cavity couples back into the

the InP waveguide both co- and counter-directionally to the incoming light. The co-directional light will interfere destructively with the InP waveguide mode while the counter-directionally coupled light propagates back into the III-V waveguide. CMOS manufacturing techniques allow for compact, high-Q silicon cavities, so this approach enables high, narrow band reflectivity over a short distance. Due to the resonant mirror design, the generated laser light can be coupled into an external silicon waveguide without the use of tapers in the III-V layers, which are often difficult to make. An external waveguide can be coupled to one (or both) of the silicon cavities to extract a small amount of the energy built up inside the cavity and guide it into the SOI circuit.

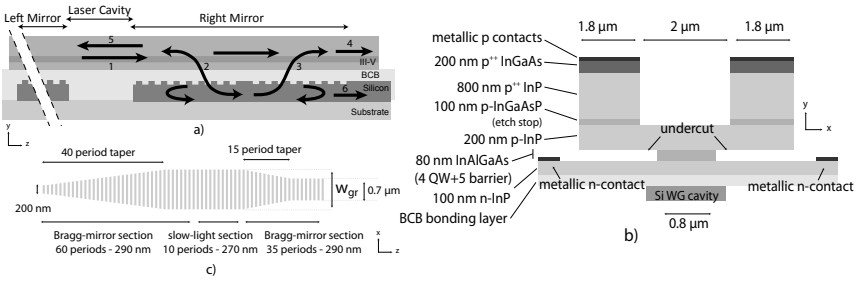

Figure 6: Schematic representation of a) the laser layout presented in this work showing the resonant mirror. b) III-V waveguide cross-section proposed in this work. c) Optimized silicon cavity design

By applying scattering theory, a mathematical framework borrowed from quantum mechanics and applicable to linear bidirectional optical resonators side-coupled to a waveguide, the maximum reflectivity R_{max} and reflection bandwidth $\Delta\lambda$ can be expressed in two surprisingly simple equations:

$$R_{max} = \frac{1}{1 + Q_\kappa / Q_i} \tag{3}$$

$$\frac{\Delta\lambda}{\lambda_c} = \frac{1}{Q_i} + \frac{1}{Q_\kappa} \tag{4}$$

where Q_i is the silicon cavity's intrinsic quality factor and Q_κ is a pseudo-Q-factor that is related to the coupling strength between the III-V waveguide and the silicon cavity. λ_c is the silicon cavity's resonance wavelength. Although these two equations are not very helpful in providing robust numerical data, they give excellent insight in the mirror's design trade-offs: high reflectivity is reached if the losses in the cavity are much lower (Q_i is high) than the coupling strength between the waveguide and the cavity (Q_κ is low). In this case the reflection bandwidth is determined by the coupling strength (λ_c / Q_κ). Using these two equations as a guideline, the properties of resonant mirrors using different types of silicon

cavities are investigated. High reflectivity of $> 90\%$ is reached with a bandwidth as narrow as a few nanometers with silicon cavities no longer than $25\,\mu m$.

First, an optically pumped proof-of-concept device is presented to confirm the potential advantages of using resonant mirrors as reflectors in III-V on silicon lasers. The total laser is only $55\,\mu m$ long and $2\,\mu m$ wide. The threshold pump power of this experimentally demonstrated device was mW-level and the laser operated in single mode with a side-mode suppression ratio of up to 39dB.

However, the practical usability of optically pumped lasers is rather limited, so the aim of this work is an electrically injected resonant mirror laser. To achieve electrical pumping, metallic contacts have to be placed on the III-V waveguide structure to allow injection of electrical carriers. These metallic structures should be placed sufficiently far away from the optical mode to prevent excessive loss due to absorption in the metal and the highly doped (and absorbing) semiconductor used to make good ohmic contacts. This leads to a relatively thick III-V waveguide ($\sim 1 - 2\mu m$) with a typical effective index of ≈ 3.4. Moreover, such a large waveguide supports multiple transversal modes. In this work, laser sources are integrated on the widely adopted $220\,nm$ SOI platform. The effective index of a $220\,nm$ silicon slab waveguide is around $n_{eff,SOI} \approx 2.8$ at 1550 nm. In other words, when using the traditional approach to heterogeneous integration, the III-V laser mesa and the underlying SOI waveguide layer are far from phase-matched. However, such severe phase-mismatch decreases the coupling strength between the silicon cavity and the III-V waveguide significantly, which deteriorates the resonant mirror effect.To make things even worse, the silicon cavity is phase-mathed to the higher-order modes of the III-V waveguide. These higher order modes can be considered as leakage paths the silicon cavity which can be modelled as a decrease of the cavity's intrinsic Q-factor.

To overcome this problem, the effective index of the III-V waveguide should be reduced to better match the silicon cavity but still allowing a path for the electrical carriers to flow to the active region. This can be accomplished by taking two measures:

- Etching a wedge in the top layers of the III-V mesa to push the optical mode down.

- Undercut the multi-quantum well (MQW) region to reduce the size and effective index of the III-V mode laterally.

The proposed design is reproduced in figure 6b. The gap in the p-layers is $2\,\mu m$ wide and the MQWs are undercut to reach a width of $800\,nm$. By making these adjustments, the effective index of the III-V mode is reduced to $n_{eff,III-V} = 2.85$. Moreover, this III-V waveguide structure only supports a handful of higher order modes, all spaced sufficiently far away from the silicon cavity's resonance mode

in both real and reciprocal space to prevent leakage from the cavity to these modes.

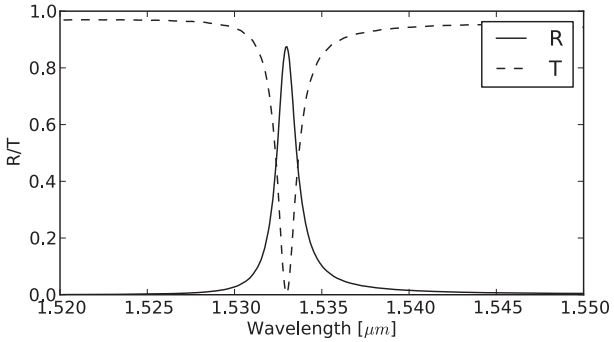

Figure 7: Simulated reflectivity and transmission spectrum of the electrically pumped resonant mirror laser

As discussed earlier, optical coupling efficiency between the III-V waveguide and the silicon cavity is not the only factor determining the maximum reflectivity of resonant mirrors. This is also determined by the intrinsic Q-factor of the silicon cavity. In the optically pumped device, the silicon cavity that is used is a 60 period shallow-etched grating with a quarter wave defect in the center. Due to scattering at the quarter-wave defect, the intrinsic Q-factor of this type of cavity saturates at around 4000, even for longer gratings. To reduce scattering at the defect, the quarter wave section can be replaced by a 10 period ($275\,nm$ pitch) long slow-light section in between the $295\,nm$ period cavity mirror gratings. This setup is shown in figure 6c. This improvement increases the intrinsic Q-factor of an 80 period (total number of periods) grating by an order of magnitude from ~ 4000 to ~ 60000.

Figure 7 shows the reflection and transmission spectrum of the resonant mirror using the III-V waveguide cross-section shown in figure 6b and the silicon cavity illustrated in figure 6c, calculated using full-vectorial 3D FDTD [5]. The silicon grating is $1.5\,\mu m$ wide (w_{gr} and the distance between the bottom of the III-V layer and the top of the silicon layer is $200\,nm$. At its resonance wavelength, the mirror reflects 88% of the incoming light in a $1.27\,nm$ FWHM wavelength band. With a spacing of $100\,\mu m$ between the silicon cavities, the total length of the device adds up to $160\,\mu m$. By using a rate equations model, it can be shown such a resonant mirror laser yields a threshold current that lies between $1.5mA$ and $10\,mA$. The large spread on this number is due to the uncertainty on the Auger recombination rate and the surface recombination rate.

Besides the threshold current, another important metric in semiconductor lasers is the device's series resistance. Especially the p-doped slab connecting the pillars to the active region is of concern. The doping levels of the different p- and n-

doped layers are designed as to trade-off low optical loss due to absorption with a low series resistance. The total series resistance is estimated to be 37.4Ω. About half of this can be attributed to the p-doped slab connecting the pillar to the active region. The other half is evenly distributed between the pillar itself and the n-InP slab connecting the active region to the metallic n-contacts.

Finally, the thermal resistance between the active region and the silicon substrate is another important metric because it determines at what rate the multi-quantum well region will heat up as a function of the dissipated power. This is of special interest because elevated temperatures tend to degrade the laser's performance.Using a commercial finite-element solver, the thermal resistance between the active region and the silicon substrate can be estimated around 1.58K/mW. This high thermal resistance is mainly due to the thick $2\mu m$ SiOx buried oxide layer that prevents efficient heat flow from the laser to the underlying substrate.

To fabricate the III-V waveguide geometry depicted in figure 6 we developed a dedicated technological process. The patterned, passive SOI wafers are fabricated in a multi-project wafer run with ePIXfab [6] and were fabricated in IMEC's 200mm CMOS pilot line. After thorough surface-clean and -preparation, a thin layer of Benzocyclobutene (BCB) [7] is spin coated on the SOI die and a 4mm by 8mm unpatterned InP die containing the appropriate epitaxial layers is bonded up-side-down on the SOI substrate. As shown on figure 6b, the III-V stack consists of a heavily p-doped InGaAs top contact layer on top of an 800 nm thick p-doped InP layer making up the pillars. Underneath this heavily p-doped InP layer lies a 100 nm thick InGaAsP etch-stop layer to assure that the height of the lightly doped InP layer underneath, connecting the pillars to the active area, is always 200 nm. The 80 nm thick active layer consists of 4 strained InAlGaAs quantum wells enclosed by strain-compensating InAlGaAs barriers layers. The n-doped InP layer connecting the active area to the n-type metallic contacts is 100 nm thick.

Before bonding, the III-V die is cleaned and a $150\,nm$ SiOx layer is deposited to increase adhesion to the BCB layer and to set the distance between the bottom of the III-V stack and the top of the silicon waveguide to the desired value. Since the BCB layer is around 40 nm and the uncertainty on PECVD-deposited silicon oxide films is low, this strategy should yield low variance on the distance between the top of the silicon layer and the bottom of the III-V layer. The III-V die is placed upside-down on the patterned SOI die containing a thin, spin coated, layer of BCB. The temperature is elevated and force is applied. After BCB curing, the InP substrate and etch-stop layers are removed and what is left is a thin (approximately $1.5\,\mu m$ thick) slab of III-V epitaxy. The pillars are defined in a SiO_2 hard mask using contact-lithography with manual alignment. The III-V layers are wet-etched in their appropriate acidic solutions (InP in HCl-based solutions and ternary/quaternary compounds in sulphuric or citric acid based solutions). After etching each layer of ternary or quaternary compound, a conformal silicon nitride film is deposited and immediately etched in a reactive ion etcher (RIE) using a

highly anisotropic recipe. This technique covers the exposed side-walls of the etched ternary or quaternary compounds and prevents etching of these layers in future steps. Because the MQW region consists of quaternary InAlGaAs-based layers that will have to be etched (undercut) for a long time this sidewall protection is of major importance.

Special attention should also be given to the mechanical stability of the InP structure. Immediately after undercutting the MQW region, the pillars are suspended and connected to the center part by the thin and fragile $200\,nm$ thick p-doped InP layer. Although gravitational forces are of limited importance at such a small scale, fluidic forces, thermal expansion and internal stress can still render the structure mechanically unstable. For this reason the gap in between the pillars is reinforced with a $200\,nm$ thick tensile strained silicon nitride layer. This increases the mechanical stability significantly and allows for safe etching of the MQW region. After the undercut is done, which takes around an hour in a stirred citric acid:H_2O_2 (20:1) bath, a thin layer of BCB is spin coated with the nitride reinforcement layer still in place. The diluted BCB solution will fill up the void created by the undercut and mechanically stabilise the structure. After the BCB is cured, all dielectric layers can be removed. The metallic n-contacts are deposited, the structure is planarized using a thick BCB layer, p-contacts are deposited, a via is etched to reach to the n-contacts underneath the BCB layer and finally thick gold-pads are deposited to facilitate electrical probing.

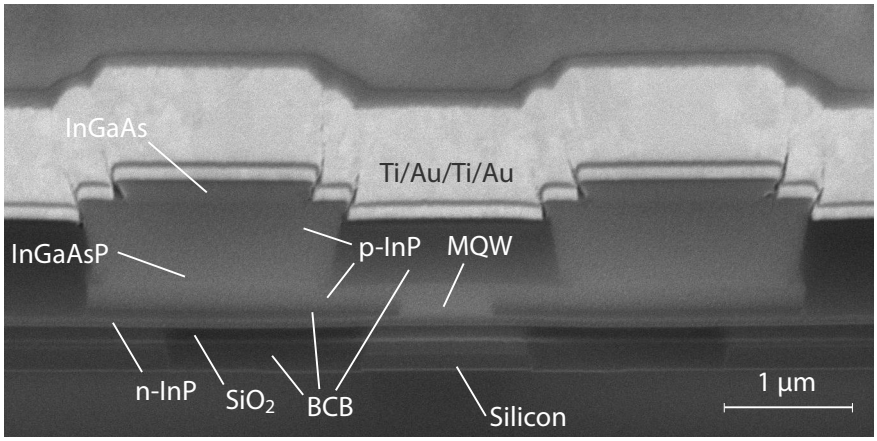

Figure 8: SEM picture of the cross-section of the fabricated devices showing the III-V waveguide and the silicon cavity.

Figure 8 shows a scanning-electron microscope (SEM) image of the device cross-section made using focused ion beam milling. The image shows the structure as proposed in the bottom panel of figure 6. The BCB layer is only 40 nm thick.

Adding the 150 nm thick SiO_2 layer deposited on the InP die before bonding results in a total distance between the bottom of the n-InP layer and the top of the silicon waveguide of 190 nm. Each silicon cavity is $30\mu m$ long and the cavities are spaced $100\,\mu m$ apart. Consequently the total device measures $160\,\mu m$ in length. The devices were measured by connecting probe needles to the on-chip electrical pads and pumping them with $100\,ns$ long current pulses with a pulse repetition interval of $5\,\mu s$. The laser couples the generated laser light into an SOI waveguide which leads to a grating coupler that diffracts the light into a single mode fiber. This fiber is directed into a 50/50 coupler sending half of the light into an optical power meter and the other half to an optical spectrum analyzer (OSA).

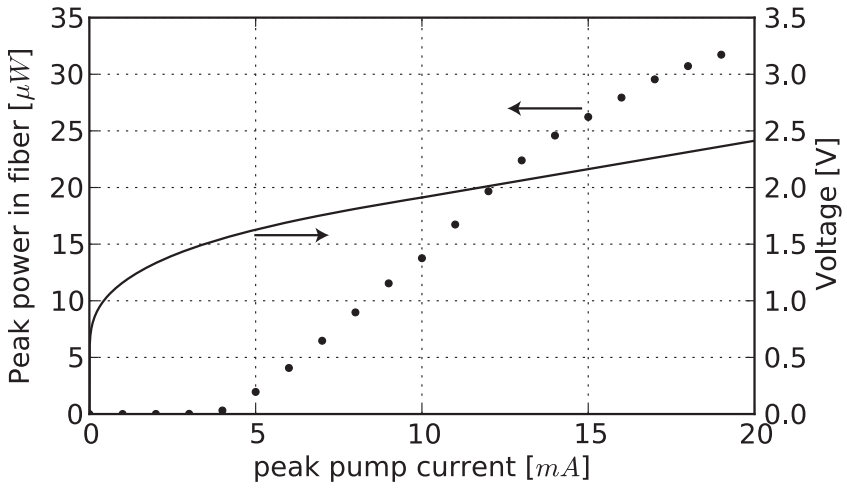

Figure 9: Peak optical power measured in the single mode fiber and voltage across the metallic contacts as a function of the current driven through the laser.

Figure 9(left axis) shows the laser's LI curve plotting the laser's peak output power as a function of the peak current injected in the device at a stabilised stage temperature of $20°C$. This image clearly shows the laser threshold at 4 mA. The optical output power shown on the graph is the measured peak output power coupled to single mode fiber. The fiber-coupler losses were measured to be 7dB and taking into consideration the fact that the laser emits on both sides (3dB), the total power emitted by the laser into the waveguide is about 10 times higher than the values measured in the fiber and reported in figure 9. This yields a differential efficiency of approximately $30\mu W/mA$. It might be possible to increase this number by optimizing both the design and fabrication process of the laser. The right axis of figure 9 shows the voltage across the device as a function of pumping current. Using this graph, the series resistance of the laser is measured to be $50\,\Omega$.

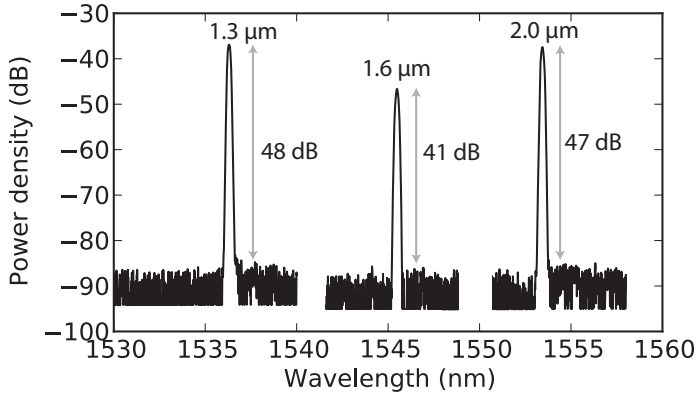

Figure 10: Spectra captured of three different devices, each with a different silicon cavity width

Figure 10 shows the spectra of 3 different lasers. These devices share the same III-V waveguide layout and length but differ in silicon cavity design: the width of the silicon grating cavity for these 3 lasers is $1.3\,\mu m$, $1.6\mu m$ and $2.0\,\mu m$ respectively. By adjusting the width of the silicon cavity waveguide, the effective index and consequently the resonance wavelength of the silicon cavity is altered. This measurement shows that the laser's operating wavelength is determined solely by the resonance wavelength of the silicon cavity. All three lasers operate in a single mode regime with a high side-mode suppression ratio of up to $48\,dB$.

It was not possible to reach continuous wave operation. This is attributed to the high thermal resistance of the device measured to be 1.6K/mW. However, according to simulations, relatively simple measures such as adding a metallic heat spreader on top of the p-contact, can reduce the thermal resistance by a factor of 3, potentially paving the way to CW operation.

In conclusion, we presented the first experimental demonstration of heterogeneously integrated III-V on silicon resonant mirror lasers. The novel concept was explained and its practical applicability verified with an optically pumped prototype. Next the difficulties with respect to electrical pumping were highlighted and a solution was proposed. The fabrication method was outlined and the experimental results were presented. The electrically pumped device measures $160\,\mu m$ in length and has a threshold current of 4mA. We showed that the lasing wavelength is determined by the resonance wavelength of the silicon cavities and that the narrow-band reflection spectrum of the resonant mirrors results in single-mode operation with a side-mode suppression ratio of up to 48dB.

References

[1] Thijs Spuesens, Johan Bauwelinck, Philippe Regreny, and Dries Van Thourhout. *Realization of a Compact Optical Interconnect on Silicon by Heterogeneous Integration of IIIV*. IEEE Photonics Technology Letters, 25(14):1332–1335, July 2013.

[2] Gunther Roelkens, Liu Liu, Di Liang, Richard Jones, Alexander Fang, Brian Koch, and John Bowers. *III-V/silicon photonics for on-chip and inter-chip optical interconnects*. Laser & Photonics Reviews, 4(6):751–779, November 2010.

[3] A W Fang, H Park, R Jones, O Cohen, M J Paniccia, and J E Bowers. *A continuous-wave hybrid AlGaInAs-silicon evanescent laser*. IEEE Photonics Technology Letters, 18(9-12):1143–1145, 2006.

[4] Chong Zhang, Sudharsanan Srinivasan, Yongbo Tang, Martijn J. R. Heck, Michael L. Davenport, and John E. Bowers. *Low threshold and high speed short cavity distributed feedback hybrid silicon lasers*. Optics Express, 22(9):10202, April 2014.

[5] Lumerical Solutions http://www.lumerical.com. *Lumerical FDTD*.

[6] The Silicon Photonics Platform-ePIXfab http://www.epixfab.eu. *ePIXfab*, 2012.

[7] S Keyvaninia, M Muneeb, S Stanković, P J Van Veldhoven, D Van Thourhout, and G Roelkens. *Ultra-thin DVS-BCB adhesive bonding of III-V wafers , dies and multiple dies to a patterned silicon-on-insulator substrate*. Optical Materials Express, 3(1):1047–1056, 2013.

1 Introduction

Most modern optical systems consist of a number of components, each fulfilling a specific task. Examples are light sources (for example, the laser), detectors, modulators, splitters, mode converters (lenses) and spectral filters. Traditionally these are lumped components that are linked together using either free-space optics or an optical fiber. However, similar to how electrical circuits using tube transistors and other lumped elements evolved into semiconductor integrated circuits during the second half of the 20^{th} century, multiple optical elements can also be integrated on a single chip, the so-called photonic integrated chip (PIC).

1.1 Photonic integrated circuits

Each chip consists of a substrate, an optional low-refractive index buffer layer and one or more (higher) refractive index material layers called the optical layer. Light is confined to the optical layer in the vertical direction (the direction perpendicular to the plane of the chip) due to the refractive index contrast between the optical layer (high) and its upper and lower cladding. The optical components are defined by etching geometrical structures in the optical layer. Such structures can be wires, often called waveguides, that guide light between different elements on the chip, filter elements, like ring-shaped structures, or wavelength-scale periodic structures that reflect or diffract light into an optical fiber. Figure 1.1 shows a schematic drawing of what the surface of a PIC looks like. Depending on the materials be-

ing used, these integrated elements are not limited to passive components alone: lasers, detectors and modulators can also be miniaturized and integrated on a single PIC.

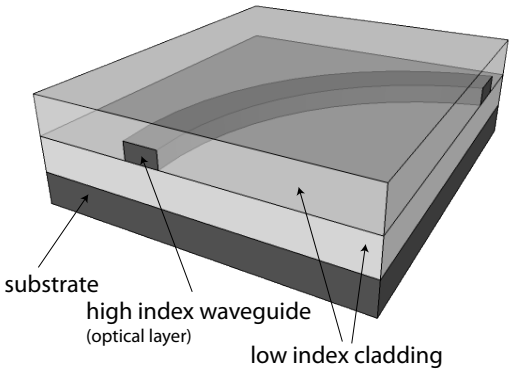

Figure 1.1: Schematic representation of the basic geometry of a PIC, showing the substrate, the optional low refractive index buffer cladding layer, the high refractive index waveguide layer and the low refractive index side- and top-cladding.

Over the years, PICs have been demonstrated on a number of material platforms, each with their distinct properties. Some of the most important material platforms are listed below:

- III-V materials: the term III-V materials refers to all the binary, ternary, quaternary and quinternary semiconductor compounds of elements from the third and fifth column in the periodic table. The starting point is usually a blank indium phosphide (InP) or gallium arsenide (GaAs) substrate wafer on which numerous layers of other III-V compounds can be grown. The thickness of these epitaxially grown layers can reach down to a few nanometers, allowing for structures that exhibit quantum properties, such as quantum wells. By using quaternary compounds, the lattice constant of the compound can be matched to that of the substrate leaving a second degree of freedom open to engineer the size of the band-gap of the grown material to meet the application's specifications. III-V PIC's are usually operated in the telecom wavelength bands. The ability to grow a layer, partially etch it and grow another layer on the substrate (regrowth) allows for seamless integration of active and passive components on the same chip. The disadvantage of III-V PICs is that it is difficult to scale them to high production volumes because the wafer sizes are limited to a few inches in diameter and the III-V materials are not allowed in existing high-volume silicon-based CMOS

pilot lines, requiring separate, expensive fabrication facilities. Currently, the main application field of III-V PIC's are high-end, long-haul telecom transceivers. Such chips reach incredibly high complexity and performance, but are, mainly due to economical reasons, limited to low-volume production.

- Silica based materials: A thick layer of native oxide is grown on a silicon wafer and the oxide (silica) is partially doped to locally increase the refractive index. The doped areas can be used as core materials and the undoped regions as the cladding. The low refractive index contrast between the doped and undoped regions results in very low waveguide losses but is not very well suited for high density integration due to the large bend radii that are necessary to reduce radiation losses. Given the fact that both the core and the cladding are dielectric materials, this technology as such does not allow for the integration of electrically pumped active components.

- Silicon nitride: Starting off with an oxidized silicon wafer, a nitride layer (medium refractive index) is grown on top of the silicon oxide layer (low refractive index). The thickness of the nitride layer can be chosen to tailor the needs of the application. In recent years there has been much interest in this technology for applications in the shorter wavelength ranges (near visible and visible). Similar to the silica based technologies, silicon nitride does not allow the integration of active components as such.

- Silicon-on-insulator: The platform consists of a silicon wafer (of diameter up to 300 mm), a layer of thermal silicon oxide ($1 - 2\,\mu m$) and a layer of silicon serving as the optical layer. The thickness of the silicon layer can vary between roughly 200 nm and close to $1\,\mu m$. This technology is the starting point for this work and is discussed in more detail below.

1.1.1 The silicon-on-insulator platform

Originally the silicon-on-insulator (SOI) platform stems from the electronics world. By insulating the thin device layer from the substrate by means of an intermediate silicon oxide layer, the parasitic device capacitance is lowered which improves the performance of electronic components. However, waveguides and other optical components can be patterned in the silicon layer. The resulting, high refractive index, silicon structures are surrounded by low cladding materials on all sides: silicon oxide below and air, silicon oxide or another low-refractive index material of choice on the sides and top. In other words, the index contrast between the waveguide core and its surroundings is very high ($\Delta n \approx 2$ at $\lambda = 1.55\,\mu m$). This results in highly confined waveguide modes and allows for very tight integration

with waveguide bend radii of only a few μm.

Because silicon has been the work-horse of the CMOS (complementary metal-oxide-semiconductor) electronics industry for almost 50 years, a wide range of high-volume, high-yield tools and technological processes have been developed to fabricate silicon-based chips. It should be no surprise that many of the technologies developed for the electronics industries can also be used to fabricate photonic integrated circuits. The promise of this readily available, high capacity fabrication infrastructure along with the high core/cladding refractive index contrast and the resulting unprecedented level of miniaturization it brings has raised high interest in *silicon photonics* as the preferred technology platform for high volume photonic integrated circuits.

Silicon photonics can be defined in a broad sense as any technology that can produce PICs taking significant advantage of the mass-production facilities that are readily available from the electronics industry. Within this definition the optical waveguide core material is not necessarily silicon, but can also be silicon nitride for example. However, this work will focus on the technologies that do use silicon as the core material, more specifically the silicon-on-insulator platform. Throughout the text, the use of the phrase *silicon photonics* will refer to this more narrow definition of technologies that benefit from the CMOS infrastructure and use silicon as the waveguide core material.

For more than a decade, research groups around the world have made tremendous advances in the design, fabrication and characterisation of silicon-based photonic integrated circuits. Throughout the years passive components with excellent properties such as fiber-grating couplers (efficiency down to -1.6dB [1]), narrow-band ring resonator filters (Q up to 510000 [2]), arrayed waveguide grating (de-) multiplexers and low-loss waveguides. Selective doping of the silicon enabled injection and depletion modulators and the development of selective germanium growth processes allows for the seamless integration of high-speed photodetectors. For a few years now, silicon photonics has reached the level of maturity necessary for high-volume commercial applications. [3] [4]

1.2 Lasers and the SOI platform

What is missing to make this integration scheme complete is a coherent light source: the laser. Unfortunately, silicon itself cannot be used as a gain medium, one of the two prerequisites for laser operation, along with an optical cavity. When a photon travels through a material it interacts with the atoms and free charge car-

riers (electrons and holes) present in the material. Roughly speaking, the photon can encounter one of two events:

- Absorption: the photon is absorbed and excites one of the bound electrons in an atom from the lattice's valence band into its conduction band. During this event, two quantities should be conserved: energy and momentum. The energy difference between the newly generated free electron and the vacant hole it leaves behind equals the photon energy (which in its turn equals hf with h the Planck constant and f the photon's optical frequency). On the other hand, momentum should also be conserved. The photon's momentum is negligible so the momentum of the new free electron should equal the momentum of the bound electron that it originates from (hence the momentum of the hole it leaves behind).
- Stimulated emission: the photon encounters an electron and hole. Due to the presence of the photon the electron and hole recombine and the energy released is converted into a new photon that has the exact same properties (phase, frequency, direction) as the photon that triggered the recombination event. In other words, the original photon is *copied*. The conditions for this to happen are the same as for absorption: energy and momentum should be conserved. The electron and hole should have the same momentum and their energy difference should be equal to the incident photon's energy.

Which mechanism is predominant is a matter of statistics: if the chance of encountering a bound electron (and a corresponding vacancy in the conduction band) is higher than encountering a free electron (and a corresponding vacant hole in the valence band), light will be absorbed and vice versa. To establish laser operation, coherent optical amplification, hence stimulated emission should be the predominant matter-light interaction mechanism.

This is easier said than done. An undoped semiconductor, like silicon, germanium or the III-V compounds such as InP or InGaAs(P), is characterized by the fact that: a) they have a bandgap on the order of $\sim 1\,eV$ and b) their Fermi-level lies close to the center of that band-gap. Because the electron energy in the crystal follows a Fermi-Dirac distribution, this means that the conduction band is virtually unpopulated at room temperature. In other words, a photon with an energy above the bandgap, traveling through such a material will have a much higher chance of being absorbed than being amplified.

To turn the tide, additional electrons and holes are required. Adding electron-hole pairs can happen in two different ways:

- Optical pumping: by illuminating the semiconductor crystal with a pump beam with photon energy higher than the material band-gap, electron-hole

pairs are generated due to absorption. The energy of the pump beam can be significantly higher than the band-gap. The generated carriers will release the excess energy as heat and assemble at the bottom of the conduction band (electrons) and the top of the valence band (holes).

- Electrical pumping: electrons and holes can also be injected electrically. Usually this is done by sandwiching the undoped active layer between a layer of n-doped and a layer of p-doped semiconductor material. The n- and p-doped layers can be connected to a current source which will force electrons and holes to flow into the undoped layer. Again, the band-gap of the surrounding media can be significantly wider than than that of the active material. Carriers will again release their excess energy as heat and assemble at the bottom of the conduction band (electrons) and the top of the valence band (holes).

It should be noted that the electrons and holes that are pumped into the semiconductor have a limited lifetime, even if they don't interact with an incident photon. They can recombine spontaneously and emit a photon with random phase or get trapped in a defect and release their energy as heat.

In general this amplification mechanism works very well, as proven by the many millions of GaAs and InP based laser diodes that are operational across the world at this very moment. However, silicon is an indirect band-gap material. This means that the electron states in the bottom of the conduction band have a different momentum than the hole states at the top of the valence band. As stated earlier, injected carriers will assemble at the extremum of their respective energy band. So even though silicon can be pumped to such a level that a photon has a high probability of encountering a conduction band electron and a valence band hole with the correct energy spacing, there will be no stimulated recombination event because the momenta of the electron and hole are different.

It should be noted that a recombination event between such an electron-hole pair is not impossible. If a certain *particle* with momentum equal to the momentum difference between the electron and hole is involved in the recombination event, total momentum can be conserved. At temperatures above 0K such particles are present in a crystal and are called *phonons*. These are lattice vibrations so essentially this is thermal energy. However, it is still very improbable that a photon, a phonon with the correct momentum and an electron-hole pair with the correct energy spacing collide simultaneously. In practice that means that stimulated emission will not occur and silicon cannot be used as a laser gain material.

Over the years, many approaches have been proposed to bring coherent light onto the silicon PIC:

- External laser sources: an external laser can be coupled into the SOI circuit using a grating coupler. The laser can be fiber-coupled or mounted directly onto the SOI chip. The advantage of such an approach is that it requires minimal technological development (since readily available lasers are being used), the lasers and the circuits can be tested separately before combining them and the laser chip can be thermally insulated from the (temperature sensitive) SOI components. The disadvantage on this approach is that it doesn't allow for a high level of integration and the number of lasers (= wavelengths) is limited due to real-estate constraints.

- Non-linear effects in silicon: optically pumped, non-linear amplification effects, such as Raman amplification and parametric amplification, have been demonstrated to be an effective laser-gain mechanism in silicon [5]. Although this still requires a second pump laser, one such external pump laser can generate laser beams at many different wavelengths on the chip.

- Strained germanium: even though undoped germanium has an indirect band-gap, a combination of tensile strain and high n-type doping can render efficient direct band-gap stimulated emission. Recently, electrically injected germanium lasers were demonstrated [6]. This technique may be very promising in the future but is still in its infancy.

- III-V epitaxy: The lattice constant of InP is so different from silicon's lattice constant that it seemed impossible for a long time to epitaxially grow high quality, defect-free films of InP on a silicon substrate. However, recent work in the electronics world to integrate III-V based high electron mobility transistors (HEMTs) onto silicon chips has led to major advances in the field of direct epitaxial growth of high-quality films of III-V compounds on silicon. Optically pumped epitaxially grown InP DFB lasers, have been demonstrated [7]. In the long term, this approach might even be more promising than germanium based integration, but there is still a very long way to go prove the viability of this technology.

- Heterogeneous integration: A small, unprocessed III-V die is bonded upside-down on a processed silicon sample. After bonding, the III-V substrate is removed and what is left is a thin sheet of III-V epitaxy. This thin sheet of III-V material can be patterned, etched and processed as if it was still on its III-V substrate. Heterogeneous integration allows for an unprecedented level of integration of high-performance III-V active components (lasers, modulators and detectors) onto the SOI platform. In the short term, this

technology might be the most promising approach and is discussed in more detail in the next paragraph.

1.3 Heterogeneous III-V on silicon integration

Figure 1.2 summarizes the different steps of the heterogeneous III-V integration process. A passive silicon-on-insulator circuit die, already patterned and etched (panel a on figure 1.2), is cleaned and prepared for bonding together with a small (typically 4mm by 7mm) III-V die. The III-V die has epitaxial layers on top but has not been patterned or processed yet. After thorough cleaning the III-V die is bonded upside down on the patterned silicon substrate (b). This can be using either direct bonding [8] or adhesive bonding [9]. After bonding, the substrate is removed and what is left is a thin sheet ($1\,\mu m$-$2\,\mu m$ typically) of III-V material (c). This sheet usually contains a multi-quantum well (MQW) region sandwiched between an n-doped and a p-doped layer. The III-V sheet can be patterned and etched to form the desired shape (d). Usually the silicon layer contains structures that are part of the active device that is to be fabricated. This can be gratings or a silicon output waveguide. In other words, the patterning on the III-V die should be aligned to the already existing silicon structures. After the III-V waveguide structure has been etched, metal contacts can be added (e). Finally the chip is planarized and the devices are contacted to the pads by etching vias in the passivation (f).

This technology is about a decade old and many different types of heterogeneously integrated lasers have been proposed and demonstrated.

1.3.1 Hybrid silicon lasers

Researchers at the University of California: Santa Barbara (UCSB) and Intel Corporation, proposed an integration scheme that relies on so-called *hybrid modes* [10]. The III-V die is bonded onto the silicon chip using direct bonding. This results in an ultra thin bonding layer such that the optical mode overlaps with both the silicon and the III-V layers: the *hybrid* mode. This is schematically drawn in figure 1.3 In its initial configuration, the III-V waveguide is very wide ($> 10\,\mu m$) and lateral confinement is provided by the narrower width of the silicon waveguide. By tweaking the width of the silicon rib waveguide, the optical mode can be pushed up into the III-V layer (narrower silicon width) or pulled down into the silicon layer (wider silicon width). Grating mirrors can be patterned into the silicon waveguide prior to bonding. In most designs, the waveguide system is designed such that the optical mode is predominantly in the silicon waveguide and only its evanescent tail overlaps with the active quantum wells.

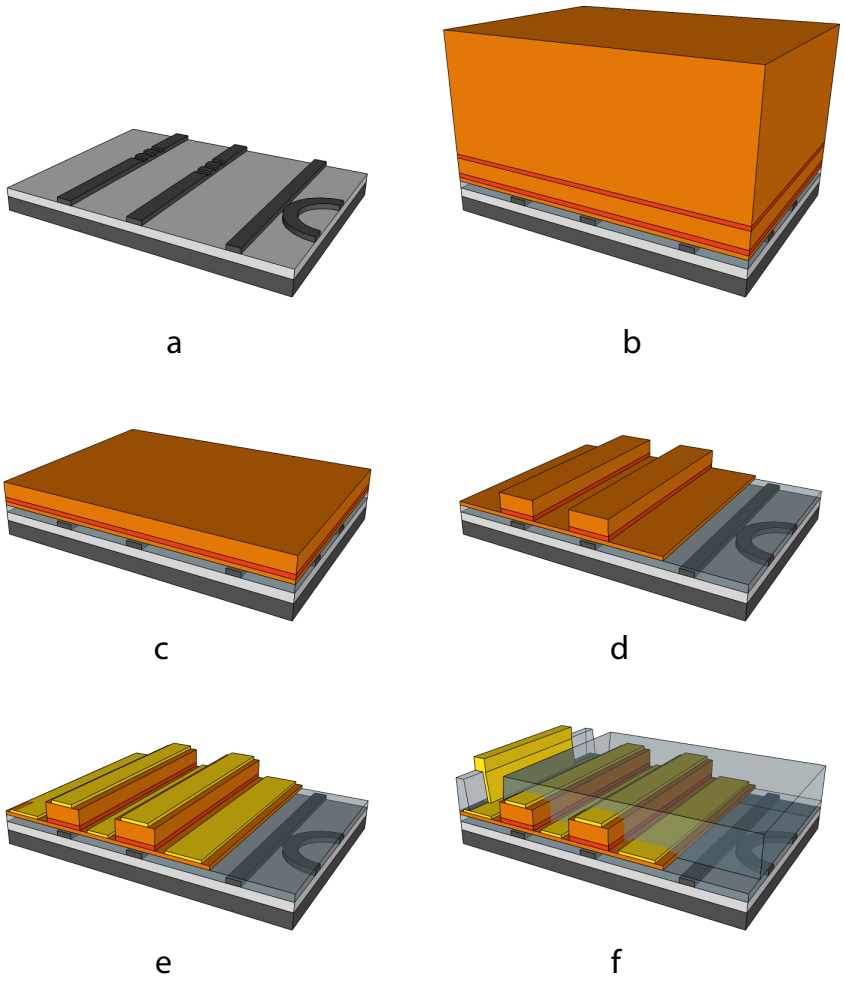

Figure 1.2: Schematic representation of the heterogeneous integration process.

Using this hybrid silicon laser platform, many different types of lasers have been demonstrated: Fabry-Perot lasers [10], DFB lasers [11], DBR lasers [12] and ring-shaped lasers [13]. In general these devices show very good performance at both the $1310\,nm$ and $1550\,nm$ bands, with thresholds currents as low as a few 10's of mA and output powers higher than 10 mW. In recent work, short cavity DFB's have been demonstrated with record low 8.8mA threshold current [14].

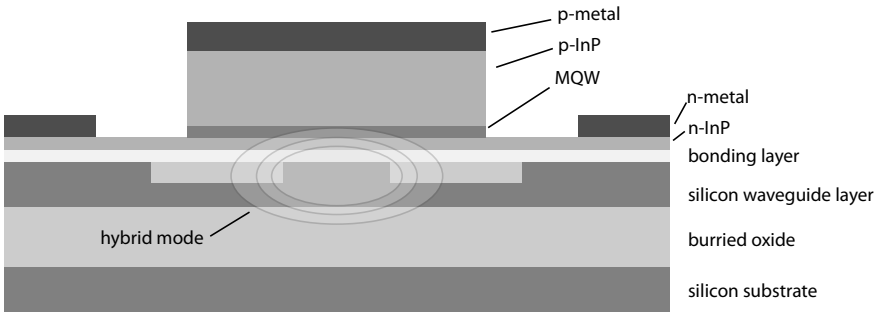

Figure 1.3: Schematic representation of the hybrid silicon laser showing the hybrid mode that is predominantly confined to the silicon layer and evanescently overlaps with the multi-quantum well region.

1.3.2 III-V confinement + tapers

As opposed to hybrid silicon lasers, the III-V and silicon waveguide geometries are designed in such a way that the optical mode is predominantly confined to the III-V waveguide inside the laser [15]. Near the facets, the III-V waveguide adiabatically tapers to a narrow tip ($\sim 500\,nm$) to push the optical mode down into the underlying silicon waveguide. Many different configurations are possible to implement the laser mirrors. The silicon gratings can be placed underneath the III-V waveguide and provide evanescent distributed feedback (panel a in figure 1.4). Alternatively, the silicon grating mirrors (or another wavelength selective reflection mechanism) can be placed in the silicon waveguide after the optical mode is pushed completely out of the III-V waveguide (b). The performance of these lasers is similar to the hybrid silicon lasers.

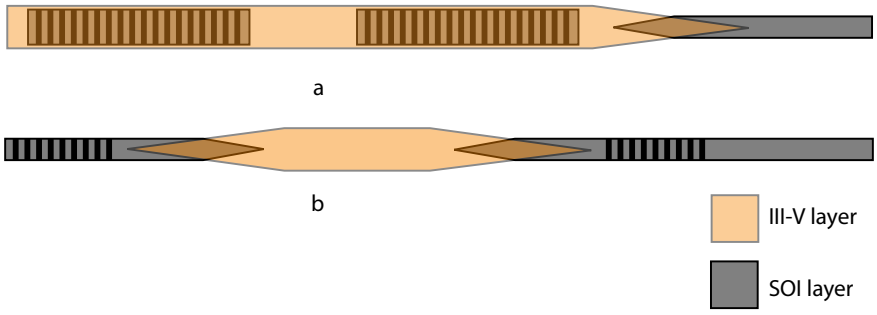

Figure 1.4: Schematic representation of the different coupling schemes in III-V confined heterogeneously integrated lasers.

1.3.3 Microdisk lasers

Instead of using rectilinear waveguides with reflecting structures at their facets, another way to create a cavity is by using ring or disk-shaped geometries. Typically the disk is fabricated in the III-V layer and is evanescently coupled to a silicon waveguide below as shown in figure 1.6. The advantage of such an approach is that the disks can be scaled down to radii of only a few μm. Consequently, microdisk lasers have threshold currents far below the $1\,mA$ level [16]. The absence of grating reflectors or any other narrow-band optical wavelength selection mechanism means that the microdisk lasers suffer from low side-mode suppression ratios.

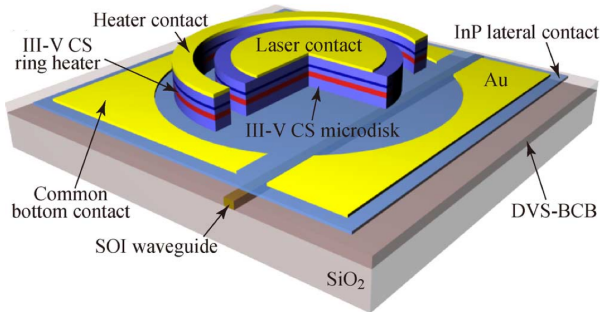

Figure 1.5: Schematic representation of the heterogeneously integrated microdisk-laser. Figure reproduced from [17]

1.3.4 III-V photonic crystal lasers

Another interesting approach is the use of photonic crystal cavities in the III-V layer. The basic setup is very similar to the microdisk lasers except for that fact that a linear photonic crystal cavity is patterned in the III-V waveguide and coupled to the silicon waveguide below. The well-designed photonic crystals can reach very high cavity quality factors and consequently have very low threshold powers [18]. This approach requires sub-micron patterning of the III-V layer.

1.3.5 Other types

The list of device types above is only a short selection of the work that has been done by many groups across the world over the last decade. More exotic designs, like vertical-cavity lasers with silicon high-contrast grating mirrors [19] and dual-waveguide lasers with grating-assisted couplers in between [20] have also been proposed.

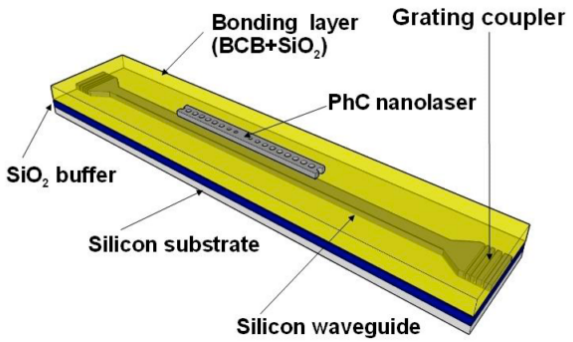

Figure 1.6: Schematic representation of the III-V on silicon photonic-crystal laser. Figure reproduced from [18]

1.4 Resonant mirror lasers

The aim of this work is to design and demonstrate a laser concept that distinguishes itself from the previous work due to the unique combination of the following properties:

- Low threshold current (mA level)
- Single mode (high side-mode suppression ratio $>$ 30dB + no mode hops)
- Precise operating wavelength definition during fabrication
- III-V waveguide patterning as simple as possible: no tapers, no gratings. Contact lithography (limited resolution + manual alignment accuracy) should be sufficient to pattern the laser's III-V layer.
- Harness the power of CMOS processing: design the laser in such a way that the wavelength selective mechanism is mainly defined in the silicon layer.

Such a laser, combining a low threshold and high spectral purity, has potential applications in different types of highly integrated, high volume PICs. Consider the following two examples: short-range multi-wavelength optical interconnects [16] and a light-source in lab-on-a-chip spectroscopic applications [21].

- **WDM optical interconnects**: during the bulk part of the 1990's the performance of a computer system was mainly measured by the clock-speed of its processor. However, as clock-speeds reached beyond the gigaHertz level, increasing the clock-speed became more and more difficult and to increase computing power even further, multiple processor cores were combined into so-called multi-core configurations. But with this new approach

came new challenges. In principle such a system can scale to very high processor counts. However, for such a configuration to work efficiently the different cores must be able to communicate with each other and the random access memory at high bitrates. As electrical interconnects reach their limitations optical communication lines seem to be the only viable solution. A simple configuration would consist of a few lasers per core, each emitting at a different wavelength either directly modulated or coupled to an external modulator. The different wavelength channels would be combined into single waveguide using a dispersive element such as an AWG and coupled into the transport channel, for example a fiber. At the receiver side the optical signal is coupled from the transport channel into a waveguide, demultiplexed using another dispersive element and captured by an array of high speed photodetectors. To enable a high level of integration, the power consumption of the lasers should be as low as possible, requiring low threshold current devices. On the other hand, high spectral purity, so no mode-hops and high side-mode suppression, is necessary for stable WDM operation.

- **Lab-on-chip spectroscopic sensor** using spectroscopic techniques an unknown liquid can be probed for its composition. Imagine this unknown liquid to be the blood flowing through your veins and having a spectroscopic sensor monitoring the glucose levels in real time. This would be of particular interest for diabetes patients who have to keep a close eye on their glucose levels. In its most advanced implementation, this sensor would be implanted under the patients skin. One possible implementation consists of an array of lasers, each emitting at one, well defined, wavelength. The output of these lasers is combined into a single waveguide and directed to a sensing area, for example a long spiral with its evanescent field overlapping with the blood that is to be tested. The output of the sensing area is directed into a photodetector that will record the power transmitted through the sensing area. By turning the different lasers on and off one by one, the spectral transmission characteristic can be measured. If such a sensor is to be operated in vivo, its power consumption should obviously be as low as possible on the order of 10 mW. In other words, a laser with a threshold power lower than this figure is required. On the other hand because the laser will be used to perform a spectroscopic measurement, its spectral purity is of the highest importance.

The current state of the art provides two types of lasers that can be considered for such applications: microdisk lasers [16] and short-cavity DFB lasers [14]. Table 1.1 benchmarks these two types of lasers against the list of requirements stated in the previous paragraph.

Property	Microdisk lasers	Short cavity DFB
Threshold current	$<$ 0.5 mA	8.8 mA
SMSR	25 dB	$>$ 55 dB
Wavelength definition	in III-V layer	in silicon layer
III-V patterning complexity	requires smooth III-V edge	requires III-V tapers width unknown
CW operation	yes	yes
silicon thickness	220 nm	500 nm

Table 1.1: Benchmarking state of the art for this work's requirements

Although both approaches fulfil most of the requirements, there is still room for improvement. As could be expected considering its title, this work will attempt to fulfil this list of requirements using *resonant mirrors*. The basic idea of resonant mirrors is fairly simple. Consider a waveguide that is side-coupled to a bidirectional optical waveguide cavity. This is a cavity in which light propagates in both directions (and a standing wave pattern appears). Examples of bidirectional waveguide cavities are Fabry-Perot type cavities or grating cavities such as band-edge grating resonators and quarter-wave defect grating resonators. Under certain circumstances, outlined in chapter 3, light, at the resonance wavelength of the cavity, that propagates through the waveguide will be reflected into the opposite propagation direction after interacting with the cavity. This idea has been implemented in the past to decrease the bandwidth of the reflectors in a laser cavity [22]. Note that, due to the SOI-platform's high index contrast and the high-resolution CMOS fabrication technology, short silicon grating cavities (few 10's of μms) with very high Q-factors ($>$ 10000) can be fabricated.

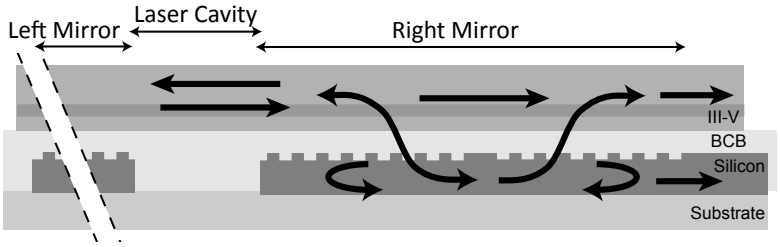

Figure 1.7: Schematic representation of the silicon cavity coupled to a III-V waveguide above.

In other words, using silicon grating cavities would allow for strong reflectivity (related to the cavity's intrinsic Q-factor as shown in chapter 3) over a short

interaction length. So, if such a silicon cavity would be placed underneath a III-V waveguide, this should result in a short, highly reflective mirror. This is schematically shown in figure 1.7. Because this reflection mechanism only works at the resonance wavelength of the silicon cavity, the reflectivity is highly wavelength selective. The III-V stack also doesn't have to be bonded ultra-close to the silicon waveguide layer because this is an evanescent coupling mechanism. As shown in chapter 4 and 6, a distance of 150 nm to 200 nm between the top of the silicon waveguide layer and the bottom of the III-V stack is usually ideal. Moreover, there is no need for tapering the III-V waveguide to push light into the silicon output waveguide. Instead, a fraction of the optical mode already present in the silicon cavity can be coupled into a silicon waveguide, for example by butt-coupling the waveguide to the cavity.

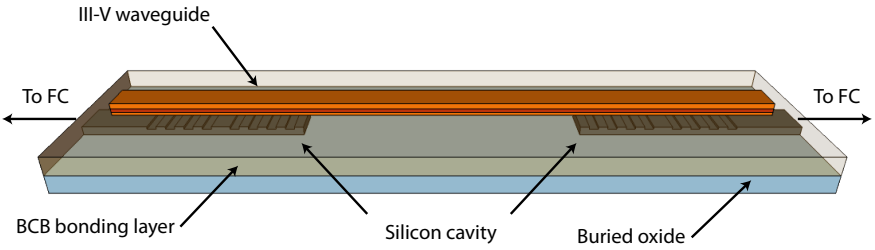

Figure 1.8: Schematic representation of the resonant mirror laser.

By placing two identical, well-designed silicon cavities underneath the same III-V waveguide, the laser cavity arises. This setup is shown schematically in figure 1.8. To improve the visual clarity of this figure, the III-V waveguide is presented as a narrow and thin waveguide without metal contacts. Because the silicon cavities can have high reflectivity, the III-V waveguide connecting the two mirror sections can be relatively short too. Adding this to the short length of the silicon cavities results in an overall short laser (order of magnitude $100\,\mu m$) which potentially requires a low threshold current (mA level).

1.5 Outline

This work consists of 4 chapters that each cover a distinct aspect of heterogeneously integrated III-V on silicon resonant mirror lasers.

A key component to building resonant mirror lasers is the silicon cavity so this hold be studied in depth first. Chapter 2 starts off with a brief description

of the theoretical aspects of optical waveguides to set the stage for the theoretical treatment of 1-dimensionally corrugated waveguides. Using the Floquet-Bloch framework, the basic properties of infinitely long silicon grating waveguides are studied. Next, the more realistic case of a finite silicon grating cavity is considered. After studying the reflection and transmission spectra of such components two interesting spectral regions are identified: the band-gap region where all incoming light is reflected and the band-edge region, near the edge of the waveguide. At the band-edge, light slows down and due to the reflections at the grating-waveguide interface Fabry-Perot like cavities arise. The properties of such cavities are studied as a function of the grating length. In an attempt to make better cavities, a quarter wave defect is introduced in the silicon cavity. Again, the reflection and transmission spectra are investigated for different grating lengths. Finally, a combination of these two kinds of cavities is proposed to overcome their inherent limitations. The resulting cavity, consisting of 2 outer grating sections with a longer period and 1 inner grating section with a shorter period proves to have superior properties in terms of quality factor and mode-spacing.

Chapter 3 in its turn elaborates on using the grating cavities studied in the first chapter in a resonant mirror configuration. First a theoretical framework is established using scattering theory, a theory borrowed from quantum mechanics and applicable to optical cavities side-coupled to an access waveguide. Using this theory 2 simple equations describing the maximum reflectivity and the reflection bandwidth are proposed as a function of the silicon cavity's intrinsic quality factor and the coupling factor. The coupling factor is further investigated and it is found that this can be decomposed into two distinct factors: modal overlap and phase-matching. This theoretical background is used as a guideline to investigate the reflection and transmission spectra of the resonant mirrors using the three types of cavities studied in chapter 2. Each time the phase-matchind condition is derived using the Fourier transform of the cavity's standing wave field profile and the III-V waveguide is constructed accordingly. Next the maximum reflectivity and bandwidth are simulated for different grating lengths bonding thicknesses and variations in III-V waveguide thickness.In conclusion, a maximum reflectivity of more than 90% can be obtained within a bandwidth as narrow as a few nanometers with a silicon cavity length of less than $30\,\mu m$.

Next, chapter 4 uses the theoretical knowledge built up in the first two chapters to simulate and design a first, optically pumped, resonant mirror laser. Using 3D FDTD simulations the proposed mirror's reflection and transmission spectrum is verified. The basic laser-properties, such as threshold power and differential efficiency are estimated using a simple rate-equation model. After discussing the fabrication method the experimental results are presented. The $50\,\mu m$ long laser

has a threshold pump power of 5 mW and a side-mode suppression ratio of up to 38dB.

Finally the last chapter describes the design, fabrication and characterisation of the world's first heterogeneously integrated, electrically pumped resonant mirror laser. The chapter starts with discussing the differences between optically and electrically pumped lasers and their implications on the design of resonant mirrors. More specifically, the III-V waveguide should be designed to have an effective index close to that of the silicon cavity. To achieve this and still provide a path for the electrical carriers to reach to the active layers, a novel waveguide layout is proposed where a slit is etched in the p-layer to push the mode down and the quantum wells are undercut to confine the optical mode laterally. The resulting resonant mirror is verified using 3D FDTD simulations. Next, the laser properties are predicted using the same rate equation model as used in the previous chapter. Also the electrical and thermal properties are modeled and investigated. The technological process that was developed to fabricate the novel waveguide geometry is outlined and the experimental results are presented. The demonstrated lasers operated in pulsed regime with a threshold current down to 4 mA and a side-mode suppression ratio of almost 50 dB. Finally, the efforts to reach continuous wave operation are discussed.

1.6 List of publications

1.6.1 Patents

- Roeland Baets, Dries Van Thourhout, Gunther Roelkens, Geert Morthier, Yannick De Koninck, *Laser light coupling into SOI CMOS photonic integrated circuit*, Patent number 8787417

1.6.2 International peer-reviewed journals

- Y. De Koninck, F. Raineri, A. Bazin, R. Raj, G. Roelkens, R. Baets, Experimental demonstration of a hybrid III-V-on-silicon micro-laser based on resonant grating cavity mirrors, *Optics Letters*, 38(14), p.2496-2498 (2013)
- Y. De Koninck, G. Roelkens, R. Baets, Design of a hybrid III-V-on-silicon microlaser with resonant cavity mirrors, *IEEE Photonics Journal*, 5(2), p.2700413 (2013)
- Y. Li, D. Vermeulen, Y. De Koninck, G. Yurtsever, G. Roelkens, R. Baets, Compact grating couplers on silicon-on-insulator with reduced backreflection, *Optics Letters*, 37(21), p.4356-4358 (2012)
- D. Vermeulen, Y. De Koninck, Y. Li, W. Bogaerts, R. Baets, G. Roelkens, Reflectionless grating couplers for SOI photonic integrated circuits , *Optics Express*, p.22278-22283 (2012)
- K. De Vos, Jordi Girones Molera, T. Claes, Y. De Koninck, Stepan Popelka, Etienne Schacht, R. Baets, P. Bienstman, Multiplexed antibody detection with an array of silicon-on-insulator microring resonators, *IEEE Photonics Journal*, 1(4), p.225-235 (2009) Download this Publication (697KB).

1.6.3 International conference Proceedings

- R. Bockstaele, E.M.P. Ryckeboer, N. Hattasan, Y. De Koninck, M. Muneeb, S. Verstuyft, D. Delbeke, W. Bogaerts, G. Roelkens, R. Baets, Glucose sensing by means of silicon photonics, *Conference on Smart Photonic and Optoelectronic Integrated Circuits XVI* (invited), 8989, United States, p.89890P (2014)
- Y. De Koninck, M. Tassaert, G. Roelkens, R. Baets, Design of an Electrically-Injected Hybrid Silicon Laser with Resonant Mirrors, *IEEE Photonics Conference 2013 (IPC)*, United States, p.paper TuH2.2 (2013)
- G. Roelkens, S. Keyvaninia, Y. De Koninck, P. Mechet, T. Spuesens, M. Tassaert, S. Stankovic, G. Morthier, R. Baets, D. Van Thourhout, G. Duan, J.M.

Fedeli, M. Smit, Heterogeneous III-V/silicon photonic integrated circuits, *Asia Communications and Photonics Conference 2013* (invited), (2013)

- G. Roelkens, D. Vermeulen, Y. Li, Y. De Koninck, S. Selvaraja, K. Van Acoleyen, D. Van Thourhout, R. Baets, Silicon grating structures for optical fiber interfacing and III-V/silicon opto-electronic components, *SPIE Photonics West Conference 2013 - High Contrast Metastructures II* (invited), 8633, United States, p.86330S (2013)

- Y. De Koninck, F. Raineri, A. Bazin, R. Raj, G. Roelkens, R. Baets, Experimental demonstration of a novel heterogeneously integrated III-V on Si microlaser, *2013 Photonics West Conference*, 8629, United States, p.paper 8629-41 (2013)

- R. Baets, Y. De Koninck, S. Keyvaninia, S. Stankovic, D. Van Thourhout, G. Roelkens, In search for the ideal hybrid silicon laser, *The 2nd International Symposium on Photonics and Electronics Convergence (ISPEC 2012)* (invited), Japan, p.5 (2012)

- Y. De Koninck, F. Raineri, A. Bazin, R. Raj, G. Roelkens, R. Baets, Demonstration of a novel single-mode hybrid silicon microlaser, *IEEE Photonics Conference*, United States, (2012)

- Y. De Koninck, S. Keyvaninia, S. Stankovic, D. Van Thourhout, G. Roelkens, R. Baets, Hybrid silicon lasers for optical interconnect, *IEEE Photonics Conference 2012* (invited), United States, p.812-813 (2012)

- Y. De Koninck, M. Tassaert, G. Roelkens, R. Baets, A. Bazin, F. Raineri, A novel electrically pumped III-V on silicon micro-laser, *16th European Conference on Integrated Optics* (ECIO 2012), Spain, p.paper 147 (2012)

- S. Keyvaninia, Y. De Koninck, D. Van Thourhout, R. Baets, G. Roelkens, A novel III-V-on-silicon distributed feedback laser design, *16th European Conference on Integrated Optics* (ECIO 2012), Spain, p.paper 197 (2012)

- T. Spuesens, Y. De Koninck, D. Van Thourhout, Efficient vertical coupling between a silicon waveguide and an InP-based microdisk, *16th European Conference on Integrated Optics* (ECIO 2012), Spain, p.paper 212 (2012) Download this Publication (537KB).

- Y. Li, D. Vermeulen, Y. De Koninck, G. Yurtsever, G. Roelkens, R. Baets, Fiber couplers for silicon-on-insulator photonic IC, *Optical Fiber Communication Conference (OFC) 2012*, p.JTh2A.8 (2012)

- G. Roelkens, S. Keyvaninia, S. Stankovic, M. Tassaert, N. Hattasan, A. Gassenq, P. De Heyn, Y. De Koninck, P. Mechet, R. Kumar, M. Muneeb, D. Vermeulen, G. Morthier, R. Baets, D. Van Thourhout, III-V-on-silicon membrane photonics for near-infrared and mid-infrared applications, 16th European *Conference on Integrated Optics (ECIO 2012)* (invited), Spain, (2012)

- D. Vermeulen, Y. De Koninck, Y. Li, E. Lambert, W. Bogaerts, R. Baets, G. Roelkens, Reflectionless Grating Coupling for Silicon-on-Insulator Integrated Circuits, *8th International Conference in Group IV Photonics 2011*, United Kingdom, p.74-76 (P1.6) (2011)

- G. Roelkens, Y. De Koninck, S. Keyvaninia, S. Stankovic, M. Tassaert, M. Lamponi, G. Duan, D. Van Thourhout, R. Baets, Hybrid Silicon Lasers, *SPIE Photonics West 2011* (invited), United States, (2011)

- Y. De Koninck, G. Roelkens, R. Baets, Hybrid III-V/silicon micro-lasers based on resonant cavity reflectors, *15th Annual Meeting of the IEEE Photonics Society Benelux chapter, Netherlands*, (2010) Download this Publication (226KB).

- Y. De Koninck, G. Roelkens, R. Baets, Cavity Enhanced Reflector Based Hybrid Silicon Laser, *23rd Annual Meeting of the IEEE Photonics Society*, United States, (2010)

- K. De Vos, J. Girones Molera, Y. De Koninck, E. Schacht, R. Baets, P. Bienstman, Multiplexed protein detection with an array of silicon-on-insulator microring resonators, *22nd Annual Meeting of the IEEE Photonics Society* (invited), Turkey, p.457-458 (2009)

- Y. De Koninck, K. Huybrechts, G. Van der Sande, J. Danckaert, R. Baets, G. Morthier, Nonlinear dynamics of asymmetrically coupled microdisk lasers, *22nd Annual Meeting of the IEEE Photonics Society*, Turkey, p.WN4 (2009)

References

[1] D Vermeulen, S Selvaraja, P Verheyen, G Lepage, W Bogaerts, P Absil, D Van Thourhout, and G Roelkens. *High-efficiency fiber-to-chip grating couplers realized using an advanced CMOS-compatible Silicon-On-Insulator platform*. Opt. Express, 18(17):18278–18283, August 2010.

[2] Lian-Wee Luo, Gustavo S Wiederhecker, Jaime Cardenas, Carl Poitras, and Michal Lipson. *High quality factor etchless silicon photonic ring resonators*. Opt. Express, 19(7):6284–6289, March 2011.

[3] A. Mekis, S. Abdalla, D. Foltz, S. Gloeckner, S. Hovey, S. Jackson, Y. Liang, M. Mack, G. Masini, M. Peterson, T. Pinguet, S. Sahni, M. Sharp, P. Sun, D. Tan, L. Verslegers, B. P. Welch, K. Yokoyama, S. Yu, and P. M. De Dobbelaere. *A CMOS photonics platform for high-speed optical interconnects*. In IEEE Photonics Conference 2012, pages 356–357. IEEE, September 2012.

[4] Acacia. *Silicon Photonics Press Release http://acacia-inc.com/acacia-communications-announces-industrys-first-single-chip-silicon-photonics-100g-coherent-transceiver/.*

[5] Haisheng Rong, Ansheng Liu, Richard Jones, Oded Cohen, Dani Hak, Remus Nicolaescu, Alexander Fang, and Mario Paniccia. *An all-silicon Raman laser.* Nature, 433(7023):292–4, January 2005.

[6] Rodolfo E Camacho-Aguilera, Yan Cai, Neil Patel, Jonathan T Bessette, Marco Romagnoli, Lionel C Kimerling, and Jurgen Michel. *An electrically pumped germanium laser.* Optics express, 20(10):11316–20, May 2012.

[7] Zhechao Wang, Bin Tian, Mohanchand Paladugu, Marianna Pantouvaki, Nicolas Le Thomas, Clement Merckling, Weiming Guo, Johan Dekoster, Joris Van Campenhout, Philippe Absil, and Dries Van Thourhout. *Polytypic InP nanolaser monolithically integrated on (001) silicon.* Nano letters, 13(11):5063–9, November 2013.

[8] Di Liang, Alexander W Fang, Hyundai Park, Tom E Reynolds, Keith Warner, Douglas C Oakley, and John E Bowers. *Low-temperature, strong SiO2-SiO2 covalent wafer bonding for III-V compound semiconductors-to-silicon photonic integrated circuits*. JOURNAL OF ELECTRONIC MATERIALS, 37(10):1552–1559, October 2008.

[9] S Keyvaninia, M Muneeb, S Stanković, P J Van Veldhoven, D Van Thourhout, and G Roelkens. *Ultra-thin DVS-BCB adhesive bonding of III-V wafers , dies and multiple dies to a patterned silicon-on-insulator substrate*. Optical Materials Express, 3(1):1047–1056, 2013.

[10] Alexander W Fang, Hyundai Park, Oded Cohen, Richard Jones, Mario J Paniccia, and John E Bowers. *Electrically pumped hybrid AlGaInAs-silicon evanescent laser.* Optics express, 14(20):9203–10, October 2006.

[11] Alexander W Fang, Erica Lively, Hao Kuo, Di Liang, and John. E Bowers. *A distributed feedback silicon evanescent laser*. Optics Express, 16(7):4413–4419, March 2008.

[12] Alexander W Fang, Brian R Koch, Richard Jones, Erica Lively, Di Liang, Ying-Hao Kuo, and John E Bowers. *A Distributed Bragg Reflector Silicon Evanescent Laser*. In 2008 5TH IEEE INTERNATIONAL CONFERENCE ON GROUP IV PHOTONICS, pages 58–60, 2008.

[13] Di Liang, Marco Fiorentino, Tadashi Okumura, Hsu-hao Chang, Daryl T Spencer, Ying-hao Kuo, Alexander W Fang, Daoxin Dai, Raymond G Beausoleil, and John E Bowers. *Electrically-pumped compact hybrid silicon microring lasers for optical interconnects*. 17(22):4309–4315, 2009.

[14] Chong Zhang, Sudharsanan Srinivasan, Yongbo Tang, Martijn J. R. Heck, Michael L. Davenport, and John E. Bowers. *Low threshold and high speed short cavity distributed feedback hybrid silicon lasers*. Optics Express, 22(9):10202, April 2014.

[15] M. Lamponi, S. Keyvaninia, F. Pommereau, F. Lelarge, G. de Valicourt, G Roelkens, D Van Thourhout, D Bordel, S. Messaoudene, J.M. Fedeli, and G.-H. Duan. *Heterogeneously integrated InP/SOI laser using double tapered single-mode waveguides through InP die to SOI wafer bonding*. In Group IV Photonics, 2010.

[16] Thijs Spuesens, Johan Bauwelinck, Philippe Regreny, and Dries Van Thourhout. *Realization of a Compact Optical Interconnect on Silicon by Heterogeneous Integration of IIIV*. IEEE Photonics Technology Letters, 25(14):1332–1335, July 2013.

[17] Liu Liu, T Spuesens, G Roelkens, D Van Thourhout, P Regreny, and P Rojo-Romeo. *A thermally tunable III-V compound semiconductor microdisk laser integrated on silicon-on-insulator circuits*. IEEE Photonics Technology Letters, 22(17):1270–1272, 2010.

[18] Y Halioua, A Bazin, P Monnier, T J Karle, G Roelkens, I Sagnes, R Raj, and F Raineri. *Hybrid III-V semiconductor/silicon nanolaser.* Optics express, 19(10):9221–31, May 2011.

[19] Corrado Sciancalepore, Badhise Ben Bakir, Xavier Letartre, Julie Harduin, Nicolas Olivier, Christian Seassal, Jean-marc Fedeli, and Pierre Viktorovitch.

CMOS-Compatible Ultra-Compact 1.55-μm Emitting VCSELs Using Double Photonic Crystal Mirrors. IEEE Photonics Technology Letters, 24(6):455–457, 2012.

[20] Tiphaine Dupont, Laurent Grenouillet, Alexei Chelnokov, and Pierre Viktorovitch. *Contradirectional coupling between III-V stacks and silicon-on-insulator corrugated waveguides for laser emission by distributed feedback effect*. IEEE Photonics Technology Letters, 22:1413–1415, 2010.

[21] E Ryckeboer, R Bockstaele, M Vanslembrouck, and R Baets. *Glucose sensing by waveguide-based absorption spectroscopy on a silicon chip.* Biomedical optics express, 5(5):1636–48, May 2014.

[22] Hermann A. Haus and Y. Lai. *Narrow-Band Dristributed Feedback Reflector Design*. Journal of Lightwave Technology, 9(6):754–760, 1991.

2 Silicon grating cavities

2.1 Introduction

Before diving into the details of designing resonant mirror lasers, it will prove useful to first conduct a thorough study of one of the most important components in such lasers: the silicon grating cavity. This chapter starts with a short introduction to the general theory of optical waveguides to progress to the treatment of periodically corrugated structures using the Floquet-Bloch treatment. After discussing the basic properties of waveguide gratings this chapter shows how to make a cavity using such waveguide gratings and examines the basic properties for each type. This chapter will only deal with the silicon layer and will not consider the InP overlay. Consequently all devices in this chapter are passive.

2.2 Waveguide gratings

2.2.1 Optical waveguides

In each material light propagates at a different speed. The actual phase velocity of a plane wave in a particular material is given by c/n where c is the speed of light in vacuum and n is the material's refractive index. A high refractive index means slow propagation and vice versa. When light passes through the interface between two materials with different refractive index, the beam refracts. This physical phenomenon is described by Snell's law. If the beam propagates from a high index material to a lower index material and is directed close to parallel to the interface,

total internal reflection will occur. The beam will not refract into the low index material but will reflect back into the high index material. This effect allows to trap a beam of light within a finite cross-section and guide it over a long distance without significant attenuation. The most well-known application of this effect are optical fibers that are used to transport optical data over hundreds of kilometers. The chip-scale alternative to optical fibers are dielectric waveguides. The high-index waveguide sits on top of a low-index substrate and is surrounded by a low-index cladding. Figure 2.1 shows 3 practical implementations: a 220 nm silicon strip waveguide, a 400 nm silicon rib waveguide and a 220 nm silicon nitride strip waveguide. The height of the waveguide is usually determined by the available technology whereas the width can be set by the designer.

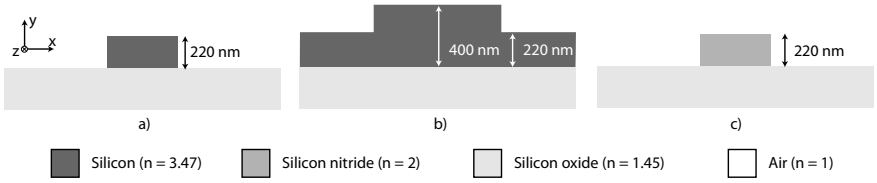

Figure 2.1: cross-section of 3 common waveguide platforms: a) a 220 nm silicon strip waveguide b) a 400 nm silicon rib waveguide c) 220 nm silicon nitride strip waveguide

A rigorous description of optical waveguides starts with Maxwell's equations:

$$\nabla \times \mathbf{E} = -\frac{\partial \mathbf{B}}{\partial t} \tag{2.1}$$

$$\nabla \times \mathbf{H} = \frac{\partial \mathbf{D}}{\partial t} + \mathbf{J} \tag{2.2}$$

$$\nabla \cdot \mathbf{D} = \rho_V \tag{2.3}$$

$$\nabla \cdot \mathbf{B} = 0 \tag{2.4}$$

In this set of equations $\mathbf{E}$, $\mathbf{H}$, $\mathbf{D}$ and $\mathbf{B}$ are the time and space dependent electric field, magnetic field, electric displacement and magnetic flux density vectors respectively. ρ_V is the local electric charge density and $\mathbf{J}$ represents the local electric current density. The fields are also related through 2 constitutive relations:

$$\mathbf{D} = \epsilon \mathbf{E} \tag{2.5}$$

$$\mathbf{B} = \mu \mathbf{H} \tag{2.6}$$

with ϵ the electrical permitivity and μ the magnetic permeability.
In this work, there are no currents or electrical charges inside or near the waveguides and materials are assumed to be:

- isotropic: ϵ is a scalar number, independent of the orientation of the electric field vector $\mathbf{E}$
- non-magnetic: μ is constant and is equal to μ_0 for all materials
- linear: ϵ is independent of the local electric field strength

Moreover, the geometry of the structures is such that the spatial distribution of the electrical permitivity ϵ is piecewise constant. This means that all derivatives of ϵ with respect to spatial components will render zero within each section. At the interface between two constant regions, the magnetic field and the tangential components of the electric field should be continuous. The electric field components normal to the interface are discontinuous and obey the following relationship:

$$\epsilon_1 E_{n,1} = \epsilon_2 E_{n,2} \tag{2.7}$$

with ϵ_x the electrical permitivity in material x and $E_{n,x}$ the electric field component normal to the interface in material x.

Assuming a harmonic time dependence with angular frequency ω of both the electric and magnetic fields and taking into account all conditions yields 2 decoupled equations for the electric and magnetic fields:

$$\nabla^2\mathbf{E} + \omega^2\epsilon\mu_0\mathbf{E} = 0 \tag{2.8}$$

$$\nabla^2\mathbf{H} + \omega^2\epsilon\mu_0\mathbf{H} = 0 \tag{2.9}$$

An equation of the form $\nabla^2\psi + k^2\psi = 0$ is referred to as a *Helmholtz equation*. For the sake of simplicity, the remainder of this chapter will deal with the Helmholtz equation for the electric field $\mathbf{E}$. Because both equations are identical apart from their boundary conditions, all conclusions can easily be applied to the magnetic field too.

Equation 2.8 can be treated as an eigenvalue problem of the operator $\Theta = 1/(\epsilon\mu_0)\nabla^2$ with eigenstates $\mathbf{E}$ and eigenvalue ω^2. The optical waveguide is invariant in the propagation direction of the light beam. Without loss of generality, assume this is the z-direction in this case. So $\epsilon(\mathbf{r}) = \epsilon(\mathbf{r} + \mathbf{R}_z)$ with $\mathbf{R}_z$ any vector parallel to the z axis. This means that the operator Θ is invariant under translations along the z axis and consequently $\mathbf{E}(\mathbf{r})$ and $\mathbf{E}(\mathbf{r} + \mathbf{R})$ have the same eigenvalue ω^2. Assuming $\mathbf{E}$ is non-degenerate, this means that $\mathbf{E}(\mathbf{r})$ and $\mathbf{E}(\mathbf{r}+\mathbf{R})$ must be proportional to each other[1]. In other words, the z-dependence of $\mathbf{E}$ must

[1]The translation invariance along the z-axis actually means that Θ commutes with the z-axis translation operator T_z. Commuting operators have simultaneous non-degenerate eigenstates, meaning that their eigenstates only differ by a constant factor. $e^{-j\beta z}$ are eigenstates of T_z, so the eigenstates of Θ must be proportional to these.

be proportional to $e^{-j\beta z}$ since $e^{-j\beta(z+R_z)} = e^{-j\beta R_z}e^{-j\beta z}$. So the solution to the Helmholtz equation should be of the form:

$$\mathbf{E} = \mathbf{e}(x, y)e^{-j\beta z} \tag{2.10}$$

where $\mathbf{e}$ is the spatial field distribution in a plane perpendicular to the propagation direction and β is the propagation constant. The propagation constant can be seen as a spatial frequency and is expressed in m^{-1}. It is common practice to decompose β into: $\beta = n_{eff}k_0$, with n_{eff} the effective refractive index of the waveguide and k_0 the vacuum wave number. The vacuum wave number is the spatial frequency of the wave in vacuum and is given by: $k_0 = 2\pi/\lambda_0$, with λ_0 the vacuum wavelength. By introducing the effective refractive index, the waveguide mode propagating through the waveguide can be treated as a plane wave propagating through a material with refractive index n_{eff}. As we will see later, n_{eff} (and by definition β) are strongly wavelength dependent.

To calculate an expression for the transversal mode profile $\mathbf{e}(x, y)$, equations 2.10 can be substituted into equations 2.8 which yields a 2D differential equation for $\mathbf{e}(x, y)$. Imposing the translational invariance has reduced the dimensionality of the system from 3 to 2, as could be expected. In finding solutions to this equation, either β or ω are given and the other number is an eigenvalue of the equation. For example, one could solve the equation to look for all the solutions with vacuum wavelength $1550\,nm$. In this case ω is given and solving the equation yields a set of solutions, each consisting of a spatial mode distribution $\mathbf{e}(x, y)$ and a corresponding eigenvalue β (or n_{eff}). These solutions are called the waveguide modes. The solution with the largest n_{eff} value is called the fundamental mode. Other modes, with smaller n_{eff} values are higher order modes. If the effective index drops below the highest bulk refractive index of the cladding materials, the solution is no longer a guided waveguide mode.

Because the waveguides are not transversally invariant in the x direction, the electric and magnetic field vectors are not linearly polarized in one direction. Nevertheless, the modes are quasi polarized. Two main directions are distinguished:

- quasi TE-polarized: the electric field is polarized parallel to the substrate in most of the waveguide
- quasi TM-polarized: the magnetic field is polarized parallel to the substrate in most of the waveguide

For the sake of simplicity, the word 'quasi' will be omitted from now on. In waveguide geometries where the width of the waveguide is larger than the height of the waveguide, the fundamental mode is TE polarized and vice versa. In case of a

square waveguide cross-section with the same cladding material on all four sides, the TE and TM mode are degenerate.

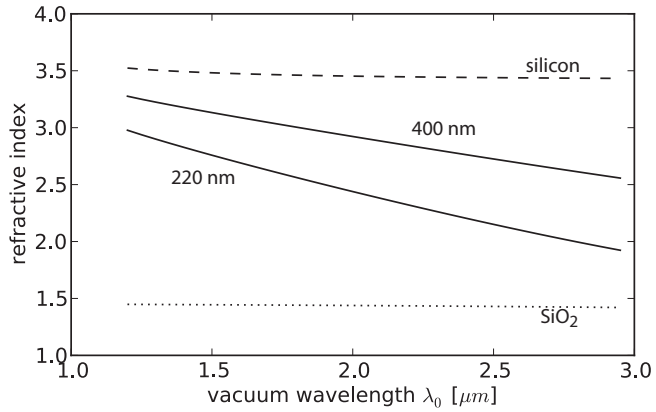

Figure 2.2: Dispersion characteristics of the 220 nm silicon strip waveguide and 400 nm silicon rib waveguide geometries shown in figure 2.1. The 220 nm strip and 400 nm rib are both $1\ \mu m$ *wide.*

Figure 2.2 shows the effective index of the fundamental TE mode of a $1\mu m$ wide 220 nm strip waveguide and a $1\ \mu m$ wide 400 nm rib waveguide with geometries as shown in figure 2.1. This data was calculated using the 1D eigenmode solver CAMFR [1]. The figure also shows the wavelength dependent bulk refractive indices of the core (silicon) and cladding (SiO_2) materials. The relationship between the temporal frequency (represented by ω, f or the vacuum wavelength λ_0) and the spatial frequency of the mode along the propagation direction (represented by β or n_{eff}) is called the dispersion relationship. Silicon waveguides as depicted in figure 2.1 are predominantly used in the telecom bands (around 1310 nm and 1550 nm) and in the mid IR region (1600 nm to 3500 nm). The cladding material, silicon oxide, heavily absorbs at wavelengths longer than 3500 nm. Silicon, the waveguide core material, has a bandgap of eV and is opaque at wavelengths close to the visible region.

As stated before, figure 2.2 also depicts the bulk refractive indices of the different materials in the waveguide structures. For longer wavelengths, it is more difficult to confine the optical beam within the waveguide core hence the effective index approaches the bulk cladding index. Vice versa the effective index asymptotically approaches the bulk core material index for shorter wavelengths because the core dimensions are much larger as compared to the optical wavelength so the beam is closely confined to the waveguide core.

2.2.2 Waveguide gratings

Introduction

One of the key concepts in this work are waveguide gratings [2] [3] [4]. A waveguide grating is an optical waveguide with a finite periodic corrugation in the propagation direction such that the light travels through a periodic sequence of regions of high and low effective index. The practical implementation of this periodic corrugation depends on the desired properties of the grating and the available technology. Figure 2.3 schematically shows the waveguide grating geometries associated with the material systems in figure 2.1:

- **220 nm silicon strip waveguide**: the grating is formed by etching shallow corrugations across the width of the strip waveguide. The corrugations are $70\,nm$ deep, resulting in subsequent regions of $150\,nm$ and $220\,nm$ high silicon. The etch depth is part of the technology definition and cannot be changed by the designer.
- **400 nm silicon rib waveguide**: a grating can also be a subsequent iteration of wider and narrower waveguide sections. This way the grating is defined during waveguide etching and does not need a separate etching step.
- **220 nm silicon nitride strip waveguide**: this is similar to the 220 nm silicon strip waveguide but with a silicon nitride waveguide instead of a silicon waveguide.

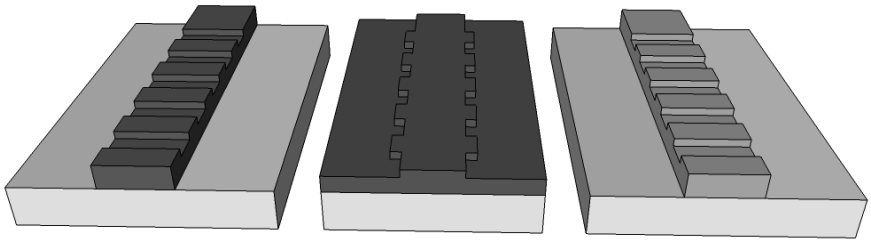

Figure 2.3: Geometries of the considered grating configurations in the different material systems: a) a shallow grating in 220 nm thick silicon strip waveguide b) a sidewall grating in a 400 nm thick silicon rib waveguide c) a shallow grating in a 220 nm thick silicon nitride strip waveguide

Bloch's theorem

In section 2.2.1, the propagation constant β was introduced as a consequence of the translational invariance of the waveguide along its propagation direction. A

waveguide grating with period Λ is only invariant under a discrete set of translations: $\epsilon(\mathbf{r}) = \epsilon(\mathbf{r} + \Lambda\mathbf{e}_z) = \epsilon(\mathbf{r} + 2\Lambda\mathbf{e}_z) =$ .. with $\mathbf{e}_z$ the unit vector along the z direction, the assumed propagation direction. The translation over a distance Λ along the z-axis can be represented by the operator T_Λ: $T_\Lambda f(z) = f(z - \Lambda)$. The fact that ϵ is invariant under T_Λ implies that T_Λ and the differential operator Θ commute. In linear algebra one can prove that if two operators commute, they have simultaneous eigenstates. This means that the eigenstates of Θ are a linear combination of the eigenstates of T_Λ. The eigenstates of T_Λ are easily found: $T_\Lambda e^{jkz} = e^{-jka}e^{jkz}$. So the eigenvectors are e^{jkz} with corresponding eigenvalues e^{-jka}. In general, these eigenfunctions are non-degenerate, they have different eigenvalues. Except for k-vectors that are spaced by $2\pi/\Lambda$. It can easily be verified that all eigenvectors of the form $e^{j(k+N2\pi/\Lambda)z}$ with N an integer number yield the same eigenvalue for the operator T_Λ. The corresponding eigenstate for Θ is a linear combination (with (x, y) dependent coefficients $\mathbf{c}_{k,N}$) of all these degenerate states:

$$\begin{aligned}
\mathbf{E}(\mathbf{r}) &= \sum_N \mathbf{c}_{k,N}(x, y)e^{j(k+N2\pi/\Lambda)z} && (2.11)\\
&= e^{jkz}\sum_N \mathbf{c}_{k,N}(x, y)e^{j(N2\pi/\Lambda)z} && (2.12)\\
&= e^{jkz}\mathbf{u}_k(x, y, z) && (2.13)
\end{aligned}$$

This shows that the eigenstates of Θ in an infinite grating waveguide is a plane wave, modulated with a function $\mathbf{u}_k$. This spatial modulation function is periodic with period Λ. These solutions are called *Bloch states*. Substituting equation 2.13 into the Helmholtz equation yields a solution for $\mathbf{u_k}$ and a value for k (or ω, if k is known). This solution is consistent with the waveguide solution in equation 2.10. A longitudinally invariant waveguide is also periodic, so it should fit into the description of equation 2.13. Indeed, equation 2.10 is a special case of 2.13 where $\mathbf{u}_k$ is no longer z-dependent.

To summarise, Bloch's theorem states that solutions of Maxwell's equation in a periodic medium are also periodic, with the same periodicity as the medium apart from a phase therm e^{jkz}.

Band diagrams

According to Bloch's theorem, solutions to $\mathbf{u}_k$ for $\mathbf{k}$ and $\mathbf{k} + N2\pi/\Lambda$ with $N \in \mathbb{N}$ are identical. Consequently, the k-space of interest can be reduced to: $-\pi/\Lambda \leq k \leq \pi/\Lambda$. This region in k-space is called the first Brillouin zone. For each point in this region solving for the Bloch states yields an infinite, discrete set of ω eigenvalues, each corresponding to a Bloch mode or order. When solving for

neighbouring $\mathbf{k}$-points, the ω solutions of identical order will form a continuous set, called a *band*, similar to the electron energy bands found in semiconductor physics. The conglomerate of these bands is called the *band diagram*. Assuming non-magnetic materials, time reversal symmetry dictates that this band diagram is symmetric along the $\mathbf{k}$-axis, so solutions for $\mathbf{k}$ and $-\mathbf{k}$ are identical.

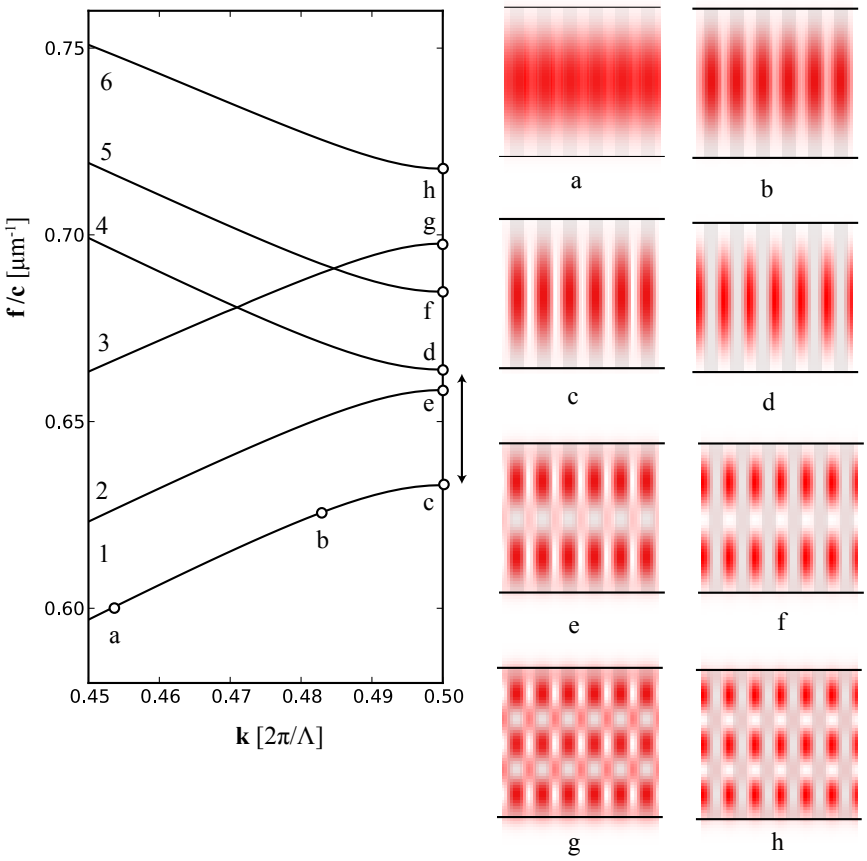

Figure 2.4: Band diagram for 220 nm thick silicon grating with a $\Lambda = 290nm$ pitch and $70\,nm$ deep corrugations as presented in figure 2.3

The left side of figure 2.4 shows the band diagrams for the waveguide grating configuration in figure 2.3a: a 220 nm thick, $1.6\,\mu m$ wide silicon waveguide grating with 70 nm deep corrugations spaced apart by $\Lambda = 290\,nm$. The band diagram is calculated using *MIT Photonic Bands* [5]. Given the geometry of the unit cell

and a list of $\mathbf{k}$-vectors, this program solves for the N lowest real eigenvalues for each $\mathbf{k}$-vector, with N an integer number set by the user. The program does not support dispersive material models as such, so the refractive index is assumed to be constant. However, in the wavelength region of interest, this is a good approximation.

On the right side of figure 2.4, each sub-figure (ranging from a to h) shows the energy density distribution of $\mathbf{u}_k(x, y, z)$ (averaged over time) in a plane through the grating, parallel to the substrate. These plots each correspond to a solution indicated on the band diagram on the left side of figure 2.4 (also ranging from a to h). Only the first six bands were calculated.

If the waveguide mode's $\mathbf{k}$-vector is significantly shorter than half the grating's k-vector, the optical wave will not feel the individual corrugations and will experience the grating as a uniform material with a refractive index that is a weighted average of the grating's refractive index variation along the propagation length.

This is illustrated by point a in figure 2.4. This point lies on the lowest order band (band number 1). The electric field vector of the solutions on this band are predominantly polarized along the x-direction. Consequently, this band corresponds to the fundamental TE-mode. At point a on band 1 there is no variation of the spatial energy distribution profile along the propagation direction. The wavelength of this mode is significantly longer than twice the grating period and consequently the interaction between the grating and the optical mode is rather limited. The optical mode behaves as if it was propagating in an unperturbed waveguide. Solutions with shorter $\mathbf{k}$-vectors behave in a similar way. For this reason, the band-diagram is drawn only for $\mathbf{k}$-vectors close to the first Brillouin zone's edge.

When the length of the $\mathbf{k}$-vector increases towards the edge of the first Brillouin zone, interaction with the grating grows stronger. This clearly shows in point b. The solution $\mathbf{u}_k(x, y, z)$ now starts to show the grating's periodicity. The optical mode has a higher intensity in the high (non-etched) part of the grating and lower intensity in the lower (etched) part of the grating. Consequently, the effective index of this mode is higher than the weighted average refractive index of point a. A higher effective index means a lower frequency for the same $\mathbf{k}$-vector. This is why the band bends down when it approaches the edge of the first Brillouin zone.

The interaction between the optical mode and the grating becomes even more apparent when considering the group-velocity. The group-velocity v_g is defined as the slope of the band diagram:

$$v_g = \frac{d\omega}{dk} = 2\pi \frac{df}{dk} \tag{2.14}$$

and is a measure for the propagation velocity of a sudden change in amplitude, for example an optical pulse. When band 1 bends downwards, its slope decreases. Consequently the group velocity decreases and the grating slows down the propagation of changes in the amplitude. Figure 2.5 paints a simplistic picture of how the grating slows down the light. If there is little to no interaction with the periodic corrugations, photons travel through the waveguide without any obstruction (figure 2.5a). At the band edge, the interaction between the fields and the grating is close to coherent. One can imagine that photons bounce back and forth in the grating, slowing down the overall propagation from left to right. It should be noted that this is still a propagating waveguide mode, so even though there is interaction with the grating and the propagation of amplitude changes is slowed down, no light is reflected throughout propagation in the grating.

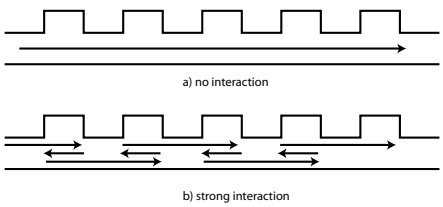

Figure 2.5: Simplistic representation light-grating interaction far away from the band-gap (top) and near the band-gap (bottom)

For even longer $\mathbf{k}$-vectors, the lowest order band becomes more and more shallow until df/dk reaches zero at $\mathbf{k} = \pi/\Lambda$. At this point (c in figure 2.4) the group velocity is zero so there is no propagation of light through the grating. Moreover, this point is degenerate. Bloch's theorem states that solutions with wave vectors $\mathbf{k}$ and $\mathbf{k} + 2\pi/\Lambda$ are identical. Because point c is at $\mathbf{k} = \pi/\Lambda$, this solution should be identical to the solution at $\mathbf{k} = -\pi/\Lambda$, its counter-propagating equivalent. In other words, both solutions cannot exist without each other: a forward propagating wave will couple into a backwards propagating wave and vice-versa. Consequently this solution is a standing wave, with maxima in the 'higher' (non-etched) part of the grating and minima in the 'lower' (etched) part of the grating.

One can easily imagine that such a standing wave solution can also exist with maxima in the etched part of the grating and minima in the non-etched part of the grating. The overall reactive index of the mode will be lower, because there is less overlap with the high-index silicon. Because this solution also has the same π/Λ wave vector, such a solution should lie at a higher frequency (shorter wavelength).

This is point d on band 4 in figure 2.4. The properties of this solution are very similar to the properties of point c, except for the spatial location of the maxima of the standing wave pattern. In fact, band 4, just like band 1, corresponds to the fundamental TE-mode. In between points c and d the solutions that correspond to the fundamental TE-mode are all standing-wave solutions that cannot propagate through the grating. For this reason, the region in between point c and d is called the band-gap for the fundamental TE mode.

The other bands in figure 2.4 correspond to higher-order TE modes. Judging from points e and f, bands 2 and 5 correspond to the first order TE-mode. Bands 3 and 6 correspond to the second order TE-mode (points g and h). Both modes also show an opening of the band albeit smaller than the band gap of the fundamental mode. The reason for this is that the higher the mode, the less confined the light is to the waveguide. Consequently the interaction with the grating decreases for increasing mode number.

Bragg waveguide grating reflectors

In deriving Bloch's theorem, the number of periods in the grating was assumed to be infinite. In reality, waveguide gratings are finite in length and strictly speaking Bloch's theorem no longer holds. This section will deal with the treatment of finite length waveguide gratings. The most straight-forward implementation of a finite waveguide grating is shown in figure 2.6. Part of a longer waveguide is corrugated over a finite length $L_g = N_g\Lambda$ with N_g the number of periods in the grating and Λ the grating period. L_g is referred to as the grating length. Light that is fed through the waveguide will encounter the grating and interact with it.

To characterise the properties of such a waveguide grating, it is interesting to monitor the fraction of the incoming light that is reflected/transmitted by the grating as a function of wavelength. More specifically: the fundamental waveguide mode (in this case the fundamental TE mode) is launched into the waveguide. The fraction of the power that is reflected back into the fundamental waveguide mode (in reverse propagation direction) is designated R. Correspondingly, the fraction of the power that is transmitted through the grating into the fundamental waveguide mode is designated T. Plotting R and T as a function of wavelength yields the R/T spectrum.

Figure 2.7 shows the R/T spectra for a $1.6\,\mu m$ wide and $220\,nm$ high silicon waveguide grating. The corrugations are etched $70\,nm$ deep into the waveguide with a period of $290\,nm$ and a duty cycle of 50%. In other words, this is a finite version of the grating discussed in the previous section on band diagrams (see fig 2.4). The number of periods in the grating varies throughout the different graphs.

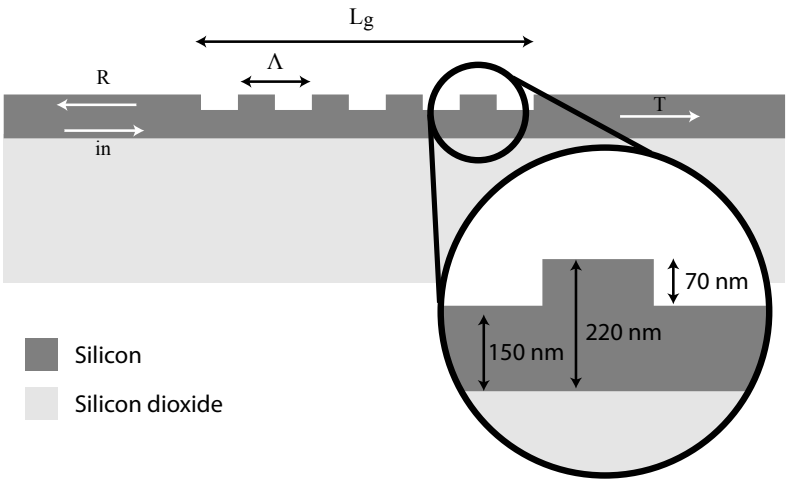

Figure 2.6: Schematic representation of the finite waveguide grating of length L_g and grating period Λ.

The spectra were calculated using the 2D eigenmode expansion tool *CAMFR* [1]. A standard effective index method was used to reduce the spatial dimensionality of the the problem from 3 to 2.

Consider the R/T spectrum for a grating with 100 periods in figure 2.7. The transmission spectrum (dotted line) shows a firm dip between approximately $\lambda = 1.502\,\mu m$ and $\lambda = 1.587\,\mu m$. This corresponds very well with the range of frequencies associated with the bandgap of the fundamental mode in figure 2.4. In this case, a grating of 100 periods resembles the behaviour of an infinite grating inside the bandgap: the transmission drops to -80 dB so virtually no light is allowed to travel through the grating waveguide. When the number of periods is reduced, the finite extent of the grating becomes more apparent: more light is transmitted through the grating (- 45.1 dB for 50 periods, - 33.8 dB for 40 periods, -24.5 dB for 30 periods, -14.5 dB for 20 periods and -5.5 dB for 10 periods). Also, the edges of the region where light transmission is reduced are blurrier.

So if light is not allowed to pass through the grating, where does it go? The answer lies in the reflection curves in figure 2.7. Within the band gap of the grating, most light is reflected back into the fundamental mode of the silicon waveguide where it was originally launched towards the grating. This does not come as a surprise. As stated in the previous paragraph, Bloch modes within the band gap are degenerate for both the forward and backward propagation direction. In other words, the forward propagating wave cannot exist without the backward propa-

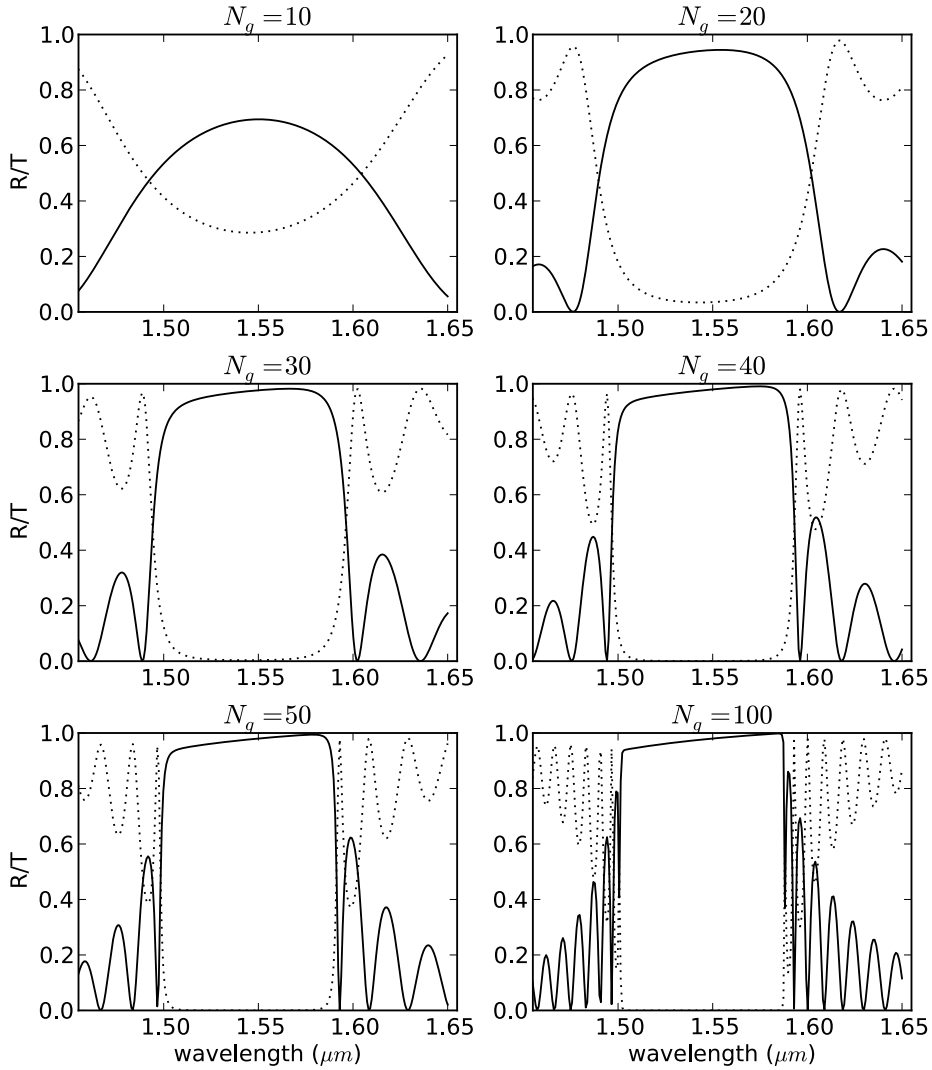

Figure 2.7: R/T spectra of $1.6\,\mu m$ *wide and* $220\,nm$ *high silicon waveguide grating with a* $290\,nm$ *period for different grating lengths.*

gating wave and vice-versa. Consequently, if a forward propagating wave with a wavelength within the band gap is launched into the grating, it will excite a backward propagating wave and light is reflected.

As expected, the reflectivity of the grating R increases with increasing number

of grating periods. The graphs show that R is quite strong: a 30 period long grating ($30 \times 0.290\,nm = 8.7\,\mu m$) results in a reflectivity of over 94% across an $80\,nm$ wavelength range. To quantify the strength of a certain grating geometry (so independent of its length) it is common practice in modern literature to use the coupling number κ, expressed in m^{-1}. This number finds is roots in coupled mode theory where it is used to quantify the coupling strength between the forward (A) and backward (B) propagating modes (in the z-direction) in the mathematical form $dA/dz \sim -j\kappa B$. More importantly, κ is related to the width of the band gap through the following relationship [6] (weak grating approximation):

$$\kappa = \pi n_0 \frac{\Delta\lambda}{\lambda_c^2} \tag{2.15}$$

with n_0 the average refractive index of the Bloch mode in the band gap, $\Delta\lambda$ the spectral width of the band gap and λ_c the center wavelength of the band gap. Since the effective index of a certain mode is the ratio of the length of its actual $\mathbf{k}$ vector in the waveguide to the length of its $\mathbf{k}$ vector in vacuum, n_0 can be estimated as follows:

$$n_0 = \frac{\pi/\Lambda}{2\pi/\lambda_c} = \frac{\lambda_c}{2\Lambda} \tag{2.16}$$

As said before, the band gap reaches from $1.502\,\mu m$ to $1.587\,\mu m$, so $\lambda_c = 1.545\,\mu m$ and $\Delta\lambda = 85\,nm$. Using these numbers: $n_0 = 2.664$ and $\kappa = 0.280\mu m^{-1}$. Usually κ is expressed in cm^{-1}, so $\kappa = 2800cm^{-1}$. Using κ, the maximum reflectivity of the grating R_{max} can be estimated using the formula [6]:

$$R_{max} = \tanh^2(\kappa L_g) \tag{2.17}$$

According to this formula, a grating of about $11\,\mu m$ will yield a maximum reflectivity of 99%. For our $290\,nm$ period grating this means approximately 40 periods. The data represented by figure 2.7 indeed shows that for $N_g = 40$ the maximum reflectivity is $99.1\,\%$.

The reason for such a high value of κ resides in the strong effective index contrast between the etched ($n_{eff} = 2.499$) and non-etched ($n_{eff} = 2.806$) parts of the grating. This leads to a big energy difference between the lower band-edge mode concentrated in the non-etched region of the grating and the upper band-edge mode concentrated in the etched region of the grating.

Apart from causing a high value for κ, the strong effective index contrast in the grating has another, more subtle, consequence. When inspecting the R/T spectra for long gratings in figure 2.7 the reflectivity maxima are not in the center of the band gap, but very close to the long wavelength edge of the band. Also, the reflectivity at the short wavelength edge of the band doesn't seem to approach $100\,\%$ but

instead is stuck at around $95\,\%$, no matter how long the grating length. The reason for this is found on the right side of figure 2.4. The Bloch mode at the longer wavelength edge of the band (point c in 2.4) is the standing wave with its maximum in the non-etched part of the grating. The lateral field profile of this mode closely resembles the lateral field profile of the unperturbed $220\,nm$ high silicon waveguide eigenmode. Because the grating is excited by such a waveguide, the incoming light coming from the unperturbed waveguide is easily coupled into the Bloch mode of the grating. This results in high reflectivity at the long-waveguide edge.

However, on the short wavelength side, the grating's Bloch mode is mainly concentrated in the etched part of the grating. Consequently the lateral field profile of the $220\,nm$ waveguide is not matched to the lateral field profile of the grating's Bloch mode. Such a mismatch leads to scattering at the waveguide/grating interface so some light is lost and not all light is reflected back into the waveguide. According to this reasoning, attaching the waveguide grating to a $150\,nm$ high waveguide should lead to maximum reflectivity near the short wavelength edge of the band. This configuration and its R/T spectrum are shown in figure 2.8.

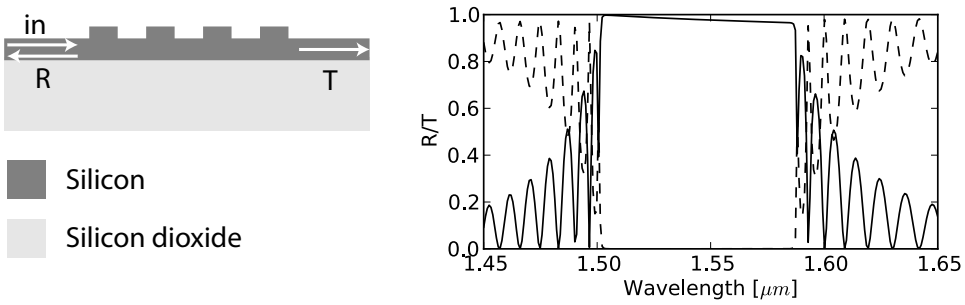

Figure 2.8: R/T spectra of $1.6\,\mu m$ *wide and* $220\,nm$ *high silicon waveguide grating with a* $290\,nm$ *period and 100 periods excited from a* $150\,nm$ *high waveguide.*

The R/T spectrum in figure 2.8 corresponds to a $1.6\,\mu m$ wide and $220\,nm$ high silicon waveguide grating with a $290\,nm$ period and 100 periods. This is the exact same grating as the R/T spectrum in figure 2.7 with $N_g = 100$ but now connected to a $150\,nm$ high access waveguide instead of a $220\,nm$ high access waveguide. As expected, the maximum reflectivity now occurs at the short wavelength side of the band. In other words, the reflectivity of the grating is high across the stopband, but due to the grating's high refractive index contrast it is not straight forward to couple into the Bloch mode efficiently at all wavelengths across the band.

Figure 2.9 shows the time-averaged spatial distribution of the electric field squared for an optical mode (non-etched access waveguide) with a wavelength within the band gap incident on the grating. To reveal the details of the plot, the color scheme is drawn in a logarithmic scale. The plot clearly shows the standing wave pattern as a result of the back reflection into the access waveguide.

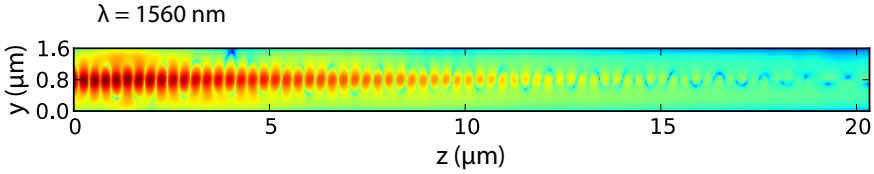

Figure 2.9: Time-averaged spatial distribution of the electric field squared for an optical mode (non-etched access waveguide) with a wavelength within the band gap incident on the grating. Color scheme is in logarithmic scale.

To gain more insight into the physics of the grating waveguide within the band gap, figure 2.10 shows a 1 dimensional cut through figure 2.9 at $y = 0.8\mu m$, also in logarithmic scale. The figure clearly shows that the power propagating through the grating decays exponentially as a function of distance (z).

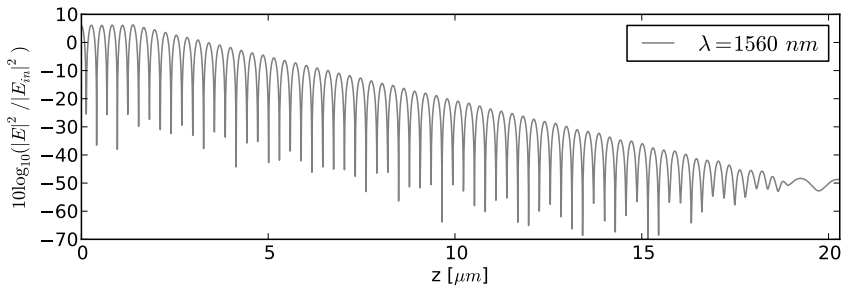

Figure 2.10: 1 dimensional cut through figure 2.9 at $y = 0.8\mu m$

This exponential decay can be understood by treating the grating as a series of semi-reflective interfaces separated by a distance Λ as schematically depicted in figure 2.11. Each grating period reflects a fixed fraction r of the optical power incident on that grating period. Because the light's k-vector within the band gap equals $k = \pi/\Lambda$, propagating back and forth through one period constitutes a

phase change of: $2\Lambda k = 2\pi$. In other words, all these reflections add up in the backward propagating direction. This effect is sometimes referred to as coherent back-scattering.

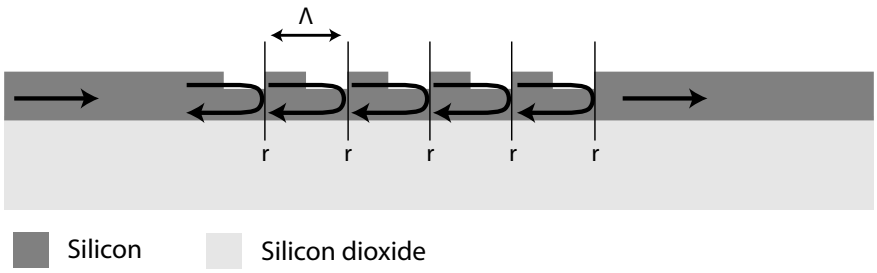

Figure 2.11: Schematic representation of the waveguide grating as a series of consecutive semi-reflective interfaces spaced by a distance Λ.

Assuming only first reflections, so once a fraction of light has been reflected, it passes straight to the access waveguide, the relationship of the forward-propagating power between two consecutive grating periods can be expressed as follows:

$$P_F(z+\Lambda) = P_F(z)(1-r) \tag{2.18}$$

$$P_F(z+\Lambda) - P_F(z) = -rP_F(z) \tag{2.19}$$

Dividing both sides by Λ and assuming Λ is sufficiently small yields:

$$\frac{dP_F(z)}{dz} = -\frac{r}{\Lambda}P_F(z) = -\kappa_P P_F(z) \tag{2.20}$$

with κ_P the power-coupling factor.

Using a similar reasoning, the equation governing the backward propagating power can be calculated:

$$\frac{dP_B(z)}{dz} = -\kappa_P P_B(z) \tag{2.21}$$

The solution to such a differential equation is an exponential dependence of the power as a function of propagation distance:

$$P_F(z) = P_0 \exp(-\kappa_P z) \tag{2.22}$$

This explains the exponential decay of the electric field in figure 2.10. The transmission of the grating, which is the forward propagating power at the end of the grating, so $T = P_F(N_g\Lambda)/P_0$, then reads:

$$T(N_g) = \exp(-\kappa_P \Lambda N_g) \tag{2.23}$$

In other words, the grating waveguide's transmission ratio decays exponentially as a function of the number of periods N_g.

2.3 Waveguide grating cavities

2.3.1 Band-edge Fabry-Perot cavities

Until now the focus of this text was mainly on the region of the R/T spectrum that corresponds to the grating's band gap. However, figure 2.4 shows that right next to the stop band, on both the long and short wavelength side, interesting features appear. The reflectivity and transmittance of the grating fluctuate as a function of wavelength. Within the band gap, the forward and backward propagating modes are degenerate, which, as discussed before, results in high reflectivity. But outside the band, even at the band-edge, the Bloch modes are non-degenerate and are not coupled by the grating. So how is it possible that the R/T spectrum shows non-zero reflection outside the band gap?

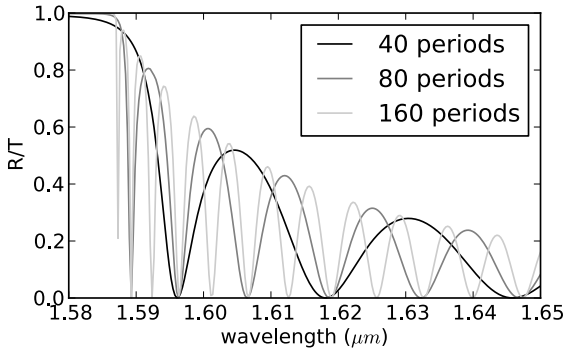

Figure 2.12: Detailed close-up of the reflection spectrum of the longer wavelength band-edge of the grating configuration of figure 2.7 with 40, 80 and 160 periods.

Figure 2.12 shows a close-up of the reflection spectrum at the long wavelength band-edge for a grating geometry identical to the one in figure 2.4 for 40, 80 and 160 periods. First of all, the envelope of the reflection maxima at the band-edge is independent of the number of periods in the grating. This length-independence suggests that the grating itself is not responsible for the reflection outside the band gap. But what the three different configurations depicted in figure 2.12 do have in common is their waveguide-grating interface. Although the Bloch modes near the band edge are propagating modes, they differ significantly from the eigenmodes in the terminating silicon waveguide in terms of mode profile, effective refractive

index and group velocity. This inevitably leads to reflections at the interface between the grating and its terminating waveguide. As illustrated in figure 2.4, the discrepancy between the grating and waveguide modes is most pronounced at the band-edge and decreases when moving away from the band gap. Consequently, the interface reflection is strongest close to the band edge and reduces away from the gap. Figure 2.13 depicts the R/T spectrum across a wide wavelength range and shows that the interface reflection occurs even far away from the band. This is typical for high-contrast gratings.

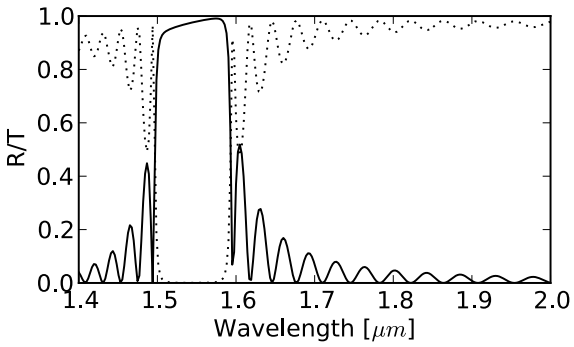

Figure 2.13: Panoramic R/T spectrum of the 40 period grating showing the spectral reach of the waveguide/grating interface reflection

The waveguide/grating interface actually occurs twice, at the beginning and at the end of the grating. In other words, the grating itself is captured in between two semi-reflecting surfaces. This set-up, where a medium is sandwiched in between two mirrors, is typically referred to as a Fabry-Perot cavity (FP-cavity). Because in this particular implementation the resonances only occur near the edge of the grating's band-gap, this type of cavities will be referred to as band-edge Fabry-Perot cavities. The interpretation of the finite grating as a FP-etalon is schematically drawn in figure 2.14. Outside the band gap, the Bloch mode in the grating can be treated as a normal waveguide mode in terms of propagation properties. Consequently, the grating can be represented as a uniform waveguide with an effective refractive index n_{gr} and group velocity $v_{g,gr}$ that can both be derived from the band diagram in figure 2.4. The field reflectivities at the waveguide/grating and grating/waveguide interfaces are r and $-r$ respectively.

When the effective optical wavelength fits an integer times in one round-trip, so twice the path length of the etalon, the wave reflected on the second grating/waveguide interface will cancel the reflection from the first waveguide/grating interface. At these wavelengths light is transmitted through the grating. Moreover, energy

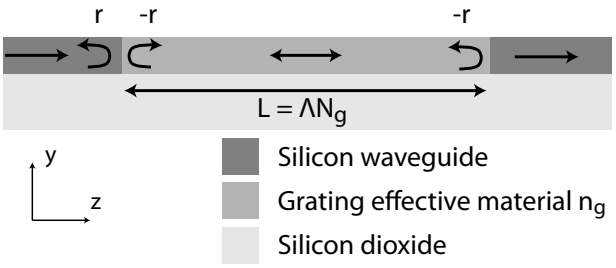

Figure 2.14: Schematic representation of the Fabry-Perot etalon formed by the grating

builds up inside the etalon and it wil act as an optical cavity. The wavelength where these resonances occur can be identified on figure 2.12 by the sharp reflectivity dip and transmittance peak. The wavelengths of the resonances obey the following mathematical condition:

$$2L_g k = M2\pi \tag{2.24}$$

with L_g the grating length, k the Bloch mode's wave vector in the grating and M an integer number. To analytically solve for the wavelengths that meet this condition, an expression for the wavelength dependence of the wave vector k should be found. Analogous to the treatment of electrons in a periodic crystal, the dispersion relationship of the Bloch modes near the band edge can be approximated by a parabolic function:

$$\omega = a(k - K)^2 + \omega_B \tag{2.25}$$

with K half the grating's k-vector ($K = 2\pi/\Lambda$), ω_b the angular frequency of the band-edge and a the fitting-parameter describing the curvature of the parabolic approximation. Fitting the long-wavelength band-edge of the fundamental TE mode in figure 2.4 yields the following parameter values:

Parameter	Value	Unit
K	5	$1/m$
ω_B	8	rad/s
a	8	$m^2 rad/s$

Using the relationship $\omega = 2\pi c/\lambda$, equation 2.25, the wavelength dependence of k can be approximated:

$$\frac{2\pi c}{\lambda} = a(k - K)^2 + \frac{2\pi c}{\lambda_B} \tag{2.26}$$

$$\Leftrightarrow \quad k = K + \sqrt{\frac{2\pi c}{a}\frac{\lambda_B - \lambda}{\lambda\lambda_B}} \tag{2.27}$$

Near the band edge, $\lambda \approx \lambda_B$, so $\lambda\lambda_B \approx \lambda_B^2$. Also, at the longer wavelength edge a is a negative number, so expression 2.27 can be simplified to:

$$k = K + b\sqrt{\lambda - \lambda_B} \tag{2.28}$$

with

$$b = \sqrt{-\frac{2\pi c}{a\lambda_B^2}} \tag{2.29}$$

Plugging equation 2.28 into the resonance condition 2.24 yields:

$$2L_g(K + b\sqrt{\lambda - \lambda_B}) = M2\pi \tag{2.30}$$

Because $L_g = N_g\Lambda$ and $K = \pi/\Lambda$, this simplifies to:

$$2L_g b\sqrt{\lambda - \lambda_B} = 2\pi(M - N_g) = 2\pi\widetilde{M} \tag{2.31}$$

Consequently the resonance wavelengths are given by:

$$\lambda = \lambda_B + \left(\frac{\pi\widetilde{M}}{L_g b}\right)^2 \tag{2.32}$$

So under the assumption of a parabolic dispersion curve near the band edge, the resonances are also spaced quadratically in wavelength space. Figure 2.15 (left axis) shows the five resonance wavelengths closest to the longer wavelength band edge as a function of "resonance mode number", with 1 being the closest to the band and 5 the furthest away from the band. The figure also shows a parabolic fit (dashed line) to the resonance wavelengths at the edge of the band. As expected, the band shape is not perfectly parabolic, especially further away from the band-gap, but the fit is reasonable and it allows for relatively accurate back of the envelope calculations of the mode spacing and, as will be discussed later, group velocity.

Figure 2.16 shows the spatial distribution of the magnitude of the electric field squared averaged over time for the first two resonant modes of the 80 period grating and at the wavelength in between these two modes. To improve the visual clarity of the figures, the color scheme is drawn in a logarithmic scale. The amplitude envelope of the first cavity mode shows a sinusoidal longitudinal dependence. To explain such an amplitude variation, first consider figure 2.4. The mode profiles on the right side of this figure clearly show that the longitudinal dependence of the eigenstates $\mathbf{u_k}$ near the edge of the band (point b) is no longer constant, but shows a clear periodic component with the grating period Λ. These modes are outside the band gap, so their propagation constant k is slightly smaller than half the grating's wave vector $K = \pi/\Lambda$, so this can be written as: $k = K - \delta k$ with δk the difference between k and K.

Because the actual mode propagating through the grating is the product of the eigenstate $\mathbf{u_k}$ and the traveling wave factor e^{jkz}, the Bloch mode has a periodicity which is the difference of the two contributing factors: $K - (K - \delta k) = \delta k$. In

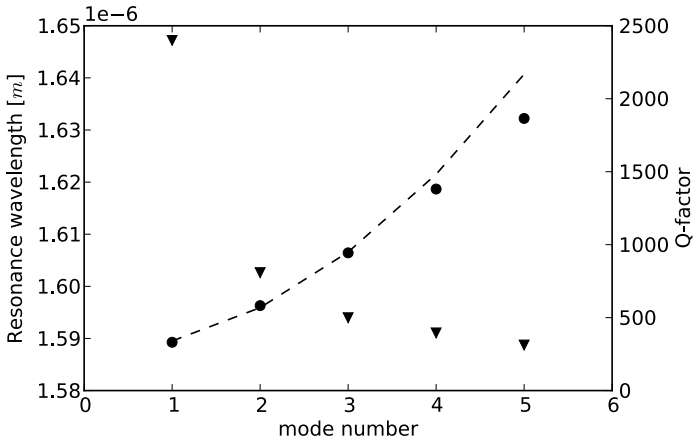

Figure 2.15: Resonance wavelength and Q-factor for the first 5 long-wavelength band-edge modes

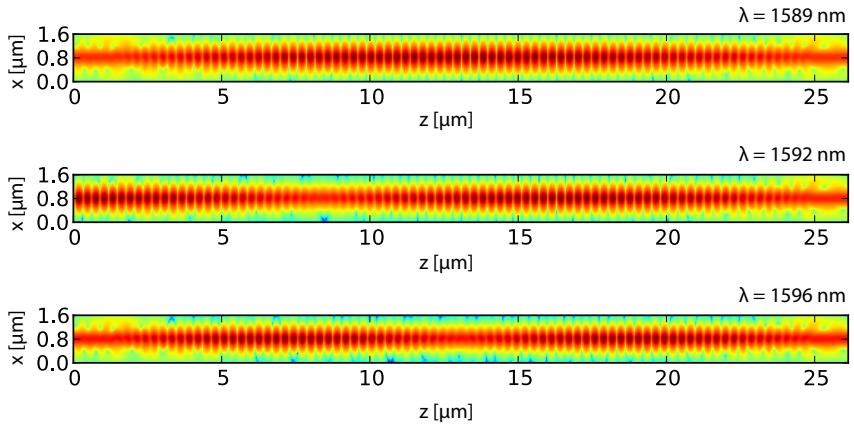

Figure 2.16: Spatial distribution for the first band-edge resonance ($\lambda = 1589\,nm$), the second band-edge resonance ($\lambda = 1596\,nm$) and at the reflection maximum in between ($\lambda = 1592\,nm$). Note: the logarithmic color scales differ between different graphs.

the parabolic approximation, equation 2.28 shows that $\delta k = b\sqrt{\lambda - \lambda_B}$. On the other hand, using equation 2.31, the resonance condition for δk yields:

$$\delta k = \frac{2\pi}{2L_g}\widetilde{M} \tag{2.33}$$

In other words, the actual spatial periodicity of the Bloch mode Λ_B should be:

$$\Lambda_B = \frac{2L_g}{\widetilde{M}} \tag{2.34}$$

For the first resonance, so $\widetilde{M} = 1$ ($\lambda = 1589\,nm$), the spatial periodicity of the propagating Bloch mode is twice that of the cavity length. But because the etalon is resonant at this wavelength, the Bloch mode will propagate back and forth in the cavity and a standing wave will arise. The spatial periodicity of a standing wave is half of the traveling wave's periodicity, so the Bloch mode fits exactly once in the cavity. That is what is shown on figure 2.16. For the second mode ($\widetilde{M} = 2$, $\lambda = 1596\,nm$) the mode fits in the length of the cavity twice and so on.

Figure 2.16 also shows the spatial distribution of the time-averaged electric field squared at the wavelength of maximum reflectivity in between resonances 1 and 2. As expected, the Bloch mode now fits 1.5 times in the grating etalon. The standing wave pattern at the beginning of the grating ($z = 0$) indicates that the grating reflects energy at this wavelength.

The color scales in figure 2.16 differ between the different images. To show the difference between the resonant mode at $\lambda = 1589\,nm$ and the reflecting mode at $\lambda = 1593\,nm$, figure 2.17 shows the time-averaged magnitude squared of the electric field (same metric as depicted in figure 2.16) in a 1D cut through the grating (at $x = 0.8$ in figure 2.16). The y-scale is the local time-averaged magnitude squared of the electric field $|E|^2$ normalised to the magnitude of the exciting mode.

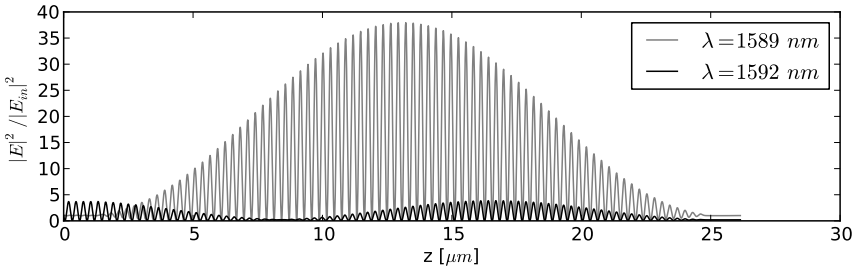

Figure 2.17: Spatial distribution of the time-averaged magnitude squared of the electric field in a 1D cut through the grating (at $x = 0.8$ in figure 2.16) for the first resonance (at $\lambda = 1589\,nm$) and the adjacent reflectivity maximum (at $\lambda = 1592\,nm$)

The plot nicely shows the sinusoidal nature of the amplitude envelopes as a result of the interplay between the 2 different periodicities of the Bloch wave at

play (k and K). The reflecting mode consists of a standing wave throughout the structure. The amplitude of this standing wave never reaches values higher than $|2E_{in}|^2$. In other words, there is no energy build-up inside the grating at this wavelength.

On the other hand, the amplitude envelope of the first resonant mode ($\lambda = 1589\,nm$) shows a significant field enhancement inside the cavity. The magnitude of the electric field squared of the standing wave pattern reaches a value of up to about 40 times the input wave's value. It should be clear that in this case the cavity stores a certain amount of energy. To characterize the ability of a grating to store energy, the Q-factor is introduced. By definition, the Q-factor is 2π times the ratio of the total energy stored in the cavity and the energy that is dissipated in the cavity during one optical period. In mathematical terms this reads:

$$Q = \frac{2\pi U}{-T_{opt} dU/dt} = \frac{2\pi U}{T_{opt} P_{dis}} = \frac{2\pi f U}{P_{dis}} \tag{2.35}$$

With U the energy stored in the cavity, P_{dis} the dissipated power in the cavity, T_{opt} the optical period and f the optical frequency ($T = 1/f$). Figure 2.15 (black triangles) shows the Q-factor for the different modes in the 80 period long grating. The Q-factor decreases quickly with increasing mode number. One of the main reasons for this is the decrease in group velocity with increasing spectral distance from the band gap. Using the parabolic approximation in equation 2.25, the group velocity $v_g = d\omega/dk$ and consequently the group index $n_g = c/v_g$ can easily be calculated:

$$v_g = \frac{d\omega}{dk} = \frac{d\omega/d\lambda}{dk/d\lambda} \tag{2.36}$$

Using 2.28 and $\omega = 2\pi c/\lambda$, this yields:

$$v_g = \frac{4\pi c\sqrt{\lambda - \lambda_B}}{b\lambda} \approx \frac{4\pi c\sqrt{\lambda - \lambda_B}}{b\lambda_B} \tag{2.37}$$

Due to the limited spectral range near the edge of the band where the parabolic approximation is applicable, it is justified to say that $b\lambda \approx b\lambda_B$ in the denominator of equation 2.37. An approximate expression for the group index n_g now reads:

$$n_g = \frac{c}{v_g} = c\frac{b\lambda_B}{4\pi c\sqrt{\lambda - \lambda_B}} \tag{2.38}$$

Using the parabolic fitting in figure 2.15 the group index at the wavelength of the first resonance is close to 13.5. This means that photons propagate 13.5 times slower in the grating than in vacuum. Hence the relatively high Q-factor of 2400.

Mode	$\lambda_r[\mu m]$	Q	n_g	T	R
1	1.589	2400	13.55	0.72	0.28
2	1.596	808	6.29	0.84	0.16
3	1.606	499	4.36	0.89	0.11
4	1.618	380	3.45	0.904	0.096
5	1.632	312	2.93	0.916	0.084

Table 2.1: Listing of all the parameters in equation 2.40 for the first five long-wavelength band-edge modes of the 80 period long grating

In fact, group index n_g and Q factor are linearly related to each other. Consider a band-edge cavity with facet reflectivity R, transitivity T (with $R+T=1$), cavity length L_g, group index n_g and resonance wavelength λ_r (resonance frequency f_r). During each roundtrip, a photon passes the facets twice. Consequently, the energy loss per roundtrip amounts to T^2. The time-of-flight of one round-trip equals L_g/v_g. Consequently the rate of change of the energy stored in the cavity can be written down as:

$$\frac{dU}{dt} = -\frac{T^2 v_g}{L_g} U \tag{2.39}$$

Rearranging terms and multiplying with $2\pi f_r$ yields:

$$2\pi f_r \frac{U}{dU/dt} = Q = \frac{2\pi L_g n_g}{T^2 \lambda_r} \tag{2.40}$$

Relating the Q-factor to the group index n_g and the grating facet (transition between grating region and non-grating region) reflectivity $R = 1 - T$. Q-factor and group index were determined earlier by considering the energy in the cavity and the parabolic approximation of the band diagram near the edge respectively. Expression 2.40 allows to find an approximate value of the facet reflectivity R. Table 2.1 lists the Q-factors, group indices (calculated using 2.38) and facet transmission/reflection (calculated using 2.40) coefficients.

The data in table 2.1 shows that the facet reflectivity is relatively low, so the high Q-factors near the band-edge are the result of the high group index. As expected, the facet reflectivity also reduces with increasing spectral distance from the band edge. As illustrated in figure 2.4, away from the band-edge the mode profile approaches that of an unperturbed waveguide, reducing the transition at the waveguide/grating interface.

To conclude the treatment on band-edge Fabry-Perot resonators, figure 2.18 shows the Q-factors (circles) and the corresponding resonance wavelengths (triangles) of the first resonant mode as a function of grating length. As expected

considering equation 2.40, the Q-factor increases with increasing grating length. However, the Q-factor increases faster than linear as a function of grating length. This is because a longer grating length results in a resonance wavelength closer to the band gap. Consequently the group index n_g and the facet reflectivity R of the first resonance also increases with growing grating length. This results in a superlinear growth of the Q-factor as a function of the grating length.

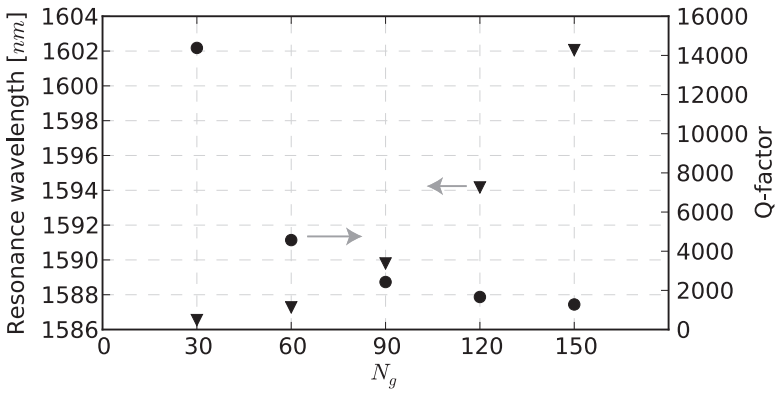

Figure 2.18: Overview of the resonance wavelengths and corresponding Q-factors for the first resonance as a function of the number of periods in the grating.

Figure 2.18 also shows that high Q-factors can be obtained. A grating containing 150 periods (this is approximately $43\mu m$ long) yields a Q-factor of more than 14000. Unfortunately such a high Q-factor comes at a certain cost. As the grating length grows longer, the spectral mode spacing between the different resonances will quickly shrink. For example, in the case of a 150 periods long grating, the second resonance is only $2\,nm$ away from the first one. In some applications this is not acceptable.

2.3.2 Band gap defect cavities

The previous section showed that a grating can be used to store optical energy at the wavelengths near the edge of the band-gap by exploiting the slow light properties of that spectral region in a Fabry-Perot configuration. However, section 2.2.2 revealed that if an optical mode with a wavelength inside the band gap is launched towards the grating waveguide, it is partially, or close to completely reflected, depending on the length of the grating. In other words, it should also be possible to trap light in between 2 such highly reflecting mirrors and obtain a cavity with a high Q-factor.

Practically speaking, the cavity should consist of two gratings with a waveguide in between. In order for such a configuration to be resonant, the total phase change accumulated during one round-trip should be an integer times 2π. The phase change over a certain length L_{wg} in the waveguide in between the gratings is easily calculated as $\Delta\phi_{wg} = k_{wg}L_{wg}$. On the other hand, the phase change after propagating back and forth through one of the grating mirrors is not easily calculated and should be simulated.

Figure 2.19 shows the R/T spectrum of the grating that was discussed in the previous section with 10, 30, 60 and $90 periods$ in grey. The plots also shows the phase change $\Delta\phi_{gr}$ of the reflected mode as compared to the phase of the incoming mode. When discussing the reflective phase change of an optical component it is important to clearly define the reference plane where the phase change is calculated. In this case, the reference plane is right before the grating and the grating starts off with an un-etched section.

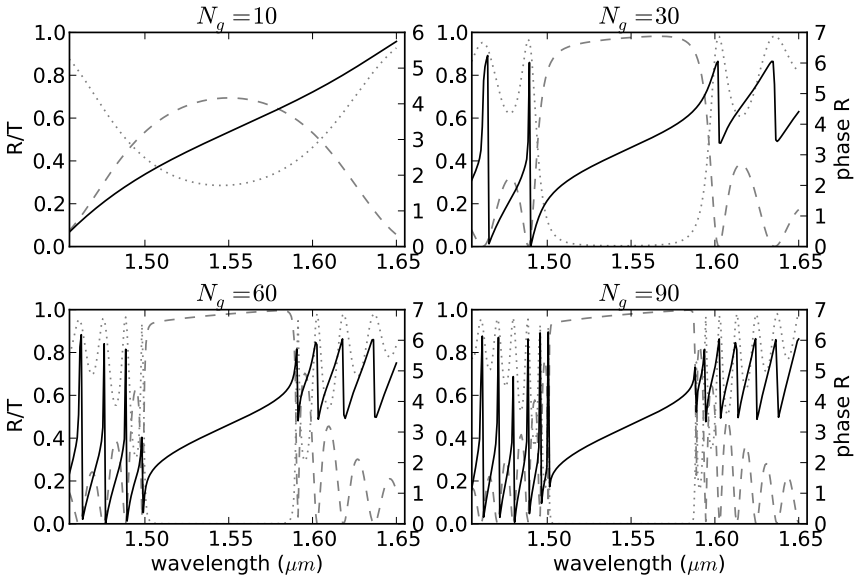

Figure 2.19: Phase of the mode after being reflected by the grating for different grating lengths.

The $\Delta\phi_{gr}$ profiles in figure 2.19 show a few interesting properties. Across the band gap, in between the first short-wavelength band-edge resonance and the first

long-wavelength band-edge resonance, the phase change $\Delta\phi$ varies by an amount of no more than 2π. The rate of change of $\Delta\phi$ as a function of wavelength is steep near the edges of the band and flattens out in the center, where it reaches a value of π.

As said before, for the cavity consisting of two gratings with a waveguide in between to be resonant, the total phase change of 1 round trip should add up to 2π. On round trip consists of being reflected by each mirror grating once and passing through the waveguide twice. Assuming both grating mirrors are identical with a phase change $\Delta\phi_{gr}$, the total accumulated phase change of 1 round-trip $\Delta\phi_{RT}$ reads:

$$\Delta\phi_{RT} = 2k_{wg}L_{wg} + 2\Delta\phi_{wg} \tag{2.41}$$

At the center of the band gap, the mirror phase change $\Delta\phi_{wg}$ is π. So the resonance condition $\Delta\phi_{RT} = N2\pi$ can be fulfilled even without putting a waveguide in between the two gratings, so $L_{wg} = 0$. Remember that the phase diagrams in figure 2.19 were calculated using a reference plane before the grating, starting with an un-etched section. In order to comply with the resonance condition in the center of the band, the two gratings should be combined at the location of that reference plane. In other words, the two un-etched sections should be put together, resulting in an un-etched section in the center of the grating that is twice the length of all the other un-etched sections in the grating (or the length of 1 full period Λ. Figure 2.20 shows a close-up of the center of the grating, showing the interface where the two gratings are stitched together. The double-length un-etched section is called a *defect*. It creates a state in the center of the band-gap where photons can get trapped.

Figure 2.20 shows the R/T diagram for a 60 period grating (same configuration as the previous section) with a defect in the center. In essence these are two 30 period gratings stitched together. The left side of figure 2.20 shows a wide spectral view across the band-gap. The spectrum looks very similar to the RT spectra in figure 2.7 except for a few details. At the edge of the band, the sharp resonances have disappeared. There are some R/T fluctuations, but not as sharp as the similar 50 period grating in figure 2.7. This was to be expected, because the point defect in the center disturbs the periodic nature of the grating. Consequently, the band-edge Bloch solution no longer exists across the entire grating.

However, the point-defect grating can be regarded as the concatenation of 2 shorter gratings in which the band-edge Fabry Perot resonances do exist. Careful inspection of the RT spectrum in figure 2.20 shows that the reflection dips near the band edge, which correspond to the FP resonance wavelengths, coincide with the FP resonance wavelengths of the 30 period grating in figure 2.7. The concatenation

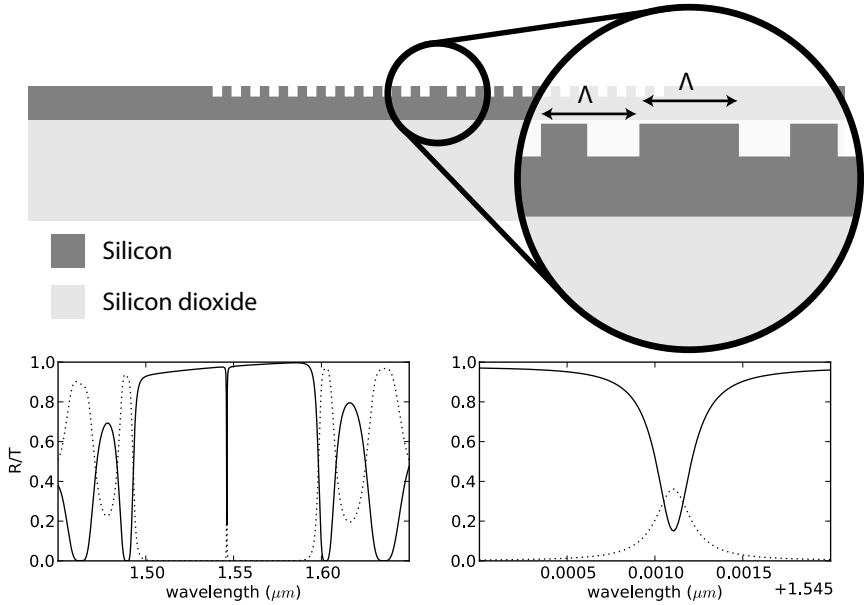

Figure 2.20: R/T spectrum of a 60 period silicon grating with a point defect in the center.

of 2 such resonators is also referred to as a second order filter and leads to flattening of the resonance peaks as shown in figure 2.20. This effect is also observed in higher order ring-resonator filters [7].

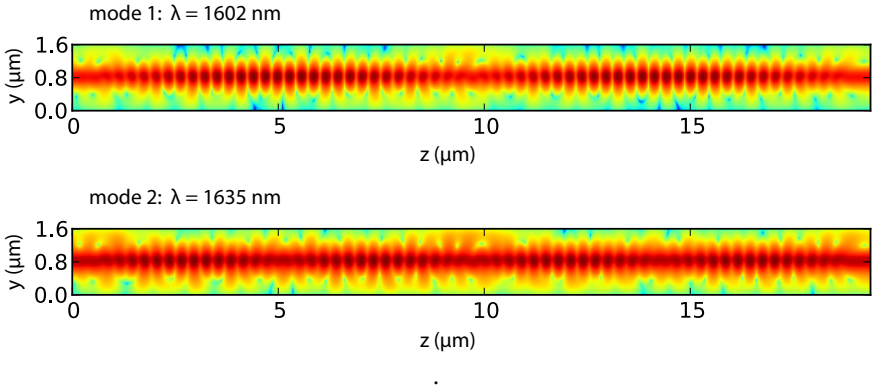

Figure 2.21: Spatial distribution of the time-averaged electric field for the first two long-wavelength band-edge resonances in figure 2.20

Figure 2.21 shows the time-averaged spatial distribution of the electric field for the first two long-wavelength band-edge resonances in the 60 period grating with point defect in figure 2.20. The first mode clearly consists of 2 separate, 30 period first order band-edge resonances, resulting in an amplitude envelope function with 2 local maxima. Similarly, the second mode consists of 2 separate 30 period second order modes, causing an amplitude envelope function with 4 local maxima.

But the most important difference between the RT spectrum of a grating with (figure 2.20) and without (figure 2.7) a point defect is the sharp resonance in the center of the band-gap, as predicted by expression 2.41 and figure 2.19. Figure 2.22 shows the spatial distribution of the time-averaged electric field at the center defect wavelength ($\lambda = 1.546\,\mu m$) and figure 2.23 shows a 1 dimensional cut through figure 2.22 at $y = 0.8\,\mu m$. Both figures show the significant field enhancement inside the silicon cavity and the exponential decay of the field envelope when traveling towards the edges of the grating. The exponential decay envelope was explained in the previous section.

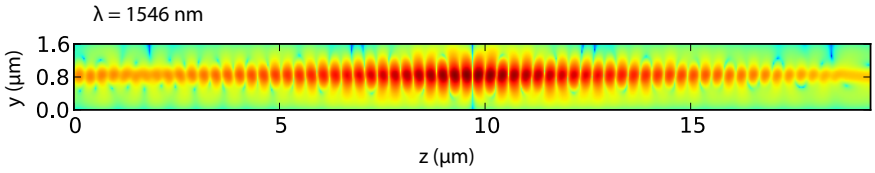

Figure 2.22: Spatial distribution of the time-averaged electric field of the defect resonance in figure 2.20. The color scheme is in a logarithmic scale.

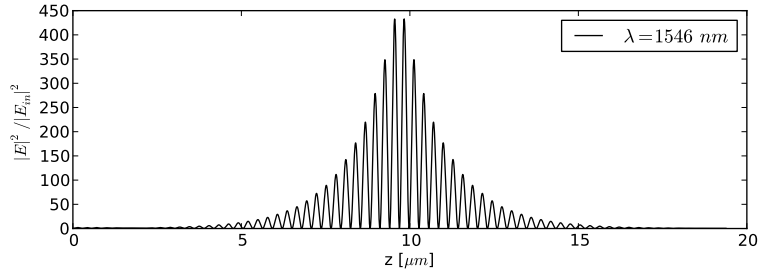

.

Figure 2.23: 1 dimensional cut through figure 2.22 at $y = 0.8\,\mu m$ of the electric field squared normalised to the electric field squared of the input mode.

In the previous section about band-edge resonators, the Q-factor, a number

quantifying the capacity of a cavity to store energy, was calculated by integrating the total energy inside the cavity under continuous wave excitation, normalized to the power of the excitation. This approach is usually used when the structure is calculated using an eigenmode expansion tool that calculates the spatial energy distribution under continuous wave excitation. Even though this approach is valid, a more practical approach exists.

Consider a cavity that is excited by a pulse at a certain point in time t_0. After the pulse excitation is finished, the cavity is filled with a certain amount of photons, or equivalently, an amount of energy U. After each round trip T_{RT} in the cavity, the energy will decay:

$$U(t + T_{RT}) = U(t) - \alpha_{RT} U(t) \tag{2.42}$$

with α_{RT} the losses per round trip. Rearranging the terms, dividing by T_{RT} and assuming T_{RT} is significantly smaller than the timescale of interest yields:

$$\frac{dU(t)}{dt} = -\frac{\alpha_{RT}}{T_{RT}} U(t) = -\frac{1}{\tau_0} U(t) \tag{2.43}$$

With $\tau_0 = \alpha_{RT}/T_{RT}$ the cavity's time constant.

Without external excitation, solving the previous differential equations states that the energy inside the cavity decays exponentially:

$$U(t) = U_0 \exp\Big(-\frac{t}{\tau_0}\Big) \tag{2.44}$$

The cavity's time-constant τ_0 indicates how long it takes until the energy in the cavity has dropped to $e^{-1} \approx 37\%$ of its original value. The time constant can easily be relate to the Q-factor using equation 2.35:

$$Q = \frac{2\pi f U(t)}{dU(t)/dt} = 2\pi f \tau_0 \tag{2.45}$$

So the Q-factor is linearly proportional to the cavity's time constant τ_0. The most common method to identify Q is to use a Finite Difference Time Domain (FDTD) simulation tool. This is a software program that will discretize the simulation in both space and time and solve Maxwell's equations using a finite difference approach. This is a particularly powerful method that allows to monitor the value of the electric field at different points in space as a function of time.The method can be used in both 2 and 3 dimensions.

To find the Q-factor of the cavity, a TE-polarized optical pulse with center wavelength $1550\,nm$ is launched from the silicon access waveguide towards the

grating. The x-component (TE) of the electric field in a point close to the center of the cavity is recorded as a function of time. Because the mode energy inside the cavity decays exponentially with a time constant τ_0, the field amplitude E_x of each TE-polarized resonant mode varies as follows:

$$E_x = E_0 \sin(2\pi f_R t + \phi) \exp(-\frac{t}{2\tau_0}) \tag{2.46}$$

With E_0 the mode amplitude at $t = 0$, f_R the resonance frequency, ϕ the phase offset and τ_0 the cavity's time constant. It is possible that more than 1 mode exists inside the cavity. In this case, the electric field E_x is the sum of all contributing modes i:

$$E_x = \sum_i E_{0,i} \sin(2\pi f_{R,i} t + \phi_i) \exp(-\frac{t}{2\tau_{0,i}}) \tag{2.47}$$

The process of decomposing the captured electric field time trace into exponentially decaying sine waves is called harmonic inversion. Dedicated software [8] is available that accepts a text file containing the field values on a fixed time grid, as generated by a FDTD program, and performs the harmonic inversion. This yields a list of amplitudes, resonance frequencies, phases, time constants, Q-factors and a figure of merit describing the quality of the fit for each mode.

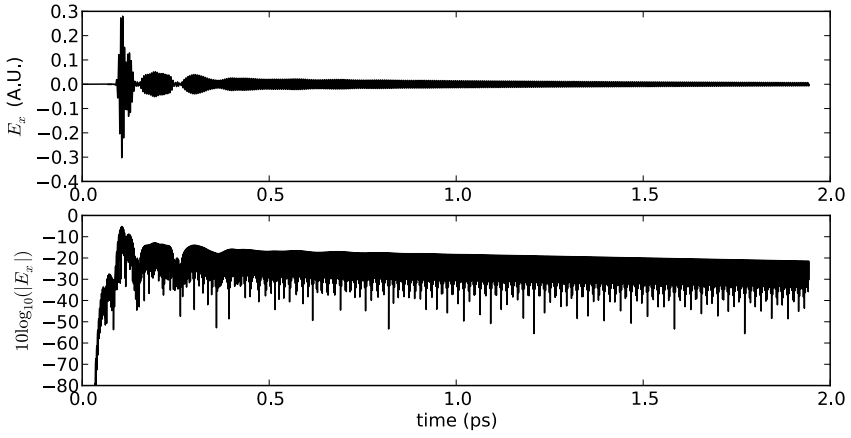

Figure 2.24: Time trace of the x-component of the electric field at a point close to the grating's center after excitation with a short pulse. The top graph shows the field in linear scale, clearly showing the exciting pulse at the beginning. The bottom graph shows the absolute value of the field in logarithmic scale to highlight the exponential decay.

The top graph in figure 2.24 shows the time trace of the x-component of the electric field for a 40 period long grating with a defect in the center. The trace

is recorded at a point near the center of the cavity. The grating is excited with a short fs pulse (recorded at $t = 100fs$) launched from the silicon access waveguide. The bottom graph shows the absolute value of the electric field in logarithmic scale. This graph clearly shows the exponential decay (linear slope in logarithmic scale) of the amplitude of the cavity resonance.

In this case there is only 1 high-Q resonance so the time-constant can easily be estimated using the bottom graph in figure 2.24. The amplitude drops by about $1.8\,dB$ per $500\,fs$, resulting in a time constant τ_0 of approximately $0.6\,ps$. Consequently, according to 2.45, the Q factor is $Q = 2\pi f\tau_0 \approx 733$. The more rigorous harmonic inversion yields a Q-factor of 786 at $\lambda_R = 1546\,nm$.

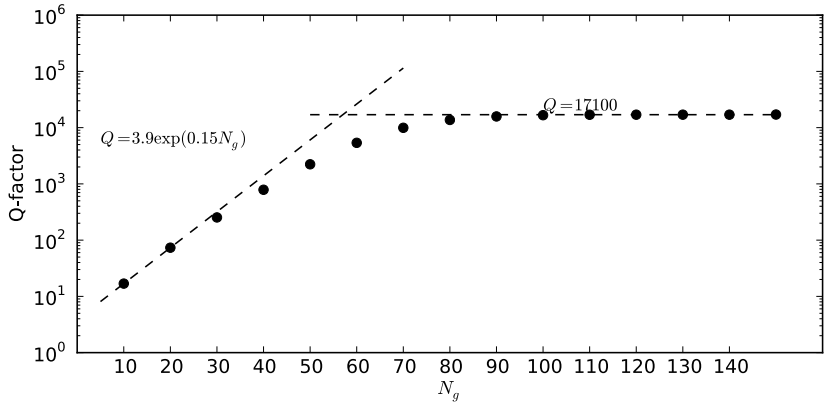

Figure 2.25: Q-factors of waveguide grating with defect in the center for different number of periods.

Figure 2.25 shows the Q-factor of waveguide gratings with a defect in the center as calculated using harmonic inversion with 2D FDTD time traces as a function of the total number of periods in the grating. Initially the Q-factor grows exponentially with increasing number of periods. For more than 40 periods, the exponential growth is hampered and eventually the Q-factor saturates at a value of 17000.

To understand this behaviour of initial exponential growth and subsequent saturation, consider the right side of figure 2.20. This graph shows a close-up of the RT spectrum near the defect resonance wavelength. The reflected and transmitted power add up to a value of 0.5. In the case of the band-edge resonances discussed in the previous section, the reflection and transmission values sum up to approximately 1. This is because the cavity loses its energy through its facets that lead

into the silicon waveguide on both sides. The fact that R and T do not add up to 1 at the defect grating resonator's resonance wavelength means that the cavity not only loses light at its facets, but also leaks a significant amount of energy out of plane.

In other words, the total energy dissipated in the cavity, dU/dt, is actually comprised of two separate components:

$$\frac{dU}{dt} = \frac{dU}{dt}_{facets} + \frac{dU}{dt}_{oop} \tag{2.48}$$

where *oop* stands for *out of plane*.

Consequently the reciprocal value of Q can also be divided into two parts:

$$\frac{1}{Q} = \frac{dU/dt}{2\pi f U} = \frac{dU/dt_{facets}}{2\pi f U} + \frac{dU/dt_{oop}}{2\pi f U} = \frac{1}{Q_{facets}} + \frac{1}{Q_{oop}} \tag{2.49}$$

In a first order approximation and in the absence of out-of-plane scattering, equation 2.40 relating the Q-factor to the cavity parameters L_g, n_g, λ_r and T in the case of band-edge Fabry Perot cavities can also be applied to defect cavities. This formula states that the Q-factor is proportional to T^{-2} with T the mirror transmissivity. According to equation 2.23, the transmissivity of the grating mirrors decays exponentially as a function of the number of periods N_g. In other words, in the absence of out-of-plane scattering, the Q-factor should increase exponentially:

$$Q_{facets} \sim \exp(2k_P \Lambda N_g) \tag{2.50}$$

Because all the gratings used in this work are first order gratings, the grating mirrors do not radiate energy out of plane. In other words, the out-of-plane scattering originates from other sources, such as the waveguide/grating interface at the facets but predominantly from the defect itself. These sources are independent of the number of periods in the grating, so $Q_{oop} = C$ with C a certain constant associated with the out-of-plane scattering. Using these results, the dependence of the Q-factor on the number of periods in the grating reads:

$$Q = \frac{1}{1/Q_{facets} + 1/Q_{oop}} \sim \frac{1}{\exp(-2k_P \Lambda N_g) + 1/C} \tag{2.51}$$

This is exactly the behaviour shown in figure 2.25. For small values of N_g, the exponential term is larger than the constant out-of-plane factor and the Q-factor grows exponentially with N_g. The cavity loses most of its light at its facets. With increasing N_g, the exponential factor decreases and at $\sim N_g = 60$ it equals $1/C$. For even longer gratings, the influence of the exponential term in 2.51 diminishes. The cavity dissipates its energy now predominantly due to scattering at the defect.

2.3.2.1 A note on 2D/3D

Like almost all the other quantities discussed until now in this chapter, the Q-factors in figure 2.25 were calculated in 2D. The dimensionality was reduced by applying the effective index method on the x direction, ending up with a structure in the 2 dimensional zy plane. This approach is justified because the waveguides considered here are relatively wide ($1.6\mu m$) hence most of the optical mode in the x-direction is confined to the waveguide. However, a small amount of the lateral mode profile in the x-direction is outside the waveguide. The effective index method only accounts for this partially and some effects are not taken into account. Most importantly: the 2D approach will over-estimate the strength of the grating and under-estimate the scattering of the grating. In other words, the Q-factors obtained here are higher than when calculated using a more rigorous 3D approach. Nevertheless, the aim of this chapter is to gain insight in the physics of such waveguide gratings and cavities. Even though the exact values of the numbers are a bit off, the physical phenomena are still the same and using a more time-efficient 2D simulation technique allows to explore more parameters. In the chapters about designing the optically and electrically pumped lasers 3D techniques are used because in these cases the actual value of the numbers does matter.

2.3.3 Hybrid band-edge defect cavities

Until now, two types of grating cavities were discussed. Section 2.3.1 dealt with band-edge grating cavities. The grating / waveguide interfaces on both ends of the cavity partially reflect light which yields Fabry-Perot-like resonances. The spectral proximity to the band-gap of the modes trapped inside the resonator significantly slows down the propagation of photons in the cavity, which results in high-Q factors that scale with the length of the grating. Unfortunately, as the length of the cavity increases, the free spectral range decreases and subsequent resonances become very closely spaced. A possible solution would be to increase the reflectivity of the facets. This way, the cavity length can be reduced, increasing the free spectral range but still obtaining the same Q-factor.

On the other hand, section 2.3.2 discussed so-called defect cavities. By inserting a quarter-wave shift defect in the center of the grating, a resonant state within the band gap is created. Light is now confined to a tiny region of the waveguide trapped between two highly reflective waveguide gratings. Figure 2.25 showed that the Q-factor of such a cavity initially grows exponentially as a function of the cavity length due to the exponentially decreasing transmissivity of the grating mirrors. However, as the length of the grating increases, the Q-factor saturates due to out-of-plane scattering, mainly at the cavity defect. A possible strategy to increase the saturation level of the Q-factor would be to make sure the quarter-wave shift is

not an abrupt interruption of the periodic structure, but more of an adiabatic transition.

In fact, a shorter band-edge cavity with highly reflective mirrors and a defect cavity with a more adiabatic quarter wave shift are the same thing. Imagine the aim is to design a cavity with a resonance at wavelength λ_1. Using a short (5-10 periods) grating with a period Λ_{BE} such that λ_1 lies in the band-edge region will yield a low-Q Fabry-Perot cavity with a wide free-spectral-range. By attaching a second grating with period Λ_R such that λ_1 lies in the center of the band gap of this grating at both ends of the first grating, the reflectivity of the Fabry-Perot cavity's facets is significantly increased while preserving the wide free spectral range. Recently this technique has also been used in 1D photonic crystals to increase the Q-factor [9]. This set-up is schematically drawn in figure 2.26.

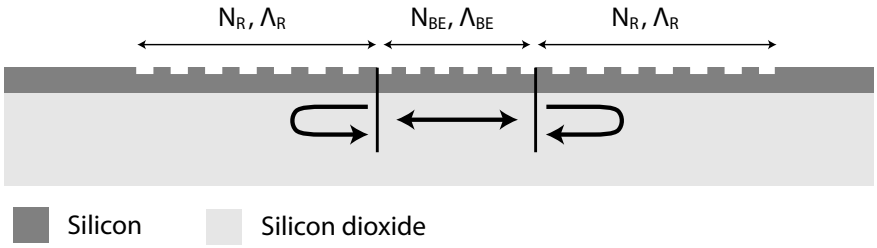

Figure 2.26: Schematic representation of the hybrid band-edge/defect cavity consisting of a center band-edge section with period Λ_{BE} and two outer mirror sections with period Λ_R

To figure out which periods should be used for each section of the resonator (ie Λ_R and Λ_{BE}), consider figure 2.27. This graph shows the band diagram of the fundamental TE-polarized mode in the $220\,nm$ high, $1.6\,\mu m$ wide silicon grating with $70\,nm$ deep corrugations. The figure depicts the diagrams for $290\,nm$ (dashed line), $280\,nm$, $270\,nm$ and $260\,nm$ (grayscale solid lines). A horizontal dotted line indicates the $1550\,nm$ wavelength mark. Suppose the aim is to design a cavity that resonates at approximately this wavelength. As shown before in the previous sections and as can be seen on figure 2.27, $1550\,nm$ lies more or less in the center of the $290\,nm$ grating's band gap. In other words, $290\,nm$ would be a good period for the outer mirror sections, so $\Lambda_R = 290\,nm$. The number of periods in the outer gratings N_R will determine the reflectivity of the facets.

The dotted line that marks $1550\,nm$ intersects with both the $280\,nm$ and $270\,nm$ bands. Consequently it should be possible to find a configuration where either one of these periods can be used as the center band-edge period Λ_{BE}. The question

is, what is the shortest number of periods required in each case to enable the resonance.

As stated before, the cavity is resonant if the total phase change $\Delta\phi$ accumulated during one roundtrip adds up to an integer multiple of 2π. When propagating through the cavity, photons encounter 2 mirror sections and propagate through the center band-edge section. The phase of the light reflected by the mirror section $\Delta\phi_R$ is depicted in figure 2.19. At the center of the band (so near the wavelength of interest) the reflected phase is approximately π.

The phase change accumulated in the band-edge region equals $2k_{BE}L_{BE}$. The length of the band-edge section equals: $L_{BE} = (N_{BE} + 1/2)\Lambda_{BE}$ because the grating mirrors should start at the same reference point (for example the non-etched part of the grating). Taking this into account, the resonance condition reads:

$$2\Delta\phi_R + 2k_{BE}(N_{BE} + 1/2)\Lambda_{BE} = M2\pi \tag{2.52}$$

With M an integer number. At the longer wavelength edge of the band, the k-vector is shorter than that of the grating, so the effective wavelength in the grating is slightly longer than the grating period. Because the cavity is $N_{BE}+1/2$ periods long, the smallest number of waves that fit into the cavity is N_{BE}. So for the first band-edge resonance: $M = N_{BE}$. Assuming the resonance is near the center of the band-gap of the mirror grating section, $\Delta\phi_R = \pi$ so this term vanishes.

Consequently solving equation 2.52 for the number of periods N_{BE} yields:

$$N_{BE} = \frac{k_{BE}/K}{1 - 2k_{BE}/K} \tag{2.53}$$

with $K = 2\pi/\Lambda_{BE}$.

The x-scale of figure 2.27 is in units k_{BE}/K so the value for N_{BE} can easily be read from inspecting the graph. For the $280\,nm$ grating, k_{BE}/K equals 0.487 at $\lambda = 1.55\,\mu m$. This results in $N_{BE} = 18.7 \approx 19$ periods. The $270\,nm$ grating's band intersects at $k_{BE} = 0.465K$, yielding $N_{BE} = 6.64 \approx 7$ periods. Although this derivation made a few crude assumptions, this is an easy way to get a sense of the order of magnitude of the size of the center grating. In both cases, the number of periods required to rotate the phase by an amount of π in the center grating is rather modest. In other words, it should be possible to make small cavities using this method.

As could be expected, the shorter band-edge grating period will yield a shorter center section. On the other hand, the longer grating period needs more periods to rotate the phase over a value of π but potentially results in a higher Q-factor

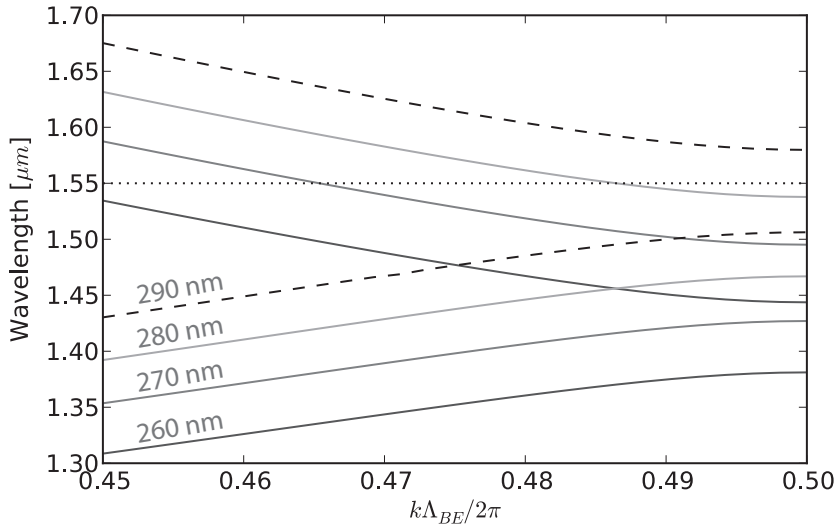

Figure 2.27: Band diagram of the first order TE mode for a $290\,nm$ *grating period (black dashed line) and* $280\,nm$*,* $270\,nm$ *and* $260\,nm$ *(grayscale).*

because the transition between the center section ($280\,nm$) and the outer sections ($290\,nm$) is softer, reducing scattering losses associated with this interface. However, as can be seen in figure 2.27, the band-gap of the $280\,nm$ grating partially overlaps with the bandgap of the $290\,nm$ grating. Because the mode in the center section of the cavity should be guided with $k < K/2$ to be able to rotate the phase with respect to the grating, this limits the range of wavelengths where the grating can be resonant. For this reason, this analysis will continue with $\Lambda_{BE} = 270\,nm$.

Figure 2.28 shows the R/T spectrum of a hybrid band-edge defect grating cavity with 10 periods of $270\,nm$ in the center of the grating and 30 periods of $290\,nm$ on both sides. This yields a total of 70 periods and will be referred to as a 30-10-30 configuration for obvious reasons. The left graph in figure 2.28 looks very similar to the R/T spectrum of a point defect grating cavity as shown in figure 2.20: there is a single reflection dip in the center of the $290\,nm$ grating's band gap and band-edge like R/T variations outside the gap. The shape of the R/T curve outside the gap is now much more complicated than before because it now consists of 3 different gratings. It is no longer straight forward to estimate the Q-factor or free spectral range of these resonances outside the $290\,nm$ band gap.

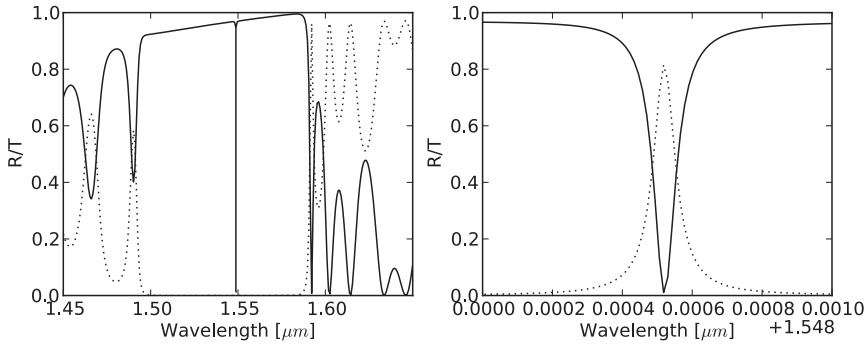

Figure 2.28: R/T spectrum of a hybrid band-edge defect grating cavity with 10 center $270\,nm$ *periods and 30* 290 *nm mirror periods on both sides (30-10-30 configuration). Wide spectral overview on the left and zoom of* $1550\,nm$ *resonance on right. The resolution of the left graph is insufficient to show the narrow reflection dip at the cavity resonance wavelength (1548 nm).*

However, the region of interest is inside the $290\,nm$ band gap. The right side of figure 2.28 shows a detailed view of the R/T spectrum near the designed resonance wavelength ($\lambda_r = 1548.5\,nm$). The width of the peak is the same order of magnitude as the point-defect grating's resonance in figure 2.20 with similar cavity length which suggests a similar Q-factor. However, the reflected and transmitted power now add up to a higher value at resonance, hinting at lower out-of-plane scattering.

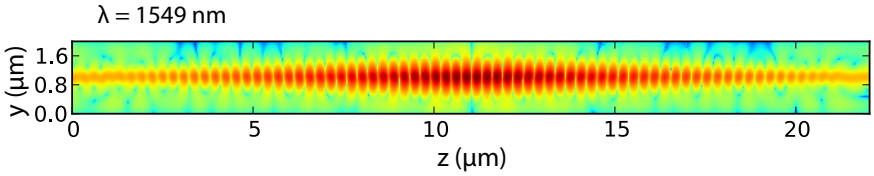

Figure 2.29: Time-averaged electric-field-squared distribution of hybrid band-edge defect grating cavity with 10 center $270\,nm$ *periods and 30* 290 *nm mirror periods on both sides (30-10-30 configuration) at resonance wavelength* $\lambda_R = 1548.5\,nm$*. The color scheme is in a logarithmic scale.*

Figure 2.29 shows the spatial distribution of the time-averaged squared electric field at the resonance wavelength $\lambda_R = 1548.5\,nm$ in a logarithmically scaled color scheme. This figure looks very similar to the squared electric field distribution of a point defect grating in figure 2.22. The difference between the two

configurations becomes more clear when inspecting the values of a 1D cut through figure 2.29 at $y = 1.0\mu m$ as shown in figure 2.30. As expected, the envelope of the squared electric field shows a sinusoidal shape in the center part of the grating where the mode is band-edge like. In the two mirror sections, where the wavelength of the resonant mode lies within the grating's band gap, the field amplitude decays exponentially when propagating towards the facets of the cavity. This is clearly different from the case of a point-defect grating cavity in figure 2.22 where the 1D squared electric field cut was composed of 2 exponentially decaying envelopes. By replacing the point defect with a band-edge grating section, the transition between the two exponentially decaying envelopes is much more adiabatic, resulting in more gentle confinement of the resonant mode which should result in a higher Q-factor.

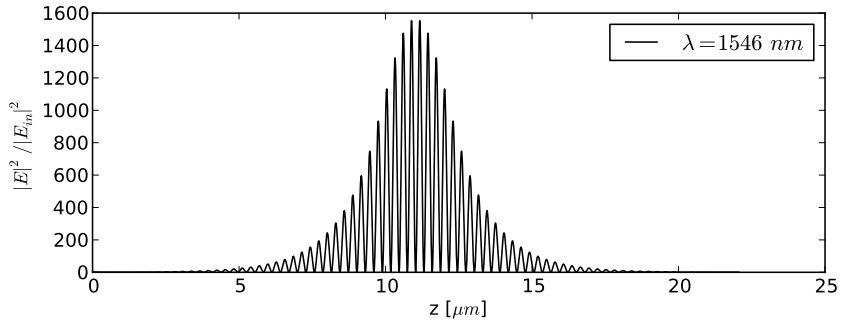

Figure 2.30: 1D cut through figure 2.29 at $y = 1.0$ showing the sinusoidal envelope in the central region and the exponential decay in the mirror region.

To assess how switching from a point defect to a more distributed phase-shifting section influences the ability of the cavity to store electro-magnetic energy, figure 2.31 shows the Q-factors of both cavities as a function of grating length. The data for the point defect grating is identical to the data shown in figure 2.25. Q-factors are calculated using FDTD and harmonic inversion. The x-axis depicts the total length of the grating. In the case of a point-defect grating, a grating length of N_g periods on the x-axis means that the grating consists of $N_g/2$ periods, the quarter wave defect and another $N_g/2$ periods. The hybrid band edge-defect cavities all have a 10 period long center section, so N_g periods means: $(N_g - 10)/2$ mirror periods, 10 center periods and another $(N_g - 10)/2$ mirror periods. This is an $(N_g - 10)/2 - 10 - (N_g - 10)/2$ configuration.

For smaller cavities, when $N_g < 60$, both approaches yield similar Q-factors.

In fact, the point-defect cavity results in slightly higher Q-factors. This is because a point-defect cavity of length N_g periods consists of $N_g/2$ Bragg grating mirror periods on each side of the defect to contain the optical mode. The hybrid band-edge grating cavity of length N_g periods depicted in figure 2.31 consists of only $(N_g - 10)/2$ Bragg grating mirror periods on each side of the 10 period defect. In other words, for equal cavity length, the Bragg mirror reflectivity of the facets is less in the case of a hybrid band-edge defect cavity as compared to a point defect cavity. However, the pitch of the grating in the center region of the hybrid band-edge defect cavity is such that the resonant mode's wavelength is near the edge of the band-gap of that grating. As shown earlier, this proximity to the band-edge reduces the group velocity significantly, so photons are slowed down when propagating in this section of the cavity. In other words, light spends a longer time in the cavity, increasing the Q-factor and bringing it on par with the Q-factor of a point defect grating cavity of equal length.

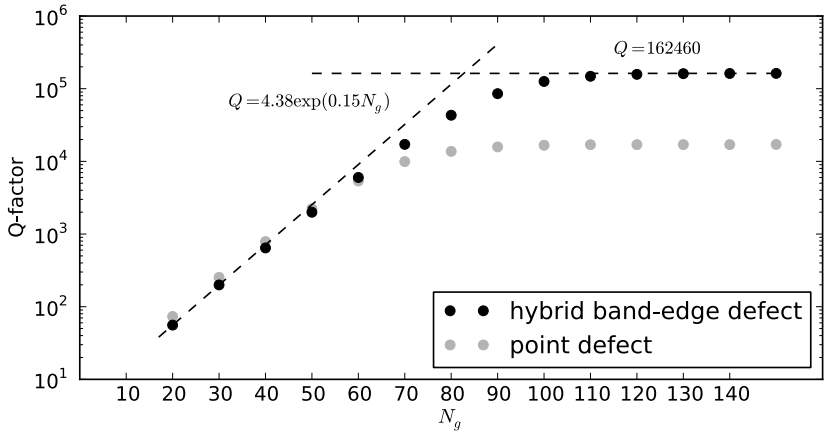

Figure 2.31: Q factors for point defect grating cavity (data from figure 2.25) and hybrid band-edge grating with 10 center periods as a function of the total number of periods in the grating cavity.

When the total number of periods in the grating exceeds $N_g = 60$, the Q-factor of the hybrid band-edge defect grating surpasses that of the point-defect grating. Due to the more adiabatic implementation of the π phase shift, scattering at the defect is reduced and the cavity is now able to store a certain amount of energy for a longer time. Eventually, the Q-factor of the hybrid band-edge defect grating cavity saturates at a level of $Q \sim 160000$, which is almost an order of magnitude higher than in the case of a point defect grating cavity.

In the previous paragraph the number of periods in the center part of the grating was fixed to 10. One can imagine that this number has an influence on both the Q-factor and the resonance wavelength of the grating cavity. Figure 2.32 shows the Q-factor and associated resonance wavelength λ_R for a hybrid band-edge defect grating cavity with 30 mirror periods on both sides ($290\,nm$ period) and N_c center periods ($270\,nm$ periods). This is a 30-N_c-30 configuration.

The resonance wavelength decreases with increasing N_c because for longer band-edge gratings the first order resonance shifts closer to the band gap, as shown in the section about band-edge grating resonators. Figure 2.27 shows that the $270\,nm$ grating is operated at its longer wavelength band-edge, so increasing the length of the grating shifts the resonance wavelength to shorter wavelengths. This figure also shows that the dispersion curve of the center grating ($\Lambda = 270\,nm$) around the $1550\,nm$ mark is still more or less linear. Combined with the approximately linear phase characteristic of the mirror grating near the center of its bandgap as shown in figure 2.19, this results in a close to linear resonance wavelength decrease.

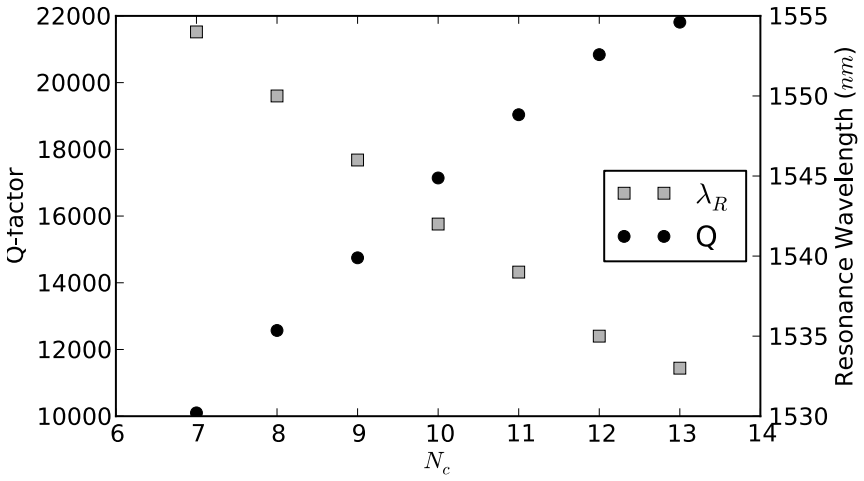

Figure 2.32: Q factors and resonance wavelength for a 30 - N_c - 30 hybrid band-edge defect grating cavity configuration as a function of the number of center periods N_c.

The Q-factor in its turn increases with increasing number of center grating periods N_c. In such a resonator, the Q-factor is linearly dependant on the cavity length,

explaining the linear trend. However, more subtle effects play a role. As the center grating length increases, the resonance wavelength shifts to shorter values. This means that the center grating is operated closer to its band-edge, decreasing the group velocity and consequently increasing the Q-factor even more. On the other hand, shifting to shorter wavelengths also means moving away from the center of the mirror grating's band gap where the reflectivity decreases and consequently the cavity's Q-factor decreases. Both effects lift each other up for small values of N_c but as N_c increases, the decremental effect of the decreasing mirror reflectivity prevails.

For long enough center grating sections the cavity supports 2 resonant modes. As the first order mode shift towards shorter wavelengths, the second order mode appears at the long wavelength side of the mirror grating's band gap.

Until now the length of the etched and non-etched part within one grating period Λ were always assumed to be identical: the etched and non-etched part were both $\Lambda/2$ long. Unfortunately, modern fabrication techniques cannot alway guarantee such a perfect balance between both. This mismatch is described by the grating's duty cycle dc. This is a number between 0 and 1 that quantifies the ratio between the length of the etched part and the length of the period Λ. In other words, the length of the etched part of the grating is $dc\Lambda$ and the length of the non-etched part is $(1 - dc)\Lambda$.

Figure 2.33 shows how the Q-factor and the resonance wavelength λ_R depend on the duty cycle in a 30 - 10 - 30 configuration hybrid band-edge defect grating with $290\,nm$ mirror period and $270\,nm$ center period. When the duty cycle increases, the physical amount of silicon in the grating decreases. Consequently, the effective index of the mode in the waveguide decreases hence the band diagrams of both the center and mirror grating shifts to shorter wavelengths. As a result, the resonance also shifts to shorter wavelengths. A deviation from the 50% duty cycle also results in a reduction of the Q-factor because the reflectivity of the mirror grating is reduced.

2.4 Conclusions

In this chapter the basic properties of silicon waveguide grating cavities were investigated. After first introducing the rigorous treatment of periodic structures using Floquet-Bloch theory, 3 types of waveguide grating cavities were considered: band-edge grating cavities, point-defect grating cavities and hybrid band-edge defect cavities. For each type of cavity the dependence of the the quality factor, a figure of merit quantifying the the ability of the cavity to store energy, and the res-

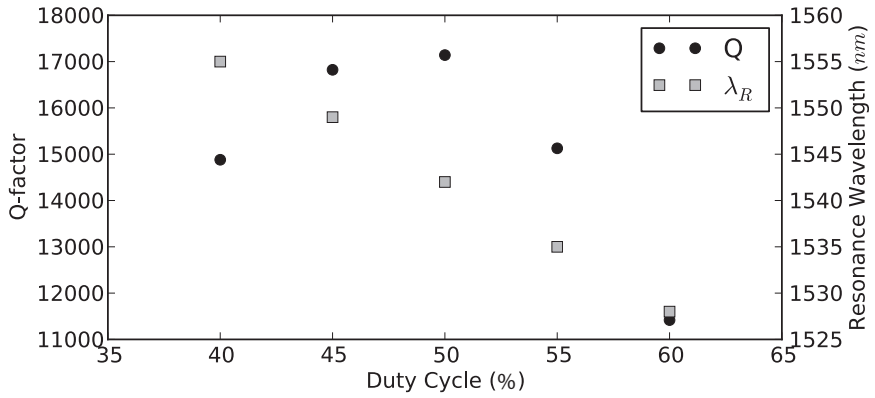

Figure 2.33: Q factors and resonance wavelength for a 30 - 10 - 30 hybrid band-edge defect grating cavity configuration as a function of the duty cycle. The duty cycle is assumed to be uniform along the entire grating.

onance wavelength on different cavity parameters was investigated. This chapter lays the groundwork for the discussion of hybrid silicon lasers based on resonant mirrors in the next chapter.

References

[1] *CAMFR - http://camfr.sourceforge.net*.

[2] Ivano Giuntoni, Andrzej Gajda, Michael Krause, Ralf Steingrüber, Jürgen Bruns, and Klaus Petermann. *Tunable Bragg reflectors on silicon-on-insulator rib waveguides*. Opt. Express, 17(21):18518–18524, October 2009.

[3] Thomas Chae, Efstratios Skafidas, and Duk-Yong Choi. *Compact Bragg Grating Reflectors in Silicon Waveguides and Their Application to Resonator Filters*. In Optical Fiber Communication Conference, page Th2A.20. Optical Society of America, 2014.

[4] I. Giuntoni, M. Krause, H. Renner, J. Bruns, A. Gajda, E. Brinkmeyer, and K. Petermann. *Numerical survey on Bragg reflectors in silicon-on-insulator waveguides*. In 2008 5th IEEE International Conference on Group IV Photonics, pages 285–287. IEEE, 2008.

[5] *MIT photonic bands - http://ab-initio.mit.edu/wiki/index.php/MIT_Photonic_Bands*.

[6] Dries Van Thourhout, Roel Baets, and Heidi Ottevaere. *Microphotonics Syllabus, UGent 2014*.

[7] Fengnian Xia, Mike Rooks, Lidija Sekaric, and Yurii Vlasov. *Ultra-compact high order ring resonator filters using submicron silicon photonic wires for on-chip optical interconnects*. Optics Express, 15(19):11934, 2007.

[8] *MIT Harmonic inversion - http://ab-initio.mit.edu/wiki/index.php/Harminv*.

[9] Parag B. Deotare, Murray W. McCutcheon, Ian W. Frank, Mughees Khan, and Marko Lončar. *High quality factor photonic crystal nanobeam cavities*. Applied Physics Letters, 94, 2009.

3

Resonant mirror lasers: theory

3.1 Introduction

The previous chapter dealt with the properties of passive silicon grating cavities. In this chapter such passive silicon cavities will be combined with a active waveguide composed of layers of different III-V compounds to form a new kind of hybrid silicon laser: the resonant mirror laser. The lion's share of this chapter will deal with the properties of grating based resonant mirrors and their use in hybrid silicon laser systems. But before diving into the details of such resonant mirrors, this chapter starts off with the basic laser layout.

3.1.1 General laser layout

As discussed in chapter 1, a hybrid silicon laser is an electro-optic device that generates coherent light and consists of 2 functional material layers: a passive silicon layer on the bottom and an active layer on top consisting of a stacked combination of III-V compounds. Establishing laser operation requires 2 ingredients: amplification and an optical resonator. The amplification is provided by the active layer in the III-V stack, in this case a mulit-quantum well (MQW) structure. The optical resonator is formed by patterning structures in either the III-V layer, the silicon layer or in both layers. This work deals with linear shaped hybrid silicon lasers. Such lasers consist of a rectilinear waveguide and semi-reflective mirrors at both ends of that waveguide to provide optical feedback, required to form a resonator. Alternatively to linearly shaped lasers, a circularly shaped structure can be used to

form a resonator to avoid the need for mirror structures [1].

Chapter 1 also mentioned that there are many different implementations of linear shaped hybrid silicon lasers. Figure 3.1 shows a 2D representation of the general layout of the hybrid silicon laser structure proposed in this work. A III-V waveguide sits on top of 2 silicon structures. The III-V waveguide is an unperturbed straight waveguide without any features patterned into it to provide reflection. As shown on the figure, the laser consists of 4 different regions, marked 1 to 4:

- **Region 1**: the back mirror. In this region a silicon structure underneath the III-V layer provides (high) reflectivity. The practical implementation of this silicon structure will be discussed later. The optical mode can reside in both the III-V and silicon layer.
- **Region 2**: the gain region. In this region there are no silicon structures underneath the III-V waveguide. Consequently all light is confined to the III-V waveguide. The main purpose of this region is to amplify the light.
- **Region 3**: the front mirror. This region is similar to region 1 in the sense that it provides (partial) feedback into the III-V waveguide by means of structures defined in the silicon layer. Again, light can be in both the silicon and III-V layer. The difference with region 1 is that in this case the structures in the silicon layer should also couple some light into an external silicon waveguide, which will serve as the laser output.
- **Region 4**: the output waveguide. There is no active III-V waveguide in this region so all light is now confined to the silicon waveguide. This waveguide guides the laser output to a photonic integrated circuit on the chip.

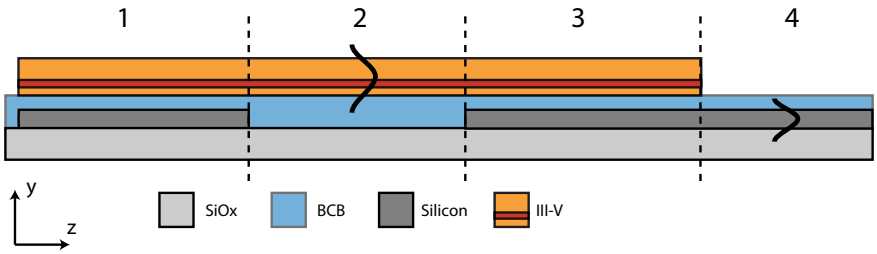

Figure 3.1: Schematic representation of the general layout of the laser structure presented in this work.

The aim of this work is to reduce the power required to reach laser threshold and assure that the laser output light is single-mode. The strategy to do this is to

design the mirror sections (regions 1 and 3 in figure 3.1) such that they provide high reflectivity over a short longitudinal distance (z-axis in figure 3.1). If the mirrors provide high reflectivity, the length of the gain section (region 2 in figure 3.1) can be reduced. If the length of the mirror section itself can be short, the total length of the III-V waveguide (regions 1, 2 and 3) is reduced, minimising the active volume that has to be pumped and consequently lowering the threshold power. If the mirror structure can provide feedback in a wavelength-selective manner, it should be possible to reflect only one longitudinal mode of the laser resonator, which guarantees single-mode operation. Finally, the mirror structure should also provide a path to lead the generated laser light into a passive silicon waveguide.

The challenge in this set-up is to find a silicon structure that can meet all the requirements stated in the previous paragraph: high, wavelength selective reflectivity over a short distance with a mechanism to output light into an external silicon waveguide.

3.2 Resonant mirrors

A possible solution can be found in using passive resonant cavities as the silicon structures in regions 1 and 3. Such a configuration, an active III-V waveguide with a passive silicon structure is called a resonant mirror. In the first part of this chapter a theoretical framework will be established that can be used as a guideline to design resonant mirrors. The second half of this chapter will study practical implementations of resonant mirrors with the type of cavities studied in the previous chapter. Using mode-expansion simulations the influence of different parameters on the reflection and transmission spectrum of the mirrors will be studied. But before diving into rather elaborate theoretical derivations it might be instructive to approach the resonant mirrors from a more phenomenological angle.

3.2.1 Phenomenological description of resonant mirrors

To start the study of resonant mirrors, consider figure 3.2. This schematic drawing represents the basic structure of a resonant mirror: a passive silicon cavity underneath an active III-V waveguide. The laser itself consists of 1 active III-V waveguide with 2 passive silicon cavities. The silicon cavities will act as partial reflectors and the laser cavity arises in the region of the III-V waveguide in between the 2 silicon cavities. But how can a silicon cavity, positioned underneath a III-V waveguide, act as a reflector for light propagating in that III-V waveguide?

First of all, assume that the silicon cavity is a linear waveguide with a backward an forward propagating mode. This can be a Fabry-Perot cavity or any of the

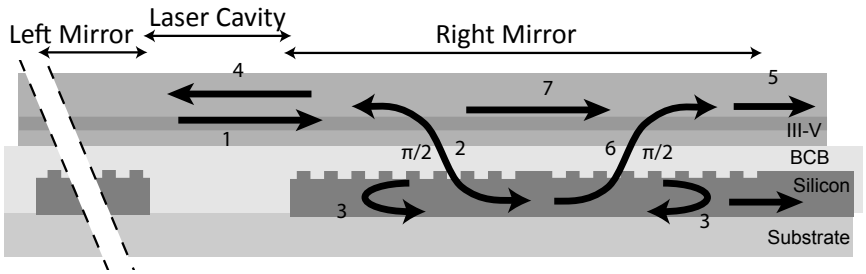

Figure 3.2: Schematic representation of a resonant mirror: a passive silicon cavity coupled to an active III-V waveguide.

3 kinds of grating-type cavities that were discussed in the previous chapter. For the sake of simplicity, assume that effective index of these forward and backward propagating modes is the same as the effective index of the III-V waveguide above. This is an important assumption and its consequences will be discussed in great detail in the remainder of this chapter. The spacing between the silicon cavities and the III-V waveguide is such that the modes in either layer can be treated separately and no *hybrid modes* arise. In other words, the silicon cavity is evanescently coupled to the III-V waveguide.

When the III-V waveguide is pumped, either optically or electrically, light is generated in the III-V waveguide and starts propagating through the III-V waveguide (1 in figure 3.2). At a certain point the mode propagating in the III-V waveguide will reach one of the two regions where a silicon cavity lies underneath. Due to their physical proximity, a fraction of the light will couple into the silicon cavity.

Now assume that the cavity's intrinsic Q-factor is very high. The intrinsic Q-factor is the Q-factor of the cavity in the absence of the III-V waveguide and *very high* means that, if the III-V waveguide is present, the cavity's most prominent leak mechanism is leakage to the fundamental mode of the III-V waveguide. This high intrinsic Q assumption will also be discussed in great detail further on in this chapter.

If the wavelength of the incident light is close to the silicon cavity's resonance wavelength, the cavity's resonant mode will be excited. Since the cavity waveguide coupled to the III-V waveguide can be treated as a directional coupler, the phase difference between the III-V waveguide mode and the silicon cavity mode is $\pi/2$. Because the silicon cavity mode consists of 2 counter-propagating modes light will couple back both co-and counter-directionally to the incoming III-V waveguide mode (6 and 2 respectively). Light coupling from the silicon cavity

back into the III-V waveguide mode will experience another $\pi/2$ phase shift. In other words, the light coupling back co-directionally from the silicon cavity to the incoming III-V waveguide mode (6) is rotated $\pi/2 + \pi/2 = \pi$ with respect to the fraction of the III-V waveguide mode that didn't couple into the silicon cavity (7) and both will interfere destructively, reducing the power transmitted through the waveguide. Of course, because the cavity mode consists of 2 counter-propagating modes, light will also couple back into the counter-directionally propagating III-V waveguide mode. This light is reflected back into the waveguide.

But how much of the light is reflected? If the coupling fraction is κ and the relative field strength (compared to the normalized input) is A, the field fraction coupling into the counter-propagating mode is κA and the transmitted field is $1 - \kappa A$. Since the cavity is assumed to be lossless, the sum of the transmitted and reflected power should add up to 1:

$$\kappa^2 A^2 + (1 - \kappa A)^2 = 1 \tag{3.1}$$

rearranging the terms yields:

$$\kappa^2 A^2 - 1 + (1 - \kappa A)^2 = (\kappa A - 1)(\kappa A + 1) + (1 - \kappa A)^2 = (\kappa A - 1)\kappa A = 0 \tag{3.2}$$

So two situations can occur:

- κA = 0: the waveguide and cavity are uncoupled so no light is reflected and all light is transmitted through the waveguide
- κA = 1: *all* the light is reflected back into the III-V waveguide and no light is transmitted

In other words, if there is non-zero coupling between the III-V waveguide and the silicon cavity, all light is reflected back into the III-V waveguide. This is of course for the ideal case of a perfectly phase-matched system with a lossless cavity. In the realistic case of of a cavity with finite loss, some energy will radiate away from the cavity and the reflection will be less than 100%.

Because the cavity mode is only excited near its resonance frequency, the mirror only works in a narrow bandwidth. This is interesting because this way the mirror itself can act as a spectral filter and suppress longitudinal side-modes. Another advantage is that, because energy is stored in the silicon cavity, light is already present in the silicon layer. The laser output can be coupled into an external silicon waveguide by tapping a fraction of the energy present in the cavity into that silicon waveguide. This can happen in 2 ways:

- The waveguide can be butt-coupled to the silicon waveguide on either one of the sides of the cavity. Light that would normally leak from the cavity facets can be collected in the silicon waveguide and used as the laser output.

- A waveguide can also be evanescently side-coupled to the silicon cavity. The disadvantage of this approach is that it introduces a new loss mechanism to the cavity which is not desirable. Usually it is possible to recuperate light from an existing cavity loss mechanism, such as leakage from one of its facets.

The remainder of this chapter will deal with how the mirror works in more realistic cases. First a theoretical framework is established that will serve as a guideline for the second part where the practical implementations of the resonant mirror using the grating cavities studied in the previous chapter will be discussed.

3.2.2 Scattering theory for coupled resonators

In literature, the problem of side-coupling a cavity to a waveguide is widely studied, mainly in the context of coupling a photonic crystal line defect waveguide to a point defect cavity. Such a system can be tackled by using coupled mode theory [2]. In this approach the waveguide and resonator are first treated separately. During a second iteration, the resonator is introduced as a first order perturbation to the waveguide and vice versa. This theory assumes that the solutions to the perturbed system is a combinations of the solutions (modes) of the unperturbed sub-systems. By assuming only small perturbations, the involved equations can be linearised and the influence of the perturbations on the amplitude of the modes in the system can be calculated.

This work will utilize a similar approach based on the Lippman-Schwinger equation [3]. This approach is used in quantum mechanics to calculate the scattering of colliding particles. However, this approach can also be used to study optical wave systems as shown in [4]. The incoming wave in the access waveguide will scatter into a forward transmitted and backward propagating mode after *colliding* with the cavity. The next paragraph will briefly outline the method described in [4].

3.2.2.1 part 1: setting up the framework

To start off, the Maxwell rotor equations are cast into a form to resemble the general time-dependent Schrodinger equation:

$$j\frac{\partial \psi}{\partial t} = \mathbf{H}\psi \tag{3.3}$$

$$\psi = \begin{bmatrix} \vec{E} \\ \vec{H} \end{bmatrix} \qquad \mathbf{H} = \begin{bmatrix} 0 & (j/\epsilon)\vec{\nabla}\times \\ (-j/\mu_0)\vec{\nabla}\times & 0 \end{bmatrix} \tag{3.4}$$

In this notation ψ is the *wave-function* that represents the space and time dependent electro-magnetic field and $\mathbf{H}$ is an operator that can act on entities similar to ψ.

At this stage, this is just a strange way of writing down Maxwell's rotor equations. The equation can be simplified by writing $\psi(t)$ in terms of its Fourier transform $\Psi(\omega) = FT(\psi(t))$:

$$\psi(t) = \int \Psi(\omega) \exp(-j\omega t) d\omega \tag{3.5}$$

When substituting this into equation 3.3 and deriving $\exp(-j\omega t)$ with respect to t, this yields:

$$\int \omega\Psi(\omega) \exp(-j\omega t) d\omega - \mathbf{H} \int \Psi(\omega) \exp(-j\omega t) d\omega = 0 \tag{3.6}$$

Because $\mathbf{H}$ is linear, it can be brought into the integral and because the integral operator is also linear, the sum of two integrals is the integral of the sum of the arguments. This leads to:

$$\int (\omega\Psi(\omega) - \mathbf{H}\Psi(\omega)) \exp(-j\omega t) d\omega = 0 \tag{3.7}$$

This integral is the inverse Fourier transform of $\omega\Psi(\omega) - \mathbf{H}\Psi(\omega)$, so Fourier transforming this equation now yields:

$$\omega\Psi = \mathbf{H}\Psi \tag{3.8}$$

Next, an inner product between two wave functions is introduced (using bra-ket notation):

$$\langle \psi_2 \,|\, \psi_1 \rangle = \frac{1}{2} \int d^3 r \epsilon(r) \vec{E}_1^* \cdot \vec{E}_2 + \frac{1}{2} \int d^3 r \vec{H}_2^* \cdot \vec{H}_1 \tag{3.9}$$

Where r denotes the spatial position. With this inner product, the operator $\mathbf{H}$ is Hermitian. This implies that the inner product of a wave function Ψ_1 with $\mathbf{H}\Psi_2$ is the complex conjugate of the inner product of $\mathbf{H}\Psi_1$ with Ψ_2, or $\langle \Psi_1 \,|\, \mathbf{H}\Psi_2 \rangle = \langle \mathbf{H}\Psi_1 \,|\, \Psi_2 \rangle^*$. Note that $\langle \Psi_1 \,|\, \Psi_1 \rangle$ is the total energy of that mode. A mode is said to be normalized if it is scaled such that its energy equals 1. If two modes Ψ_1 and Ψ_2 are normalized, the inner product $\langle \Psi_1 \,|\, \Psi_2 \rangle$ yields the percentage of energy shared between the two modes. If this number is zero, the modes are orthogonal to each other and will not couple. On the other hand, if the inner product between two normalized modes is non-zero, they share a certain percentage of their energy and exciting one of both modes will inevitably excite the other mode.

The physical geometry of the studied structure is contained by the operator $\mathbf{H}$ in the form of ϵ. There are 3 different forms of ϵ that are important:

- $\epsilon_w(r)$: the spatial permittivity distribution of the access waveguide without the cavity

- $\epsilon_c(r)$: the spatial permittivity distribution of the cavity without the access waveguide
- $\epsilon_t(r)$: the spatial permittivity distribution of the cavity and the waveguide

3.2.2.2 part 2: Lippman-Schwinger equation

Scattering theory now postulates that in a weakly-coupled regime, the operator $\mathbf{H}$ associated with the coupled structure (ϵ_{tot}) can be decomposed into two parts:

$$\mathbf{H} = \mathbf{H_0} + \mathbf{V} \tag{3.10}$$

with $\mathbf{H_0}$ the operator associated with the unperturbed (uncoupled) structures and $\mathbf{V}$ the perturbation operator. The solutions to $\mathbf{H_0}$ are ψ_0 and the solutions to $\mathbf{H}$ are Ψ_{tot}. An important assumption of the Lippman-Schwinger equation is that both Ψ_{tot} and Ψ_0 share the same eigenvalue: ω.

The solutions to the full structure,Ψ_{tot} obey Maxwell's equation:

$$\mathbf{H}\left|\psi_{tot}\right\rangle = \omega\left|\psi_{tot}\right\rangle \tag{3.11}$$

Substituting $\mathbf{H}$:

$$\mathbf{H_0}\left|\psi_{tot}\right\rangle + \mathbf{V}\left|\psi_{tot}\right\rangle = \omega\left|\psi_{tot}\right\rangle \tag{3.12}$$

Now define the scattered wave function $\psi_s = \psi_{tot} - \psi_0$, and substitute ψ_{tot} in the previous equation (except for the instance on which $\mathbf{V}$ operates):

$$\mathbf{H_0}\left|\psi_s\right\rangle + \mathbf{V}\left|\psi_{tot}\right\rangle = \omega\left|\psi_s\right\rangle \tag{3.13}$$

In the previous the identity $\mathbf{H_0}\left|\psi_0\right\rangle = \omega\left|\psi_0\right\rangle$ cancels. Rearranging the terms yields:

$$\left|\psi_s\right\rangle = \frac{\mathbf{V}}{\omega - \mathbf{H_0}}\left|\psi_{tot}\right\rangle \tag{3.14}$$

Adding $\left|\psi_0\right\rangle$ on both sides finally yields:

$$\left|\psi_{tot}\right\rangle = \left|\psi_0\right\rangle + \frac{\mathbf{V}}{\omega - \mathbf{H_0}}\left|\psi_{tot}\right\rangle \tag{3.15}$$

This equation is the Lippman-Schwinger equation applied to an optical system. It states that the result in field $\left|\psi_{tot}\right\rangle$ consists of the unperturbed field $\left|\psi_0\right\rangle$ and a contribution which is related to the perturbation of the field. Solving this equation is not straight forward because the unknown end state $\left|\psi_{tot}\right\rangle$ appears on both sides. An approximate way to find a solution that also provides insight into the physics of this equation is to consider it as an iterative procedure:

$$\left|\psi_{new}\right\rangle = \left|\psi_0\right\rangle + \frac{\mathbf{V}}{\omega - \mathbf{H_0}}\left|\psi_{old}\right\rangle \tag{3.16}$$

In the zeroth order approximation, the incident field $|\psi_0\rangle$ is used as $|\psi_{old}\rangle$ to yield $|\psi_{new,0}\rangle$. Next, $|\psi_{new,0}\rangle$ can be used as $|\psi_{old}\rangle$ again to yield $|\psi_{new,1}\rangle$ and so on. Hence the solution reads:

$$|\psi_{tot}\rangle = |\psi_0\rangle + \frac{\mathbf{V}}{\mathbf{H_0}+\omega}(1+\frac{\mathbf{V}}{\mathbf{H_0}+\omega}(1+\frac{\mathbf{V}}{\mathbf{H_0}+\omega}(...)))\,|\psi_0\rangle \tag{3.17}$$

This approach to solving the Lippman-Schwinger equation is called the Born approximation [5]. Rigorously solving this equation is a tedious task and is beyond the scope of this text. Interested readers are invited to read [4]. This text states that, after solving the equations, the field reflectivity r and transmissivity t of a waveguide coupled to a resonator is:

$$r = -j\sum_n \frac{1}{\omega_{k_i}-\omega_n+j\Gamma_n}\frac{LV_{-k_i,n}V_{n,k_i}}{v_g} \tag{3.18}$$

$$t = 1 - j\sum_n \frac{1}{\omega_{k_i}-\omega_n+j\Gamma_n}\frac{L|V_{k_i,n}|^2}{v_g} \tag{3.19}$$

$$\Gamma_n = \Gamma_0 + \frac{L(|V_{k_i,n}|^2+|V_{-k_i,n}|^2)}{2v_g} \tag{3.20}$$

In these equations the subscript k_i designates the waveguide mode (with propagation constant k_i) and n designates the n^{th} resonance in the cavity. The waveguide mode frequency and the cavity's resonance frequency are ω_{k_i} and ω_n respectively. Γ_n is the cavity's decay factor (in units [1/time]). It consists of the cavity's intrinsic decay factor Γ_0 and a contribution that is related to coupling to the waveguide, which is, from the cavity's point of view, another loss mechanism. The quantities L and v_g are the waveguide length and its group velocity respectively.

3.2.2.3 part 3: an expression for V_{Ψ_i,Ψ_j}

The coupling term V_{ψ_i,ψ_j} is shorthand for $\langle\psi_i\,|\,\mathbf{V}\,|\,\psi_j\rangle$. The operator $\mathbf{V}$ acts on Ψ_j and the result is projected onto Ψ_i. In other words, what part of ψ_j is scattered into ψ_i due to the perturbation $\mathbf{V}$? To find an expression for this inner product, consider 3.10 and the definition of the operator $\mathbf{H}$ in equation 3.4.

$$\mathbf{V} = \mathbf{H} - \mathbf{H_0} = \begin{bmatrix} 0 & (j/\epsilon_{tot} - j/\epsilon_{H0})\vec{\nabla}\times \\ 0 & 0 \end{bmatrix} \tag{3.21}$$

With ϵ_{H0} the spatial epsilon distribution associated with $\mathbf{H_0}$. This is a function of ϵ_w and ϵ_c. If $\mathbf{V}$ acts on a wave function, the result does not have a magnetic field component, only an electric field component, namely $(j/\epsilon_{tot} - j/\epsilon_{H_0})\vec{\nabla}\times\vec{H}$. From Maxwell's equations 3.3 and 3.4, it is obvious that $\nabla\times\vec{H} = j\epsilon_{H_0}\omega\vec{E}$ and consequently:

$$\mathbf{V}\,|\psi\rangle = \begin{bmatrix} 0 & (j/\epsilon_{tot} - j/\epsilon_{H_0})\vec{\nabla}\times \\ 0 & 0 \end{bmatrix} \begin{bmatrix} \vec{E} \\ \vec{H} \end{bmatrix} = \begin{bmatrix} \omega(1/\epsilon_{H_0} - 1/\epsilon_{tot})\epsilon_{H_0}\vec{E} \\ 0 \end{bmatrix} \quad (3.22)$$

After renaming $1/\epsilon_{H_0} - 1/\epsilon_{tot}$ to $\Delta\frac{1}{\epsilon}$, the expression for $\langle\psi_i\,|\,\mathbf{V}\,|\,\psi_j\rangle$ now reads:

$$\langle\psi_i\,|\,\mathbf{V}\,|\,\psi_j\rangle = \frac{\omega_j}{2}\int d^3r\epsilon_{H_0}^2(r)\Delta\frac{1}{\epsilon}\vec{E}_i^*\cdot\vec{E}_j \quad (3.23)$$

3.2.3 Scattering theory applied to resonant mirrors

3.2.3.1 Reflectivity, bandwidth and phase

The expressions for field reflectivity and transmissivity (eqns 3.18 and 3.19) are the general equations that roll out of scattering theory. It is a good idea to cast these in a more specific form that resembles the problem of resonant mirrors for hybrid silicon microlasers. In doing so, two assumptions are made:

- The silicon cavity has only one resonance in the frequency region of interest. This way the sum reduces to a single term. This assumption is true for defect grating cavities, hybrid band-edge defect grating cavities and short band-edge cavities. In the case of longer band-edge cavities the cavity modes are closely spaced and all have to be taken into account.
- The cavity has a symmetry plane perpendicular to the propagation axis z. This way $V_{-k_i,n} = V_{k_i,n}$.

Taking these assumptions into account, the field reflectivity now reads:

$$r = -j\frac{1}{\omega_w - \omega_c + j\Gamma_c}\frac{L|V_{c,w}|^2}{v_g} \quad (3.24)$$

$$\Gamma_c = \Gamma_0 + \frac{L|V_{c,w}|^2}{v_g} \quad (3.25)$$

The subscript c designates the cavity properties and w the III-V access waveguide properties. Using this expression, the frequency dependent power reflectivity $R(\omega)$, which is $|r|^2$, equals:

$$R(\omega_w) = \frac{1}{(\omega_c - \omega_w)^2 + \Gamma_c^2}\frac{L^2|V_{c,w}|^4}{v_g^2} \quad (3.26)$$

The factor $L|V_{c,w}|^2/v_g$ can be rewritten as the coupling factor κ that models the coupling between the cavity and the waveguide. In this case the power reflectivity becomes:

$$R(\omega_w) = \frac{\kappa^2}{(\omega_c - \omega_w)^2 + (\Gamma_0 + \kappa)^2} \quad (3.27)$$

This is a Lorentzian line shape function centered around ω_c with maximum reflectivity $\kappa^2/(\Gamma_0+\kappa)^2$ and full width at half maximum $2(\Gamma_0+\kappa)$. It is easy to see that this expression can reach values close to 1 if only the waveguide is excited with a frequency near the cavity's resonance frequency and $\Gamma_0 << \kappa$. In other words, even though the coupling between the waveguide and cavity should not be very good, the mirror will still reflect a high fraction of the incoming light if only the cavity's decay rate is small enough.

In the previous chapter the ability of a silicon grating cavity to store energy was not expressed in terms of its field decay rate Γ_0, but rather in terms of its quality factor Q_i. These two quantities are related through:

$$\Gamma_0 = \frac{1}{2}\frac{dU/dt}{U} = \frac{\omega_c}{2Q_i} \tag{3.28}$$

Substituting this into equation 3.27, renaming $\omega_c - \omega_w$ to $\delta\omega$ and dividing nominator and denominator by ω_c yields:

$$R(\omega_w) = \frac{(\kappa/\omega_c)^2}{(\delta\omega/\omega_c)^2 + (\frac{1}{2}(1/Q_i + 2\kappa/\omega_c))^2} \tag{3.29}$$

It is convenient to view $2\kappa/\omega_c$ as a pseudo-Q-factor $1/Q_\kappa$. This way the expression for the power reflectivity $R(\omega_w)$ yields:

$$R(\omega_w) = \frac{(\frac{1}{2}(1/Q_\kappa))^2}{(\delta\omega/\omega_c)^2 + (\frac{1}{2}(1/Q_i + 1/Q_\kappa))^2} \tag{3.30}$$

In this form, the maximum reflectivity R_{max} and full width at half the maximum (FWHM) $\Delta\omega$ (or $\Delta\lambda$) of the reflection peak are:

$$R_{max} = \frac{1}{(1+Q_\kappa/Q_i)^2} \tag{3.31}$$

$$\frac{\Delta\omega}{\omega_c} = \frac{\Delta\lambda}{\lambda_c} = \frac{1}{Q_i} + \frac{1}{Q_\kappa} \tag{3.32}$$

These two very simple equations give profound insight in the physics of the two most important properties of a resonant mirror. The reflectivity of such a mirror can be high, if only the silicon cavity's intrinsic Q-factor is high enough. If $Q_i >> Q_\kappa$, the mirror's bandwidth is mainly determined by the coupling (in the form of Q_κ). Also, the maximum reflectivity depends on the relative fraction of both Q-factors where the bandwidth is determined by their absolute value.

Another important property of the resonant mirror is the phase of the reflected light, as this is a factor in determining the resonance of the laser. Since the coupling factor is real, it is easy to see from equation 3.18 that:

- at resonance r is real (phase = 0)
- when $\omega_w << \omega_c$, r is proportional to j (phase = $\pi/2$)
- when $\omega_w >> \omega_c$, r is proportional to $-j$ (phase = $-\pi/2$)

In other words, the phase is rotated over π radians across the reflection peak.

3.2.3.2 The coupling factor

The intrinsic Q-factor of the silicon cavities was studied extensively in the previous chapter. In this section the general properties of that other defining quantity is investigated: the Q-factor associated with the coupling between the III-V waveguide and the cavity Q_κ.

Consider the generic resonant mirror scheme in figure 3.3. The III-V access waveguide is excited with its fundamental eigenmode ψ_w. This mode has a frequency ω, transversal mode profile $\phi_w(x, y)$ and a wave vector $\vec{k}_w$ pointing in the z direction. The cavity consists of a waveguide of length L with cavity mode ψ_c. This is a 'standing wave'-like localised mode with a certain longitudinal mode profile $\Theta(z)$ and transversal mode profile $\phi_c(x, y)$. The distance between the access waveguide and the top of the cavity is h. This number is sometimes also referred to as the BCB-thickness, for obvious reasons.

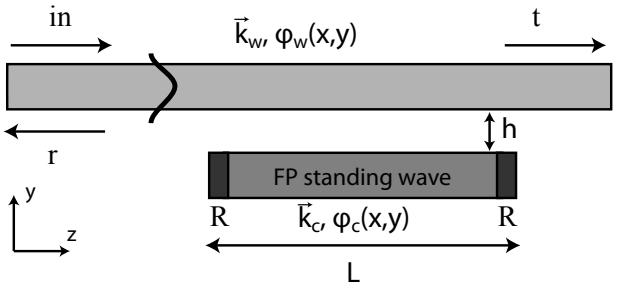

Figure 3.3: Schematic representation of the scattering theory model of the resonant mirror with Fabry-Perot cavity.

Unperturbed access waveguide The main feature of the waveguide mode is its spatial electric field profile. This can be written as:

$$\psi_w(x, y, z, \omega) = A_w(x, y, \omega) \exp(jk_w(\omega)z) \tag{3.33}$$

In this equation $A_w(x, y, \omega)$ is the mode profiles of the electric field. A_w is scaled such that the mode is normalized with respect to the inner product defined in 3.9, so: $\langle \psi_w \,|\, \psi_w \rangle = 1$.

Unperturbed cavity The localized mode in the silicon cavity ψ_c can be written as:

$$\psi_c(x, y, z, \omega) = A_c(x, y, \omega)\theta(z) \tag{3.34}$$

with A_c again the normalized mode profile of the cavity waveguide cross-section and $\theta(z)$ the cavity's z-dependence. The longitudinal amplitude function $\theta(z)$ of the grating based cavities that are discussed in this work consist of a standing wave pattern with wave vector k_c that is modulated with a slowly varying envelope function:

$$\theta(z) = \Theta(z)(\exp(jk_c z) + \exp(-jk_c z)) \tag{3.35}$$

The cavity's Q-factor is Q_i.

The coupled system Using the definitions proposed in the previous two paragraphs, the coupling factor V_{ψ_c,ψ_w} becomes:

$$\langle \psi_c \,|\, V \,|\, \psi_w \rangle = \frac{\omega_c}{2} \int \epsilon_{int}(x, y, z) A_c^*(x, y) A_w(x, y) \theta^*(z) \exp(jk_w z) d^3r \tag{3.36}$$

With $\epsilon_{int} = \epsilon_{H_0}^2(1/\epsilon_{H_0} - 1/\epsilon_{tot})$. This epsilon distribution is zero in the cladding regions and non-zero in the waveguide and the grating cavity. Consequently it can be decomposed into $\epsilon_{int} = \epsilon_1 + \epsilon_2$, with ϵ_1 being zero everywhere except for in the waveguide and ϵ_2 being zero everywhere except for in the cavity. The distribution ϵ_1 is independent of z but ϵ_2 is not since it contains the corrugated grating.This z-dependence can be modeled by approximating ϵ_2 by its first two Fourier terms:

$$\begin{aligned} \epsilon_2(x, y, z) &= \epsilon_{2,xy}(x, y)(\epsilon_{2,0} + \epsilon_{2,1}(\exp(ik_c z) + \exp(-ik_c z))) & (3.37) \\ &= \epsilon_{2,xy}(x, y)\epsilon_{2,z}(z) & (3.38) \end{aligned}$$

Hence the integral in equation 3.36 is the sum of two independent integrals: one across ϵ_1 (the waveguide) and one across ϵ_2 (the cavity):

$$\langle \psi_c \,|\, V \,|\, \psi_w \rangle = \langle \psi_c \,|\, V \,|\, \psi_w \rangle_1 + \langle \psi_c \,|\, V \,|\, \psi_w \rangle_2 \tag{3.39}$$

Integral term 1: the waveguide First consider the first term $\langle \psi_c \,|\, V \,|\, \psi_w \rangle_1$. Because ϵ_1 is independent of the longitudinal coordinate z, the xy dependence can be split from the z dependence:

$$\langle \psi_c \,|\, V \,|\, \psi_w \rangle_1 = \frac{\omega_c}{2} \int \epsilon_1(x,y) A_c^*(x,y) A_w(x,y) dxdy \int_0^L \theta^*(z) \exp(jk_w z) dz \tag{3.40}$$

The first integral, the lateral, xy-dependent part, describes the spatial overlap between the two modal cross-sections. This factor will mainly depend on the physical proximity of the waveguides and the spatial extent of their mode profiles. This factor cannot be evaluated analytically and should be solved using an optical mode solver. This 2D integral will be referred to as the *modal overlap condition*. Because the lateral decay of a waveguide eigenmode's evanescent field is exponential, this integral will decrease exponentially as a function of the lateral distance h between the access waveguide and the cavity.

The second integral, the longitudinal, z-dependent factor models the dependence of the coupling on the propagation constants of the different modes and the longitudinal extent of the cavity. The integral factor over the z-coordinate can be seen as a 1D spatial Fourier transform of $\theta^*(z)$, evaluated at the waveguides wavenumber k_w. In other words, if the spatial Fourier transform of the cavity's longitudinal amplitude profile $\theta(z)$ contains the waveguides k-vector k_w, the coupling term can be non-zero. Because in most practical cases the cavity is finite in length, its spatial Fourier transform will have a certain width in k-space. If the cavity is short, its Fourier transform will be wide and contain a large range of k-vectors and the cavity will couple to the waveguide at a wide range of wavelengths (corresponding to a wide range of k_w's). If, on the other hand, the cavity mode spreads out over a long distance, its Fourier image will be narrow and the coupling condition will be more stringent. This factor is called the *phase matching condition*, because it is maximum if the two waves (waveguide and cavity) have similar k-vectors (so if their phase propagation is *matched*).

To gain insight into this phase matching condition, assume for a moment that the silicon cavity is not a grating cavity but a Fabry-Perot cavity: an ordinary waveguide with reflective facets. In this case the slowly varying amplitude function $\Theta(z)$ is 1 between $z = 0$ and $z = L$ and zero outside. In this case, the phase-matching-condition can be calculated analytically easily:

$$\int_0^L \theta^*(z) \exp(jk_w z) dz = \int_0^L (\exp(jk_c z) + \exp(-jk_c z)) \exp(jk_w z) dz \tag{3.41}$$

This is the sum of two integrated exponential functions. The one with exponent $-j(k_w + k_c)z$ and the other one with exponent $-j(k_w - k_c)z$. Both are evaluated

between $z = 0$ and $z = L$. The first term yields:

$$\int_0^L \exp(-j(k_w + k_c)z)dz = [\frac{j}{k_w + k_c} \exp(-j(k_w + k_c)z)]_0^L \tag{3.42}$$

So finally:

$$\Theta(k_w) = L \exp(j\frac{k_w + k_c}{2}L)sinc(\frac{k_w + k_c}{2}L) + L \exp(j\frac{k_w - k_c}{2}L)sinc(\frac{k_w - k_c}{2}L) \tag{3.43}$$

$\Theta(k_w)$ is the sum of 2 $sinc$ functions. One has a k_w dependence of $(k_w - k_c)L/2$ and the other has $(k_w + k_c)L/2$. The $sinc$ function is maximum if its argument equals zero, so the access waveguide and cavity are coupled if $k_w = k_c$ or $k_w = -k_c$. This means: if the waveguide mode has the same propagation constant as the cavity, either propagating forward (k_c) or backward($-k_c$), hence the name *phase matching condition*. The center lobe of the sinc function has a certain width, so the phase matching condition is not that strict. The $sinc(x)$ function reaches its first zero at $x = \pi$, so with either $k_w + k_c$ or $k_w - k_c$ as Δk, the range of waveguide k's Δk_0 that lie within the $sinc$'s main lobe are given by:

$$\frac{\Delta k_0}{2}L = 2\pi \Leftrightarrow \Delta k_0 = \frac{4\pi}{L} \tag{3.44}$$

Approximating the FWHM of this lobe as half the distance between the zeros at $-\pi$ and π yields:

$$\Delta k_{FWHM} = \frac{2\pi}{L} \tag{3.45}$$

Assuming that this formula holds for any cavity with longitudinal mode length L and propagation constant k_c, the waveguide's k-vector k_w must satisfy the condition $k_w = k_c \pm \pi/L$. Assuming the waveguide is excited at the cavity's resonance wavelength λ_R and because $k = 2\pi n/\lambda$, and consequently $\Delta_k = 2\pi/\lambda\Delta n$, the mismatch between the effective indices between the cavity and the waveguide can be on the order of:

$$\Delta n_{FWHM} = \frac{\lambda_R}{2\pi}\Delta k = \frac{\lambda_R}{L} \tag{3.46}$$

This gives an idea of the order of magnitude of the mismatch that can be tolerated. For example, if the cavity is $15\mu m$ long and the resonance wavelength Λ_R equals $1.55\mu m$, the tolerable deviation in effective index is around 0.1. This number scales inversely proportional with L, so a 10 times longer cavity results in a 10 times lower Δn tolerance. Because the effective index of a waveguide can be very dependent on the dimensions, that can vary significantly due to fabrication imperfections, it can be advantageous to make the cavity as small as possible.

Integral term 2: the cavity The second term in the integral in equation 3.39 runs over ϵ_2. This epsilon distribution (equation 3.38) now contains a constant part ($\epsilon_{2,0)}$) and a z-dependent part (proportional to $\epsilon_{2,1}$). It is easy to see that this will break the integral $\langle \Psi_c \,|\, V \,|\, \Psi_w \rangle_2$ into two separate terms:

$$\langle \Psi_c \,|\, V \,|\, \Psi_w \rangle_2 = \langle \Psi_c \,|\, V \,|\, \Psi_w \rangle_{2a} + \langle \Psi_c \,|\, V \,|\, \Psi_w \rangle_{2b} \tag{3.47}$$

The first term is similar to the treatment in the previous paragraph of $\langle \Psi_c \,|\, V \,|\, \Psi_w \rangle_1$. The only difference is the xy overlap integral that now runs over the cavity cross-section instead of the waveguide cross-section. The z-dependent integration is identical. But the second term (2b) contains the z-dependent epsilon distribution and should be studied separately. Again, integral can be separated into a xy dependent part and a z dependent part. The treatment of that xy dependent part is identical to the previous treatment and only the z dependent integral will be discussed. That integral now looks like this:

$$\epsilon_{2,1} \int \theta(z)^* \exp(-jk_w z)(\exp(jk_g z) + \exp(-jk_g z))dz \tag{3.48}$$

Simplifying this result now yields:

$$\epsilon_{2,1}(\int \theta(z)^* \exp(-j(k_w - k_g)z)dz + \int \theta(z)^* \exp(-j(k_w + k_g)z)dz) \tag{3.49}$$

This is just the sum of the spatial Fourier transform of $\theta^*(z)$ shifted by an amount k_g and $-k_g$. Using a derivation parallel to the one in the previous section about $\langle \Psi_c \,|\, V \,|\, \Psi_w \rangle_1$, this will result in the sum of 4 functions with the following phase matching conditions:

1. $k_w = k_g + k_c$
2. $k_w = k_g - k_c$
3. $k_w = -k_g + k_c$
4. $k_w = -k_g - k_c$

In other words, the presence of the grating can enhance the coupling between forward and backward propagating waves in both the III-V waveguide and the silicon cavity. This phenomenon is called grating-assisted coupling. Two situations can occur:

- Defect grating: if the cavity mode is inside the grating's band-gap, the mode's k-vector equals exactly half the grating's k-vector. In this case the cavity mode and the waveguide mode have to be matched for this coupling mechanism to occur. The presence of the grating enhances the coupling of $\langle \Psi_c \,|\, V \,|\, \Psi_w \rangle_1$ and $\langle \Psi_c \,|\, V \,|\, \Psi_w \rangle_{2a}$.

- Band-edge grating: in a band-edge grating resonator the cavity mode's k-vector is smaller than half the grating's k-vector. In this case, coupling occurs if the cavity mode and waveguide mode are not phase matched. The phase-mismatch is compensated by the grating. In this case the grating assisted coupling adds new k_w vectors that can couple to the grating (end vice-versa).

3.2.4 Scattering theory: conclusions

This section has provided insight in the physics of resonant mirrors for hybrid silicon micro lasers. The following list states the most important conclusions and design guidelines that can be drawn from this analysis.

- **Wavelength selectivity** The spectral response of a resonant mirror is a Lorentzian line shape function centred around the silicon cavity's resonance wavelength λ_c.

- **Peak reflectivity** The peak reflectivity of this line shape function is given by:

$$R_{max} = \frac{1}{(1 + Q_\kappa/Q_i)^2} \tag{3.50}$$

  with Q_i the cavity's intrinsic Q-factor and Q_κ a Q-factor that is related to the coupling between the cavity and the III-V waveguide.

- **Reflection bandwidth** The FWHM of the Lorentzian line shape function is given by:

$$\Delta\lambda = (\frac{1}{Q_i} + \frac{1}{Q_\kappa})\lambda_c \tag{3.51}$$

- **Coupling Q-factor** The Q-factor related to the coupling Q_κ is defined as:

$$Q_\kappa = \frac{\omega_c v_g}{2L|V_{c,w}|^2} \tag{3.52}$$

  with ω_c the cavity's resonance frequency, v_g the waveguide's group velocity, L the length of the cavity and $V_{c,w}$ the coupling integral.

- **The coupling integral $V_{c,w}$** The coupling integral $V_{c,w}$ is the product of 2 factors:

  - a transversal factor that is proportional to the overlap of the III-V waveguide's eigenmode profile and the silicon cavity's eigenmode profile. The most important parameter that influences this factor is the BCB thickness.

– a longitudinal factor that determines the range of III-V waveguide k vectors that will couple to the silicon cavity. The coupling strength is given by the spatial Fourier transform of the longitudinal amplitude function $\theta(z)$ evaluated at the waveguide's k vector. Short cavities support a wide range of waveguide k-vectors, long cavities support a narrow range of waveguide k vectors. In the case of a band-edge grating cavity, grating assisted coupling will allow for non-phase-matched k vectors to couple to the silicon cavity.

Simulation approach

The remainder of this chapter will study the practical implementation of resonant mirrors using the 3 silicon cavity types presented in the previous chapter. Numerical simulations will be used extensively. This chapter utilises 2D mode expansion [7] to simulate the light propagation in a resonant mirror. The R/T diagrams in this chapter are so-called mode-to-mode reflection and transmission characteristics. This means that an eigenmode of the III-V waveguide is launched and the reflection R is the total power fraction that is reflected back into that same eigenmode. The transmission is the total power that is transmitted through the III-V waveguide in its fundamental eigenmode.

3.3 Band-edge grating cavity resonant mirrors

The previous section discussed the feasibility of using a resonator coupled to a waveguide as a way to reflect light back into that waveguide. The analytical model resulted in clear design guidelines. This section will deal with the first practical implementation of resonant mirrors using the simplest grating cavity discussed in the previous chapter: the band-edge grating cavity. The properties of this resonator were examined in depth in section 2.3.1.

Figure 3.4 shows the schematic representation of the resonant mirror that will be studied in this section. The silicon cavity is a band-edge Fabry-Perot grating cavity of width w_{Si} and height $220\,nm$ with $70\,nm$ deep corrugations. The grating consists of N_g periods of length Λ each. On top of the silicon cavity lies a III-V waveguide of width w_{III-V} and thickness h_{III-V}. It consists of 3 layers: a bottom InP layer (usually n-doped), an InGaAsP or InAlGaAs active region (usually not doped) and a top InP p layer. The thickness of the active region is h_{act} and the thickness of the bottom InP layer is h_n. Consequently the thickness of the top InP layer is $h_p = h_{III-V} - h_{act} - h_n$. The active region might consist of a number of quantum wells separated by barrier layers but it is modelled as one homogeneous material. This assumption is justified by the fact that the individual thicknesses of

the wells and barriers is much smaller than the optical wavelength. In between the III-V waveguide and the silicon cavity is the adhesive BCB layer. The distance between the top of the uncorrugated silicon waveguide and the bottom of the III-V waveguide is h_{BCB}.

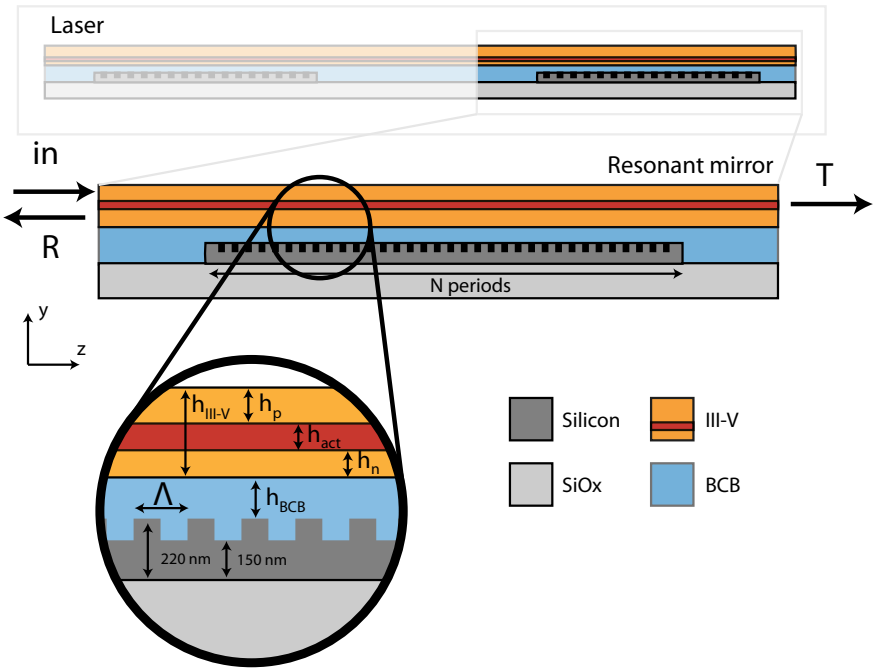

Figure 3.4: Schematic representation of resonant mirror with band-edge Fabry-Perot grating cavity.

3.3.1 k-vector analysis of the silicon band-edge cavity

One of the conclusions that was drawn from scattering theory was that the coupling between the silicon cavity and the III-V waveguide is proportional to the spatial Fourier transform of the longitudinal amplitude function of the cavity mode, evaluated at the waveguide's wave vector k_w. To start off, consider the $1.6\,\mu m$ wide silicon band-edge Fabry-Perot cavity with 80 periods of $290\,nm$ that was studied in section 2.3.1 of the previous chapter. The top part of figure 3.5 depicts the longitudinal electric field amplitude profile $\Theta(z)$ that was shown (squared) in figure 2.17.

The bottom panel of figure 3.5 shows the squared amplitude of the spatial Fourier transform of $\Theta(z)$ as a function of its k vector. This high resolution Fourier transform was created by padding the amplitude profile in the top panel with zeros. The Fourier image is a distribution with a certain width, as a consequence of the finite length of $\Theta(z)$. Because the traveling mode in this Fabry-Perot resonator is at the edge (so not inside) the grating's band-gap, the distribution is not centred at $k_g/2$, but at a k-vector k_c that is smaller than $k_g/2 = 10.83/\mu m$, in this case $k_c = 10.79/\mu m$.

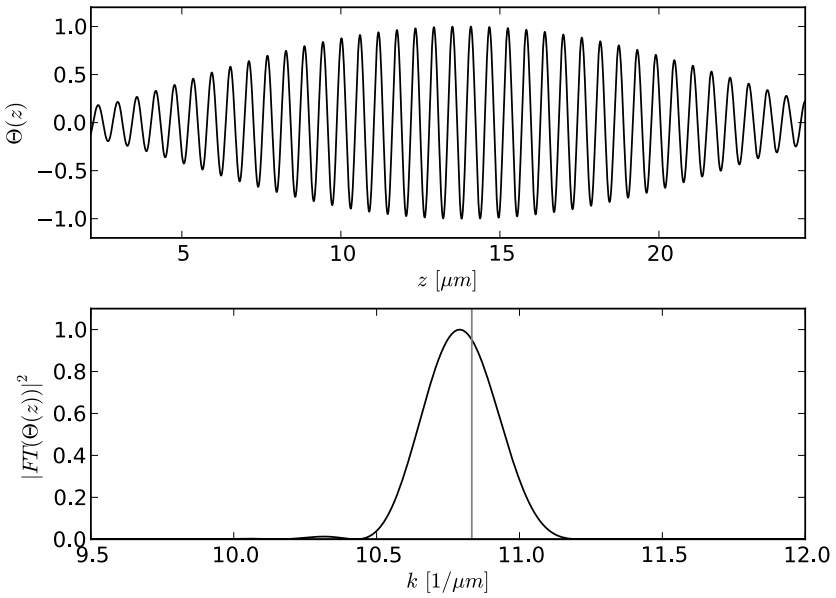

Figure 3.5: Top panel: longitudinal amplitude function $\Theta(z)$ for an 80 period grating with $0.29\,\mu m$ pitch. Bottom panel: spatial Fourier transform squared of $\Theta(z)$. The vertical line indicates $k_g/2$.

To allow for good coupling, the waveguide's wave vector k_w should be close to the k vector where the spatial Fourier transform of $\Theta(z)$ is maximum, so $k_w = 10.79/\mu m$. The waveguide mode should have this wave vector at the cavity's resonance wavelength, so at $\lambda = 1589.2\,nm$. In other words, the III-V waveguide's effective index n_{eff} at $\lambda = 1589.2\,nm$ should be:

$$n_{eff} = \frac{k_w \lambda}{2\pi} = 2.729 \tag{3.53}$$

The FWHM of the $\Theta(z)$'s Fourier image Δk_{FWHM} equals $0.3107/\mu m$. Conse-

quently the variation in n_{eff} that is allowed is:

$$\frac{\Delta n_{FWHM}}{n_{eff}} = \frac{\Delta k_{FWMH}}{k_c} = \frac{0.3107/\mu m}{10.79/\mu m} \Leftrightarrow \Delta n_{FWHM} = 0.0785 \quad (3.54)$$

To get an idea of how this will influence the maximum reflectivity of the mirror, remember that $R_{max} = 1/(1 + Q_\kappa/Q_i)$ and that Q_κ is inversely proportional to $|V_{c,w}|^2$ and consequently to $|FT(\Theta(z))|^2$. Assuming that Q_κ/Q_i is small compared to 1, R_{max} can be approximated by its first order Taylor expansion:

$$R_{max} = \frac{1}{1 - Q_\kappa/Q_i} \approx 1 - \frac{Q_\kappa}{Q_i} \quad (3.55)$$

So if $|FT(\Theta(z))|^2$ halves, the mirror loss $(1-R_{max})$ doubles. Of course, $|FT(\Theta(z))|^2$ is not the only factor that influences Q_κ, the 2D xy overlap function contributes equally to $V_{c,w}$ and because this figure depends on the spatial overlap of the evanescent modes, which decay exponentially, its impact can be very significant.

3.3.2 III-V waveguide design

As shown in figure 3.4, the III-V waveguide consists of an active InGaAsP or InAlGaAs region sandwiched between two InP cladding layers. The thickness of these layers will determine the effective index of the III-V waveguide. A prototype of such a device would be fabricated at the in-house clean room. The III-V features would be defined using contact lithography. This limits the minimum width of the waveguide to around $1.6\mu m$, so in the following discussion this width will be used.

Figure 3.6 shows the effective index of a $1.6\mu m$ wide III-V waveguide that consists of an InGaAsP layer ($n = 3.42$ at $\lambda = 1550\,nm$ and bandgap also near $1550\,nm$ [6]) sandwiched between two equally thick InP layers ($n = 3.17$ at $1550\,nm$ [6]). The effective index is shown as a function of the total thickness of the stack (h_{wg} on y-axis) and the percentage of active material in the waveguide (h_{act}/h_{wg} on x-axis). The map also shows the effective index of the cavity ($n_{eff} - line$) and the indices where the Fourier image of $\Theta(z)$ is half of its maximum ($n_{eff} \pm \Delta n/2$). Any III-V waveguide configuration on the n_{eff} line should be phase matched to the cavity. Unless mentioned otherwise, the remainder of this section will assume a waveguide height $h_{III-V} = 280\,nm$ and consequently $h_{act} = 56\,nm$ to meet the phase matching criterion.

Figure 3.7 shows how the effective index of such a $280\,nm$ thick InP waveguide with a $56\,nm$ thick InGaAsP active layer in the center depends on the waveguide width. The waveguide mode considered is the fundamental TE mode at the

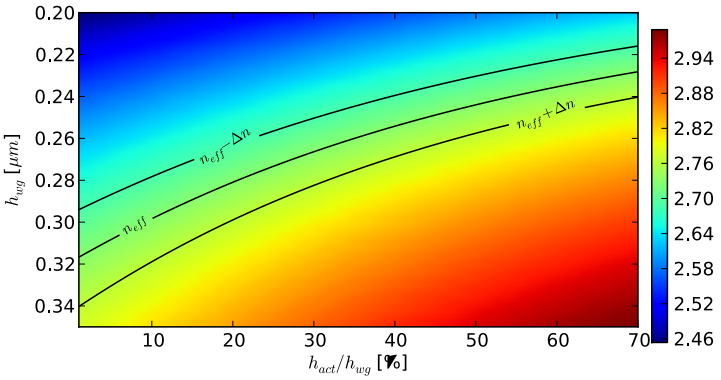

Figure 3.6: Effective index map of a $1.6\mu m$ wide III-V waveguide containing 2 InP cladding layers and an InGaAsP active layer as a function of the total stack height and the percentage of active material in the waveguide. The active part is assumed to be in the center of the waveguide

80 period grating's fundamental resonance mode's frequency $1589\,nm$. The graph also shows the waveguide width required to meet the phase-matching condition ($1.6\mu m$ as defined in the previous paragraph) and the lower tolerance boundary $n_{eff} - \Delta n/2$. The upper tolerance boundary $n_{eff} - \Delta n/2$ is not on the graph. This shows that the phase matching condition is relatively tolerant towards width deviations. However, changing the width of the III-V waveguide, given a certain silicon cavity, will also change the 2D xy overlap integral, which will also influence the coupling factor. This is especially true for very wide III-V waveguides.

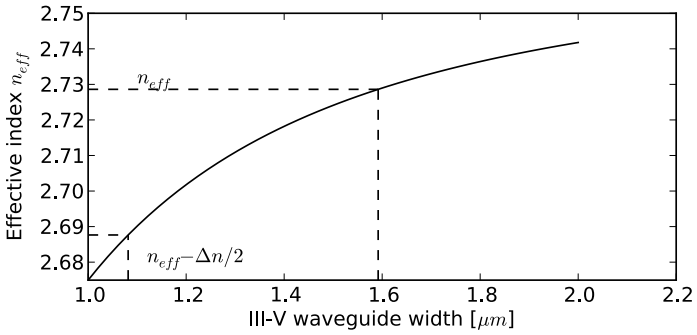

Figure 3.7: Effective index of a TE-polarized $280\,nm$ high InP waveguide with a $56\,nm$ thick InGaAsP layer in the center as a function of waveguide width. The figure also shows n_{eff} required for phase matching and $|\Theta(z)|^2$'s FWHM.

Symbol	Value	Unit	Description
w_{si}	1.6	μm	width of silicon waveguide grating
n_{si}	3.47		bulk refractive index of silicon
Λ	290	nm	grating period
N_g	80		number of periods in grating
h_{BCB}	350	nm	BCB thickness above waveguide
n_{BCB}	1.55		bulk refractive index BCB
h_{III-V}	280	nm	height of III-V waveguide
h_n	112	nm	height of bottom InP cladding layer
h_{act}	56	nm	height of InGaAsP active layer
h_p	112	nm	height of top InP layer
w_{III-V}	1.6	μm	width of III-V waveguide
n_{InP}	3.17		bulk refractive index of InP at $1550\,nm$
n_{act}	3.42		bulk refractive index of InGaAsP (Q=1.55) at $1550\,nm$

Table 3.1: Listing of all parameters in the resonant mirror structure based on a band-edge Fabry-Perot cavity with standard values.

3.3.3 Band-edge grating cavity resonant mirror: the standard component

Throughout this section the influence of many of the parameters that define a band-edge grating cavity resonant mirror will be discussed. In order to keep a clear overview, table 3.1 lists all the parameters of the resonant mirror represented in figure 3.4 along with their standard value. Unless mentioned otherwise, the values used for each parameter in the simulations in this section are the standard values listed in table 3.1. This standard model consists of an 80 period long grating with $290\,nm$ grating period and the accompanying III-V waveguide that was proposed in the previous paragraph. Throughout this section TE-polarized light is assumed. All simulations are performed in 2 dimensions. The third dimension, the x dimension, is reduced using the effective index method, similar to the simulations in the previous chapter.

3.3.3.1 R/T spectrum of the standard Fabry Perot band-edge cavity resonant mirror

Figure 3.8 shows the R/T spectrum of the resonant mirror using a band-edge Fabry-Perot grating cavity as shown in figure 3.4 with the standard parameters in table 3.1. The silicon Fabry-Perot cavity used in this example is identical to the 80-period cavity discussed in section 2.3.1. The wavelength of the reflection peak in figure 3.8 corresponds to the resonance wavelength of the first cavity mode on

the long-wavelength side of this grating's stop band, as shown in figure 2.15. At this wavelength, $\lambda = 1.589\,\mu m$, the resonant mirror structure reflects 68% of the power that was launched in the forward propagating fundamental mode of the III-V waveguide into the backward propagating fundamental mode of that III-V waveguide. Virtually no light is transmitted through the III-V waveguide. The remaining 32% is most probably lost at the silicon cavity's facets. The full spectral width at half the reflection peak's maximum (FWHM) of the reflection peak is $6.3\,nm$. The transmission spectrum also shows a dip at $\lambda = 1596.3\,nm$. This corresponds to the resonance wavelength of the second longitudinal band-edge mode, also shown in figure 2.15.

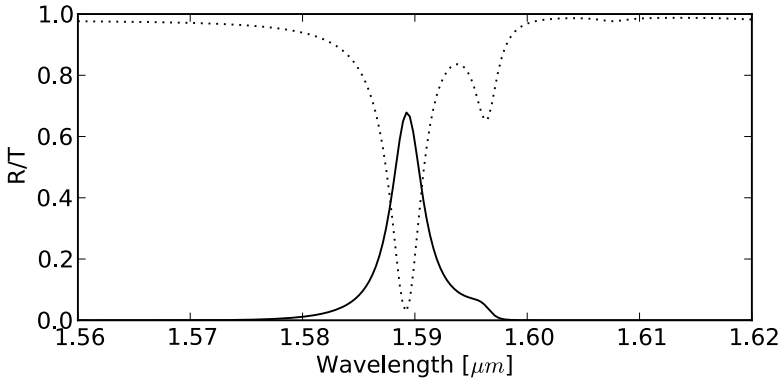

Figure 3.8: R/T spectrum of resonant mirror using a band-edge Fabry-Perot grating cavity with the standard properties in table 3.1

3.3.3.2 2D Field profiles of the standard Fabry Perot band-edge cavity resonant mirror

To investigate the nature of the different features in this R/T spectrum, figure 3.9 shows the time-averaged spatial distribution of the magnitude of the electric field squared $|E|^2$ at three different wavelengths. The colour scheme is in logarithmic scale.

- **1570 nm** This wavelength lies within the band-gap of the silicon grating, away from the band-edge resonances. Around 97% of the light passes through the III-V waveguide. The remaining 3% couples to the silicon grating and is lost at its facets. In other words, there is very little interaction between the III-V waveguide and the silicon grating underneath.

- **1589 nm** At this wavelength, the reflectivity of the resonant mirror structure is maximal. As can be seen in figure 2.15, the first long-wavelength band-edge resonance of the passive grating cavity lies at this wavelength. Inspecting figure 3.9 shows that this resonance is excited in the silicon cavity. The graph clearly shows that the grating and waveguide are phase-matched in this configuration because the phase of the standing wave patterns in both layers differs by $\pi/2$ radians all along the length of the mirror. 68% of the incoming light is reflected and 2.8% is transmitted through the active waveguide. The remaining 29% is radiated from the grating's facets. The field distribution at this wavelength will be discussed in more detail in the next paragraph.
- **1596 nm** This wavelength corresponds to the second long-wavelength band-edge resonance of the 80 period silicon Fabri-Perot band-edge grating cavity. About 5% of the incoming light is reflected and 65% is transmitted. The remaining 30% is lost at the grating's facets. It should be clear from the image that this configuration is not phase-matched, because the difference between the phases of the waveguide and cavity mode vary as a function of the longitudinal coordinate z.

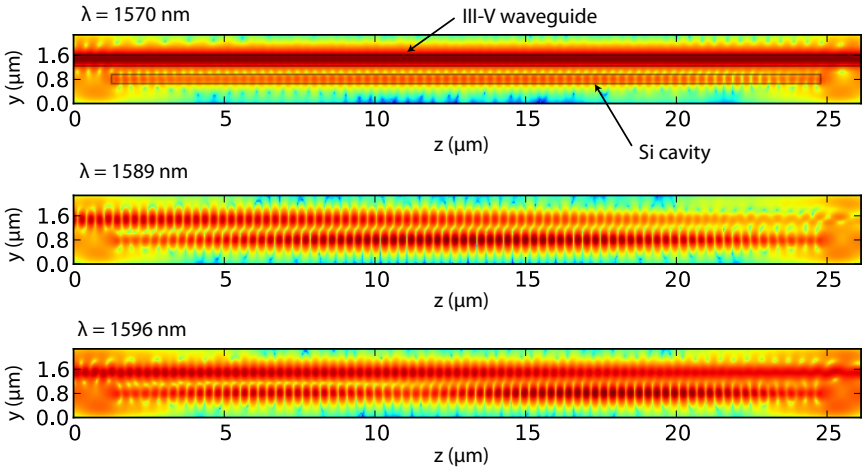

Figure 3.9: Time-averaged spatial distribution of the magnitude of the electric field squared $|E|^2$ at three different wavelengths of the resonant mirror in figure 3.8.

3.3.3.3 1D field profiles cross section at the resonance wavelength $\lambda = 1589\,nm$

Figure 3.10 shows the spatial distribution of the electric field at the wavelength of maximum reflectivity $\lambda = 1589\,nm$. The black line shows the field distribution

in the center of the III-V waveguide ($y = 1.46\mu m$) and the grey line shows the distribution in the cavity ($y = 0.8\mu m$). The grating starts at $z = 1.4\mu m$. As expected, the cavity field profile clearly resembles the fundamental cavity mode's profile in figure 2.17. The amplitude of the electric field in the III-V waveguide follows a shape that corresponds to the integrated cavity field profile. Given the fixed amplitude profile of the cavity, the rate of change of the amplitude in the waveguide is proportional to the field in the cavity, explaining this shape.

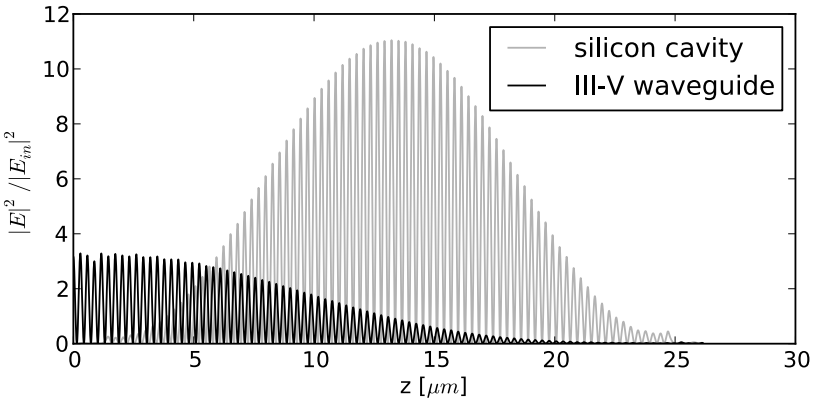

Figure 3.10: Time-averaged 1D spatial distribution of the magnitude of the electric field squared $|E|^2$ at the wavelength of maximum reflectivity $\lambda = 1589\,nm$. The field in the cavity (grey line) and waveguide (black line) are shown.

The III-V waveguide is phase-matched to the band-edge mode in the cavity. The k-vector of the band-edge mode k_c in the cavity is very close to the half the grating's k-vector $k_g/2$. Consequently, the waveguide's k-vector k_w also lies very close to the grating's k-vector $k_g/2$. In other words, the waveguide mode, that feels the grating corrugations at its evanescent tail, should experience evanescent distributed Bragg reflection (eDBR). One could think that this is the main cause of the reflection peak instead of the resonant mirror effect. If this would be the case, the amplitude of the III-V waveguide mode should decay exponentially. Clearly this is not true, so the main reason for the hybrid structure to reflect light is not evanescent distributed Bragg reflection but the resonant mirror effect. Also, to satisfy the Bragg relation ($\lambda = 2n_{eff}\Lambda$), the peak wavelength should be at $1582\,nm$. It is possible though that a certain fraction of the reflectivity is caused by eDBR, but it is certainly not the predominant reflection mechanism.

3.3.4 Influence of the BCB thickness h_{BCB}

One of the most important parameters in the design of hybrid silicon lasers is the thickness of the BCB layer. This section will investigate the influence of this number on the R/T spectrum of Fabry-Perot band edge grating cavity resonant mirrors. Figure 3.11 shows how the BCB-thickness influences the R/T spectrum of the standard Fabry-Perot band-edge grating cavity resonant mirror. The peak reflectivity decreases from 95% for a $300\,nm$ thick BCB layer to 86% ($350\,nm$), 68% ($400\,nm$) and finally 39% for a $450\,nm$ thick BCB layer. This decrease is very close to exponential (fitting $R^2 = 0.994$).

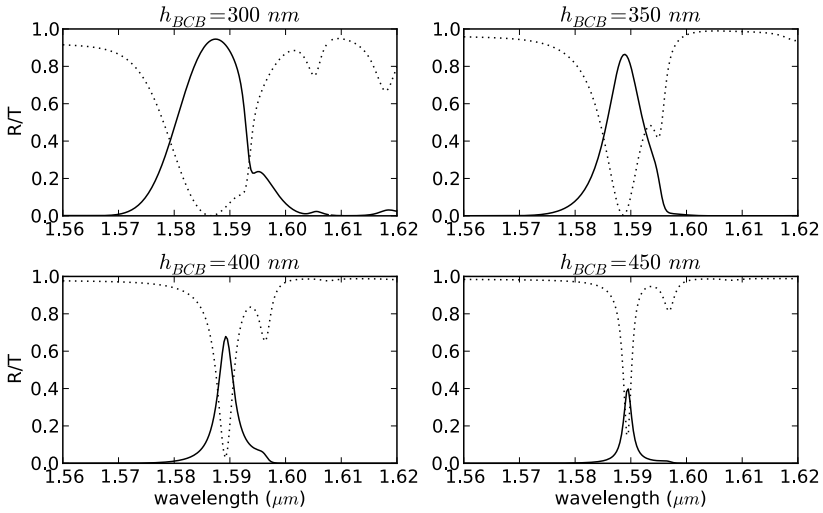

Figure 3.11: Influence of the thickness of the BCB layer h_{BCB} on the R/T spectrum of the standard Fabry-Perot band-edge grating cavity resonant mirror.

The reason for this is the fact that, when the BCB layer thickness increases, the overlap between the evanescent tail of the cavity or waveguide mode and the other waveguide or cavity mode decreases. This evanescent tail decreases laterally in an exponential fashion, resulting in an exponential increase in Q_κ. The reflection bandwidth increases as expected with decreasing BCB thickness for the same reason. With a $300\,nm$ thick BCB layer, the FWHM of the reflection peak is $12\,nm$ and drops to $1.1\,nm$ for $h_{BCB} = 450\,nm$. It is clear though that the main lobe in the reflection spectrum is a combination of the fundamental cavity mode (at $1589\,nm$) and the second cavity mode (at $1596\,nm$) for BCB thicknesses below $400\,nm$.

3.3.5 Influence of the III-V waveguide height h_{III-V}

As illustrated in figure 3.6, the coupling factor Q_κ is very sensitive to the thickness of the III-V waveguide. This section will focus on how that dependence influences the R/T spectrum. In general, changing the height of the III-V waveguide has two consequences:

- The effective index of the mode changes so the phase-matching condition will no longer be satisfied. A thicker waveguide yields a higher effective index, a thinner waveguide will result in a smaller effective index.

- The transversal mode distribution will change. In a thinner waveguide the mode will be pushed out and the overlap with the silicon cavity will increase, given a fixed BCB thickness. Analogously, by making the waveguide thicker, the mode is pulled inside the waveguide and the overlap with the cavity will decrease.

In an attempt to make comparison between the different results easier, the thickness of the top p-InP h_p is varied. This way the layers closest to the silicon cavity remain unchanged.

Figure 3.12 shows the R/T spectrum of the standard Fabry-Perot band-edge grating cavity resonant mirror for different values of h_{III-V}. The $h_{III-V} = 280\,nm$ case is the standard component that was discussed before. When decreasing the III-V waveguide width, the effective index decreases and consequently the waveguide mode's wave vector k_w will shorten at the same wavelength. This means that the waveguide is now closer to phase-matching to higher order cavity modes in the band-edge grating cavity. This is apparent in figure 3.12, where the reflectivity at the higher order mode resonances is enhanced at thinner h_{III-V}.

On the other hand, when the thickness increases, the effective index increases and the waveguide's wave vector k_w grows longer than the fundamental mode's wave vector k_c. The waveguide is no longer phase-matched to any of the cavity modes and the interaction between the grating and the waveguide fades away.

According to this analysis the resonant mirror is extremely sensitive to height variations. Fortunately, the height of a III-V waveguide is very precisely determined using epitaxial growth. So being sensitive to this parameter is not as bad as it seems at first, because it can be fabricated on target.

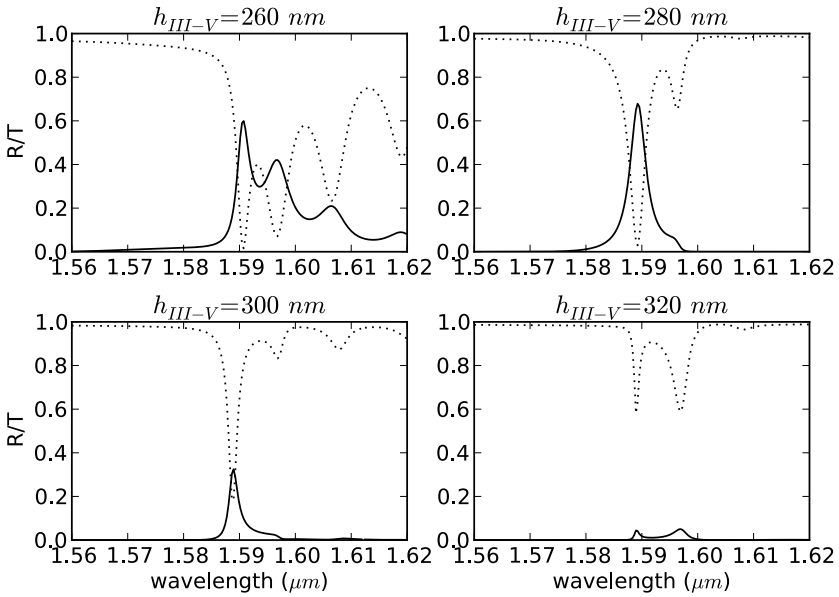

Figure 3.12: Influence of the thickness of the III-V layer h_{III-V} on the R/T spectrum of the standard Fabry-Perot band-edge grating cavity resonant mirror. The thickness of the n-InP and active InGaAsP layer remains unchanged, only h_p is altered.

3.3.6 Influence of the number of periods in the silicon grating N_g

Finally the number of periods in the silicon grating also greatly influences the R/T spectrum of a resonant mirror:

- **Intrinsic Q-factor**: By elongating the silicon cavity the intrinsic Q-factor increases
- **Resonance wavelength**: A longer band-edge cavity will shift the resonance wavelength of the fundamental cavity mode closer to the grating's band-gap
- **Coupling**: In a longer grating the interaction length between the cavity and the waveguide increases, so the overall Q_κ will decrease when the phase matching condition is satisfied. On the other hand, $FT(|\Theta(z)|^2)$ will become narrower and the sensitivity to for example waveguide thickness will increase.

Figure 3.13 shows the R/T spectrum of the standard Fabri-Perot band-edge grating cavity mirror for different numbers of periods in the silicon grating N_g. In

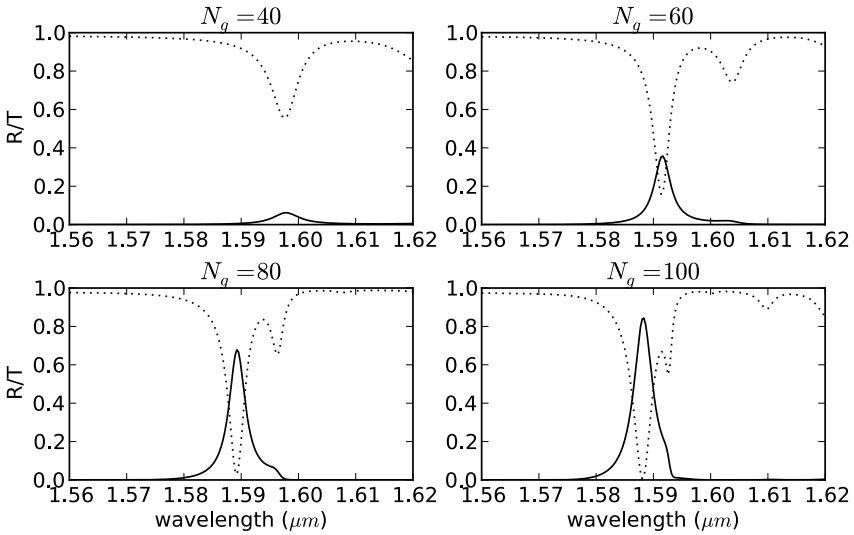

Figure 3.13: Influence of the number of periods in the silicon band-edge grating on the R/T spectrum of the standard Fabry-Perot band-edge grating cavity resonant mirror.

the case of $N_g = 40$ periods, the mirror reflectivity is less than 10%. Increasing the length of the grating quickly enhances the reflectivity to 36% ($N_g = 60$), 68% ($N_g = 80$) and finally 85% for $N_g = 100$ periods.

3.3.7 Fabry-perot band edge grating cavity mirrors: conclusions

The easy to design Fabry-Perot band-edge grating cavities are valid candidates for resonant mirror structures. They can provide high reflectivity ($> 90\%$) over a relatively short length ($23\mu m$). The elongated mode-length results in a narrow $|FT(\Theta(z)|^2$ so this structure is very sensitive to the phase matching condition. For example, changes in waveguide thickness as small as $20\,nm$ can adversely influence the R/T spectrum.

3.4 Grating defect cavity resonant mirrors

The second type of silicon cavity that was introduced in chapter 2 was the grating defect cavity. This is a silicon grating waveguide with a quarter-wave phase-shift section (the *defect*) in the center. In this section the properties of a resonant mirror using such a cavity are investigated following the same steps as used in the previ-

ous section on Fabry-Perot band-edge grating cavity resonant mirrors.

Figure 3.14 shows the schematic layout of the investigated mirror with all involved parameters that define the structure. The most important difference with the band-edge grating mirror is the quarter wave phase section of length Λ_d in the center of the grating. For a cavity mode in the center of the band gap, Λ_d must equal the grating period Λ.

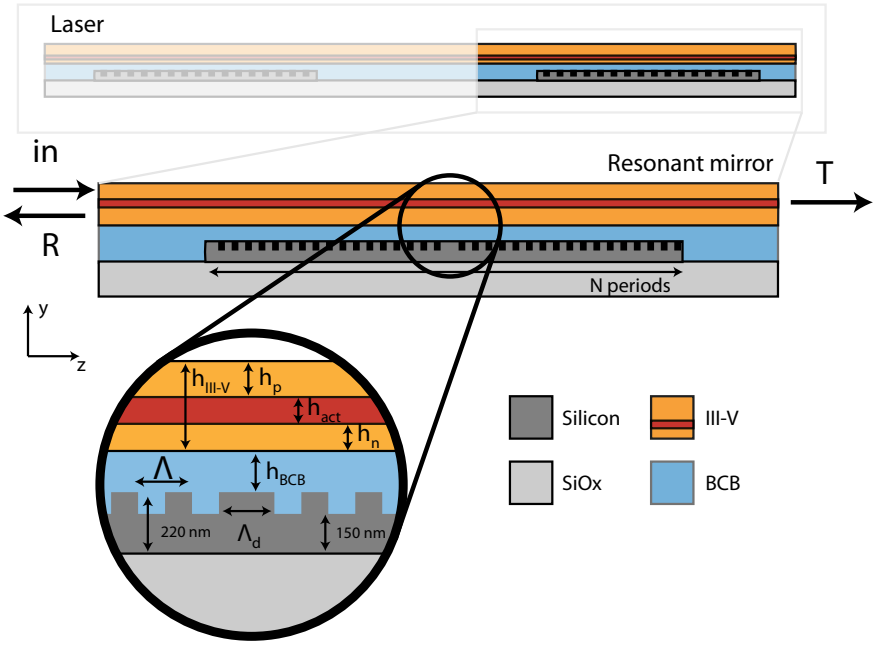

Figure 3.14: Schematic representation of the defect grating cavity resonant mirror with all involved parameters.

3.4.1 k-vector analysis of the silicon defect grating cavity

Consider a 60 period silicon cavity with a 290 nm period pitch as shown in figure 2.20. The top panel in figure 3.15 shows the longitudinal variation of the electric field $\Theta(z)$ at the cavity's center bandgap resonance wavelength $\lambda_r = 1546\,nm$. As discussed in the previous chapter, the electric field is much more concentrated around the center of the cavity as compared to the band-edge grating's more spread-out mode profile. In fact, the field decays exponentially with growing distance from the defect.

This more concentrated field profile naturally translates into a wider Fourier image $|FT(\Theta(z)|^2$ as shown in the bottom panel of figure 3.15. The curve is centred around half the grating's k-vector $k_g/2$, so considering the resonance wavelength, the waveguide's effective index n_{eff} should be:

$$n_{eff} = \frac{k_c \lambda_R}{2\pi} = \frac{10.833\mu m^{-1}\, 1.546\mu m}{2\pi} = 2.665 \tag{3.56}$$

The FWHM of $\Theta(z)$'s Fourier image squared, Δk_{FWHM} is now $0.5742/\mu m$, yielding a Δn:

$$\Delta n = \frac{\Delta k}{k_c} n_{eff} = 0.141 \tag{3.57}$$

This is almost double the band-edge grating cavity's effective index tolerance. Contrary to band-edge gratings, the Fourier image's width is almost independent of the grating length because the cavity mode remains concentrated around the defect.

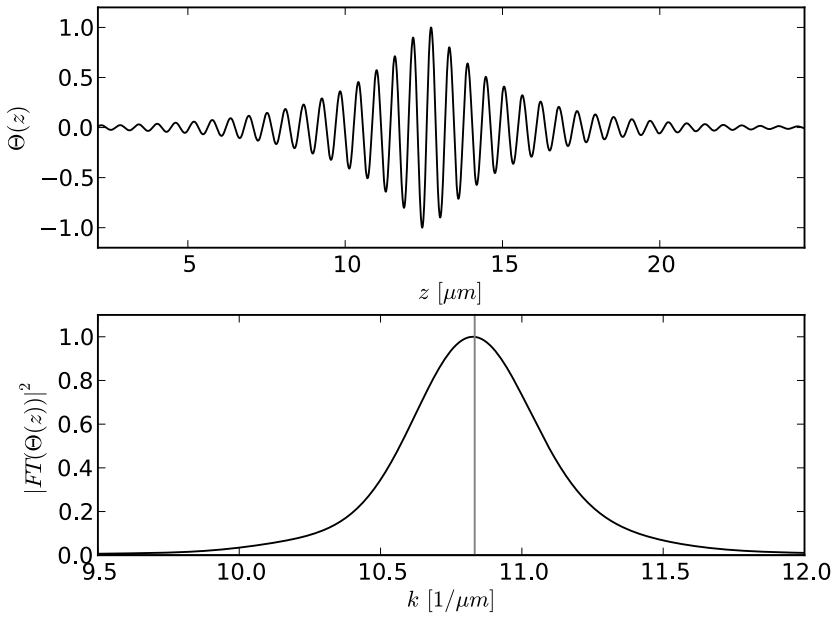

Figure 3.15: Top panel: longitudinal electric field profile $\Theta(z)$ for a 60 period silicon grating at the resonance wavelength $\lambda_R = 1.546\,nm$. Bottom panel: Fourier image squared of $\Theta(z)$.

3.4.2 III-V waveguide design

Figure 3.15 shows the same effective index map of the III-V waveguide as shown in figure 3.16 but with the effective index condition for the defect grating cavity overlaid on top. Using this map, the III-V waveguide thickness can be designed. Any combination on the n_{eff} line should result in a phase-matched waveguide-cavity combination. Unless explicitly mentioned otherwise, the remainder of this section will assume $h_{III-V} = 260\,nm$ and consequently an InGaAsP layer of $38\,nm$ thick.

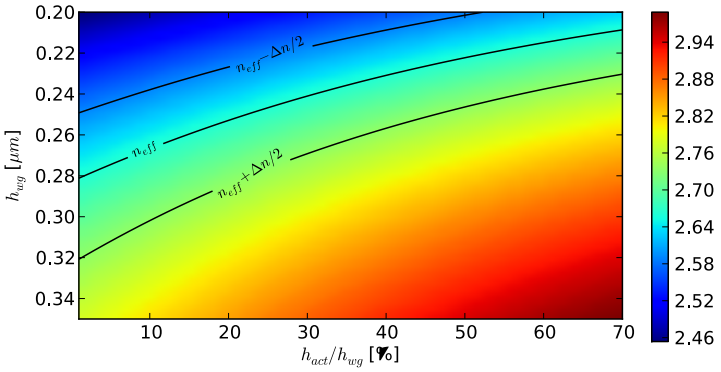

Figure 3.16: Schematic representation of the defect grating cavity resonant mirror with all involved parameters.

3.4.3 Defect grating cavity resonant mirror: the standard component

Analogously to the treatment of Fabry-Perot band-edge grating cavities, table 3.2 lists the default values for the study of the defect grating cavity resonant mirror. In summary: the mirror consists of a 60 period silicon grating (pitch: $290\,nm$) with a $290\,nm$ quarter wave defect in the center (so 30 periods - defect - 30 periods). The III-V waveguide geometry is chosen according the the phase-matching criterion outlined in the previous paragraph with $h_{III-V} = 260\,nm$. All calculations are performed using the 1D mode-solver and 2D eigenmode mode-expansion tool CAMFR [7]. The spatial dimensionality of the problem is reduced from 3 to 2 using the effective index method. Again, TE polarised light is assumed.

Symbol	Value	Unit	Description
w_{si}	1.6	μm	width of silicon waveguide grating
n_{si}	3.47		bulk refractive index of silicon
Λ	290	nm	grating period
Λ_d	290	nm	grating defect length
N_g	80		number of periods in grating
h_{BCB}	350	nm	BCB thickness above waveguide
n_{BCB}	1.55		bulk refractive index BCB
h_{III-V}	280	nm	height of III-V waveguide
h_n	112	nm	height of bottom InP cladding layer
h_{act}	56	nm	height of InGaAsP active layer
h_p	112	nm	height of top InP layer
w_{III-V}	1.6	μm	width of III-V waveguide
n_{InP}	3.17		bulk refractive index of InP at $1550\,nm$
n_{act}	3.42		bulk refractive index of InGaAsP (Q=1.55) at $1550\,nm$

Table 3.2: Listing of all parameters in the resonant mirror structure based on a defect grating cavity with default values.

3.4.3.1 R/T spectrum of the standard defect grating cavity resonant mirror

Figure 3.17 shows the R/T spectrum of the defect grating cavity with default parameters as shown in table 3.2. The reflection peak is centred at the silicon cavity's intrinsic resonance wavelength $\lambda_R = 1546\,nm$ where it provides 82% reflectivity. The peak measures $3.1\,nm$ wide at half its maximum reflectivity value. The transmissivity goes to below 1% at the resonance wavelength. As expected, there is no sign of any other resonances within this spectral window. Away from the reflection peak the transmissivity of the grating does not reach to 100%. In other words, even off-resonance there is some interaction between the silicon grating and III-V waveguide. This will be discussed in more detail in the next paragraph.

3.4.3.2 2D field profiles of the standard defect grating cavity resonant mirror

To find more insight in the different features in the R/T curve, figure 3.18 depicts the time-averaged 2D spatial electric field distribution of the defect grating resonant mirror with default parameters for two different wavelengths: on-resonance ($\lambda = \lambda_R = 1546\,nm$) and off-resonance ($\lambda = 1530\,nm$).

- **1530 nm**: At this wavelength 0.8% of the incoming light is reflected and 90.2% is transmitted through the III-V waveguide. The remaining 9% is apparently lost. According to the top panel of figure 3.18, this is mainly at the grating's facets. The grating is not resonant at this wavelength, so energy cannot build up inside. But obviously light can still couple to the

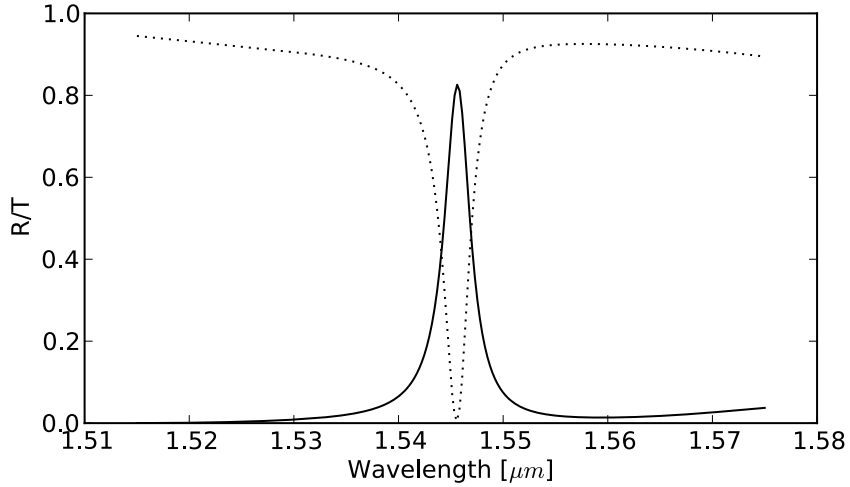

Figure 3.17: R/T spectrum of a defect grating cavity resonant mirror with default parameters as shown in table 3.2

silicon grating and a fraction of this coupled light is radiated at the grating's facets.

- **1546 nm**: At the resonance wavelength 82.6% of the incident light in the III-V waveguide's fundamental mode is reflected back into that same eigenmode. Only 0.5% is transmitted. The remaining 17% is mainly radiated at the back facet of the silicon cavity. Since the silicon cavity is symmetric along the z-axis, It might strike as peculiar that the light radiating from the silicon cavity is not symmetric (more from back facet, less from front facet). The reason for this should be sought in the asymmetric injection of the grating. More particularly, the light that couples back into the backward propagating III-V waveguide mode near the silicon cavity's defect still has to travel all the way to the front of the mirror ($z = 1.4\mu m$ in figure 3.18). During this time, a small amount of light can couple from the III-V waveguide back into the silicon cavity, destructively interfering with the backward propagating mode in the cavity and reducing the energy that radiates from the front facet.

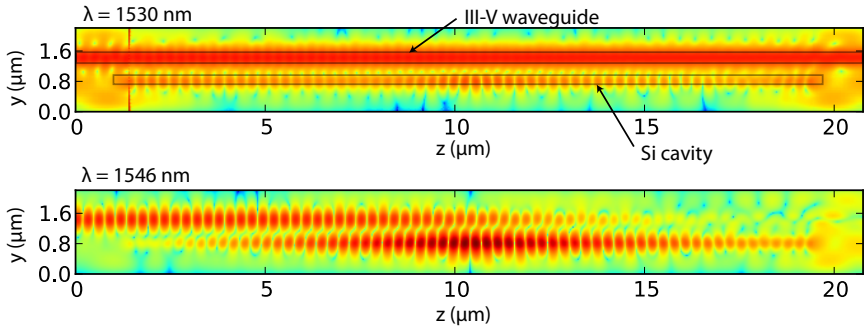

Figure 3.18: 2D time-averaged electric field amplitude squared on-resonance ($\lambda = 1.546\,nm$) and off-resonance ($\lambda = 1.530\,nm$)

3.4.3.3 1D field profile of the standard defect grating cavity resonant mirror at resonance

To get an ever better idea of the field amplitude in the III-V waveguide and silicon cavity, figure 3.19 shows the electric field squared in two 1D cross-sections through the 2D representation of the mirror: through the silicon cavity ($y = 0.81\mu m$) and through the III-V waveguide ($y = 1.4\mu m$). The graph clearly shows the longitudinal mode profile of the defect mode discussed in section 2.3.2. The field enhancement inside the silicon cavity is significant. The electric field reaches values that are up to 6 ($\approx \sqrt{40}$) times the amplitude of the input field. Although the grating starts at $z = 1.4\mu m$, the amplitude of the optical field in the III-V waveguide remains almost constant until it reaches close to the longitudinal position of the defect, where the amplitude rapidly drops. This is the same effect that was observed for band-edge grating cavities where the longitudinal rate of change of field amplitude in the III-V waveguide is proportional to the field amplitude in the silicon cavity.

3.4.4 Influence of the BCB thickness h_{BCB}

The influence of the thickness of the BCB layer h_{BCB} is illustrated in figure 3.20. The wavelength scales differ from panel to panel to ensure all interesting features are presented clearly on the graph. Similarly to the band-edge case, the defect grating resonant mirror's peak mirror loss ($= 1 - R$) increases exponentially ($R^2 = 0.995$): $R = 91.5\%$ for $300\,nm$, $R = 82\%$ for $350\,nm$, $R = 61.5\%$ for $400\,nm$ and $R = 32.5\%$ for $450\,nm$. As discussed before, this exponential decay is due to the decreasing overlap between the exponentially decaying lateral mode tails of the waveguide and cavity modes. The peak's bandwidth follows a

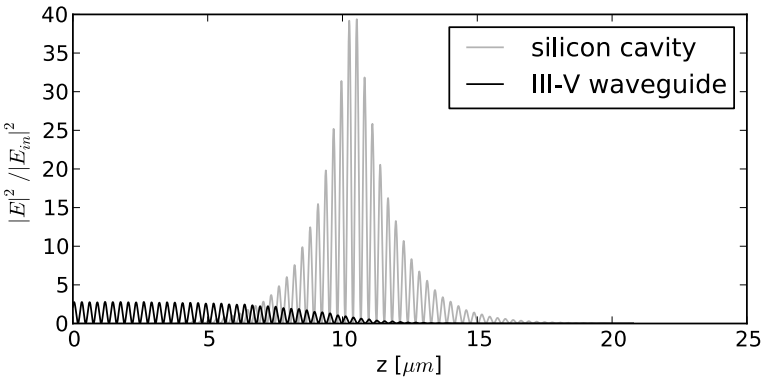

Figure 3.19: 1D cross-sections through the silicon cavity and III-V waveguide of the time-averaged electric field squared of the structure shown in figure 3.18 at resonance

similar trend reducing from $8\,nm$ for a $300\,nm$ thick BCB layer to $0.7\,nm$ in the $h_{BCB} = 45\,nm$ case.

The R/T panel for the $300\,nm$ thick BCB layer reveals an interesting feature: there appears a second reflection maximum around $1580\,nm$. Figure 3.21 shows the time-averaged 2D spatial electric field distribution squared for the standard resonant mirror with $h_{BCB} = 300\,nm$ at the second reflectivity maxima's wavelength $1580\,nm$. This field plot shows that the closer proximity of the III-V waveguide now excites the twin band-edge resonance in the defect grating. The influence of this peak is rather limited, but it is interesting to see

3.4.5 Influence of the III-V waveguide height h_{III-V}

In general, the influence of the III-V height on the defect grating resonant mirror's R/T spectrum is similar to the band-edge grating mirror's case: the effective index (and consequently phase-matching) changes and the III-V waveguide's modal profile, hence its lateral overlap with the silicon cavity mode, is altered.

Figure 3.22 shows the R/T spectrum of the standard defect grating cavity with different values for h_{III-V}. Similar to the study of the III-V waveguide height in the band-edge grating cavity resonant mirrors, the bottom InP layer and the active layer are kept constant and only the top InP layer's height varies. This way the interface between the silicon cavity and III-V waveguide remains unchanged throughout the different simulations.

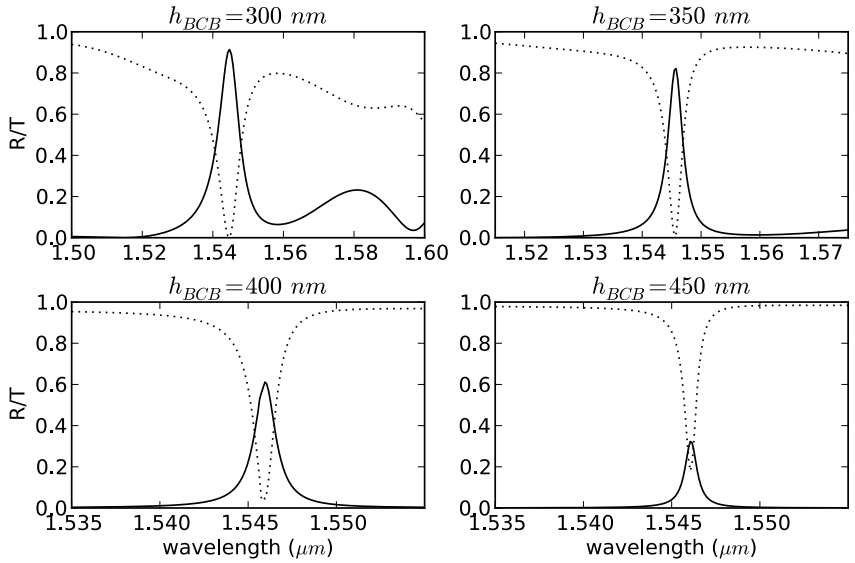

Figure 3.20: Influence of the BCB thickness h_{BCB} on the R/T spectrum of the standard defect grating cavity resonant mirror. Remark: the different graphs are plotted on different wavelength ranges to make sure all features of the R/T spectrum are visible

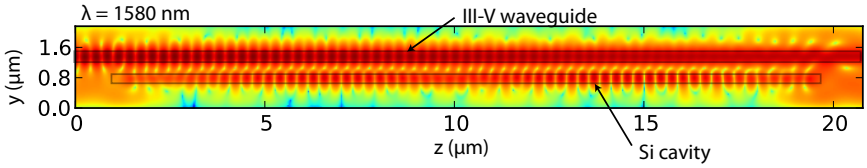

Figure 3.21: Time-averaged electric field squared distribution for a standard defect grating cavity resonant mirror with a $300\,nm$ thick BCB layer at the second reflection maximum wavelength $\lambda = 1580\,nm$.

When h_{III-V} is reduced from $260\,nm$ to $240\,nm$, the maximum reflectivity increases from 82.5% to 85%. The phase-matching condition is no longer completely fulfilled, but because $|FT(\Theta(z))|^2$ is relatively wide, the coupling penalty is modest. Moreover, because the waveguide mode is squeezed out of the III-V waveguide towards the silicon cavity, the overall coupling coefficient is increased hence the maximum mirror reflectivity increases.

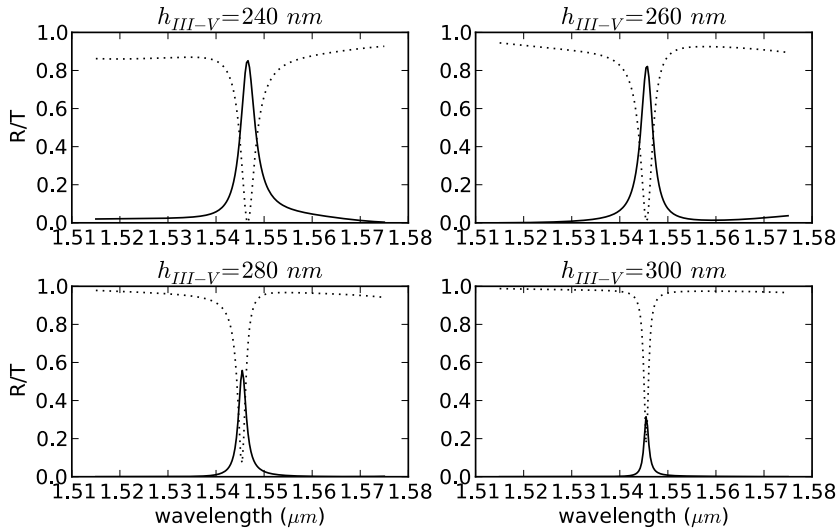

Figure 3.22: Influence of the total thickness of the III-V waveguide on the R/T spectrum of the standard defect grating cavity resonant mirror. The variation in total height is translated into a variation of the top InP layer h_p.

Increasing the III-V waveguide thickness has an adverse effect in two ways: the phase-matching condition is no longer fulfilled and the optical mode is pulled inside the III-V waveguide, decreasing the overlap with the silicon cavity mode. Consequently the maximum reflectivity reduces to 56% for $h_{III-V} = 280\,nm$ and further to 32% when $h_{III-V} = 300\,nm$. Because the Fourier image of $\Theta(z)$ of a defect grating cavity is wider than its band-edge grating counterpart, the decay in reflectivity is less spectacular.

3.4.6 Influence of the number of periods in the silicon grating N_g

Finally, figure 3.23 shows how the total number of periods in the grating affect the R/T spectrum of the resonant mirror. In case of a short grating, the intrinsic Q-factor is too low to provide significant reflectivity. It is interesting though that the transmissivity drops by a large amount, even for such a short grating. It is for this reason that resonant mirrors are also utilised in the context of optical filters and modulators [8].

Increasing the number of periods initially makes the intrinsic Q-factor grow exponentially, as shown in figure 2.25. A 60 period grating reflects 82% of the in-

coming light and an 80 period grating will even reflect 92% of the power incident on the resonant mirror structure. However, as can be read from the same figure 2.25, the cavity's intrinsic Q-factor saturates for longer gratings. Also, because the amplitude of a defect grating cavity mode decays exponentially as a function of the longitudinal z component, the Fourier image of $\Theta(z)$ of the 80 and 100 period gratings is very similar. Consequently, the maximum reflectivity and reflection peak bandwidth are virtually identical for an 80 period and 100 period grating.

The only noticeable difference between these two R/T spectra is how the reflection peak associated with the twin-band-edge mode in the defect grating emerges. This was to be expected, because increasing the grating length will increase both the Q-factor and the interaction length of this mode. In other words, it is more advantageous to utilise the shorter 80 period grating, since they yield identical peak reflectivity and bandwidth but the shorter grating supports less unwanted cavity modes.

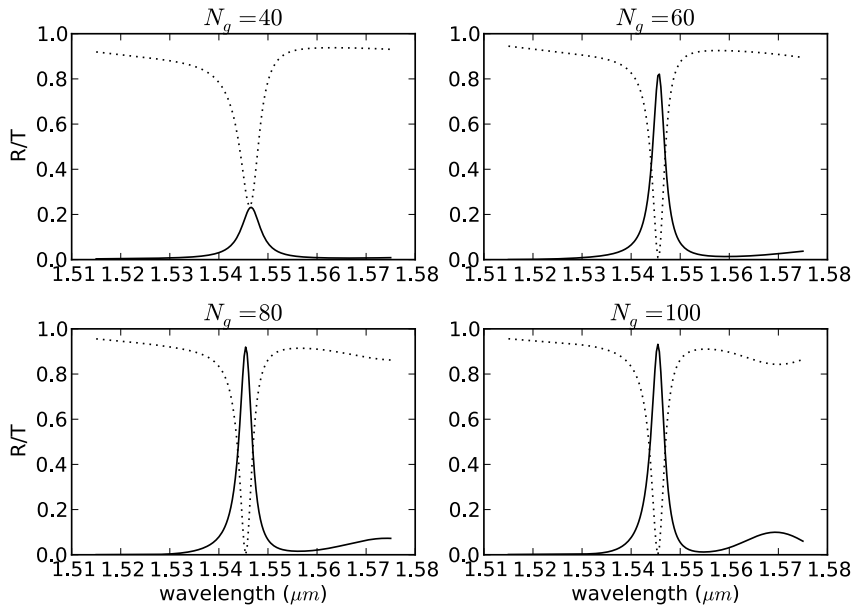

Figure 3.23: Influence of the total number of periods in the silicon grating cavity N_g on the R/T spectrum of the standard defect grating cavity resonant mirror. The defect is always positioned in the center of the grating.

3.5 Hybrid band-edge defect grating cavity resonant mirrors

The last type of silicon cavity that was discussed in the previous chapter is the hybrid band-edge defect grating cavity. This silicon grating cavity consists of 3 sections: two outer sections of N_R periods with Λ_R grating pitch and one inner section with N_{BE} periods of pitch Λ_{BE}. This setup is illustrated in figure 3.24. Given a certain target resonance wavelength λ_R, the grating periods Λ_R and Λ_{BE} are chosen such that λ_R lies within the band-gap of Λ_R and near the band-edge of Λ_{BE}. The R/T spectra of this mirror were very similar to the defect grating cavity's R/T spectrum except for the fact that the length-dependent intrinsic Q-factor saturation occurred at longer cavities and consequently the maximum attainable Q-factor is one order of magnitude larger. This study will be analogous to the previous two sections.

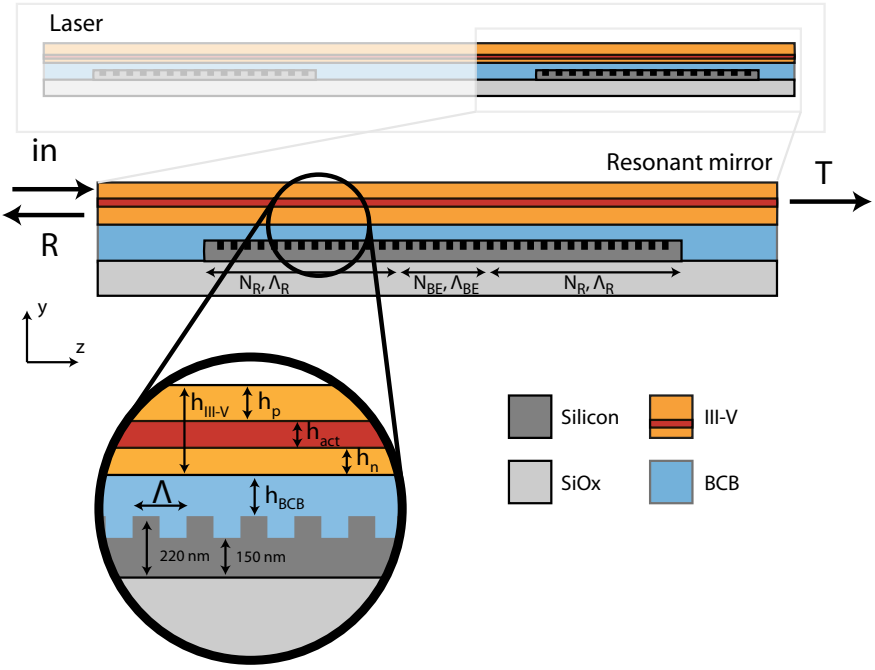

Figure 3.24: Schematic representation of the resonant mirror with silicon hybrid band-edge defect grating cavity. The figure also depicts all the parameters listed in table 3.3.

3.5.1 k-vector analysis of the silicon hybrid band-edge defect grating cavity

The top panel of figure 3.25 shows the longitudinal electric field profile $\Theta(z)$ for a hybrid band-edge defect grating cavity with $N_R = 25$ periods on both ends with $\Lambda_R = 290\,nm$ and center grating with $N_{BE} = 10$ periods and $\Lambda_{BE} = 270\,nm$. This is a so-called 25-10-25 configuration. The total number of periods in the grating equals 60, so this allows for a good comparison with the standard defect grating cavity discussed in the previous section, that also counted 60 periods. This longitudinal field profile is taken at the cavity's resonance wavelength $\lambda_R = 1548\,nm$.

Because the grating contains 2 different grating periods, the resonant mode profile also contains 2 different periodicities:

- Outer grating: In the outer grating, the resonance frequency of the cavity mode lies within the grating's band-gap. Consequently, the mode has the periodicity associated with $k_{g,290}/2$
- Inner grating: the mode resides in the long-wavelength band-edge of the grating, meaning its local k-vector must be shorter than $k_{g,270}/2$.

The resulting spatial Fourier image squared of $\Theta(z)$ is shown in the bottom panel of figure 3.25. The figure also shows the grating k-vectors of the outer ($k_{g,290}$) and inner ($k_{g,270}$) grating sections. The top of the Fourier image is close to $k_{g,290}/2$ but is slightly pulled towards $k_{g,270}/2$ due to the band-edge portion of the mode. The effective index necessary to meet the phase-matching criterion now reads:

$$n_{eff} = \frac{k_c \lambda_r}{2\pi} = \frac{10.895\mu m^{-1} 1.5485\mu m}{2\pi} = 2.685 \tag{3.58}$$

The peak width is very similar to the point defect case and is found to be $\Delta k_{FWHM} = 0.5762\mu m^{-1}$, so the Δn FWHM region is found to be:

$$\Delta n = \frac{\Delta k}{k_c} n_{eff} = 0.142 \tag{3.59}$$

So very similar to the defect grating case discussed in the previous section.

3.5.2 III-V waveguide design

Using the information drawn from the Fourier analysis in the previous paragraph, the ideal phase-matched III-V stack can be designed using the effective index map shown in figure 3.26. Adhering to the $260\,nm$ thick III-V layer proposed in the previous section, the InGaAsP active layer should be $54\,nm$ thick to meet the phase-matching criterion.

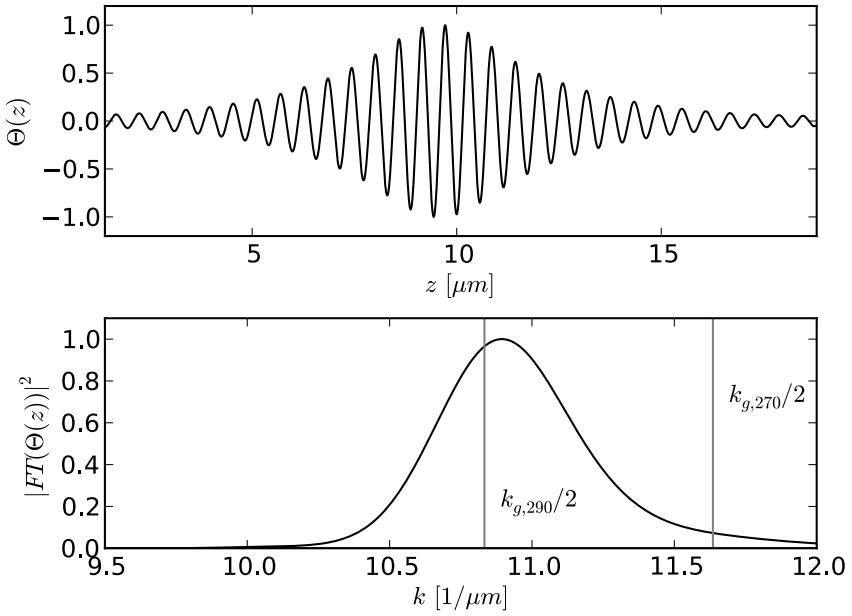

Figure 3.25: Top panel: longitudinal electric field profile $\Theta(z)$ for a 25-10-25 hybrid band-edge defect grating cavity at the resonance wavelength $\lambda_R = 1.548\,nm$. Bottom panel: spatial Fourier image squared of $\Theta(z)$

3.5.3 Hybrid band-edge defect grating cavity resonant mirror: the standard component

Table 3.3 lists the default values of the parameters that define the hybrid band-edge grating cavity resonant mirror as outlined in figure 3.24. The standard component consists of the 25-10-25 configuration discussed in section 3.5.1 and the associated phase-matched III-V waveguide proposed in the previous section. Similar to the analysis of the other grating cavity types, all calculations are performed using the mode-expansion tool CAMFR [7] in 2D where the third dimension (x-axis) is reduced by means of the effective index method. TE-polarized light is assumed throughout this section.

3.5.3.1 R/T spectrum of the standard hybrid band-edge defect grating cavity resonant mirror

Figure 3.27 shows the R/T spectrum of the standard hybrid band-edge defect grating cavity resonant mirror with the parameter values shown in figure 3.3. As

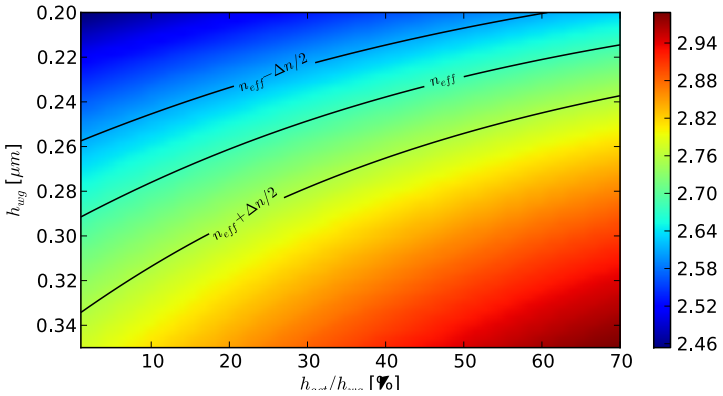

Figure 3.26: Map of the III-V waveguide's effective index as a function of the total thickness h_{III-V} and the fraction of the active layer h_{act}/h_{III-V}. The map also shows the

expected, the R/T spectrum looks very similar to the defect grating cavity resonant mirror's R/T spectrum shown in figure 3.17. The mirror now reflects 80.2% and the III-V waveguide's transmittance is around 1%. The reflection band-width (FWHM) is $2.98\,nm$.

At first sight it is surprising that the reflectivity of the hybrid band-edge defect mirror is (slightly) lower than the defect grating mirror because figure 2.31 shows that a hybrid band-edge defect grating cavity of 60 periods total length has a (slightly) higher intrinsic Q-factor than an equally long defect grating cavity. However, the more narrow lineshape hints at a reduced coupling (so increased Q_κ). The reason for this is probably that the III-V waveguide is no longer phase-matched to the grating's wave vector $k_{g,290}$, so grating-assisted coupling no longer occurs, reducing the overall coupling. Fortunately the difference between both cavity types is very small for this configuration and can be neglected.

3.5.3.2 2D field profiles of the standard hybrid band-edge defect grating cavity resonant mirror

Figure 3.28 shows the 2D time-averaged spatial electric field squared distribution for the standard hybrid band-edge defect grating cavity resonant mirror at two different wavelengths:

- **1530 nm**: This wavelength lies outside of the reflection peak. About 0.3% of the incoming light is reflected and 92.6% is transmitted. The remaining 7% is lost at the grating facets.

Symbol	Value	Unit	Description
w_{si}	1.6	μm	width of silicon waveguide grating
n_{si}	3.47		bulk refractive index of silicon
Λ_R	290	nm	grating period in outer grating
Λ_{BE}	270	nm	grating period in inner grating
N_R	25		number of periods in each outer grating
N_{BE}	10		number of periods in the inner grating
h_{BCB}	350	nm	BCB thickness above waveguide
n_{BCB}	1.55		bulk refractive index BCB
h_{III-V}	260	nm	height of III-V waveguide
h_n	112	nm	height of bottom InP cladding layer
h_{act}	54	nm	height of InGaAsP active layer
h_p	103	nm	height of top InP layer
w_{III-V}	1.6	μm	width of III-V waveguide
n_{InP}	3.17		bulk refractive index of InP at $1550\,nm$
n_{act}	3.42		bulk refractive index of InGaAsP (Q=1.55) at $1550\,nm$

Table 3.3: Listing of all parameters in the resonant mirror structure based on a hybrid band-edge defect grating cavity with default values.

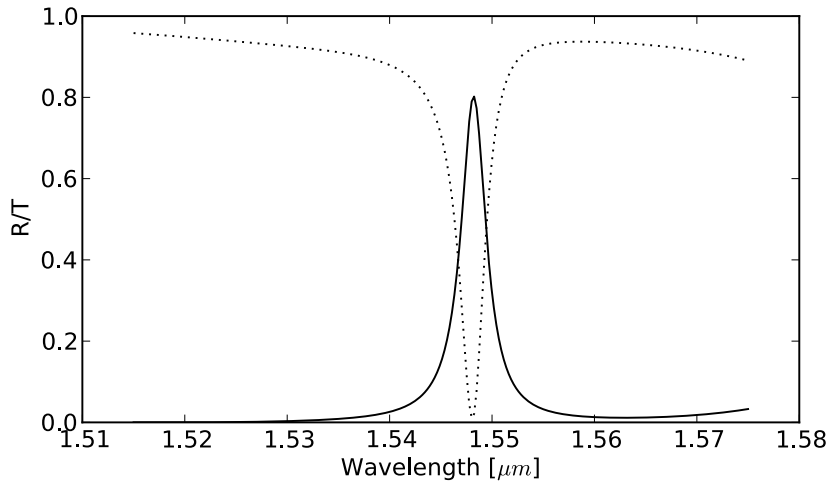

Figure 3.27: R/T spectrum of the standard hybrid band-edge defect grating cavity resonant mirror with parameters as listed in table 3.3

- **1548 nm**: At the maximum of the reflection peak 80.3% of the incoming light is reflected and 1.6% is transmitted through the III-V waveguide. The

remaining 18% is lost at the grating's facets. Due to the reduced coupling, especially in the outer gratings due to the absence of grating assisted coupling, the front facet now also leaks light, contrary to the defect grating case. However, the graph shows that the leakage from the back facet is significantly more than the leakage from the front facet.

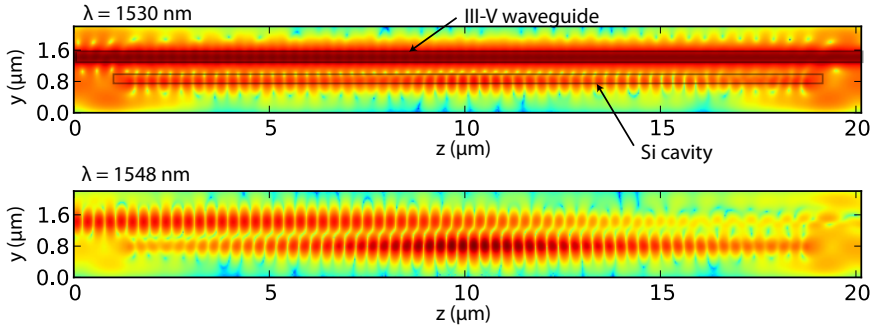

Figure 3.28: R/T spectrum of the standard hybrid band-edge defect grating cavity resonant mirror with parameters as listed in table 3.3

3.5.3.3 1D field profile of the standard hybrid band-edge grating cavity resonant mirror at the peak reflectivity

Figure 3.29 shows the 1 dimensional cross-section of the time-averaged spatial electric field distribution squared in the cavity ($y = 0.81\mu m$) and the III-V waveguide ($y = 1.4\mu m$) at the peak reflectivity wavelength $\lambda = 1548\,nm$. Because the defect is now spread out across 10 periods, the peak electric field value is slightly smaller than in the case of a defect grating. The field enhancement inside the cavity is now approximately a factor 6.3 ($= \sqrt{40}$).

3.5.4 Difference between hybrid band-edge defect grating cavity and defect grating cavity resonant mirrors

The previous section shows that resonant mirrors that use the standard defect grating cavity or the standard hybrid band-edge defect grating cavity exhibit very similar properties regarding their R/T spectrum: the peak wavelength are very close ($1546\,nm$ vs $1548\,nm$) while the maximum reflectivity (82% vs 80%) and especially the bandwidth (3.1 vs $2.98\,nm$) are nearly identical.

It turns out that if the analysis as presented in the previous section is performed on the standard hybrid band-edge defect grating cavity, the dependence of the R/T

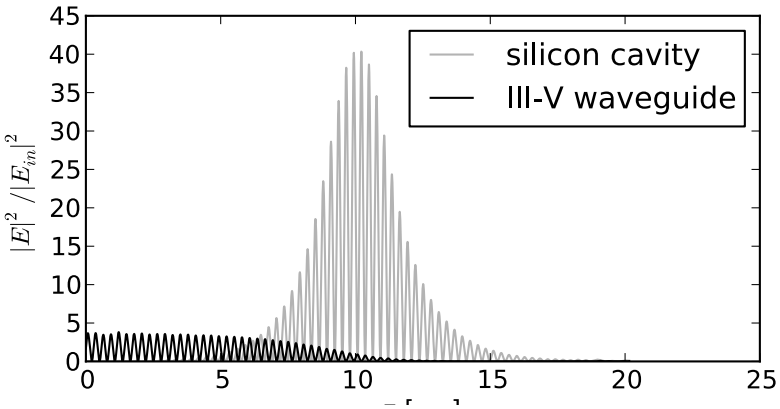

Figure 3.29: R/T spectrum of the standard hybrid band-edge defect grating cavity resonant mirror with parameters as listed in table 3.3

spectrum on the BCB-thickness, the number of periods in the grating or the height of the III-V waveguide is very similar to that of the standard defect grating cavity resonant mirror. Instead of repeating such an analysis, this section will focus on the differences between both cavity types.

The most important advantage of the more complicated hybrid band-edge grating cavity over an ordinary defect grating cavity is its ability to reach much higher intrinsic Q-factors. This property is well illustrated by figure 2.31. This figure shows that short gratings of both types have similar intrinsic Q-factors, but in case of longer gratings the difference can be more than an order of magnitude. For example, a 110 periods long defect grating cavity has an intrinsic Q-factor close to 17000 where an equally long hybrid band-edge defect grating cavity has an intrinsic quality factor in the vicinity of 160000.

Equation 3.31 indicates that an order of magnitude increase of intrinsic Q-factor allows for an order of magnitude worse coupling and still yields the same maximum reflectivity R_{max}. From a practical point of view, this is a very powerful fact. The next two chapters will cover the implementation of resonant mirror lasers in two different varieties:

- **optically pumped**: The III-V waveguide is illuminated by an external pump laser which allows for a wealth of design freedom. The III-V waveguide can be as thick or as thin as it needs to be, the only restriction is the width: that should be above $1.6\mu m$ to allow easy patterning using contact lithography.

In other words, the relatively thin, phase-matched films that were proposed in this chapter are a realistic choice

- **electrically pumped**: Carriers are injected into the III-V waveguide by means of metallic electrical contacts. Because metals heavily absorb light of the wavelength ranges considered in this work, the III-V waveguide is subject to stringent design limitations. This usually requires thicker III-V waveguides, so phase matching becomes impossible, because this work is committed to the $220\,nm$ thick silicon platform. However, if the silicon cavity's intrinsic Q-factor is high enough it should be possible to compensate for the not-ideal coupling.

With this in mind, it should be interesting to see how both cavity types perform if the III-V waveguide thickness is increased. Because this inevitably leads to a violation of the phase-matching condition, the cavity's intrinsic Q-factor should be as high as possible. For this reason the default value of 60 periods is increased to 110 periods, where the intrinsic Q-factor reaches its saturation value for both cavity types. Except for the grating length and the III-V waveguide thickness, both mirrors are evaluated using their default parameters.

Figure 3.30 shows how the 110 periods long default defect grating cavity resonant mirror's R/T spectrum evolves as the III-V waveguide grows thicker. The longer cavity can accommodate some phase-mismatch, for $h_{III-V} = 300\,nm$ the mirror reflects an acceptable 75% of the incoming light. Unfortunately the maximum reflectivity quickly drops with increasing III-V waveguide thickness to 25.5% in the case of a $360\,nm$ thick waveguide.

The III-V waveguide height dependence of the 110 periods long standard hybrid band-edge defect grating cavity resonant mirror is shown in figure 3.31. Although both cavity types performed in a very similar fashion in the phase-matched case, this graph shows that the hybrid band-edge grating cavity is much more robust in terms of phase mismatch (or reduced coupling in general). The maximum reflectivity does decrease but remains at an acceptable level throughout, still reaching 87.9% reflectivity in the case of a $360\,nm$ thick active waveguide. The results of figures 3.30 and 3.31 are summarised in figure 3.32.

Figure 3.33 show the time-averaged electric field square distributions for the $h_{III-V} = 360\,nm$ case for both cavities. The figure clearly shows that in both cases the cavity and III-V waveguide are severely phase-mismatched. However, in the hybrid band-edge defect grating case, the intrinsic Q-factor is high enough to compensate for this mismatch. This analysis shows that hybrid band-edge defect grating cavities are a potential candidate for use in electrically pumped resonant mirror lasers based on a $220\,nm$ thick silicon layer.

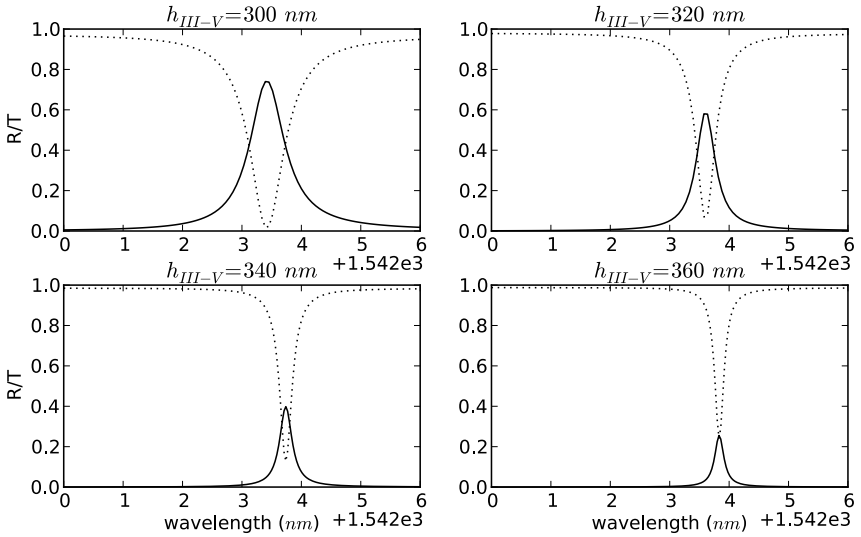

Figure 3.30: R/T spectrum of the standard defect grating cavity resonant mirror with 110 periods as a function of the III-V waveguide thickness

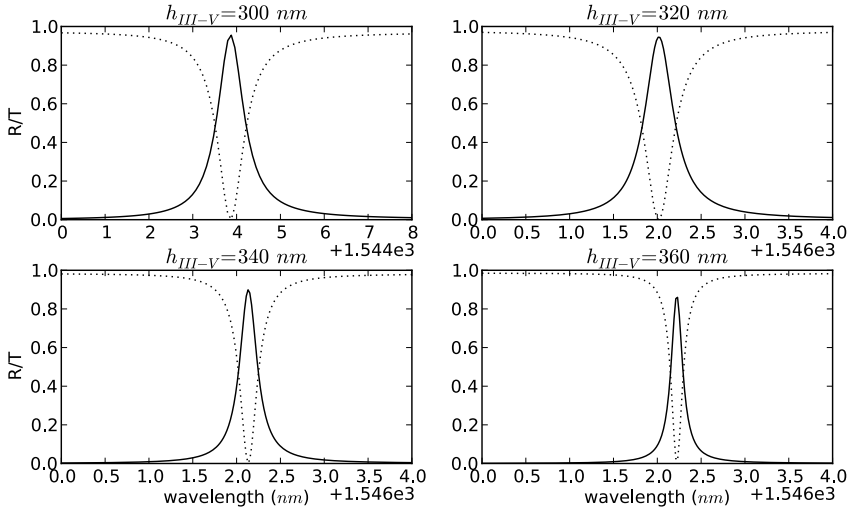

Figure 3.31: R/T spectrum of the standard hybrid band-edge defect grating cavity resonant mirror with 110 periods as a function of the III-V waveguide thickness. remark: x-axis scale may very among different graphs

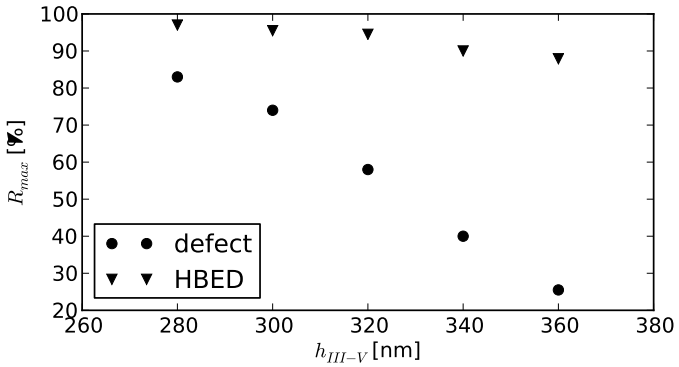

Figure 3.32: Summary of the dependence of the maximum reflectivity R_{max} on the height of the III-V waveguide for the110 period long standard defect grating and hybrid band-edge defect (HBED) grating resonant mirrors.

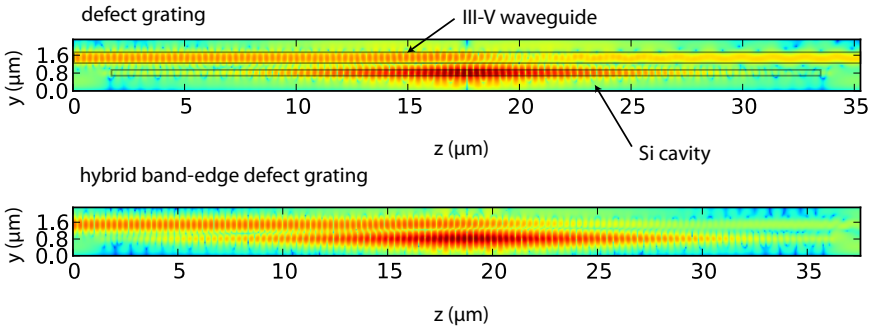

Figure 3.33: 2D time-averaged spatial electric field squared distribution at resonance for the two cavity types.

3.6 Conclusions

This chapter discussed the use of passive silicon cavities coupled to an active III-V waveguide to serve as a short, wavelength selective reflector. The analysis started with a brief description of scattering theory based on the Lippman-Schwinger equations and how it could be applied to this problem. This theoretical framework provided profound understanding of the key design aspects of resonant mirrors:

- The maximum reflectivity and reflection bandwidth are determined by 2 macroscopic quantities: the silicon cavity's intrinsic quality factor and the coupling between the III-V waveguide and the silicon cavity

- Even if the coupling between the III-V waveguide and the silicon cavity is far below 100%, the mirror can still provide high reflectivity if only the cavity's intrinsic Q-factor is sufficiently high.
- The coupling is determined by two factors:
  - phase-matching: the III-V waveguide and silicon cavity should be (close to) phase matched. This condition is determined by evaluating the spatial Fourier transform of the silicon cavity mode at the III-V waveguide's wave vector. The presence of the grating corrugation results in an additional grating-assisted coupling term.
  - lateral overlap: the III-V waveguide and silicon cavity should be sufficiently close to ensure good coupling.

With these key aspects in mind, the three different silicon cavity types discussed in the previous chapter were analysed in detail for use in resonant mirrors. First the III-V waveguide was designed for optimal phase-matching. Next, the reflection and transmission spectra were analysed and the spatial electric field distribution at key wavelengths was investigated. Also, the dependence of the R/T spectrum on the BCB thickness, the number of grating periods and the thickness of the III-V waveguide was investigated. After this thorough analysis the following conclusions can be drawn:

- If the technology allows for arbitrary thin III-V waveguides, the defect grating cavity resonant mirror can provide high, wavelength selective reflectivity over a very short distance. A 60 period grating ($17.4\mu m$) can provide $> 90\%$ reflectivity for a $260\,nm$ III-V waveguide. This especially applies to optically pumped devices
- In the case of electrically pumped devices, the III-V waveguide cannot be arbitrarily thin and phase matching becomes an issue. The high intrinsic q-factor of hybrid band-edge defect grating cavity resonant mirrors relaxes the phase-matching condition and allows for high reflectivity, even for thicker (phase-mismatched) III-V waveguides.

The aim of this chapter was primarily to provide insight into the different design aspects of resonant mirrors. Because all simulations were performed in 2D, they did not capture some of the physical details that might have a significant impact on the mirror performance. However, the chapter did provide a range of techniques that can be used to successfully design resonant mirrors. The next two chapters will discuss the practical implementation of resonant mirror lasers both optically and electrically pumped.

References

[1] Thijs Spuesens, Johan Bauwelinck, Philippe Regreny, and Dries Van Thourhout. *Realization of a Compact Optical Interconnect on Silicon by Heterogeneous Integration of IIIV*. IEEE Photonics Technology Letters, 25(14):1332–1335, July 2013.

[2] Edo Waks and Jelena Vuckovic. *Coupled mode theory for photonic crystal cavity-waveguide interaction*. Optics Express, 13(13):5064, 2005.

[3] B. Lippmann and Julian Schwinger. *Variational Principles for Scattering Processes. I.* Physical Review, 79(3):469–480, August 1950.

[4] Yong Xu, Yi Li, Reginald Lee, and Amnon Yariv. *Scattering-theory analysis of waveguide-resonator coupling*. Physical Review E, 62(5):7389–7404, November 2000.

[5] *The Born approximation - wikipedia Http://en.wikipedia.org/wiki/Born_approximation*.

[6] Joachim Piprek. *Semiconductor Optoelectronic Devices*. Academic Press, 2003.

[7] *CAMFR - http://camfr.sourceforge.net*.

[8] Kapil Debnath, Karl Welna, Marcello Ferrera, Kieran Deasy, David G Lidzey, and Liam O'Faolain. *Highly efficient optical filter based on vertically coupled photonic crystal cavity and bus waveguide*. Opt. Lett., 38(2):154–156, January 2013.

4

Optically pumped resonant mirror lasers

4.1 Introduction

This chapter will elaborate on the design, fabrication and characterisation of the first optically pumped hybrid silicon resonant mirror laser. The specific aspects of the mirror design are investigated using both 2D and 3D simulations. With these mirror characteristics at our disposal, the laser properties are estimated using a rate-equation model. Next the dedicated III-V fabrication procedure is presented in detail. Finally the measurement approach is outlined and the results will be discussed.

Figure 4.1 shows the schematic representation of the proposed optically pumped resonant mirror laser. The device consists of a thin III-V waveguide with an active layer on top of 2 identical silicon grating cavities. There are no silicon structures in between the two grating cavities. Both cavities are terminated by a silicon waveguide that leads to a fiber grating coupler that can diffract the generated laser light into an optical fiber. The laser will be pumped by illuminating it from the top with a pump laser beam. Preferably the shape of this pump-beam closely resembles the shape of the III-V waveguide.

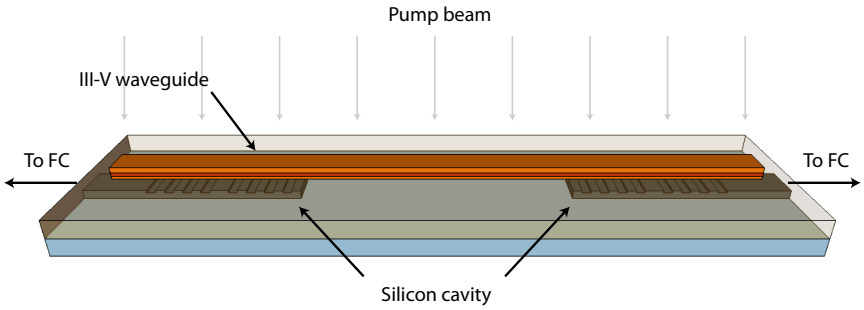

Figure 4.1: Schematic representation of the optically pumped resonant mirror laser layout

4.2 Resonant mirror design

The first step in designing a hybrid silicon resonant mirror laser is to determine the silicon cavity layout along with the appropriate III-V waveguide layer stack and dimensions. The previous chapter provided significant insight in how these two structures determine the properties of a resonant mirror. In the following sections the specific design aspects of both the cavity and the III-V waveguide for an optically pumped prototype will be discussed.

4.2.1 Silicon cavity

One of the main results of the previous chapter was that a silicon defect grating cavity can provide high reflectivity but requires a relatively thin III-V waveguide to allow for good phase-matching. An optically pumped III-V waveguide does not require metallic contacts, so there are no stringent restrictions on how thick or thin the III-V waveguide should be.

The results in chapter 3 were obtained by using 2D simulations. This was justified by the fact that this allows for much shorter simulation times and consequently allows to explore a broad parameter space. This provided thorough insight into how resonant mirrors work and what the design challenges are. However, 2D simulations do not capture all the subtle physical aspects of the optical system. For that reason, this chapter will also present some full-vectorial 3D FDTD simulations to verify the design and get a better idea of what can be expected in a real-world device.

The silicon cavity that will be used for this optically pumped prototype is a 60 period long grating with a quarter wave defect in the center. Analogously to the cavities treated in the previous chapter, the silicon layer is $220\,nm$ thick with

$70\,nm$ deep corrugations. The grating is $1.6\mu m$ wide and the grating pitch is $285\,nm$. Assuming the effective index of the similar $290\,nm$ pitch grating calculated using 2D simulations found in equation 3.56, the resonance wavelength of this cavity should be:

$$\lambda_R = 2n_{eff}\Lambda = 2 \times 2.665 \times 285\,nm = 1519.05\,nm \tag{4.1}$$

A more rigorous 3D FDTD analysis of the intrinsic cavity (without III-V overlay) yields a resonance wavelength of $1517.5\,nm$, which is virtually identical. However, such a 3D analysis yields a much lower intrinsic Q-factor of 2392 as compared to 5368 for the 2D case, which is 2.2 times higher. The reason for this significant reduction should be sought in the finite width of the grating and the accompanying effects that are not accurately modelled by the 2D simulations.

The most important consequence of this reduced intrinsic Q-factor is that the coupling between the cavity and the III-V waveguide should be increased 2.2 times to obtain the same reflectivity. Inevitably this means that the reflection bandwidth will also increase about 2.2 times. However, the simulations in chapter 3 show that there is plenty of room to increase the coupling by reducing the BCB thickness.

4.2.2 III-V waveguide

The previous chapter showed that one of the most sensitive parameters in the resonant mirror design process is the height of the III-V waveguide. To be able to tweak the III-V waveguide height after fabrication, the layer stack and dimensions depicted in figure 4.2 were used. The waveguide contains an 80 nm InGaAsP layer with composition such that its gain peak is around $1550\,nm$. This InGaAsP layer is sandwiched between two InP layers. InP has a larger band gap than this InGaAsP layer, so this will help to confine the electrical carriers to stay confined to the InGaAsP layer.

Because of the high refractive index of the InGaAsP layer and the thin $20\,nm$ bottom InP layer, the optical mode is mostly confined to the lower half of the III-V waveguide, close to the silicon cavity. This increases the overlap, hence the coupling between the silicon cavity and the III-V waveguide. On top of the $80\,nm$ top InP layer there are 4 pairs of $10\,nm$ of InGaAsP (bandgap at $1.2\mu m$) and $10\,nm$ of InP. The purpose of these layers is to be able to adjust the height of the III-V waveguide and tweak its effective index to meet the phase matching condition. Both InP and InGaAsP can be etched very selectively with respect to one-another using either an HCl based etching solution to etch InP or a H_2SO_4 based solution to etch InGaAsP. By etching away the required number of layers the desired effective index can be reached.

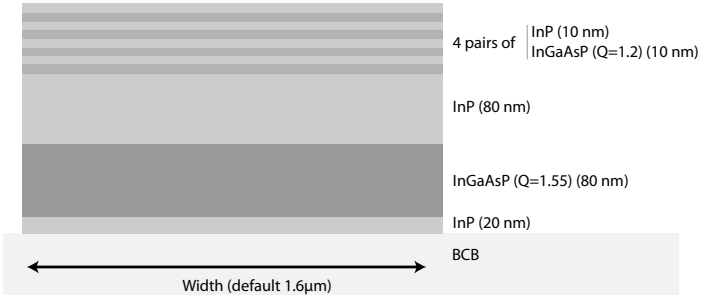

Figure 4.2: Schematic representation of the layer stack used in the optically pumped resonant mirror laser.

Figure 4.3 shows how the effective index (TE polarisation, wavelength 1550 nm) of the III-V waveguide depends on its waveguide width and the number of (InP/InGaAsP) pairs that are still on the III-V waveguide. The effective indices are calculated using an in-house developed 2D optical mode solver based on the publicly available WGModes project [1]. As expected, increasing the number of (InP/InGaAsP) pairs or widening the waveguide will increase the effective index of the mode. The graph also shows the silicon cavity's effective index n_{eff}. For optimal phase-matching, the III-V waveguide's effective index should be as close as possible to this number. In the case of 3 (InP/InGaAsP) pairs and a waveguide width of $1.5\mu m$, both graphs intersect.

The FWHM regions of the maximal reflection from the resonant mirror $n_{eff} - \Delta n$ and $n_{eff} + \Delta n$ are also drawn on the figure. Roughly speaking, these boundaries correspond to adding or removing one (InP/InGaAsP) pair from the ideal 3 pair configuration. This also shows that the coupling, at least from a phase-matching perspective, should be relatively robust. Widening the III-V waveguide will also widen its fundamental eigenmode, changing the lateral overlap with the silicon cavity mode, which also influences the waveguide-cavity coupling.

4.2.3 Resonant mirror properties

According to figure 4.3 the ideal waveguide configuration consists of 3 (InP/InGaAsP) pairs and a width of $1.5\mu m$. Because at the time of design it was believed that the smallest feature that can be defined using contact lithography is $1.6\mu m$, the remainder of this section will assume a III-V waveguide width of $1.6\mu m$. All the relevant parameters are listed in table 4.1 based on the naming of figure 3.14.

Figure 4.4 shows the reflection and transmission (R/T) spectrum of the res-

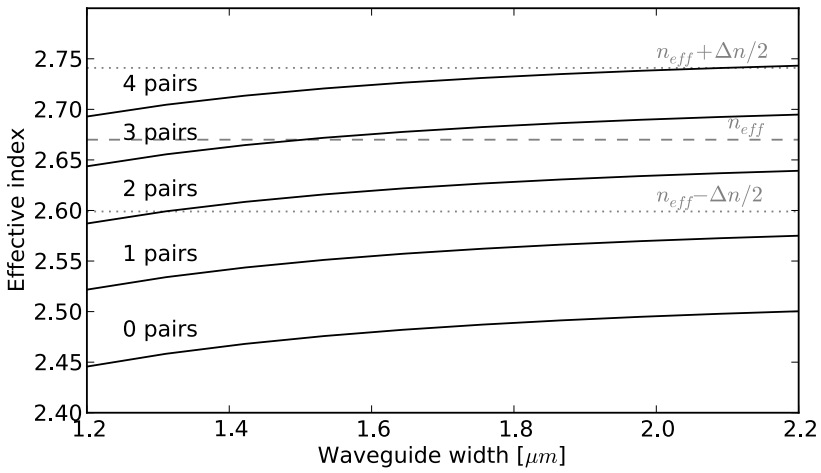

Figure 4.3: Effective index of the III-V waveguide shown in figure 4.2 as a function of the number of (InP,InGaAsP) pairs. The figure also shows the cavity's effective index n_{eff} required to meet the phase-matching condition.

onant mirror with parameters as described in table 4.1 and the III-V waveguide layout of figure 4.2. This R/T spectrum is calculated using full-vectorial 3D FDTD [2]. The reflection and transmission spectra are both so-called mode-to-mode power transfer spectra: when launching the III-V waveguide's fundamental eigenmode, R is the fraction of the incoming power that is reflected into the III-V waveguide's backward propagating fundamental eigenmode and T is the fraction of the incoming power that is transmitted to the forward propagating fundamental eigenmode at the end of the III-V waveguide.

The figure shows that the mirror reflects 84.9% of the incoming light back into the III-V waveguide and transmits virtually no light (0.3%) at its resonance frequency. The reflection peak is very close to the silicon cavity's intrinsic cavity resonance wavelength of 1517 nm.

The full width at half the reflection peak's maximum is now $7.6\,nm$, which is close to the predicted factor 2.2 increase with respect to the 2D calculated bandwidth ($3.1\,nm$) as a result of the 2.2 times lower intrinsic Q-factor in the 3D case. The figure also shows what fraction of the incident power is redirected to the silicon waveguide. At resonance 4.89% of the power is coupled into the silicon waveguide leading to the grating coupler. The bulk part of remaining 10% is lost

Symbol	Value	Unit	Description
w_{si}	1.6	μm	width of silicon waveguide grating
Λ	285	nm	grating period
Λ_d	285	nm	grating defect length
N_g	60		number of periods in grating
h_{BCB}	300	nm	BCB thickness above waveguide
$N_{InP/InGaAsP}$	3		number of (InP/InGaAsP) pairs
w_{III-V}	1.6	μm	width of III-V waveguide
n_{si}	3.47		bulk refractive index of silicon
n_{InP}	3.17		bulk refractive index of InP at $1550\,nm$
$n_{Q1.5}$	3.42		bulk refractive index of InGaAsP (Q=1.55) at $1550\,nm$
$n_{Q1.2}$	3.35		bulk refractive index of InGaAsP (Q=1.2) at $1550\,nm$
n_{BCB}	1.55		bulk refractive index BCB

Table 4.1: Listing of all parameters in the defect grating cavity resonant mirror for the optically pumped prototype. Refer to figure 3.14 for the mirror schematics and figure 4.2 for a detailed III-V waveguide layout.

at the other grating facet or scattered at the defect.

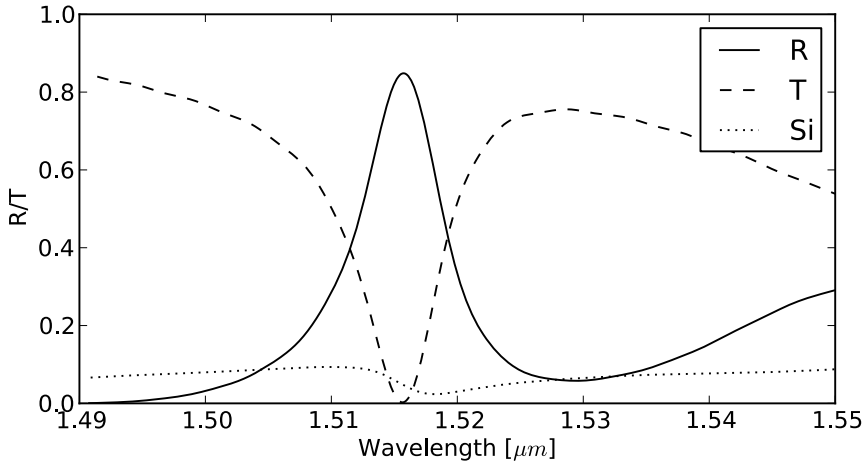

Figure 4.4: Reflection and Transmission (R/T) spectrum of the as-designed resonant mirror calculated using full-vectorial 3D FDTD simulations. The figure also shows the coupling to the silicon waveguide (dotted line).

Figure 4.5 shows the time-averaged spatial electric field distribution squared at

the reflection peak maximum extracted from the 3D FDTD simulation. This cross-section is taken at the symmetry plane running through the silicon cavity and III-V waveguide to resemble the electric field plots shown in the previous chapter. The graph clearly shows the silicon grating's resonance is excited and that the resonant mirror-effect is the predominant reflection mechanism: the amplitude in the III-V waveguide remains virtually constant until it reaches to the defect and then rapidly decreases. This is the same behaviour that was discussed in figure 3.19.

This plot does not show new information but confirms the conclusions that were drawn from the 2D analysis. The only major difference is that, except for the slightly different (also phase-matched) III-V waveguide layout, the BCB layer is now $50\,nm$ thinner to increase the coupling. As stated before, this is necessary because the 3D simulations show that the 2D analysis in the previous chapter over-estimated the intrinsic cavity Q-factor by about a factor of 2, meaning that the coupling should be increased to reach to a similar maximum reflectivity.

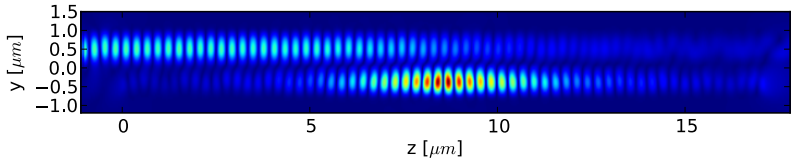

Figure 4.5: Time-averaged magnitude of the electric field in the mirror's (z,y) symmetry plane at the wavelength of maximum reflectivity ($1515.7\,nm$). Color scale is linear.

4.3 Laser properties

In chapter 3 and the first part of this chapter, the focus has always been on the reflection spectrum of the resonant mirror and more specifically on the maximum reflectivity and reflection bandwidth. However, these numbers serve a higher purpose: building a laser. So the figures of merit that really matter are the measurable laser properties, such as the threshold power, side-mode suppression ratio and (differential) efficiency. This section will link the mirror characteristics to these measurable laser properties.

4.3.1 Laser rate equations

Any laser analysis starts with the laser's rate equations. This is a set of coupled differential equations that couple the free-carrier density to the optical photon density. The number of free carriers per unit volume N_c on a location r and a time t is governed by the continuity relation [3]:

$$q\frac{\partial N_c(r,t)}{\partial t} = \nabla \cdot \vec{j}_N(\vec{r},t) - q(R(\vec{r},t) - G(\vec{r},t)) \tag{4.2}$$

with q the electric charge of 1 electron, N_c the time and space dependent free carrier density in the active layer, $\vec{j}_N$ the time and space dependent current density, R the time and space dependent carrier density recombination rate and G the time and space dependent carrier density generation rate. The current density term consists of two parts:

- diffusion: carriers will flow due to spatial density gradients, so this contribution is proportional to $\nabla N_c(\vec{r},t)$
- drift: if an electric field is applied across (part) of the layer stack, the free electrons and holes will respond to that. The electric field can be either externally applied or internal due to doping gradients.

Rigorously solving this equation requires numerical techniques due to the 4 dimensional nature of this equation. The problem can be simplified significantly by assuming a uniform carrier distribution in the active layer. Because the structure is undoped and no external electric field is applied, the current density term renders zero.

In other words, the carrier density N_c is determined by the difference between how many carriers are generated and recombine per unit time. The generation and recombination rates are assumed to be uniform across the device. Both effects will be discussed below.

4.3.1.1 Carrier generation

Carriers are generated by illuminating the III-V material with a pump beam of a frequency higher than the active layer's bandgap (1550 nm). In this case the pump photons will be absorbed by the active layer and create electron-hole pairs. If the pump beam's frequency is even higher than InP's band gap (1.34 eV = 925 nm), electron hole pairs will be generated in the cladding layers that can also diffuse into the active layer.

Each layer in the III-V stack will absorb a fraction of the light that passes through. The pump power $P_{a,i}$ that is absorbed by layer i is given by:

$$P_{a,i} = [1 - \exp(-\alpha_i h_i)]P_{i,i} \tag{4.3}$$

with α_i layer i's absorption coefficient, h_i layer i's thickness and $P_{i,i}$ the power incident on that layer, given by:

$$P_{i,i} = \prod_{j=0}^{(} i-1) \exp(-\alpha_j h_i) P_0 \tag{4.4}$$

with P_0 the power incident on the top layer of the III-V stack and taking the product over all the layers that are on top of layer i.

Dividing the absorbed power in layer i by the pump laser's photon energy $\hbar\omega_p$ yields the total number of carriers that are generated per unit time. Dividing this number by the volume of layer i, V_i, finally gives the carrier generation rate G_i in layer i:

$$G_i = \frac{P_{a,i}}{\hbar\omega_p V_i} \tag{4.5}$$

4.3.1.2 Carrier recombination

Free carriers can recombine in a number of ways in a semiconductor material:

- **Shockley-Read-Hall recombination (SRH)**: A carrier can be trapped by a defect in the semiconductor's crystalline structure and recombine. As the carrier recombines, it releases its energy as lattice vibrations (phonons) which is essentially heat. This recombination process does not require other carriers so the probability that this mechanism occurs is proportional to N_c:

  $$R_{SRH} = AN_c \tag{4.6}$$

  with A the SRH constant expressed in $[s^{-1}]$. This number depends on the defect density of the semiconductor crystal. Modern-day epitaxy yields a relatively low defect density, so SRH is usually small compared to other recombination mechanisms ($A \approx 10^8 s^{-1}$).

- **Surface recombination**: At the III-V waveguide's surface the III-V semiconductor crystal is abruptly interrupted, which can result in dangling bonds. If the surface is not passivated well, these dangling bonds will also serve as recombination traps. The associated recombination rate is given by:

  $$R_{sr} = \frac{A_s}{V_s} v_s N_c \tag{4.7}$$

with A_s the exposed surface area, V_s the waveguide volume and v_s the surface recombination velocity. v_s increases dramatically with increasing Gallium content and the surface recombination velocity for InGaAs can reach values up to $10^5 cm/s$. With a $1.6\mu m$ wide InGaAsP active layer, $A_s/V_s v_s$ amounts to $\sim 10^9 s^{-1}$, which is already an order of magnitude more than SRH recombination.

- **Spontaneous radiative recombination** An electron-hole pair can recombine spontaneously and release a photon upon doing so. Because two different carriers have to be at the same place simultaneously, the probability of this recombination mechanism to occur is proportional to N^2:

$$R_{spon} = BN^2 \tag{4.8}$$

with B on the order of $1 - 2 \times 10^{-10} cm^3 s^{-1}$

- **Stimulated radiative recombination** The recombination of an electron-hole pair can also be triggered when a photon with energy equal to the energy difference between the electron and hole collides with the carrier pair. In that case the newly generated photon is an exact copy of the incident photon. This mechanism of stimulated radiative recombination is the origin of optical gain. The associated recombination rate is given by:

$$R_{stim} = v_g G(N) S \tag{4.9}$$

with v_g the group velocity of the fundamental mode in the III-V waveguide, S the photon density and $G(N)$ the carrier dependent optical gain. In bulk active layers, this gain function is approximated by a linear function:

$$G(N) = G_0(N - N_0) \tag{4.10}$$

with G_0 the differential gain and N_0 the transparency carrier density.

- **Auger recombination** Probably the most concerning recombination mechanism in InP based lasers at telecom wavelengths is Auger recombination. When a carrier collides with an electron-hole pair, the electron hole pair can recombine and give its energy to the carrier that is then excited high into the conduction band (or deep into the valence band if the carrier is a hole). This mechanism requires 3 different carriers, consequently it is proportional to N^3:

$$R_{auger} = CN^3 \tag{4.11}$$

The Auger coefficient C increases exponentially with temperature.

Assembling all the generation and recombination mechanisms into equation 4.2 now yields the carrier rate equation:

$$\frac{dN_c}{dt} = \frac{P_a}{\hbar\omega_p V} - (A + \frac{A_s}{V_s}v_s)N_c - BN_c^2 - CN_c^3 - v_g G(N_c)S \tag{4.12}$$

The time dependence of the photon density S in the III-V waveguide's fundamental mode is determined by the cavity losses and the generation of new photons due to stimulated emission. This translates into the following rate equation, neglecting the spontaneous emission coupling into the laser mode:

$$\frac{dS}{dt} = \Gamma v_g G(N)S - v_g \alpha_{tot} S \tag{4.13}$$

with Γ the confinement factor that expresses what fraction of the III-V waveguide's fundamental eigenmode overlaps with the active region, v_g the mode's group velocity and α_{tot} the distributed losses in the cavity. These losses include material absorption α_m, scattering losses α_s and mirror losses α_R. Assuming mirror power reflectivities $R_{m,1}$ and $R_{m,2}$ and cavity length L, the corresponding loss factor is given by:

$$\alpha_R = -\frac{1}{2L}\ln\left(R_{m,1}R_{m,2}\right) \tag{4.14}$$

The total losses α_{tot} are then given by:

$$\alpha_{tot} = \alpha_m + \alpha_s + \alpha_R \tag{4.15}$$

4.3.2 Basic laser properties

Using the rate equations for the carriers 4.12 and the photon density 4.13, some basic laser properties can be derived. Given a constant pumping of the device, both the carrier distribution and the photon density will reach a steady state after the transient behaviour has died out. in this constant state, the derivatives with respect to time are zero. Plugging this condition into the photon density rate equation yields an expression for the necessary G(N):

$$G_{th}(N_{th}) = \frac{\alpha_{tot}}{\Gamma} \tag{4.16}$$

This simple expression says that the gain in the laser is clamped to a value such that it exactly compensates the optical losses, again neglecting the spontaneous emission coupling into the laser mode.

Before the laser is pumped, the gain in the cavity is negative : the active layer absorbs the light in the cavity (equation 4.10). As the pumping grows stronger, more carriers are generated and the absorption loss decreases until the transparency

carrier density N_0 is reached. At this carrier density the active layer absorbs nor amplifies the III-V waveguide mode. At higher carrier densities the active layer amplifies the light and when the amount of amplification is such that it can compensate all the cavity losses the laser turns on. This is the laser threshold condition, hence the name G_{th}. The carrier density at which the threshold condition is fulfilled is labeled N_{th}. Pumping even more will not increase the carrier density (hence it will also not increase the gain) but it will allow for a higher photon density in the cavity: per unit time, more photons can be amplified because more carriers are available. In other words, the gain is clamped to the threshold gain.

Using expression 4.10, the threshold carrier density is given by:

$$N_{th} = N_0 + \frac{\alpha_{tot}}{G_0 \Gamma} \tag{4.17}$$

The absorbed pump power required at threshold is then calculated by plugging N_{th} into 4.12 and assuming that at the threshold point the photon density is still very low and can be set to zero:

$$P_{a,th} = \hbar \omega_p V_a [(A + \frac{A_s}{V_s} v_s) N_{th} + B N_{th}^2 + C N_{th}^3] \tag{4.18}$$

Above threshold, the photon density in the cavity is given by:

$$S = \frac{1}{v_g G_{th}} \frac{P_a - P_{a,th}}{\hbar \omega_p V_a} \tag{4.19}$$

The laser's output power is then given by:

$$P_{out} = T \frac{S V_m}{2L/v_g} \hbar \omega_l \tag{4.20}$$

with T the power transmittance of the mirror connected to the output waveguide, V_m the modal volume ($V_m = V_a/\Gamma$), L the III-V waveguide length and ω_l the laser light's angular frequency.

The laser's overall efficiency η is given by dividing the optical output power P_{out} by the total pump power P_0. Defining the pump efficiency η_p as $\eta_p = P_a/P_0$ yields:

$$\eta = \frac{P_{out}}{P_0} = \frac{T}{2L\alpha_{tot}} \frac{\omega_l}{\omega_p} \eta_p \frac{P_a - P_{a,th}}{P_a} \tag{4.21}$$

In other words: an efficient laser has

- good out coupling T
- short length L

- low loss α_{tot}
- good pumping efficiency η_p
- low threshold $P_{a,th}$

Of course, most of these parameters are intertwined, meaning that increasing one parameter might deteriorate the other.

4.3.3 Laser properties of the designed component

To calculate the laser properties presented in the previous section, the first thing to do is to identify the laser's longitudinal cavity modes. These are the wavelengths for which the III-V waveguide with the two mirrors at the end is resonant. In other words, the wavelengths λ_R for which:

$$2k_w L + 2\Delta\phi_m(\lambda_R) = N2\pi \tag{4.22}$$

with $k_w = \frac{2\pi}{\lambda_R} n_{eff}$ and $\Delta\phi_m$ the wavelength dependent phase-change caused by the mirror. The effective index of the III-V waveguide's fundamental mode n_{eff} is shown in figure 4.3.

The mirror's phase change $\Delta\phi$ is difficult to simulate accurately using FDTD. However, expression 3.24 provides an approximate analytical expression for the field reflectivity of the resonant mirror that is composed of κ, Γ_0 and ω_c. By fitting the power reflection curve obtained by 3D FDTD simulation shown in figure 4.4 to the Lorentzian power reflection formula in 3.27, an approximation for κ, Γ_0 and ω_c can be found and the field-reflectivity equation 3.24 can be reconstructed. From this equation the phase change can easily be derived.

Figure 4.6 shows the power reflectivity curve shown in figure 4.4 along with the fitted Lorentzian (dotted line) and the derived phase $\Delta\phi_m(\lambda)$. As expected, $\Delta\phi_m$ swings from $\pi/2$ to $-\pi/2$ across the resonance. The phase response is steepest near the reflection maximum. This means that if the effective index of the III-V waveguide changes, for example due to increased temperature, the mirror will make sure that the wavelength drift is limited:

$$\frac{d\lambda}{dk_w} = \frac{1}{dk_w/d\lambda} = -\frac{L}{d\Delta\phi_m/d\lambda} \tag{4.23}$$

So the steeper $\Delta\phi_m$, the larger $d\Delta\phi_m/d\lambda$ and consequently the smaller the wavelength shift as a result of a change in k_w. The narrower the reflection peak, the steeper $\Delta\phi_m$.

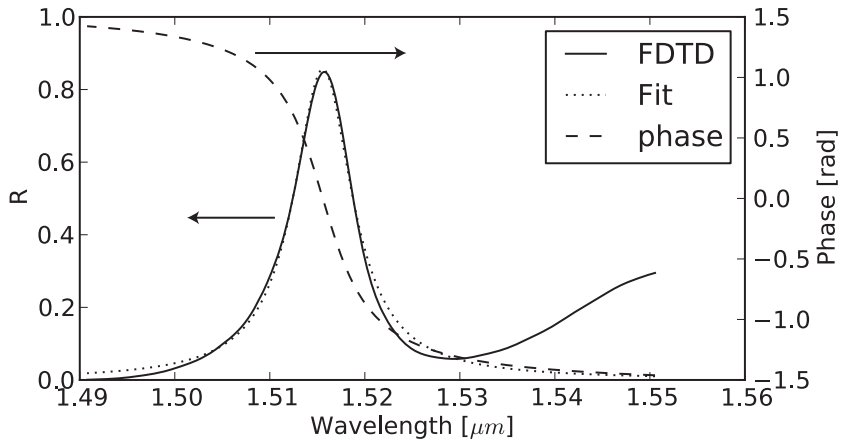

Figure 4.6: 3D FDTD power reflectivity from figure 4.4 fitted to a Lorentzian curve along with the extracted phase response $\Delta\phi_m$

Wavelength	Mirror reflectivity
$1.4978\mu m$	1.7%
$1.5082\mu m$	19.13%
$1.5158\mu m$	84.8%
$1.5233\mu m$	12.5%
$1.5342\mu m$	8.1%
$1.546\mu m$	24.8%

Table 4.2: Resonance wavelengths of the resonant mirror laser with $20\mu m$ gap between the silicon cavities along with the mirror reflectivity at each resonance wavelength.

Figure 4.7 shows $2k_wL+2\Delta\phi_m$ for a resonant mirror laser with the mirror depicted in figure 4.6 and a $20\mu m$ distance between the two mirrors. The horizontal grey lines indicate the integer times 2π and the wavelengths where they cross the phase curve are the laser's resonances. The length of the laser is slightly adjusted to have one of the resonances aligned with the top of the reflection curve. The relevant resonance wavelengths along with the mirror reflectivity at that wavelength are listed in table 4.2.

The laser-mode that is aligned to the reflection maximum will experience the lowest losses hence this mode will start lasing and suppress the other modes (assuming that it is relatively well aligned to the active material's gain spectrum).

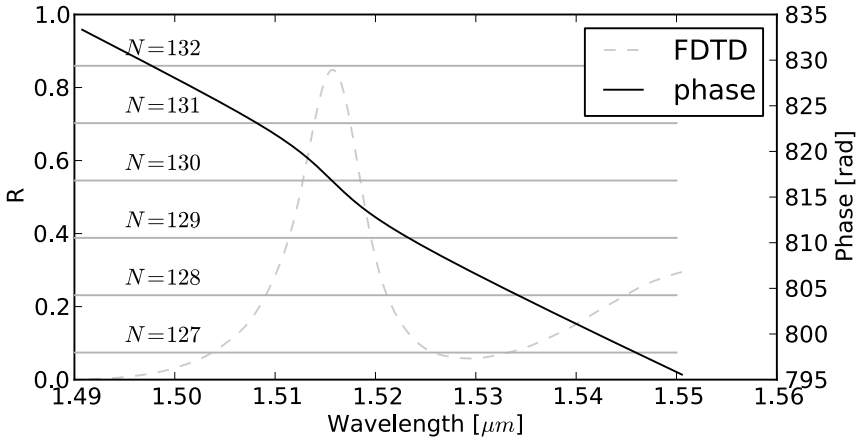

Figure 4.7: Total round-trip phase in case of $20\mu m$ *spacing between the silicon grating cavities. The horizontal grey lines indicate the total round-trip phases that satisfy the resonance condition.*

Until further notice, this mode will be assumed in the following treatment. Using this information, all the properties in the previous section can be calculated. The parameters used in this analysis are shown in table 4.3. The length of the optical mode is taken as the distance between the two defects in the grating cavity mirrors. This is motivated by the observation that at this point the intensity in the III-V waveguide decreases significantly. So the modal length $L_m = 2 \times 30 \times 0.285\,nm + 20\mu m = 37.1\mu m$.

4.3.3.1 Threshold power

To calculate the threshold power, the first thing to calculate is the modal threshold gain. Because the III-V materials used in this structure are undoped, material absorption outside the active layer is very minimal. This means that the only significant loss mechanism in the laser cavity are the mirrors. The losses associated with the mirrors are calculated using equation 4.14 and accounts to $44/cm$ at the $1515\,nm$ laser peak. This translates into $112.5/cm$ required threshold gain, taking into account the confinement factor. Such a gain value is reached for $N_{th} = 1.09 \times 10^{18}/cm^3$, which is around 1.5 times the transparency carrier density. The associated carrier recombination rates are given in table 4.4. This table clearly shows that both surface recombination and Auger recombination are the predominant carrier recombination mechanisms. In literature, the Auger recombination parameter C varies over 2 orders of magnitude for InGaAsP in this

Symbol	Parameter	Value	Reference
A	SRH-recombination coefficient	$10^8 s^{-1}$	[3]
A_s	Active layer exposed surface	$80\,nm \times 37.1\,\mu m$	
V_s	Active layer volume	$80\,nm \times 37\,\mu m \times 1.6\,\mu m$	
v_s	Surface recombination velocity	$10^5 cm/s$	[3]
B	Spontaneous recombination coefficient	$1 \times 10^{-10} cm^3/s$	[3]
C	Auger recombination worst case	$1. \times 10^{-27} cm^6/s$	[3]
C	Auger recombination best case	$1. \times 10^{-28} cm^6/s$	[3]
v_g	group velocity	$c/3.732$	simulation
G_0	differential gain	$3.13 \times 10^{-16} cm^2$	[4]
N_0	transparency carrier density	$6.5 \times 10^{17} cm^{-3}$	[4]
Γ	confinement factor	39.5%	simulation
ω_p	pump angular frequency	$2\pi \times 375 THz$	
ω_l	laser angular frequency	$2\pi \times 193.5 THz$	
T	transmission to SOI	4.89%	

Table 4.3: Parameters and corresponding values for the rate equation model of the optically pumped resonant mirror laser

Mechanism	Loss
AN_{th}	$1.01 \times 10^{26} cm^{-3} s^{-1}$
$A_s/V_s \times v_s N_{th}$	$1.26 \times 10^{27} cm^{-3} s^{-1}$
BN_{th}^2	$2.04 \times 10^{26} cm^{-3} s^{-1}$
CN_{th}^3	$1.028 \times 10^{27} cm^{-3} s^{-1}$

Table 4.4: Total carrier recombination rate due to the different recombination mechanisms for the worst case Auger recombination

wavelength range. The calculation in table 4.4 assumes the worst-case scenario. Surface recombination on the other hand can be reduced significantly by passivating the InGaAsP surface. Again, this simulation assumes the worst-case scenario, namely that the waveguide walls are not passivated.

The total carrier density recombination rate adds up to $2.59 \times 10^{27} cm^{-3} s^{-1}$. With an $800\,nm$ pump laser the laser power that should be absorbed to reach laser threshold in this worst-case scenario is $\mathbf{3.06\,mW}$. Assuming the waveguide is passivated and the Auger recombination rate is an order of magnitude lower results in a required absorbed threshold power of $0.48\,mW$. These numbers can be used as upper and lower limits of what threshold power can be expected.

Material	E_g [eV]	$\alpha_0[\times 10^4 cm^{-1}]$	$\alpha_i[\times 10^4 cm^{-1}]$
InP	1.344	5	1.96
InGaAsP (Q=1.55)	0.8	6.67	6.46
InGaAsP (Q=1.2)	1.03	5.73	4.05

Table 4.5: Pump laser absorption parameters in III-V waveguide

4.3.3.2 Slope efficiency

A laser's slope efficiency is the increase in output power due to an increase in pump power above threshold. This number is easily calculated as:

$$\eta_{slope} = \frac{T}{2L\alpha_{tot}} \frac{\omega_l}{\omega_p} \eta_p = 7.47\% \times \eta_p \tag{4.24}$$

The pump efficiency η_p is hard to predict because an $800\,nm$ pump laser will also generate carriers in the InP layers that might diffuse into the InGaAsP layer and add up to the absorbed pump power.

The material absorption for energies above the band-gap can be approximated using the following formula [3]:

$$\alpha = \alpha_0 \sqrt{\frac{E_p - E_g}{E_g}} \tag{4.25}$$

with E_g the bandgap energy and E_p the photon energy of the pump laser. α_0 is a material parameter. Table 4.5 lists the absorption coefficients for all the materials in the III-V waveguide stack, assuming an 800nm (1.55 eV) pump laser. The InGaAsP parameters are interpolated using InP, GaAs and InAs values.

Using the approximate absorption values in table 4.5, table 4.6 shows the fraction of the incident power that is absorbed by the different layers in the III-V waveguide. As expected, the active InGaAsP layer is the most absorbent. To determine the pump efficiency η_p, two cases can be distinguished:

- Only the carriers generated in the active InGaAsP layer contribute to the gain. In this case $\eta_p = 27.15\%$
- Carriers generated in the InP layers diffuse into the InGaAsP layer and can contribute to the optical gain. In this case $\eta_p = 11.4\% + 27.15\% + 1.54\% = 40.09\%$ in the best case.

So roughly speaking, the pump efficiency will be somewhere between 30% and 40%, depending on how many carriers generated in the InP layers actually con-

Layer	$\exp(-\alpha_i L_i)$	P_a/P_0
InP	98.06%	1.94%
InGaAsP (Q=1.2)	96.03%	3.89%
InP	98.06%	1.82%
InGaAsP (Q=1.2)	96.03%	3.67%
InP	98.06%	1.72%
InGaAsP (Q=1.2)	96.03%	3.45%
InP	98.06%	1.62%
InGaAsP (Q=1.2)	96.03%	3.25%
InP	85.5%	11.40%
InGaAsP (Q=1.55)	59.6%	27.15%
InP	96.1%	1.54%

Table 4.6: Absorbed power per layer

tribute to the optical gain. Consequently the total slope efficiency will be somewhere between 2.05% and 2.99%

4.3.3.3 Output power

The output power P_{out} as a function of pump power P_p can easily be calculated by taking into account the threshold pump power $P_{th} = P_{a,th}/\eta_p$ and slope efficiency η_{slope}:

$$P_{out} = \eta_{slope} \times (P_p - \frac{P_{a,th}}{\eta_p}) \tag{4.26}$$

In the worst case (high lasing threshold and low pumping efficiency, the output power in the silicon waveguide reaches $76\mu W$ for $15\,mW$ of pump power. This results in 0.5% wall-plug efficiency. On the other hand, assuming the best case scenario (low lasing threshold and high pumping efficiency), $114\mu W$ of power should couple into the silicon waveguide at only $5mW$ pump power, resulting in a wall-plug efficiency of 2.27%, which approaches the slope efficiency of 2.99%.

4.4 Fabrication

4.4.1 Mask design

The silicon part of the laser, namely the grating cavities, access waveguides and grating couplers, were fabricated in imec's 200 nm CMOS pilot line as part of an ePIXfab multi-project wafer (MPW) run called *Sipp16*. The mask consisted of 1 $2\,mm$ wide column of 120 devices. Each device was duplicated 3 times as explained later, so in total there are 40 unique designs on the chip. All combinations

of the following parameters are on the chip:

- grating periods Λ_g: $285\,nm$, $290\,nm$
- number of grating periods N_g: 60 periods, 40 periods
- gap between the silicon cavities: $20\mu m$, $20.075\mu m$, $20.15\mu m$, $20.225\mu m$, $20.3\mu m$, $40\mu m$, $40.15\mu m$, $40.3\mu m$, $80\mu m$, $100\mu m$

The sub-micrometer variations in length serve the purpose of aligning the top of the reflection curve to one of the laser structure's longitudinal resonances. Each silicon grating is connected to a waveguide that leads to a grating coupler. The delivered samples had no silicon-oxide top cladding but were covered with photoresist for protection.

The III-V waveguide was designed as a $1.6\,\mu m$ wide, straight waveguide with angled facets to minimize any form of facet reflection. As said before, each silicon design was duplicated three times. The III-V waveguide of one of each design in these 3-piece sets was aligned perfectly to the silicon structure below. The other two had a lateral offset of $+250\,nm$ and $-250\,nm$. This measure was taken to accommodate alignment errors during III-V processing.

Figure 4.8 shows an extract from the GDS file containing both the silicon layer (red) and the III-V waveguide (blue). The image clearly shows the silicon grating cavities, the angled facets of the III-V waveguide and the $\pm 250\,nm$ offset on the bottom and top device as compared to the center device.

4.4.2 III-V processing

As said before, the silicon layer of the chip was processed at imec's 200 mm CMOS fab. The III-V processing was done in-house. This section will give an overview of the different steps in the fabrication process.

4.4.2.1 III-V wafer

The 2-inch III-V wafer was ordered at ITME (Poland) and consisted of an InP substrate, a 300 nm InGaAs etch-stop layer, four pairs of InP/InGaAsP, 80 nm of InP, 80 nm of InGaAsP, 20 nm of InP and 2 sacrificial protection layers: 100 nm InGaAs and 100 nm InP. The wafer was protected with photoresist upon arrival in the cleanroom and cleaved into $7\,mm \times 4\,mm$ pieces.

4.4.2.2 Surface preparation

The process starts with a thorough cleaning of the SOI die. The protective photoresist is removed using acetone and iso-propyl alcohol (IPA). In a second step the

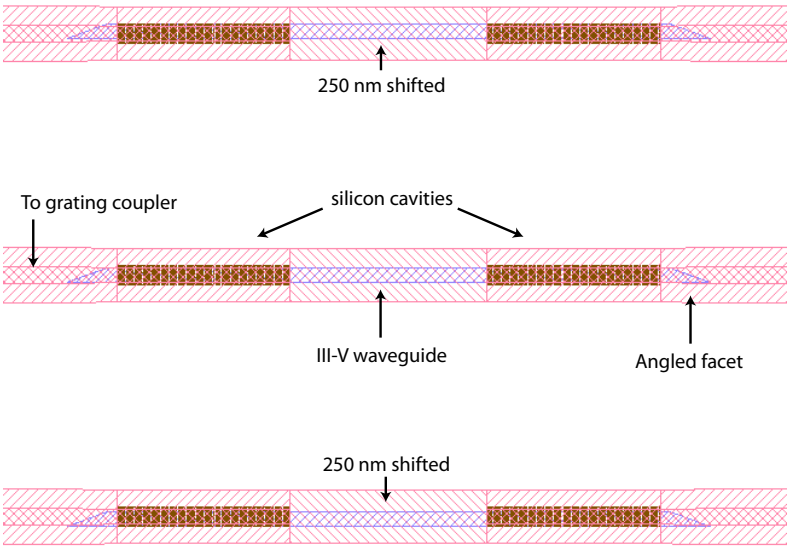

Figure 4.8: Extract from the GDS file of the optically pumped resonant mirror laser showing the silicon layer (red) and III-V layer (blue) of 3 different devices.

sample is immerged in an $80°C$ SC1 solution. This solution consists of de-ionised water (150cc), hydrogen peroxide (30cc) and ammonia (30cc). SC1 is known to remove particles from a semiconductor surface and slightly oxidises the exposed silicon, making it hydrophilic, which significantly improves the adhesion to BCB.

The protective photoresist is removed from the III-V die and the InP and InGaAs layers are removed using HCl and $H_2SO_4 : H_2O_2 : H_2O$ (5cc : 5cc : 90cc) respectively. Finally, a $200\,nm$ oxide layer is deposited on the III-V surface to improve adhesion to BCB and set the define the distance between the bottom of the III-V waveguide and the top of the silicon waveguide, assuming that the BCB layer will be very thin.

4.4.2.3 Bonding

Before bonding, an adhesion promotor (AP3000, spin-speed: 3000RPM) is spin coated on the silicon die and baked for 3 minutes on a $120°C$ hot plate. Next a layer of benzo-cyclo-butene (BCB) is spin coated on the SOI sample. This solution consists of 1 volume of Dow Chemical's Cyclotene 3022-35 solution and 2 volumes of mesitylene. This was spin-coated at 3000 RPM. Using a well-defined BCB solution and spin-coating at the correct spin velocity should result in repro-

ducible values for the BCB thickness. The BCB thickness can be checked after bonding using Focussed Ion Beam (FIB) milling and Scanning Electron Microscope (SEM) imaging.

Both the silicon die and III-V die were mounted into the machine bonder. The bonder applies pressure to the sample pair and cures the BCB for 1 hour at $250°C$.

4.4.3 Substrate removal

After bonding, the $380\,\mu m$ thick InP substrate is thinned down to approximately $100\,\mu m$ using mechanical grinding. The remaining InP is removed using HCl, which stops etching at the InGaAs etch-stop layer. After wet-etching it is possible that some InP ears are left on the edge of the bonded die. To remove them, photoresist is first spin coated and baked at $100°C$ as a protective layer and then the ears are scratched away using a scalpel. The photoresist is removed using acetone and IPA and the remaining InGaAs etch-stop layer can be etched using H_2SO_4 : H_2O_2 : H_2O (5cc : 5cc : 90cc).

4.4.4 Waveguide definition

To define the III-V waveguides, a $120\,nm$ thick silicon oxide hard mask is deposited using a plasma-enhanced chemical vapour deposition (PECVD) machine. Next, the waveguide patterns are defined using contact lithography. After development, the waveguide pattern is transferred to the silicon oxide hard-mask by dry etching in a reactive ion etcher (RIE) using a mixture of SF_6 and O_2. The photoresist is removed using aceton, IPA and an O_2 RIE treatment. Finally the silicon oxide structures are transferred to the III-V layer by etching the III-V layer using an inductively coupled plasma (ICP) etcher. The sample is now ready for measurement. For the time being, the silicon oxide hard-mask can stay on the III-V waveguide.

4.5 Characterisation

4.5.1 Properties of the fabricated device

Figure 4.9 shows a top SEM image of 3 finished devices. In the center device the III-V waveguide is close to perfectly aligned to the silicon structures underneath, with a slight deviation to the left. The left device's alignment is quite off. As could be expected from the low-resolution lithography process, the taper tips are rounded. More importantly, the image shows that the III-V waveguide is wider than the intended $1.6\mu m$, close to $2\mu m$.

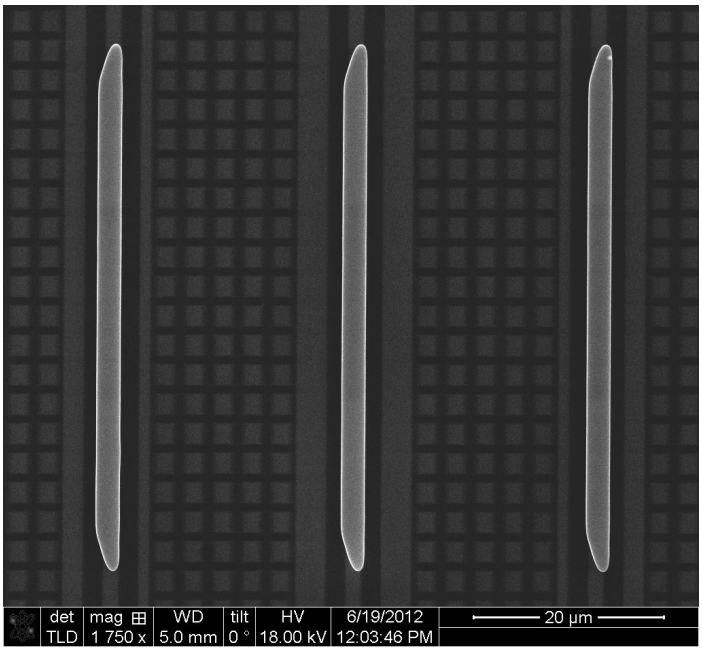

Figure 4.9: SEM image of three finished devices

Figure 4.10 shows the simulated reflection curve of the resonant mirror as fabricated: $2\mu m$ wide III-V waveguide, 4 Inp/InGaAsP pairs and $200\,nm$ separation between the silicon layer and the III-V layer. There are a few distinct differences as compared to the designed component in figure 4.4.

- Maximum reflectivity: At resonance the mirror now reflects only 56%. This corresponds to a required modal threshold gain of $156/cm$ and a worst-case (high Auger and high surface recombination) absorbed threshold power of $11.6\,mW$ and a best case (low Auger + low surface recombination) absorbed threshold power of $1.9\,mW$

- Resonance wavelength: Due to the reduced BCB thickness, the resonance has shifted to shorter wavelengths. The reason for this could be that the closer proximity of the III-V waveguide pulls a higher fraction of the silicon mode into the BCB layer in between, which might reduce the overall effective index.

- Outcoupling: The reduced BCB thickness increases the coupling efficiency to the silicon output waveguide. Now close to 10% of the light incident on the mirror is redirected into the silicon output waveguide.

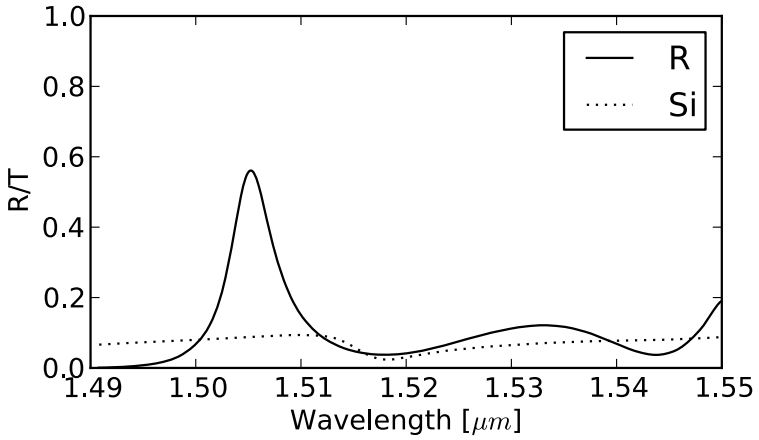

Figure 4.10: Simulated reflection spectrum of the as-fabricated structure.

4.5.2 Measurement setup

The chip was characterised at CNRS/LPN [5] in Marcoussis, France. This lab has built a measurement setup that is specifically designed to characterise optically pumped lasers that couple to a fiber. The measurement setup is shown in figure 4.11. The pump laser beam, an 800 nm DFB laser, is coupled to free space and forced into a parallel beam using two convex lenses. Next, the beam shape is transformed from a circular beam into an elliptical beam to fit the elongated shape of the laser. The beam is then focussed to the sample using a $5\times$ long working distance objective. The long working distance allows for a fiber to be positioned on the grating couplers and to collect the generated laser light. The fiber leads to a grating-based spectrometer with a liquid nitrogen cooled 1D InGaAs detector array.

To roughly align the pump laser, the chip is illuminated with a visible fiber light source that allows the chip to be imaged on a camera. A variable attenuator wheel regulated the pump intensity.

4.5.3 Results

Figure 4.12 shows the output spectrum as picked up from the grating couplers of a resonant mirror containing 60 periods in each grating ($285\,nm$ grating pitch) and $20.225\mu m$ distance between the silicon grating cavities. This is the device where the III-V waveguide is aligned to the silicon cavity.

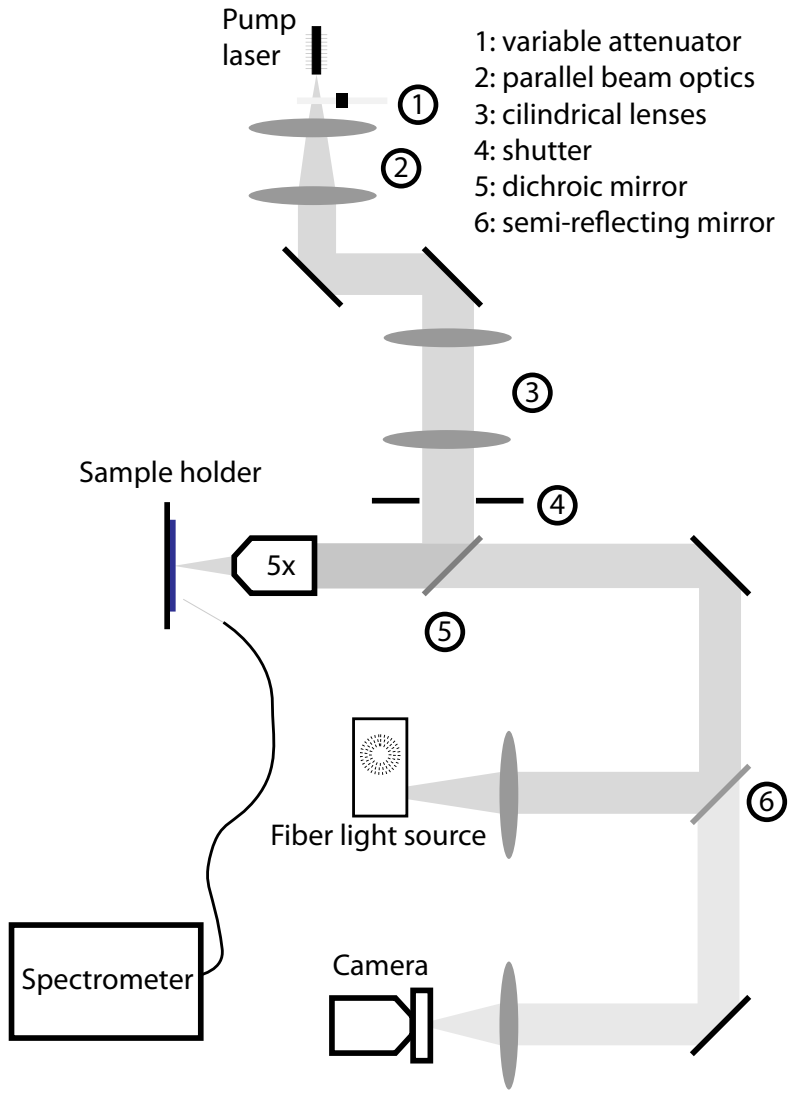

Figure 4.11: Schematic representation of the measurement setup used to characterise the optically pumped resonant mirror lasers.

The device is illuminated with $20\,ns$ long pulses with a $1.5\,\mu s$ repetition time. The plot clearly shows how the laser resonance first enhances the spontaneous emission and after the threshold condition is fulfilled the device starts lasing.

Using these different spectra, the laser's output power versus input pump power (light-light curve) can be determined and is plotted in figure 4.13. The logarith-

mic plot clearly shows the expected s-shape: exponential increase at threshold and linear increase (hence logarithmic increase on a logarithmic scale) above threshold. The threshold pump power is around $5.2mW$. Assuming the best-case scenario where the carriers generated in the InP layers diffuse into the InGaAsP layer, $\eta_p = 40\%$, the absorbed pump power would be $2.08mW$. This number is very close to the best-case scenario absorbed threshold power of $1.9mW$.

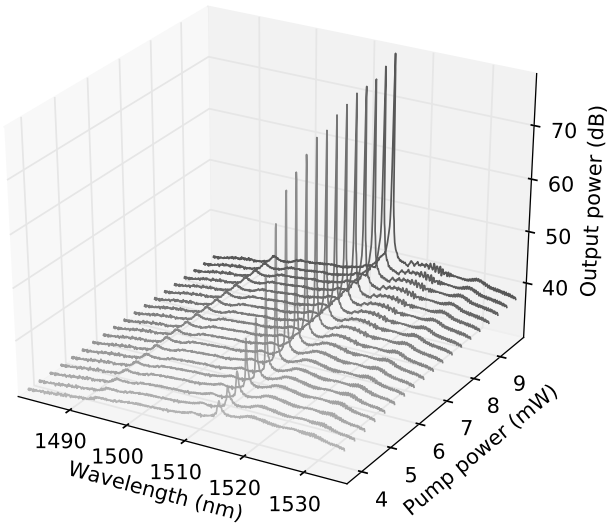

Figure 4.12: Schematic representation of the measurement setup used to characterise the optically pumped resonant mirror lasers.

Figure 4.14 shows a detailed output spectrum at 10mW pump power. This figure shows two important features:

- The lasing wavelength of $1505.39\,nm$ corresponds very well to the top of the simulated resonant mirror reflection curve of the as-fabricated laser in figure 4.10.
- There are no side-modes and the laser rises $37dB$ above the spontaneous emission background level.

The pulse-length of the pump laser was increased from $20\,ns$ and lasing stopped

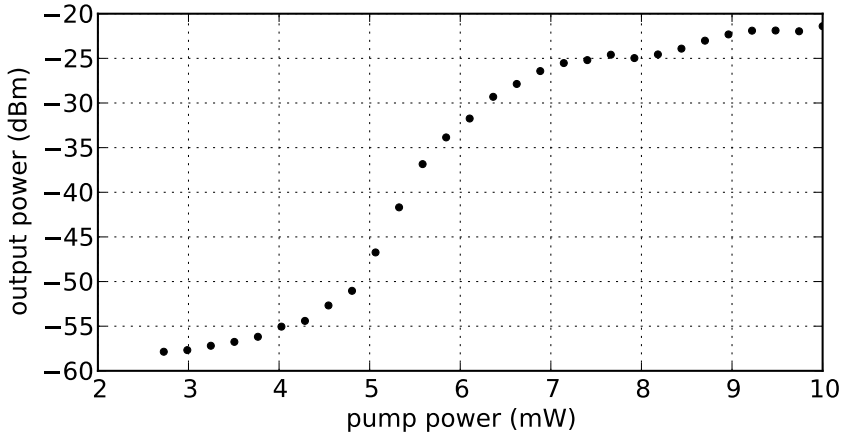

Figure 4.13: Laser output power versus total pump power based on the captured spectra in figure 4.12

at a $1.2\mu s$ long pulse. Given the pulse period of $1.5\mu s$, this is very close to CW operation. It is very likely that CW lasing was obstructed by excessive self-heating.

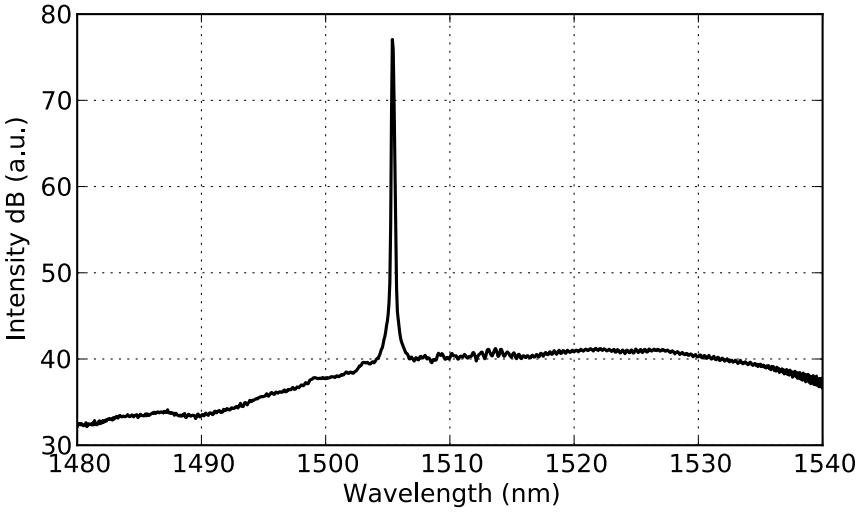

Figure 4.14: Output spectrum at 10mW pump power.

Due to the limited time that was available with the measurement setup, only 15 devices could be measured: the 60 period $285\,nm$ gratings with $20\mu m$, $20.075\mu m$, $20.150\mu m$, $20.225\mu m$ and $20.30\mu m$ spacing between the gratings and $-250\,nm$, $0\,nm$ and $250\,nm$ lateral offset of the III-V waveguide. The $+250\,nm$ devices did not work, probably because the coupling between the III-V waveguide and the silicon cavity was not good enough to allow for lasing.

Figure 4.15 shows the lasing spectra of the $0\,nm$ offset lasers with silicon cavity spacing of $20\,\mu m$. $20.15\,\mu m$ and $20.225\,\mu m$. The lasers where the laser resonances is not aligned have higher threshold and produce less power. Figure 4.16 shows the lasing spectra of the $-250\,nm$ offset devices. This figure very nicely shows the mirror reflection envelope. Because the coupling and consequently the reflectivity in these devices is lower, the photon density is also lower and some of the devices (especially the $20.075\mu m$ device that is clearly aligned to the edges of the reflection curve) is multi-mode.

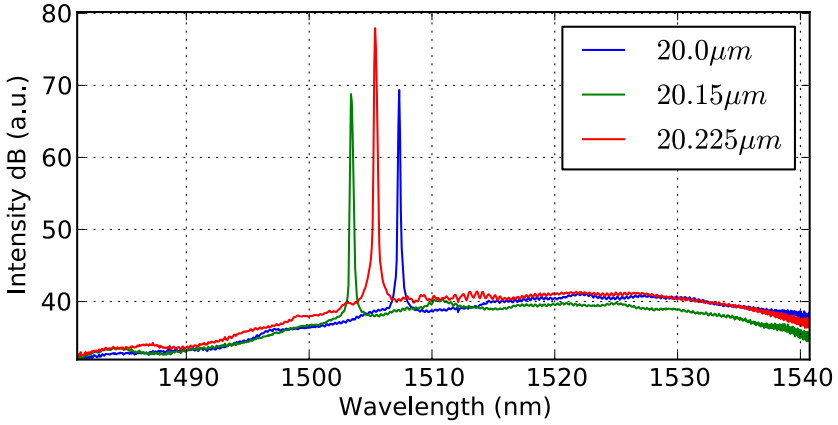

Figure 4.15: Output spectrum at 10mW pump power for 3 different lasers with $0\,nm$ lateral offset.

4.6 Conclusions

This chapter discussed the design, fabrication and characterisation of the world's first demonstration of hybrid silicon resonant mirror lasers. The theoretical knowledge of hybrid silicon resonant mirrors gained in the previous chapters was put into practice. A design was proposed and verified using 3D FDTD simulations.

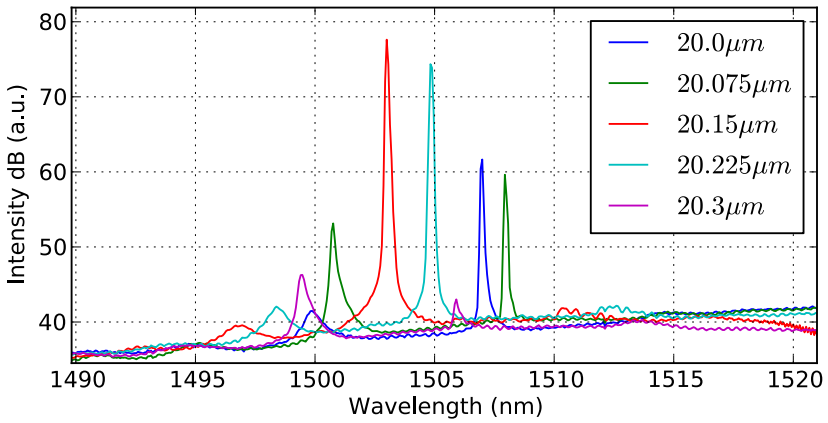

Figure 4.16: Output spectrum at 10mW pump power for 5 different lasers with $-250\,nm$ lateral offset, cleary showing the resonant mirror envelope.

The most important properties of a laser utilising this mirror were estimated using a simple rate-equation model. The in house fabrication process of the III-V layer was outlined and the measurement strategy and results were shown. The most important conclusion is that the measured laser properties (lasing wavelength, threshold power) resemble the theoretically predicted values quite well. Although this is a very exciting result, the holy grail of this work is an electrically pumped resonant mirror laser. Such a device is discussed in the next chapter.

References

[1] Photonics Research Laborator - University of Maryland - http://www.photonics.umd.edu/software/wgmodes/. *WGMODES*.

[2] Lumerical Solutions http://www.lumerical.com. *Lumerical FDTD*.

[3] Joachim Piprek. *Semiconductor Optoelectronic Devices*. Academic Press, 2003.

[4] Joris Van Campenhout. *Thin film microlasers for the integration of electronic and photonic integrated circuits (PhD Thesis)*. 2007.

[5] LPN/CNRS http://www.lpn.cnrs.fr. *LPN/CNRS*.

5

Electrically pumped resonant mirror lasers

5.1 Introduction

The previous chapter detailed the design, fabrication and characterization of the world's first hybrid silicon resonant mirror laser. To reduce the complexity of this device to a minimum, it was optically pumped. However, the applicability of optically pumped devices is rather limited because it requires a second pump laser, so the holy grail of this work is an electrically injected resonant mirror laser.

In principle, all the design aspects that were discussed in chapter 3 still hold. The most important difficulty of electrical injection is that the III-V waveguide now requires metallic electrical contacts for electrical injection. Metals are known to be highly absorptive in our wavelength region of interest. Consequently, the III-V waveguide should be designed in such a way that the optical mode does not overlap with the metallic contacts. Because the lasers in this work are designed for the widely adopted 220 nm SOI platform, this wil prove to be a hard nut to crack.

This chapter will first discuss the design issues specific to electrically pumped resonant mirror lasers, including the optical, electrical and thermal matters. Next, the technological process that has been developed to fabricate the designed structures will be discussed in detail. Finally, the experimental results will be presented.

5.2 Design aspects

As discussed in the previous paragraph, the III-V waveguide cannot be chosen arbitrarily thin so its effective index can not easily be matched to that of the silicon cavity. Consequently, it will prove beneficial to use hybrid band-edge defect grating cavities instead of the simpler defect grating cavities, that can provide higher Q-factors and compensate for reduced phase-matching that results in lower coupling, as discussed in section 3.5.4.

5.2.1 Intrinsic silicon cavity

The hybrid band-edge defect grating cavity was studied extensively in section 2.3.3. This study was performed using 2D simulations to reduce calculation time. However, most conclusions that were drawn in that section can also be applied to the more realistic 3D case. Similar to the defect grating treatment in the optically pumped laser in chapter 4, the most important difference between the 2D and 3D caseis that the 2D case overestimates the cavity's intrinsic Q-factor. In the 2D case this was around 160000 (see figure 2.31). Rigorous full-vectorial 3D FDTD shows that a 50-10-50 configuration has a Q-factor of 141883. Compared with the defect case, there now is a much better agreement between the 2D and 3D simulations.

5.2.2 III-V waveguide

5.2.2.1 Geometry

As stated earlier, electrical carriers should be provided to the III-V waveguide by means of metallic contacts. Because the metallic contacts and the highly-doped semiconductor contact layers are known to absorb heavily in the wavelength range of interest, the III-V waveguide should be designed such that the optical mode is confined far away from the metallic contacts.

Classically this is accomplished by utilising a waveguide cross-section as shown in figure 5.1a [1]. The higher index quaternary multi-quantum-well (MQW) layers confine the fundamental mode to the bottom of the waveguide, far away from the absorptive layers on top, as shown on figure 5.1b. Sometimes the MQW layers are sandwiched between wider band-gap quarternary layers with a refractive index higher than InP to increase confinement in the bottom part of the waveguide. These layers are often referred to as Separate Confinement Heterostructure (SCH) layers.

Such a waveguide typically has an effective index of 3.1 or more at $1550\,nm$. Comparing this with the phase-matching condition for hybrid band-edge defect grating cavities discussed in section 3.5.1 where n_{eff} should be 2.685, it is clear

that such a classic III-V waveguide is severely phase mismatched with the cavity. To make matters worse, such a classic waveguide is far from single-mode. A large number of higher order modes exist in this waveguide, as shown in figure 5.1c and 5.1d.

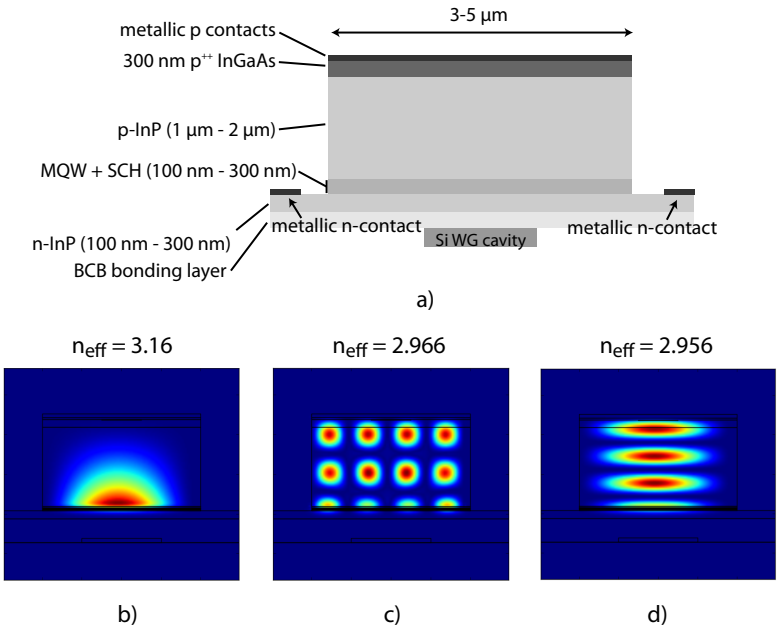

Figure 5.1: a) layout of a tradition hybrid silicon laser III-V waveguide cross-section. b) Fundamental TE eigenmode of such a waveguide. c) d) two examples of higher order modes in such a waveguide structure.

These higher order modes overlap with the metallic p-contact and consequently they have high modal losses. Also, these modes have a lower effective index, so they are closer to phase matching with the silicon cavity. So if light couples from the fundamental mode into the silicon cavity mode, the cavity mode will leak into the higher order modes, drastically reducing the cavity's Q-factor and deteriorating the resonant mirror effect.

In summary, the classical III-V waveguide poses two problems: the effective index of its fundamental mode is too high and the waveguide possesses too many higher order modes where the silicon cavity can leak into. The approach to solve this problem that is proposed in this work is shown in figure 5.2. A slit is etched into the p-type InP layer to push the mode down and to reduce the number of

modes in the waveguide. To prevent the fundamental mode to leak into the resulting p-doped InP pillars, the quantum wells are under-etched to confine the optical mode to the region underneath the etched slit.

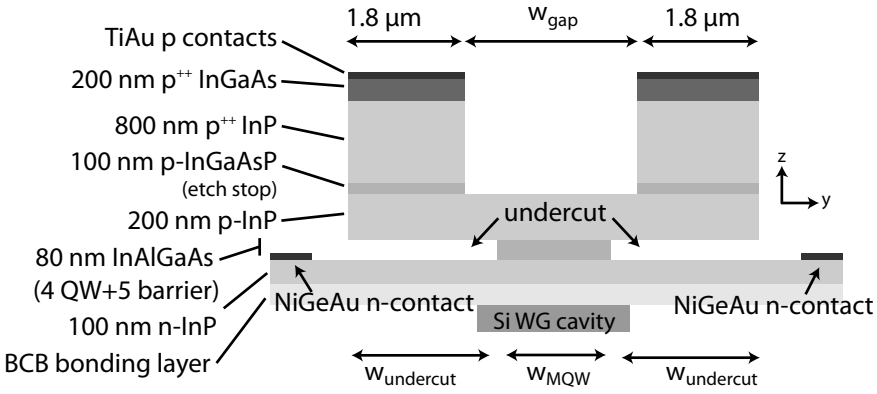

Figure 5.2: Layout of the proposed hybrid silicon laser III-V waveguide cross-section with a slit in the p-InP layer and undercut MQW region.

The n-InP is as thin as possible: $100\,nm$, to bring the waveguide mode close to the silicon layer. The p-InP above the MQW region is thicker: $200\,nm$. The reason for this is that holes are not as mobile as electrons. Consequently, for a certain doping level, the resistance in a p-doped region will be higher. Moreover, p-doping a semiconductor promotes inter-valence-band-absorption (IVBA), so high p-doping of a certain layer is not possible if the optical mode overlaps with this layer. Making the layer thicker reduces the electrical series resistance of this layer (see 5.2.5). Underneath the p-InP pillars there is an InGaAsP etch-stop layer to assure that the slit is always the same depth and consequently the thickness of the p-InP layer underneath is always 200 nm. This is important because the effective index of the optical mode is partially determined by the thickness of the p-InP layer.

Figure 5.3 shows the effective index of the fundamental mode of the proposed III-V waveguide as a function of the width of the MQW region. Even for very narrow active layer widths, the III-V waveguide cannot be phase-matched to the silicon cavity. However, the mismatch is significantly lower than in the case of a traditional III-V waveguide cross-section. Moreover, the number of higher order mode in this structure that will couple to the III-V mode is reduced.

If only the optical design would be considered, one could argue that the MQW region should be as narrow as possible to decrease the effective index as much as

possible. But there are a few other factors that contradict this:

- Series resistance: by making the MQW region narrower, the length that the electrical carriers have to travel through the 200 nm thin p-doped region increases, assuming that the slit cannot be made much narrower due to lithographic constraints. Consequently the series resistance will increase.
- Surface recombination: if the MQW region width is reduced, its surface to volume ratio increases, which in its turn will increase the rate at which carriers are lost due to surface recombination
- Mechanical stability: because the entire p-region is attached to the substrate through the MQW region, it should be clear that decreasing the MQW region width will decrease the mechanical stability of the III-V waveguide.

These factors will be discussed in more detail later.

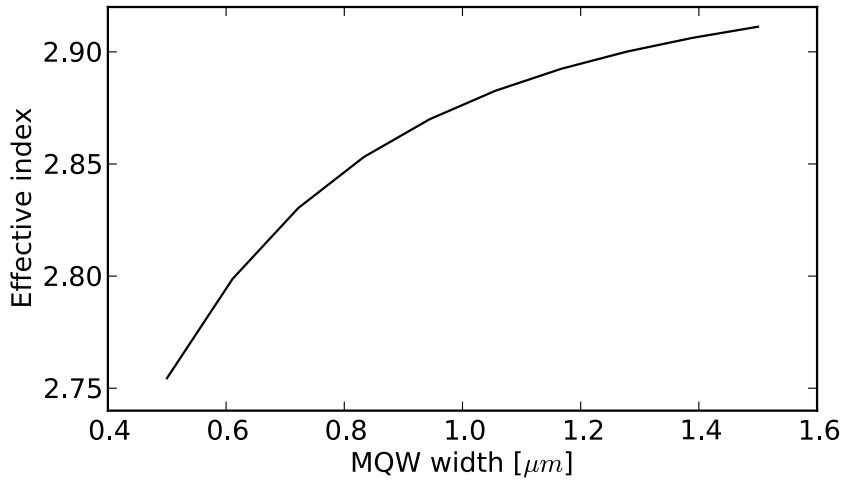

Figure 5.3: Effective index of the fundamental TE eigenmode of the proposed III-V waveguide mode as a function of the width of the MQW region. [$\lambda = 1550\,nm$]

Taking into account all these considerations, an $800\,nm$ wide MQW region is chosen. The remainder of this section will assume that the MQW region is $800\,nm$ wide. To make sure there is no coupling to the pillars, the width of the gap is assumed to be $2.0\mu m$.

In this work two different laser lengths are considered: a short laser with $20\,\mu m$ between the two silicon cavities and a long laser with $100\,\mu m$ between the silicon

Layer	Doping level [$10^{17} cm^{-3}$]	Confinement factor Γ_i
p-InGaAs	100	0%
p-InP	50	0%
p-InGaAsP	5	0%
p-InP	3	49.4%
barriers	nid	18.3%
wells	nid	10.9%
n-InP	20	18.7%

Table 5.1: Doping levels and optical confinement factors of the different layers in the electrically pumped III-V waveguide structure with $w_{MQW} = 800\,nm$.

cavities. Adding up the approximately $30\,\mu m$ long silicon grating cavities yields a total length of $80\,\mu m$ and $160\,\mu m$ respectively.

5.2.2.2 Doping levels

Unlike the optically pumped III-V waveguide, the electrically pumped version will be doped by acceptor and donor atoms to improve the conductivity of the different semiconductor layers. Table 5.1 shows the doping levels of the different layers in the III-V waveguide stack. Increased doping levels lead to better electrical conductivity but also to higher optical losses. Away from the optical mode, in the p-pillars, doping levels are set relatively high for low resistance. The InGaAs contact layer is doped at a very high level to ensure good electrical contact with the p-metal. In the p-InP optical cladding layer the doping is lower to reduce optical absorption losses. The n-InP layer serves, as an optical cladding, as a narrow channel towards the n-metal contact and as a contact layer to the n-metal. Fortunately, optical absorption is lower for n-doped materials, allowing for higher doping levels and the mobility of electrons is higher than that of holes, so very high doping levels are not required. The barriers and wells are not intentionally doped.

5.2.2.3 Confinement factors

Unfortunately, doping comes at the cost of optical absorption. The absorption in a particular layer is calculated by multiplying the material absorption with the confinement factor of that particular layer. The total absorption is the sum of all contributions. The optical confinement factors are listed in table 5.1. They are calculated using an in-house developed optical mode-solver based on the WG-MODES project [2]. The corresponding optical losses are discussed in section 5.2.4.

5.2.3 Resonant mirror properties

Some minor adjustments were done to the silicon cavity design.

- The cavity is tapered to avoid unwanted coupling in the grating's long-grating period section and to push the mode back into the III-V waveguide.
- The cavity's back mirror is shorter (35 periods) than the front mirror (60 periods) to promote facet leakage into the silicon output waveguide.

The resulting cavity has a Q-factor of about 40000. This reduction is mainly due to the shorter back mirror. The cavity is schematically drawn in figure 5.4.

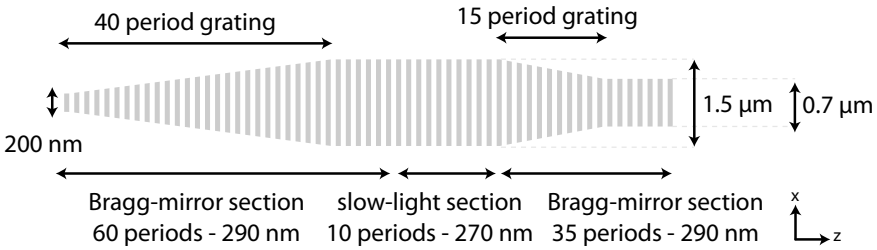

Figure 5.4: Schematic representation of the silicon cavity used for the electrically pumped resonant mirror.

Using this cavity in conjunction with the III-V waveguide cross section shown in figure 5.2 with $w_{MQW} = 800\,nm$ and $w_{gap} = 2.0\,\mu m$ results in the R/T spectrum shown in figure 5.5. The BCB thickness is $200\,nm$. This response was calculated using full-vectorial 3D FDTD. At resonance, the mirror reflects around 88% of the incoming light back into the III-V waveguide's fundamental eigenmode. At this wavelength, the transmissivity is below 1%.

The FWHM of the reflection peak is $1.27\,nm$. At resonance, around 3% of the incident light is coupled into the silicon waveguide. Due to the severe phase-mismatch, the silicon cavity's Q-factor should be kept high in order to provide sufficient reflectivity. This means that the number of periods in the cavity's back mirror grating cannot be reduced too much and consequently the output efficiency is rather low.

Figure 5.6 shows the time-averaged spatial distribution of the magnitude of the electric field (linear scale) at the mirror's resonance wavelength $\lambda_R = 1533\,nm$. The silicon cavity starts at $z = 0\,\mu m$. The image clearly shows the field enhancement in the silicon cavity and the standing wave pattern in the III-V waveguide, indicating the high reflectivity. The figure also shows how the tapered silicon cavity prevents coupling at the silicon cavity's front mirror grating.

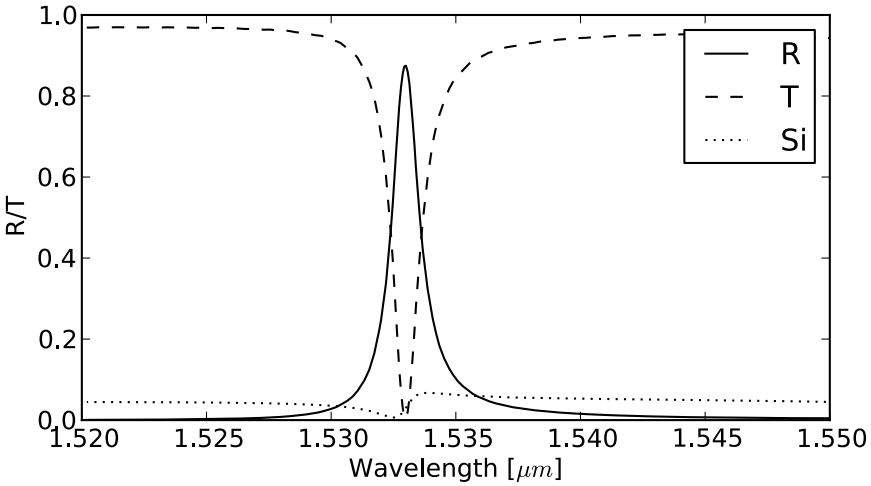

Figure 5.5: Simulated reflection and transmission spectrum of the III-V waveguide in figure 5.2 and silicon cavity in figure 5.4. The figure also shows the coupling efficiency into the silicon output waveguide.

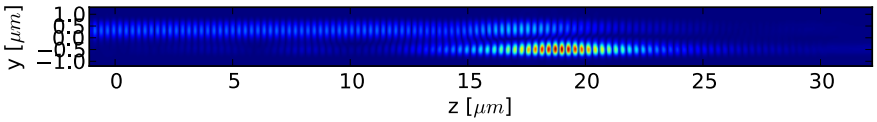

Figure 5.6: Simulated time-averaged spatial distribution of the magnitude of the electric field at the reflection peak of the electrically pumped resonant mirror in figure 5.4. The figure is in linear scale.

5.2.4 Threshold current

This section will elaborate on what electrical current is required through the MQW region to operate the laser. In essence, calculating the threshold condition in case of the electrically injected laser is very similar to the optically pumped equivalent. The most important differences are listed below:

- Instead of generating electrical carriers by absorbing a pump laser beam, the electron-hole pairs are now provided through an electrical current.

- The electrically injected III-V waveguide utilises a MQW stack instead of a bulk active layer. The carrier dependent gain coefficient is no longer linear,

but obeys a logarithmic law:

$$G(N) = G_0 \ln(\frac{N}{N_0}) \tag{5.1}$$

with $G_0 = 1800cm^{-1}$ and $N_0 = 2.2 \times 10^{18}cm^{-3}$ according to [3] for InP based quantum wells.

- The InP cladding layers are now doped, which will induce optical losses. Especially in p-doped materials, where an abundance of holes promotes transitions between the different valence bands (heavy-hole, light-hole and spin-split-off) and results in significant optical absorption. This mechanism is called inter-valence band-absorption (IVBA). Contrary to the optically pumped case, mirror losses an scattering losses will not be the only loss mechanism in the laser cavity.

5.2.4.1 Threshold gain

Again, the first step in determining the laser's threshold condition is to find the gain that is necessary to compensate for all the losses. The loss-mechanisms considered in this analysis are mirror losses and material absorption due to doping:

$$\Gamma_{act} G_{th} = \alpha_{tot} = -\frac{1}{2L_{eff}} \ln(R_1 R_2) + \sum_i \Gamma_i \alpha_i \tag{5.2}$$

with Γ_{act} the confinement factor of the quantum wells, G_{th} the material gain per unit length, α_{tot} the total losses per unit length, L the effective laser cavity length in the III-V material, R_1 and R_2 the front and back mirror power reflectivity, Γ_i the confinement factor of layer i and finally α_i the material loss of layer i. The confinement factors of all the different layers are given in table 5.2. Note that the effective laser cavity length is the distance the optical mode travels in the III-V waveguide between two *reflections*. To a good approximation this length can be chosen als the distance between the two slow-light sections of the silicon cavities.

The doping induced losses are given by:

$$\alpha_{dop} = k_n n + k_p p \tag{5.3}$$

with n and p the electron and hole concentration respectively. At $1550\,nm$, k_n is around $3.85 \times 10^{-18}cm^2$ for InP lattice matched materials and k_p is found to be $25 \times 10^{-18}cm^2$. Assuming that the doped materials are completely ionized, the carrier concentration equals the doping level and the material absorption can readily be calculated. The results are shown in table 5.2.

Layer	Γ_i (%)	α_i (cm^{-1})	$\Gamma_i\alpha_i$ (cm^{-1})
p-InP	49.4	7.5	3.7
wells	10.9	/	/
barriers	18.3	0	0
n-InP	18.7	7.7	1.44
BCB	2.7	0	0

Table 5.2: Confinement factor, material loss and contribution to the modal loss of the different layers in the III-V waveguide

	L_{eff} (μm)	α_{dop} (cm^{-1})	α_R (cm^{-1})	α_{tot} (cm^{-1})	G_{th} (cm^{-1})	N_{th} $10^{18}cm^{-3}$
short	54.8	5.14	23.3	28.44	260.917	2.54
long	134.8	5.14	9.48	14.62	134.13	2.37

Table 5.3: Summary of the absorption losses, mirror losses and required threshold material gain for the short and long laser.

Assuming two identical mirrors with the mirror characteristics depicted in figure 5.5, $R_1 = R_2 = 88\%$. Consequently $\alpha_{mirror} = 0.1278/L_{eff}$. As stated relier, two different laser lengths are considered: a short version with $20\mu m$ between the gratings and a longer version with $100\mu m$ between the cavities. The actual length that the light passes in the III-V waveguide is longer than the spacing between the gratings. Similar to the treatment of the optically pumped laser, this *effective cavity length* L_{eff} can be taken as the spacing between the 2 silicon grating's defects. The silicon cavity gratings have a front mirror grating of 60 periods $(290\,nm)$ which adds up to $17.4\mu m$ on each side. So the effective distance that the light travels through the III-V waveguide is $L_{eff} = 54.8\,\mu m$ in the short laser and $L_{eff} = 134.8\mu m$ in the long laser. Consequently, the mirror losses are $23.3/cm$ for the short laser and $9.48/cm$ for the long laser.

Table 5.3 summarises the different losses due to doping induced optical absorption and mirror losses. The second to last column shows what material gain is required to compensate all the optical losses and reach threshold. As expected, the longer laser requires a lower threshold gain per unit length to cancel the losses because the mirrors are spaced further apart.

The carrier density at threshold N_{th} is calculated from the required material gain by considering the carrier dependent gain function of the quantum wells in equation 5.1. The results are listed in the last column of table 5.3

Symbol	Parameter	Value	Reference
A_s/V_s	exposed surface to active volume ratio	$2/800\,nm$	/
v_g	group velocity	$c/3.732$	simulation
G_0	MQW gain coefficient	$1800\,cm^{-1}$	[3]
N_0	transparency carrier density	$2.2 \times 10^{18} cm^{-3}$	[3]
Γ	MQW confinement factor	10.09%	simulation
T	transmission to SOI	3.0%	simulation

Table 5.4: Carrier rate equation model parameters

5.2.4.2 Carrier rate equation

The threshold current is calculated using a rate equation describing the time-evolution of the carrier density. This equation is identical to 4.12 except for the pumping term:

$$\frac{dN_c}{dt} = \frac{I}{qV_p} - (A + \frac{A_s}{V_s}v_s)N_c - BN_c^2 - CN_c^3 - v_g G(N_c)S \qquad (5.4)$$

with I the total current flowing through the quantum wells, q the elementary electron charge and V_p the total pumped active volume. The carrier recombination mechanisms are identical to the ones considered in the optically pumped case:

- SRH recombination AN_c
- surface recombination $A_s/V_s v_s N_c$
- radiative recombination BN^2
- Auger recombination CN^3

The values for A, v_s, B and C are identical to the values in table 4.3. Again, two cases are considered:

- Best case scenario: low Auger recombination and no surface recombination
- Worst case scenario: high Auger recombination and surface recombination

The parameters that are unique to the electrically injected device are listed in table 5.4. The other parameters can be taken from table 4.3.

5.2.4.3 Threshold current

The threshold current is once again calculated assuming that after transient effects have died out, $dN_c/dt = 0$ and that at the threshold point the photon density S is very small and can be neglected. So:

$$I_{th} = qV_p[(A + \frac{A_s}{V_s}v_s)N_{th} + BN_{th}^2 + CN_{th}^3] \qquad (5.5)$$

In the best case scenario (low Auger recombination and negligible surface recombination) this yields $I_{th} = 0.912\,mA$ for the short laser and $I_{th} = 1.54\,mA$ for the long laser. The worst case scenario results in a threshold current of $I_{th} = 6.96\,mA$ for the short laser and $I_{th} = 11.8\,mA$ for the long laser.

5.2.4.4 Output power

Using equation 5.4, the photon density S at a certain injection current I above threshold I_{th} is calculated as:

$$S = \frac{I - I_{th}}{qV_{act,p}v_g G_{th}} \tag{5.6}$$

The total amount of photons in the cavity is given by SV_m. Per roundtrip ($2L_{eff}/v_g$), a fraction T is coupled into the silicon output wire on each side, so 2T in total (see figure 5.5 for T). The energy of one generated photon is $\hbar\omega_l$. Consequently, the laser's output power is given by:

$$P_{out} = 2T\frac{SV_m v_g}{2L} = T\frac{(I - I_{th})\hbar\omega_l}{q\alpha_{tot}L} \tag{5.7}$$

With $V_p/V_m = \Gamma$ and $\Gamma G_{th} = \alpha_{tot}$. The laser's current slope efficiency, $(I - I_t h)/P_{out}$ is given by:

$$\eta_{slope,I} = T\frac{\hbar\omega_l}{q\alpha_{tot}L_{eff}} \tag{5.8}$$

This results in $0.154W/A$ for the short laser and $0.12W/A$ for the longer laser. The power efficiency will be discussed later if the electrical properties of the structure are known.

5.2.5 Electrical design

The power that is dissipated in the device is the product of the current running through times the voltage that is across the contacts. The previous section investigated how much current should be flowing through the junction to operate the laser. This section will calculate what voltage is found across the contacts, given a certain current.

Rigorous analysis requires solving the drift and diffusion equations across the entire structure. This is a resources-intensive operation and doesn't provide a lot of insight. The problem can be simplified significantly by reducing the structure to a lumped elements model. In this model the different layers and interfaces are approximated as lumped elements with relatively simple individual I-V characteristics. The overall I-V characteristics are then calculated by using simple lumped

element circuit analysis methods.

Figure 5.7 shows a simple lumped elements model of the III-V waveguide structure proposed in figure 5.2. It consists of the following elements:

- $R_{c,p}$: contact resistance between the p++ InGaAs contact layer and the TiAu metallic top contacts
- $R_{p,1}$: Sheet resistance of 1 pillar. It consists of the passage through the p++ InGaAs, the p++ InP, the p+ InGaAsP and the p-InP.
- D_1: The series of voltage drops across the following heterojunctions: InGaAs-InP, InP-InGaAsP and InGaAsP-InP. As will be shown below, they can be modelled as diodes.
- $R_{p,2}$: resistance through the narrow p-InP channel connecting the pillar to the MQW region
- D_2: The MQWs are modelled as a carrier controlled voltage source
- R_n: resistance of the n-InP channel that connects the MQW region to the NiGeAu metallic n-contacts
- $R_{c,n}$: contact resistance between the n-InP and the NiGeAu metallic n-metal.

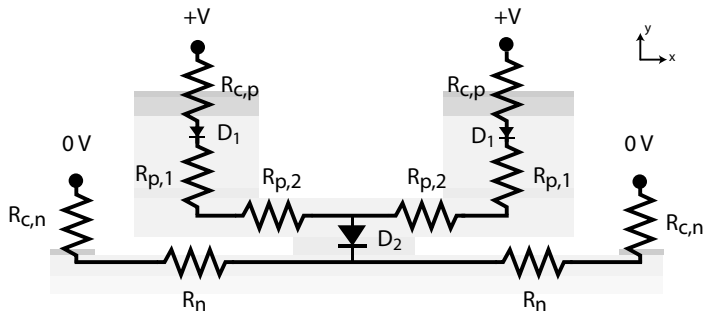

Figure 5.7: Lumped element model of the III-V waveguide for an electrically pumped resonant mirror scheme.

The laser will be pumped along its full length, spanning between the outer edges of the silicon mirrors. So for the electrical analysis, the length of the short laser is $80.5\,\mu m$ and the long laser is $160.5\,\mu m$.

Layer	N_{dop} $(10^{18}cm^{-3})$	μ_0 (cm^2/Vs)	μ_{dop} (cm^2/Vs)	N_{ref} $(10^{17}cm^{-3})$	α
p++- InGaAs	10	320	10	4.9	0.403
p++ InP	5	170	10	4.87	0.62
p+ InGaAsP	0.5	226	10	4.89	0.54
p InP	0.3	170	10	4.87	0.62
n InP	2	5200	400	3.0	0.42

Table 5.5: Doping levels and mobility parameters for the different materials in the III-V waveguide stack

Before discussing these different contributions in more detail, table 5.5 lists all the doping levels that are used in the III-V stack. The resistance of a particular layer is calculated by:

$$R = \frac{1}{\sigma}\frac{l}{A} \tag{5.9}$$

with σ the materials conductivity, l the distance that should be traversed and A the surface area perpendicular to the current flow. The conductivity is material and dopant dependent and obeys the following relationship:

$$\sigma = q\mu N \tag{5.10}$$

with q the elementary electron charge, μ the carrier mobility and N the carrier density (electrons in n-doped material and holes in p-doped material). In a doped material it is safe to assume that $N = N_{dop}$ The mobility decreases with increasing doping levels because adding impurities to the semiconductor crystal will limit the flow of carriers. This is modelled by the following equation [4]:

$$\mu(N_{dop}) = \mu_{dop} + \frac{\mu_0 - \mu_{dop}}{1 + (N_{dop}/N_{ref})^{\alpha}} \tag{5.11}$$

with μ_0 the maximum mobility (undoped material) and μ_{dop} the minimum mobility. All the material dependent parameters to evaluate the mobility are also listed in table 5.5.

5.2.5.1 p-contact resistance $R_{c,p}$

The contact resistance was measured using a transmission line measurement (TLM) on the bonded III-V epi. For the p-contact (TiAu) it was found to be $7.5 \times 10^{-5}\Omega cm^2$. The pillars are $1.8\,\mu m$ wide, so the contact resistance per pillar is $52.1\,\Omega$ for the short laser and $26.0\,\Omega$ for the long laser.

Layer	l (nm)	σ $(\Omega^{-1}cm^{-1}/)$	R $(160\,\mu m)$ (Ω)	R $(80\,\mu m)$ (Ω)
p++- InGaAs	200	130	0.107	0.054
p++ InP	800	32.5	1.71	0.85
p+ InGaAsP	100	9.38	0.74	0.37
p InP	200	4.9	2.84	1.42
$R_{p,1}$			2.7	5.39

Table 5.6: Sheet resistance of the different layers in the p-doped pillar assuming a $100\mu m$ *long device.*

5.2.5.2 pillar sheet resistance $R_{p,1}$

Each pillar consists of 3 different materials: InGaAs, InP and InGaAsP and 3 interfaces: InGaAs-InP, InP-InGaAsP and InGaAsP-InP. The sheet-resistance of the different layers is easily calculated using formula 5.9. The results are shown in table 5.6 for both the long and the short laser. The resistance scales inversely proportional with device length: halving the length will double the sheet resistance. As could be expected, the sheet resistance of these layers is very low and will prove insignificant as compared to other sources of electrical resistance.

5.2.5.3 Pillar layer interface I-V characteristic

The voltage drop across the different interfaces between the layers in the p-pillar is much more difficult to assess. When two different doped semiconductor materials are connected (this is a heterojunction), charges will redistribute which will result in a potential barrier between the two materials. Despite this potential barrier, charges can flow across the interface when a voltage is applied. This is due to two distinct mechanisms:

- Thermionic emission: the electrons in a material at a temperature $>$ 0K are distributed across the energy spectrum according to a Fermi-Dirac distribution. Consequently, a fraction of the electrons will have an energy that is larger than the potential barrier and can traverse to the other material.
- Tunneling: According to quantum mechanics, there is a finite chance that particles with an energy lower than that of a potential barrier can *tunnel* through that barrier. The actual probability of this event happening depends on the height and width of the potential barrier.

Tunneling is difficult to estimate, so as a worst-case approximation, only thermionic emission is considered. According to [4], the hole current density j_p across an interface due to thermionic emission (Boltzman approximation: $E - E_{v,min} >$

$3k_BT \approx 75meV$) is given by:

$$j_p = A_p^* T^2 [\exp -\frac{E_{Fp,left} - E_{v,min}}{k_B T} - \exp -\frac{E_{Fp,right} - E_{v,min}}{k_B T}] \quad (5.12)$$

with $E_{v,min}$ the bottom of the potential barrier, $E_{Fp,x}$ the fermi level on the left or right side of the interface, T the temperature, k_B the Boltzman constant and A_p^* the Richardson constant given by:

$$A_p^* = \frac{q m_v k_B^2}{2\pi^2 \hbar^3} = 120 A cm^{-2} K^{-2} m_v/m_0 \quad (5.13)$$

where m_v is the average effective hole mass. To simplify equation 5.12 even further, assume that the energy reference point $E = 0$ lies at the Fermi level in the case of zero voltage ($V = 0$). In this case, the different energy levels become:

$$E_{Fp,left} = -qV \quad (5.14)$$

$$E_{Fp,right} = 0 \quad (5.15)$$

$$E_{v,min} = -\Delta E_v \quad (5.16)$$

with V the applied voltage. The barrier energy minimum $E_{v,min}$ is taken as the valence band offset ΔE_v. This is a crude approximation assuming that the Fermi levels are close to the valence band level and that the barrier is as high as the valence band offset. Following these assumptions, equation 5.12 becomes:

$$j_p = A_p^* T^2 \exp \frac{-\Delta E_v}{k_B T} [\exp \frac{qV}{k_B T} - 1] \quad (5.17)$$

This is the diode-like dependence that could be expected from a heterojunction. In solving laser problems it is more common that the current is given and the voltage is unknown. Inverting the previous equation yields:

$$V = \frac{k_B T}{q} \ln[1 + \frac{I}{A_j A_p^* T^2} \exp \frac{\Delta E_v}{k_B T}] \quad (5.18)$$

with A_j the surface area of the junction and I the current flowing through the junction. Table 5.8 shows the conduction band offset, hole effective mass and the voltage drop across each junction in the case of $5\,mA$ of current. In this particular case, the voltage drop adds up to approximately half a Volt and due to the logarithmic dependence this is only weakly dependent on the laser length and current. It should be stressed that this is a crude, worst case estimate. In reality the barrier will be lower than the valence band offset and carriers will also be able to tunnel through the barrier.

Interface	ΔE_v (meV)	m_h (m_0)	V $(80\,\mu m)$ (mV)	V $(160\,\mu m)$ (mV)
InGaAs/InP	437	0.573	258	240
InP/InGaAsP	353	0.59	170	153
InGaAsP/InP	353	0.59	170	153
Total			598	546

Table 5.7: Voltage drop across the different interfaces in the p-pillar assuming worst-case thermionic emission and $5\,mA$ of current flowing through the pillar

5.2.5.4 p-cladding sheet resistance

To flow from the pillar to the MQW region, the current has to pass through a slab of modestly p-doped InP. Contrary to the wide pillar, this p-doped channel is narrow and relatively long $(600\,nm)$. Using the parameters in table 5.6, this results in a resistance of $76.6\,\Omega$ per channel for the short laser and $37.8\,\Omega$ per channel for the long laser.

5.2.5.5 MQW region

The multi quantum well region can be modelled as a carrier dependent voltage source [3]:

$$V_{MQW} = V_0 \ln(1 + \frac{N}{N_e}) \tag{5.19}$$

with N_e the intrinsic carrier density and $V_0 = nk_BT/q$ where n is the diode's ideality factor, which is assumed to be 2, so at room temperature $V_0 = 51.7mV$. The intrinsic carrier density in the active region is $2.5 \times 10^{11} cm^{-3}$ [3]. At threshold, the carrier density $N = N_{th}$, so $V_{MQW} = 834mV$ for the short laser. The long laser's MQW voltage is $4\,mV$ lower.

5.2.5.6 n-InP sheet resistance

To improve optical coupling, the bottom n-doped InP layer is chosen as thin as possible, $100\,nm$. To reduce the risk of short-circuit during fabrication, the n-contacts are $4.2\mu m$ away from the pillars, so adding the under-etched region length, the total length of n-doped InP dat should be traversed is $6.6\mu m$. At first sight, this looks at least an order of magnitude worse than the thicker and shorter p-channel. Fortunately, the mobility of electrons is much higher than that of holes. Also, the absorption induced by n-doping InP is significantly lower than the inter-valence band absorption in p-doped InP. Consequently, the material can be n-doped at a higher level, so there are more free electrons, which reduces the material resistivity. Using the parameters in table 5.5, the resistance of the $80\,\mu m$ long sheet is

$13.6\,\Omega$ and the $160\,\mu m$ device is $6.81\,\Omega$.

5.2.5.7 n-contact resistance $R_{c,n}$

The specific contact resistance of the NiGeAu contacts was measured to be $7.68 \times 10^{-7}\Omega cm^2$ with an interaction length of $0.56\,\mu m$. This yields a resistance of 0.857Ω per contact for a $160\mu m$ long laser and $1.71\,\Omega$ for an $80\,\mu m$ long laser.

5.2.5.8 I-V characteristics

The total I-V characteristic is calculated by considering all the different contributions discussed in the previous paragraphs. Looking at the lumped elements model in figure 5.7, the scheme actually consists of two identical arms in parallel (the pillars), the MQW region and two other identical arms in parallel (the n-sheets + contacts). In other words, the circuit can be simplified into a circuit as shown in figure 5.8. The resistance of this circuit is the laser's *series resistance* and will be the slope of the IV curve. This resistance is given by:

$$R_s = \frac{1}{2}[R_{c,p} + R_{p,1} + R_{p,2} + R_n + R_{c,n}] \tag{5.20}$$

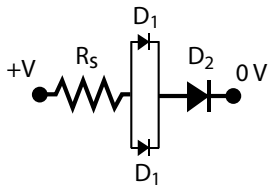

Figure 5.8: Simplified lumped elements model based on figure 5.7. The series resistance R_s is given by equation 5.20

This adds up to $74.7\,\Omega$ for an $80\mu m$ long laser and $37.4\,\Omega$ for 160 μm.

The total voltage across the device is then given by:

$$V_{tot} = R_s I + V_{D1}(I/2) + V_{D2}(I) \tag{5.21}$$

with the diode voltages according to equations 5.18 and 5.19.

5.2.5.9 Laser power consumption

Knowing the device's I-V characteristic allows to calculate the total power consumption of the laser. The most important metric is the power that is consumed at threshold. This is calculated by multiplying the threshold current with the voltage across the device. The results for the different laser lengths are depicted in table

Length (μm)	Case	I_{th} (mA)	V_{th} (V)	P_{th} (mW)
$80\,\mu m$	Best	0.912	1.21	1.1
$80\,\mu m$	Worst	6.96	1.76	12.3
$160\,\mu m$	Best	1.54	1.18	1.82
$160\,\mu m$	Worst	11.8	1.67	19.7

Table 5.8: Voltages and consumed power at threshold for the short and long laser in both the best and worst case scenario.

5.8 for both the best-case and worst-case situations.

The most striking conclusion is that the best- and worst-case power dissipation differs about an order of magnitude: from very good ($1mW$) to very bad ($10\,mW$). The main reason for this is the spread on the Auger recombination parameter C. The analysis of the optically pumped laser in the previous chapter showed that the experimental data corresponds closer to the best-case scenario with low Auger recombination and no surface recombination. However, it is not justified to claim the best-case performance and the worst-case scenario should also be taken into account.

5.2.6 Thermal analysis

When considering the slope efficiency of the laser calculated in section 5.2.4.4 and taking into account the operating voltages discussed in the previous paragraph, it should be clear that there is a large discrepancy between the electrical power that is pumped into the laser device and the optical power that is coupled to the silicon output power. This has various reasons:

- Electrical carriers lose energy traveling towards the MQW region: sheet resistance, crossing potential barriers, contact resistance. All these mechanisms cause a certain voltage drop and the power that is dissipated is the product of the current flowing through that section times that voltage drop.

- Once carriers are trapped in the quantum wells, only a fraction will recombine to contribute to the output power. The different non-radiative and spontaneous recombination mechanisms consume all the other carriers.

All this energy is lost into heat. Since the optical output efficiency is rather modest, most energy that is pumped into the laser is converted into heat. Consequently, the device heats up. This self-heating limits the performance of opto-electronic devices due to various reasons, for example the exponential temperature dependence

Material	Thermal conductivity κ_L $(WK^{-1}m^{-1})$
InP	68
BCB	0.3
SiO_2	1.27
Silicon	131
Gold	150

Table 5.9: Thermal conductivity of the relevant materials used in the thermal resistance simulations.

of Auger recombination and spilling of carriers out of the MQW region.

The generated heat should be sunk from the active region to the substrate underneath. The efficiency by which this is accomplished is given by the devices thermal resistance R_{th}:

$$R_{th} = \frac{\Delta T}{P_{heat}} \tag{5.22}$$

with ΔT the temperature difference between the active region and the substrate and P_{heat} the power that is dissipated as heat in the quantum wells. To calculate the thermal resistance, the heat equation should be solved across the device [4]:

$$\rho_L C_L \frac{\partial T}{\partial t} = \nabla \cdot \kappa_L \nabla T + H_{heat} \tag{5.23}$$

with ρ_L the local material density, C_L the local specific heat of the material, T the local temperature, κ_L the local thermal conductivity and H_{heat} the heat power density. To estimate the thermal resistance, it is assumed that all the thermal power is dissipated in the quantum wells.

Thermal resistance is a steady-state phenomenon, so the time-derivative in equation 5.23 is set to zero and the only relevant parameter in the equation is the thermal conductivity κ_L. Table 5.9 lists the thermal conductivities of all the involved materials as used in the simulation. As can be seen in the table, the thermal conductivity of BCB is very poor and because the device is planarized using BCB this will have a significant effect on the thermal resistance of the device.

The heat equation was solved using the commercial multi-physics software COMSOL [5]. Figure 5.9 shows the temperature profile in the cross-section of the $160\,\mu m$ long laser with a $40\,nm$ thick BCB layer above the silicon waveguide level and 150 nm of silicon oxide deposited on the III-V waveguide prior to bonding. The sample is planarized with BCB and the BCB is back-etched to $300\,nm$

below the top of the InGaAs level. The gold p-metal is $9\,\mu m$ wide and 800 nm thick. The power dissipated in the MQW region is $1\,mW$. As can be seen in the image, the MQW reaches a temperature of $1.58K$. Consequently, the devices thermal resistance is $1.58K/mW$. The $80\,\mu m$ device has double the thermal resistance: $3.16K/mW$. When the laser is operated at twice the threshold power, the temperature increase in the short laser's MQW region will be $6.95\,K$ in the best-case scenario and $77.7\,K$ in the worst case scenario. The longer laser will heat up $5.75K$ in the best case and $62.25K$ in the worst case.

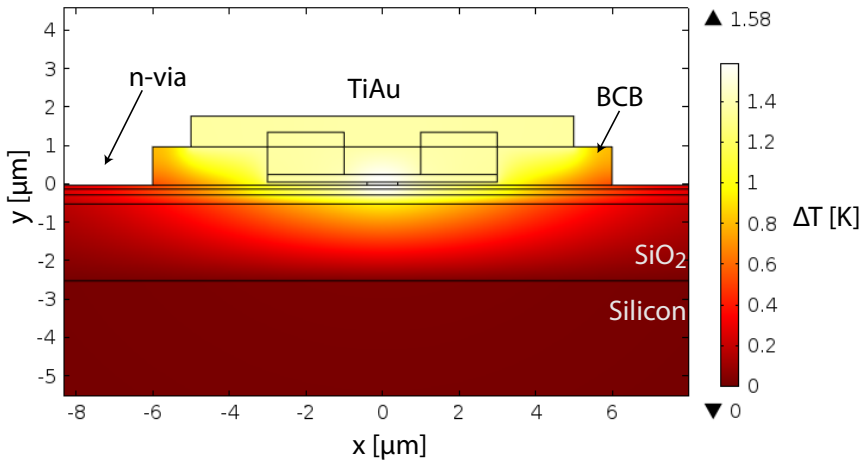

Figure 5.9: Temperature distribution through the $160\,\mu m$ long device as a result of dissipating $1\,mW$ of power in the MQW region.

To illustrate the impact of self heating, consider the most important recombination mechanism in the laser: Auger recombination. According to [] the temperature dependence of Auger recombination is given by:

$$C(T) = C_0 \exp[-\frac{E_a}{k_B T}] \tag{5.24}$$

with E_a the activation energy and k_B the Boltzmann constant. Assuming the activation energy is $60\,meV$ [], the increase of the Auger parameter due to self heating is given by: $C(372.32K)/C(300K) \approx 1.57$. In other words, the Auger recombination constant increases by approximately 60% in the worst case scenario.But it should be noted that the increase in Auger temperature will cause an increase in current density. In other words, to obtain the same output power, more current should be added, which in its turn will increase the temperature even more.

5.3 Fabrication

Looking at the proposed III-V waveguide cross-section in figure 5.2 raises questions about the manufacturability of such a laser. Almost a quarter of the time spent on this work was committed to developing a technological process to fabricate such a structure. This section will elaborate on these efforts. Similar to the optically pumped case, the silicon waveguide layer is fabricated at imec's 200mm CMOS pilot line through a multi-project wafer run organised by ePIXfab [6]. The III-V processing is done in-house.

5.3.1 Mask design

The first step in fabricating such a structure is to design a proper set of lithographic masks. Figure 5.10 shows an image of the full mask-layout including the silicon layers (pink color) and the III- V layers (other colors). Except for the laser structures, the mask also contains a number of test and helper structures, indicated numbers 1 to 5:

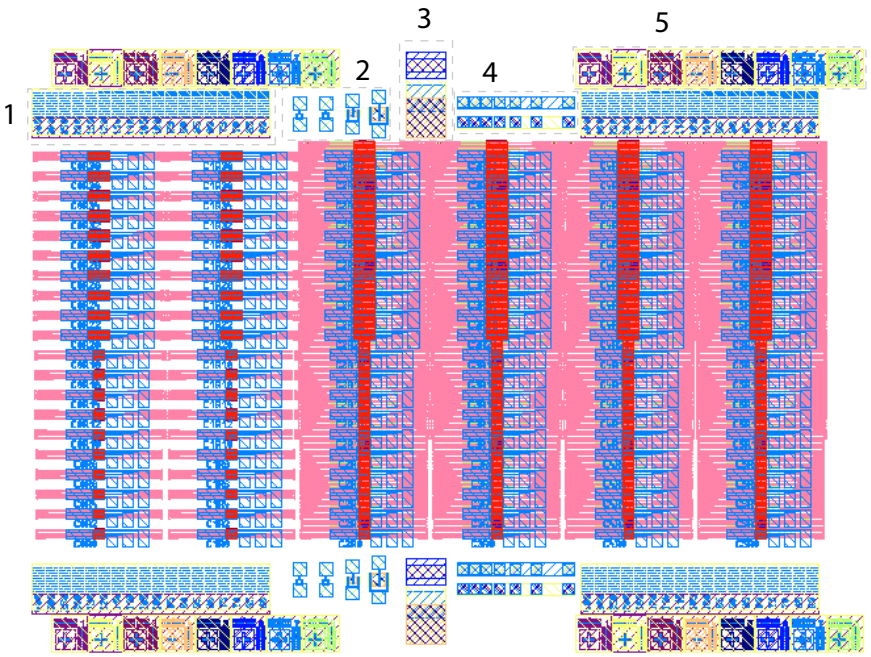

Figure 5.10: Full mask layout for the electrically pumped resonant mirror laser including the silicon layer (pink) and III-V layers (other colours).

- Undercut lift-off monitors [1]: 4 sets of lines of different width that will help determine the level of MQW undercut. This structure will be discussed in more detail later.
- Diodes [2]: 2 sets of 4 diodes each to test the electrical properties of the III-V stack
- Magnified laser structure [3]: 2 magnified partial laser structures that will help determine etch-depth during fabrication. These structures are big enough such that the height differences can be measured easily using a profilometer.
- TLM structures [4]: 2 sets of n- and p-TLM structures to measure the contact resistance.
- Alignment markers [5]: 4 sets of alignment markers to aid precise alignment during lithography. Each marker consists of an alignment cross and a vertical and horizontal Vernier marker.

The III-V processing mask consists of 7 layers:

- p-pillar definition
- p-pillar protection
- island definition
- n-metal definition
- p-metal definition
- n-via opening
- pad metal definition

The last layer actually consists of 2 physical layers because the silicon devices are so closely spaced that only half of them can be provided with electrical pads. The lasers are all processed together and in the very last step it should be decided which half will get electrical pads.

5.3.2 Processing

This section will discuss the different steps in the technological process to fabricate an electrically injected resonant mirror laser as proposed in the first part of this chapter. The most important challenges to fabricate the structure is to undercut the InAlGaAs MQW layers without etching the p-InGaAs contact layer. Because InAlGaAs with a bandgap near 0.8 eV (1550 nm) is very similar to InGaAs, both will be etched by the same chemistries. Consequently, the InGaAs layer should be protected to avoid etching.

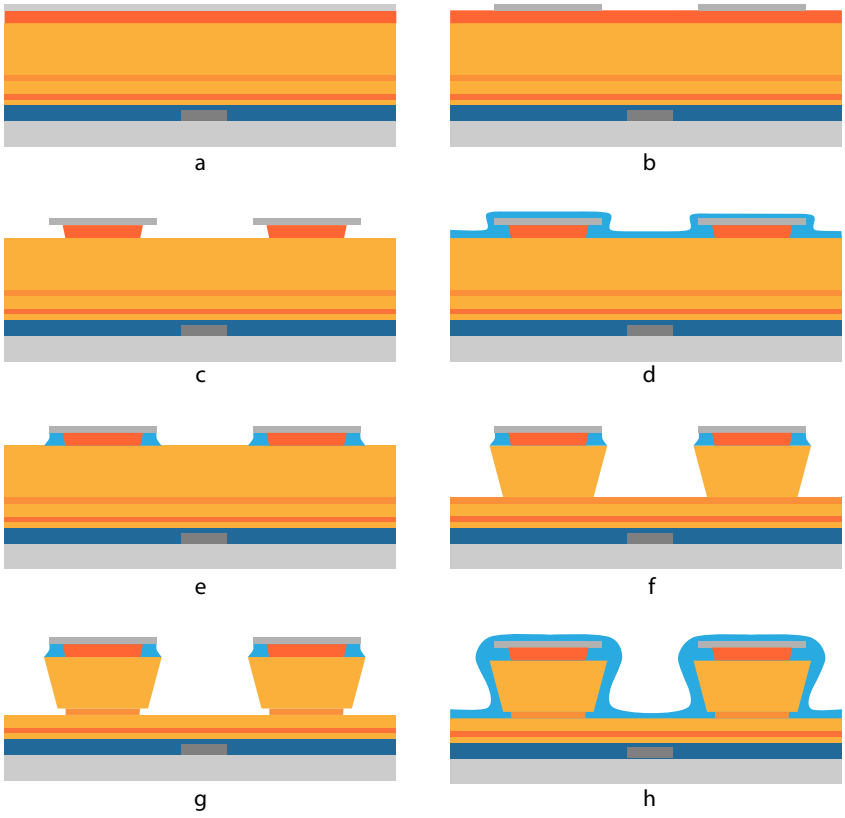

Figure 5.11: Schematic representation of the III-V waveguide cross-section throughout the different processing steps (part 1)

5.3.2.1 Surface preparation

III-V substrate The III-V wafer is cleaved into bars of 8mm wide and a few centimeters long. The short end of the bar should be parallel to the long flat of the III-V wafer. The reason for this is explained later. The epitaxy is grown upside-down on the III-V wafer: on the bottom are the p-doped layers and on top is the n-doped InP. The epitaxy is protected by a sacrificial InGaAs/InP (300nm/300nm) pair. After removing these two protective layers, $150\,nm$ of silicon oxide is deposited using plasma-enhanced chemical vapour deposition (PECVD). After oxide deposition the bar is cleaved into $6\,mm$ by $8\,mm$ dies that are ready for bonding.

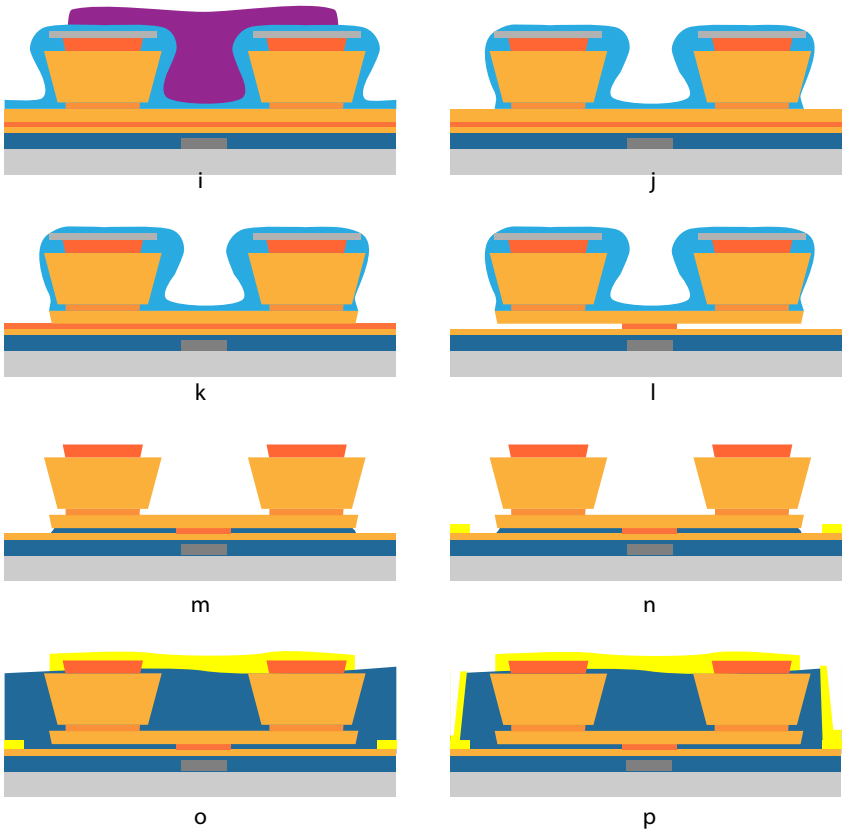

Figure 5.12: Schematic representation of the III-V waveguide cross-section throughout the different processing steps (part 2)

SOI substrate The silicon layer is processed at imec through an ePIXfab multi project wafer run. The run used for the electrically pumped resonant mirror laser is called *EP3642*. The air clad wafer is already diced and still covered with protective photoresist (PR). A sample is taken from the wafer and the PR is cleaned off with acetone and iso-propyl alcohol (IPA). Then the sample is cleaned in a microwave oxygen plasma for about 40-60 minutes to remove any remaining polymers and to oxidize the naked silicon structures for a few nanometers. This greatly increases the adhesion to the BCB glueing layer. After the oxygen plasma a 1:3 BCB layer is spin coated and cured at $180°C$ for 30 minutes to partially cure and consequently stiffen the film. This is found to increase bonding layer thickness uniformity dramatically.

5.3.2.2 Bonding and substrate removal

The III-V die is placed on the BCB-containing SOI die by hand using a pair of tweezers. Course alignment is done by eye. Alignment precision is approximately 0.5 mm so no microscope is necessary for alignment. The die pair is put on a 4-inch pyrex wafer and mounted in the bonding tool. The bonding chamber is pumped to vacuum and the sample stage is heated to $150°C$. Next the bonding tool applies force to the III-V and silicon die pair while gradually increasing the temperature to $250°C$. Finally the BCB film is cured at $250°C$ for one hour and cooled down slowly to finalize the bonding.

After the bonded die is unloaded from the bonding tool it is placed in a HCl solution to dissolve the InP substrate. The HCl solution is heated to around $40°C$ to increase the etching speed. Underneath the InP substrate there is a pair of InGaAs/InP (300nm / 300nm) layers that will act as etch-stop layers. After approximately 20-30 minutes the InP substrate has completely dissolved except for the InP 'ears' that are left on the 6mm edges of the bonded die. These are removed manually using a scalpel after protecting the die with photoresist. Next the InGaAs/InP etch stop pair is removed using $H_2SO_4 : H_2O_2 : H_2O$ and HCl respectively.

5.3.2.3 P-pillar definition

After removing the etch-stop layers, the p-doped InGaAs contact layer is exposed. First a $200\,nm$ silicon oxide layer is deposited using PECVD on the sample (step a in figure 5.11). This layer will be used as a hard mask to etch the underlying InGaAs layer. After patterning the layer using contact lithography, the hard mask is dry-etched using a reactive ion etcher (RIE) tool (step b). Next the InGaAs layer is etched using a citric acid (40cc) and hydrogen peroxide (2cc) solution. This quasi-isotropic etchant will also remove some of the InGaAs material underneath the silicon oxide hard mask (step c)

Now a silicon nitride film is deposited using PECVD. The recipe is chosen such that stress in the layer is minimised. This deposition is close to conformal and will also fill the undercut region (step d). Using an anisotropic dry etching recipe that contains CF_4 and H_2, all the silicon nitride is removed except for the fraction that is protected by the silicon oxide hard mask (step e). This way the InGaAs layer is now protected from any further etching. The InP (step f) and InGaAsP (step g) layers can now be etched using $HCl : H_2O$ (40cc:35cc) and $H_2SO_4 : H_2O_2 : H_2O$ (5cc:5cc:90cc) respectively. The InGaAsP layer serves as an etch-stop layer that will make sure that the p-doped InP layer that overlaps with the optical mode is alway the same thickness.

5.3.2.4 Center protection and MQW undercut etching

Another silicon nitride layer is deposited using PECVD (step h). The recipe of the deposition is altered to give the layer tensile stress. The reason for this will be clear soon. The nitride layer is patterned using contact lithography to cover the central part of the structure between the two pillars (i in figure 5.12). Etching the nitride layer with the same anisotropic dry etching recipe results in step j: the central part and the InGaAsP etch-stop layers are protected from any further etching.

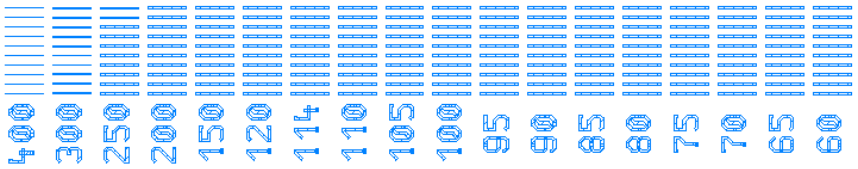

Figure 5.13: Test structures used to determine the level of undercut of the MQW region.

Now the p-doped InP layer is etched using $HCl : H_2O$ (40cc:35cc) (step k). Next the MQW region is under-etched using citric acid : hydrogen peroxide (40cc:2cc) (step l) [7]. To determine the level of undercut, the mask contains 4 sets of test structures that each consist of a series of lines of different width (1 in figure 5.10). Figure 5.13 shows a detail of one of these test structures. The width of the lines in each column is chosen such that they will lift off when the undercut region is as wide as the number indicates underneath each column. The unit of this number is 10's of nanometers, so 400 means 4000 nanometers.

After the undercut etching has finished, the bare III-V structure would be relatively unstable. The nitride layer provides extra support and the tensile strain actually opens up the undercut region and prevents it from collapsing. To permanently stabilise the structure, diluted BCB is spin coated and fully cured. After this curing the chip is once again loaded into the RIE tool to remove the BCB that is not covered by the InP. The remaining dielectrics (SiOx and SiNx) can now be removed, resulting in step m.

5.3.2.5 Metalization

After defining the appropriate areas using contact lithography, the n-metal (NiGeAu) can be deposited using the electron gun tool. After lift-off, the sample is planarized by spincoating a thick ($> 5\,\mu m$) BCB layer on the sample. After curing this layer the topography on the sample is typically around $100\,nm$. The BCB layer is etched

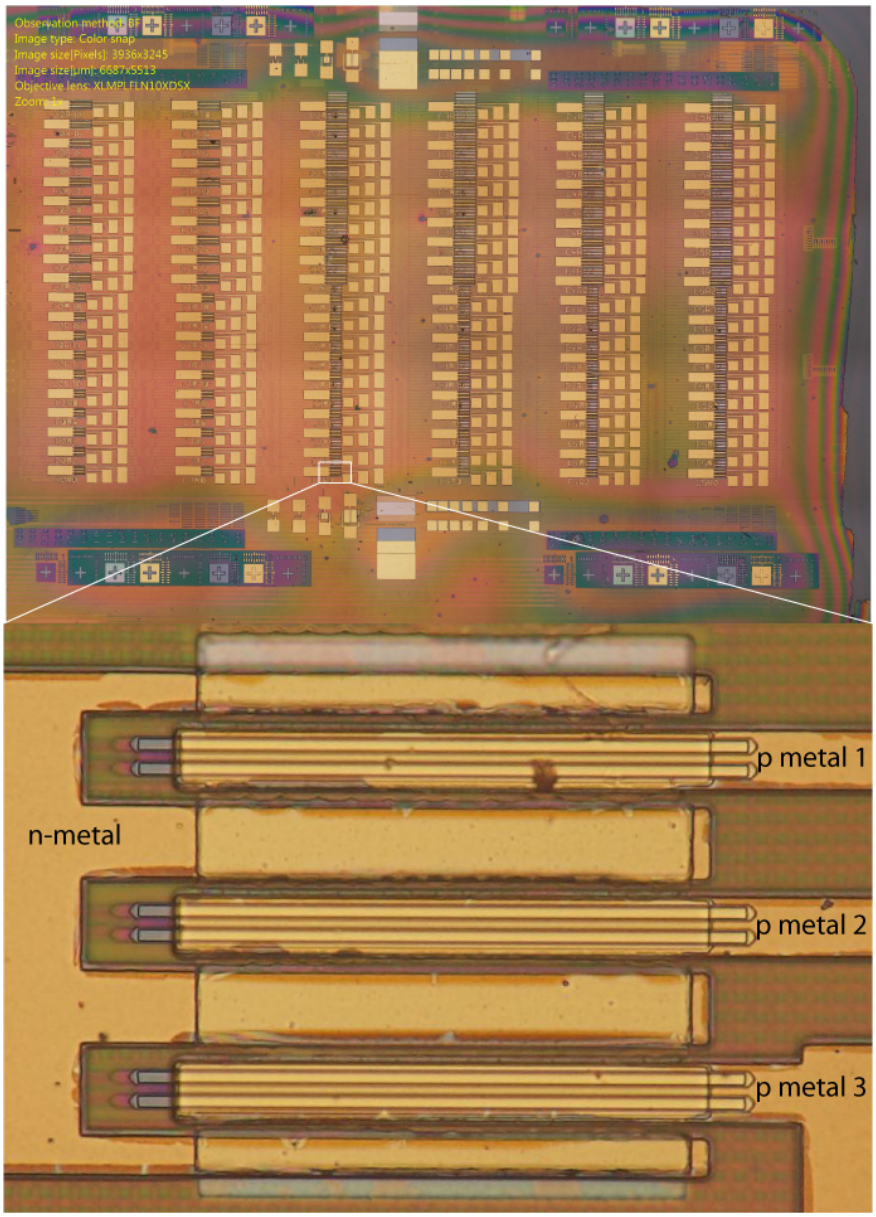

Figure 5.14: Microscopic overview of the finished chip fabricated with the mask in figure 5.10. The bottom figure shows a magnified shot of 3 devices.

back to around $300\,nm$ below the top of the p-doped InGaAs layer. Next the p-

metal (TiAu) can be patterned, deposited and lifted-off (step o). To finalise the sample, openings are defined and etched in the BCB layer to reach to the n-metal and thick gold pads are patterned, deposited and lifted-off (step p).

5.3.3 Results

Figure 5.14 shows the finished chip fabricated using the mask in figure 5.10. The inset shows a detailed picture of 3 devices that are connected to the pads. The n-contacts are interconnected to a common pad per every 3 devices. Each pair of p-pillars is addressed through metallic pads so each laser can be pumped individually. The silicon access waveguides are visible on the left side of the devices.

Figure 5.15 shows an SEM image of a cross-section of one of the devices made using focused ion beam milling. The undercut region is clearly visible. The BCB layer is approximately 40 nm thick. Adding up the 150 nm silicon oxide deposited on the III-V die prior to bonding results in a total distance between the top of the silicon layer and the bottom of the III-V layer of approximately 200 nm. The MQW region is somewhere between 750 nm and 800 nm wide and well-aligned to the silicon cavity. The undercut region is nicely filled with BCB.

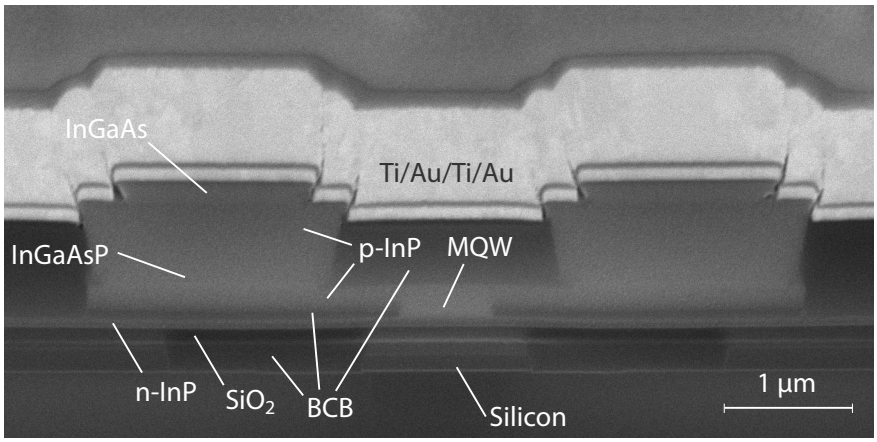

Figure 5.15: SEM picture of the cross-section of one of the fabricated devices.

5.4 Characterization

The fabricated devices were characterized in-house. The metallic contact pads were connected to a pulsed current source using standard probing needles. The

optical output of the left facet (n-pad side) is coupled into a single mode fiber using standard straight fiber couplers. A 3dB splitter couples half of the captured output light into an optical power meter and the other half into an optical spectrum analyser (OSA). The sample is fixed to a Peltier stage to set the substrate temperature.

5.4.1 IV curve

Before testing the optical properties of the device, its DC electrical response is characterised. Figure 5.16 (right axis) shows the voltage across the p- and n- pads as a function of the current (CW, not pulsed) that flows through the laser. This curve was only measured for a maximum current of $10\,mA$ (solid line). This was to make sure that the device would not be damaged. However, at this current level the laser diode reached its linear regime and the series resistance can be measured as the slope of the curve and used to extract the voltage at higher currents (dashed line). For this device the series resistance is $50\,\Omega$. This is significantly higher than the estimated $37.5\,\Omega$. However, this theoretical estimate assumes metallic contacts that underwent rapid thermal annealing whereas the measured sample did not receive this treatment.

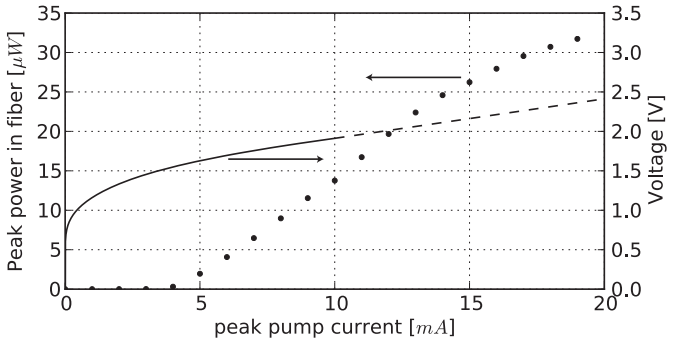

Figure 5.16: Left axis - dots: output power captured by the optical power meter and corrected for the 3dB splitter as a function of pump current for a $160\mu m$ *long device. Right axis: IV curve for the same* $160\,\mu m$ *long device (solid line) and prediction for higher currents (dashed line) extrapolated using the estimated series resistance.*

5.4.2 LI curve

Figure 5.16 (lef axis) also shows the peak power captured by the optical power meter and corrected for the 3dB splitter as a function of pump current. The Peltier

stage is set to $20°C$. The current pulse duration is $100\,ns$ and is repeated every $5\,\mu s$. The laser consists of 2 identical resonant mirrors that each contain 60 back grating periods ($290\,nm$), 10 defect periods (270 nm) and 30 front grating periods ($290\,nm$). There is $100.1\,\mu m$ in between the silicon grating cavities.

The figure clearly shows the laser threshold at $4\,mA$ and an initial linear behaviour for currents above threshold. The external slope efficiency, defined as the increase in optical power in the fiber divided by the increase in pump current above threshold is $25\mu W/mA$.

However, of much more interest is the power in the silicon waveguide, which is higher than the power in the fiber, mainly due to grating-coupler inefficiency. The mask contains a test waveguide specifically designed to evaluate grating coupler losses that consists of 2 grating couplers connected by a $1.6\mu m$ wide silicon waveguide. The measured grating coupler losses were 7dB per grating coupler. Taking ingot account the fact that the laser emits from both sides (3dB) yields a total slope efficiency in the silicon waveguide of 0.25mW/mA and a total output power of $300\,\mu W$.

5.4.3 Spectral properties

The spectral properties of the device with LI curve in figure 5.16 are shown in figure 5.17. The graph shows the spectrum for 4 different values of the injection current in the same pulsed configuration as discussed earlier. Below threshold, at $I = 3\,mA$ the spectrum is nearly flat. There is a small enhancement of the spontaneous emission into the laser resonance at 1553.4 nm. Slightly above threshold, at $4\,mA$, a single laser peak reaches out almost 30dB above the floor level. Increasing the current now increases the height of the laser peak up to 47dB above the floor level at 20mA current injection, proving the laser's single-mode behaviour. The width of the peak is determined by the finite resolution (200 pm) of the optical spectrum analyser used to study the spectral properties.

5.4.4 Thermal behaviour

The LI curve and the spectra shown in figures 5.16 and 5.17 were measured by injecting short $100\,ns$ current pulses into the device with a long repetition rate of $10\,\mu s$. The reason for this us that $100\,ns$ is much shorter than the thermal time constant of the laser and because the pulse repetition interval is relatively long, the laser does not heat up. In other words, thermal effects due to self-heating do not play a significant role in such pulsed operation.

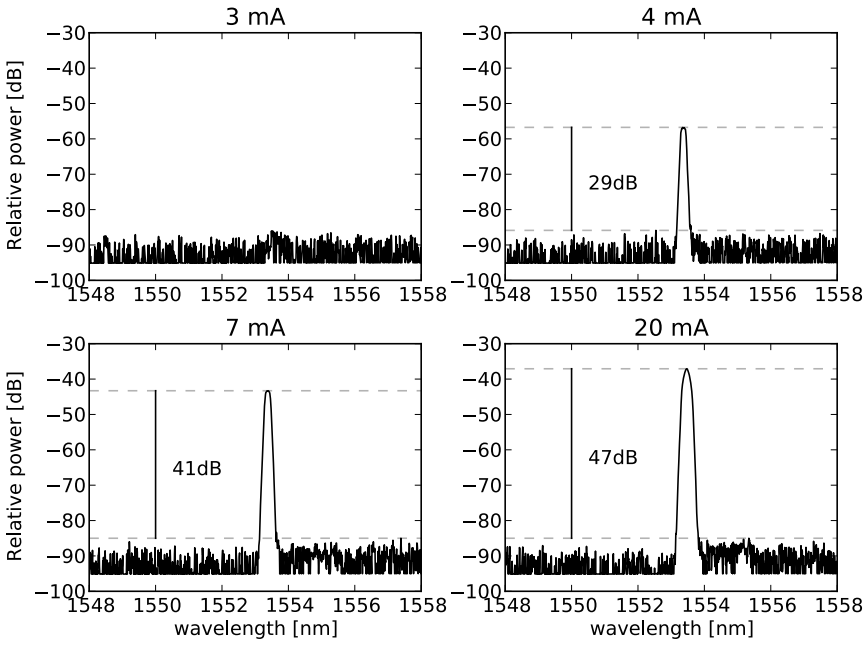

Figure 5.17: Spectrum of the $160\mu m$ *long resonant mirror laser with LI curve of figure 5.16 for different injection currents.*

However, for most applications continuous wave operation is required. In this case the laser will heat up due to the power consumption in the device (self-heating). The fabricated lasers did not work in a continuous wave regime, most likely due to excessive self-heating. Consequently it is very interesting to study the thermal properties of the device in order to improve the design of future generations and eventually enable continuous wave operation.

5.4.4.1 Stage temperature sweep

The thermal study starts by operating the laser in the same pulsed behaviour as before ($100\,ns$ pulses at $5\,\mu s$ intervals) to rule out self-heating. The chip is kept on a Peltier stage so the temperature of the substrate can be varied. Because there is no self-heating due to the pulsed operation, the laser MQW junction temperature is in first approximation equal to the stage temperature. This way the laser performance (threshold current and lasing wavelength) can be mapped out as a function of junction temperature.

The results of this measurement are shown in figure 5.18. The top panel shows how the spectrum, captured at 15mA injection current, shifts to longer wavelengths with increasing stage temperature. This data is summarised in figure 5.19. As expected, the lasing wavelength increases linearly with temperature at a rate of $82.3pm/K$. This corresponds well to the spectral shifts observed in comparable structures such as microdisk lasers [3].

The bottom panel of figure 5.18 shows the LI curve for different values of the stage temperature. The data is plotted in logarithmic scale to enable clear comparison between the different graphs. As expected, the threshold current increases rapidly with increasing stage temperature. Fitting the datapoints to an exponential curve yields a thermal constant T_0 of $16.86K$ and a threshold at $T = 0K$ of $2.63\,mA$.

In comparable InP based devices the thermal constant T_0 is much higher, typically around $70K$ [3]. In these devices the decrease in performance at higher temperatures is mainly due to decreased gain and increased non-radiative recombination, hence inherent material properties. The low thermal constant in the first generation resonant mirror laser most likely means that, apart from a reduction in optical gain and an increase in carrier losses, the optical laser cavity Q-factor also decreases with increasing temperature. Due to the increased temperature the effective indices of the silicon cavity and the III-V waveguide can drift apart, decreasing the optical coupling and consequently the mirror reflectivity.

5.4.4.2 Pulse length sweep

Mapping out the laser properties as a function of junction temperature as shown in the previous paragraph delivers all the necessary tools to study the laser's self heating. To do so, the pump pulse repetition rate was fixed at $10\,\mu s$, but the pulse length was varied from $100\,ns$ to $5\,\mu s$ in $100\,ns$ increments. The resulting spectrum at $10\,mA$ peak injection current is shown in figure 5.20 (grey curves). Increasing the duty-cycle heats up the structure and shifts the laser resonance to longer wavelengths. Three different spectra are highlighted in a solid black color and will be discussed below.

- The highlighted laser spectrum on the short-wavelength side is captured at a very short duty cycle (1%). There is no self-heating and the laser linewidth is limited by the resolution of the OSA.

- The second highlighted laser spectrum is taken for a duty cycle of 25%. This curve is significantly broadened as compared to the short DC curve. The reason for this is simple: during one pump pulse cycle, the laser heats

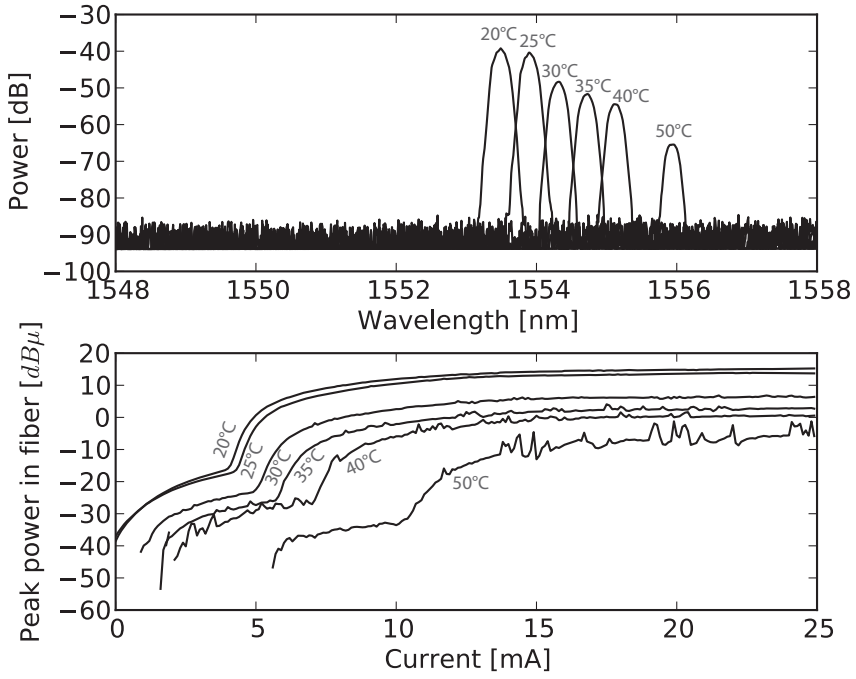

Figure 5.18: Spectrum at 15mA injection current (top) and LI curve (bottom) of pulsed measurement as a function of stage temperature.

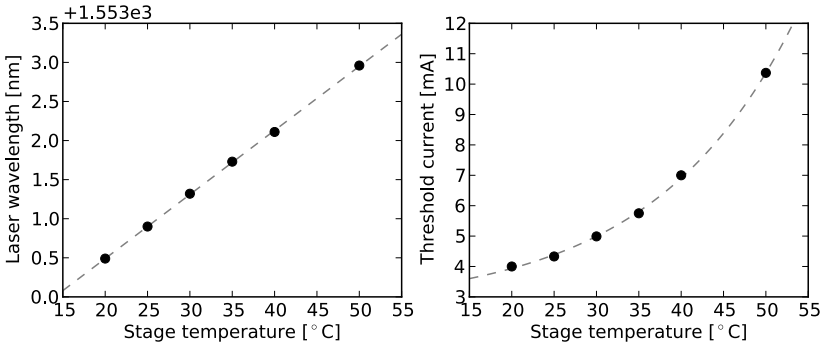

Figure 5.19: Spectral shift of the laser resonance (left) and threshold current (right) as a function of stage temperature

up and consequently its lasing wavelength shifts to longer wavelengths. This

dynamic spectral shift is captured by the OSA as a broader line shape.

- The third highlighted laser spectrum shows different characteristics than the previous two. The line-shape has a sharp short wavelength edge but its longer wavelength edge drops to a level above the OSA's noise floor. It is plausible that at the beginning of a pump cycle the laser turn on but as time progresses within each pump cycle, self-heating reaches a critical point and the laser shuts off.

To get more insight in the laser's behaviour, the most important aspects of this experiment are summarized in figure 5.21. This figure shows the shift of the short wavelength edge of the line shape (solid line), the long wavelength edge of the line shape (dashed line) and the difference between these two: the captured line width corrected for the OSA's limited resolution. The y-axis is both in wavelength units (left axis) and corresponding temperature change (right axis) calculated using the measured laser wavelength slope of $82.3\,pm/K$. The short wavelength edge is proportional to the laser temperature at the beginning of each pump cycle. This parameter is close to linearly proportional to the duty cycle. This is to be expected because as the duty cycle increases, the average power that is pumped into the device increases proportional to that.

The plot clearly shows the critical turn-off point at a 35% duty cycle. The long wavelength edge no longer shifts to even longer wavelengths and the line shape width starts decreasing. Surprisingly, the plot indicates that the laser turns off at a temperature increase of $10K$. This is not compatible with the measurements shown in figure 5.18 that show that the laser even operates at a temperature of $50°C$. A possible, yet speculative, explanation for this is that due to the dynamic nature of the pulse-length experiment, a temperature gradient arises between the III-V waveguide and the silicon cavity that detunes both in such a way that the mirror no longer functions and the laser shuts down. However, this should be investigated in more detail but lies beyond the scope of this work.

5.4.5 Multi-wavelength laser array

Because the laser wavelength is determined by the resonance wavelength of the silicon cavity, changing some of the properties of the silicon cavity will alter the laser's operating wavelength. One of the easiest adjustments that can be made to the silicon resonators is to change the width of the grating waveguide. By doing so, the effective index of the cavity mode changes slightly and the resonance shifts to shorter wavelengths for narrower cavities and to longer wavelengths for wider cavities. The fabricated chip contained 3 different silicon cavity widths: $1.3\,\mu m$, $1.6\,\mu m$ and $2.0\,\mu m$. The resulting spectra are shown in figure 5.22. The threshold

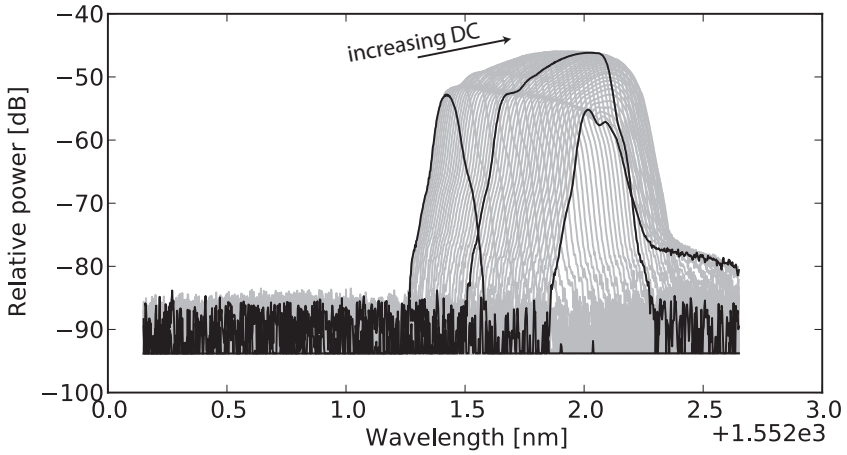

Figure 5.20: Captured laser spectra for $10\,mA$ *peak injection current as a function of pumping pulse duty-cycle ranging from* 1% *(shorter wavelengths) to* 50% *(longer wavelengths)*

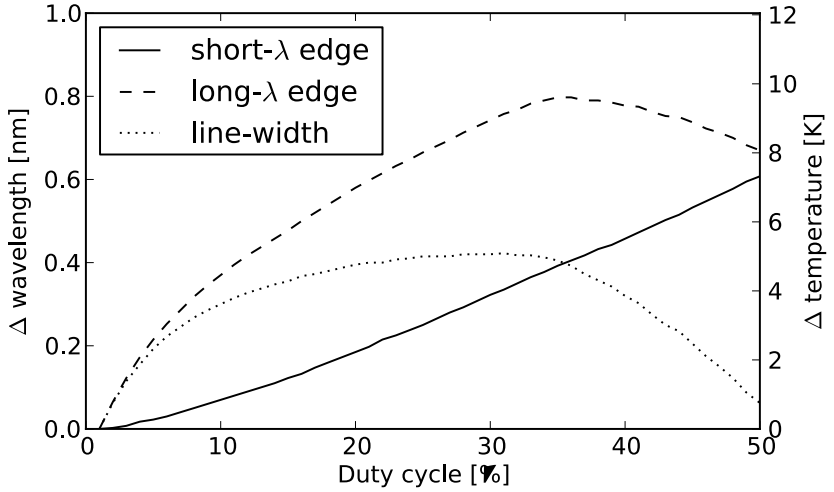

Figure 5.21: Summary of the pulse-length experiment shown in figure 5.20: the shift of the short wavelength edge, the long-wavelength edge and the difference between these two (the pulse-width) as a function of duty-cycle.

current of all three lasers is comparable (in the 4-5mA range) and each laser shows single-mode behaviour with a high side-mode suppression ratio. The spectra were captured at a peak pump current of $15\,mA$.

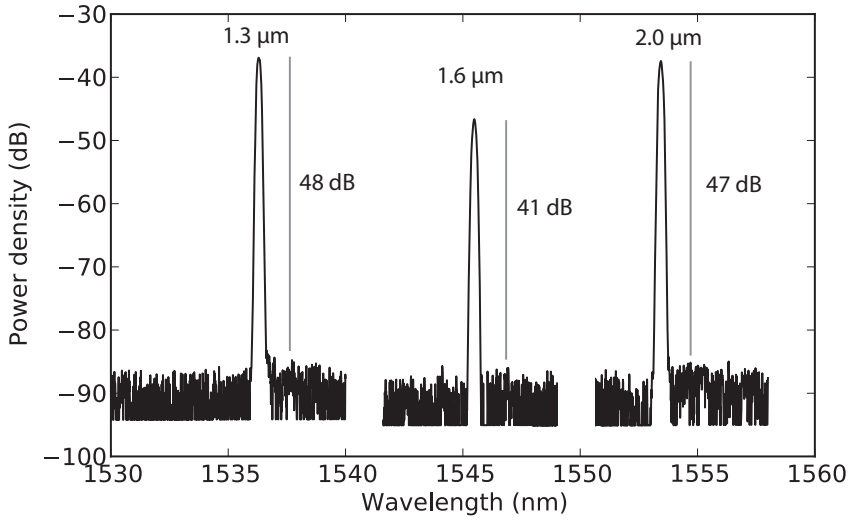

Figure 5.22: Output spectra of 3 different lasers with different silicon cavity widths as indicated above each laser line.

5.5 Conclusion

This chapter started with pointing out the particular difficulties in implementing an electrical pumping scheme in a resonant mirror laser on the $220\,nm$ SOI platform. To ensure phase-matching between the silicon cavity and the III-V waveguide, the geometry of the latter should be adjusted to reduce its effective index. It was shown that by etching a slit in the top p-layers and by undercutting the MQW region, the effective index can be reduced sufficiently. The optical, electrical and thermal properties of the device were simulated. Next the fabrication method that was developed was outlined. The fabricated devices were tested and the results were presented. The threshold current in pulsed regime went down to $4\,mA$ in single mode regime with a side-mode suppression ratio of almost 50dB. The thermal dependence of the laser was investigated and the efforts to operate the laser in a continuous-wave regime were described. Finally the ability of this approach to integrate multiple lasers, each lasing at a different, well-defined wavelength was demonstrated.

References

[1] S. Stankovic, R. Jones, M. N. Sysak, J. M. Heck, G. Roelkens, and D. Van Thourhout. *Hybrid IIIV/Si Distributed-Feedback Laser Based on Adhesive Bonding*. IEEE Photonics Technology Letters, 24(23):2155–2158, December 2012.

[2] Photonics Research Laborator - University of Maryland - http://www.photonics.umd.edu/software/wgmodes/. *WGMODES*.

[3] Joris Van Campenhout. *Thin film microlasers for the integration of electronic and photonic integrated circuits (PhD Thesis)*. 2007.

[4] Joachim Piprek. *Semiconductor Optoelectronic Devices*. Academic Press, 2003.

[5] Http://www.comsol.com. *Comsol*.

[6] The Silicon Photonics Platform-ePIXfab http://www.epixfab.eu. *ePIXfab*, 2012.

[7] Gregory C Desalvo, Wen F Tseng, and James Comas. *Etch Rates and Selectivities of Citric Acid / Hydrogen Peroxide on and InP*. Journal of The Electrochemical Society, 139(3), 1992.

6 Conclusions and future outlook

6.1 Introduction

In this final chapter the main results of this work will be summarized and possible future work will be discussed. First of all the study of linear grating cavities and the theoretical model describing resonant mirrors will be treated. Next the design, fabrication and characterisation of both the optically pumped and the electrically pumped resonant mirror lasers are outlined. Finally this chapter will provide some ideas for improving the performance of resonant mirror lasers.

6.2 Theory

The theoretic treatment in this work consists of 2 main parts: the first part (chapter 2) deals with the silicon grating cavities whereas the second part (chapter 3) studies what happens when such a silicon grating cavity is evanescently coupled to a III-V waveguide above (the *resonant mirror*).

6.2.1 Silicon grating cavities

One of the fundamental components of the resonant mirror lasers treated in this work is the silicon grating cavity. In chapter 2 the basic properties of three different silicon cavities are discussed:

- Band-edge cavity: a finite length periodic grating. The transition between the corrugated grating section and the uncorrugated waveguide section induces some reflectivity so Fabry-Perot-like resonances exist within the grating. Close to the grating's bandgap the propagating mode's group velocity is significantly slowed down which can result in high Q-factor resonances. However, as the grating gets longer, the free spectral range of the different resonances becomes smaller which limits its use for resonant mirrors

- Defect grating cavity: introducing a quarter wave defect in the center of a finite grating will create a single defect state in the center of the band-gap. Although the free spectral range of such resonances is sufficient to yield single mode lasers, the Q-factor is limited by scattering at the quarter wave defect.

- Hybrid band-egde/defect cavity: by surrounding a few periods of a shorter pitch grating (the band-edge section) and surrounding it with a longer pitch grating (the reflectors) a cavity is obtained that has a large free spectral range and reduced scattering at the defect (which is no longer a quarter wave section but the shorter pitch grating) which results in an order of magnitude increase in the Q-factor as compared to quarter wave defect gratings of similar size.

6.2.2 Resonant mirrors

This work presented *resonant mirrors* as reflectors in a heterogeneously integrated III-V on silicon laser. A resonant mirror as presented in this work is a passive silicon grating cavity that is evanescently coupled to an active III-V waveguide above. This work showed that in such a configuration the light that propagates in the III-V waveguide and interacts with the III-V waveguide/silicon cavity combination will experience high, narrow band reflection at the silicon cavity's resonance wavelength. To study this phenomenon, an implementation of scattering theory was employed. This is a theoretical framework that is mainly used in quantum mechanics to study how particles interact ('*scatter*') upon collision. It was shown in previous studies that this framework can be transferred to the optical domain to investigate the interaction between a propagating mode and localised resonant modes. By applying this theory to the resonant mirror configuration, two surprisingly simple formulas can be derived that describe the peak reflectivity R_{max} and the reflection bandwidth $\Delta\lambda$ of resonant mirrors solely as a function of the silicon cavity's intrinsic Q-factor Q_i and a *pseudo* Q-factor Q_κ that describes the coupling

between the waveguide and cavity:

$$R_{max} = \frac{1}{1 + Q_\kappa / Q_i} \tag{6.1}$$

$$\Delta\lambda = (\frac{1}{Q_i} + \frac{1}{Q_\kappa})\lambda_c \tag{6.2}$$

These formulae can serve as a guideline to obtain a preliminary estimate of the design parameters and provide insight in how these parameters will influence the performance of the resonant mirror.

By using 2D numerical simulations the aforementioned silicon cavity types can be assessed to be used in resonant mirror lasers. The easy to design defect grating cavity performs well if the phase matching condition is fulfilled. Because this work is focused on 220 nm SOI substrates, this means that in practice only optically pumped devices can be built using these grating cavities.

The hybrid band-edge/defect cavities can be designed to possess a higher intrinsic Q-factor which means that they are better suited if the phase-matching condition is hard to fulfil. This is in general the case for electrically injected lasers because the presence of electrical contacts and the fact that the optical mode should be spaced sufficiently far away from these contacts poses limitations on how thin the III-V layers can be. In both cases, numerical 2D simulations show that maximum reflectivities of above 90% can be achieved.

6.3 Proof of principle

In this work two proof-of-principle devices were demonstrated:

- An optically pumped device that is relatively easy to design to proof the resonant mirror approach works. However, optically pumped devices have a rather limited applicability.
- An electrically pumped devices that is more complicated to design and fabricate but has a high relevance.

6.3.1 Optically pumped device

The optically pumped resonant mirror laser prototype consists of a 260 nm thin, $1.6\mu m$ wide III-V waveguide with an 80 nm thick InGaAsP active layer on top of two identical silicon grating cavities. The grating cavities are 60 periods long and contain a quarter wave defect in the center of each grating. Full vectorial 3D FDTD simulations show that this configuration can yield a maximum reflectivity

of 80%. A simple rate-equation model predicts that the absorbed optical threshold power necessary to turn on the laser is between 0.5 and 3.0 mW, mainly depending on the Auger recombination parameter.

The laser was fabricated in our in-house cleanroom starting from a set of silicon chips processed by imec containing the grating cavities and lead-out waveguides connected to grating couplers for characterization. The III-V fabrication process is straight forward. The most notable steps are the bonding step and 1 lithographic step to define the III-V waveguide.

The lasers were characterized on a dedicated measurement setup at the CNRS Laboratory for Photonics and Nanostructures (LPN) in Marcoussis, France. The measured lasers had an absorbed threshold power down to 2.08 mW and a side mode suppression ratio of up to 38 dB with no side-modes visible on the spectrum. These measurement showed the potential of resonant mirrors for heterogeneously integrated lasers and paved the way for electrically pumped lasers.

6.3.2 Electrically pumped device

The practical relevance of optically pumped lasers is rather limited and the most important milestone of this work is the demonstration of an electrically pumped III-V on silicon laser with resonant mirrors. The most important hurdle to accomplish this is the phase-matching requirement between the III-V waveguide and the silicon cavity. As stated earlier, using a high Q-factor cavity such as a hybrid band-edge/defect grating relaxes this requirement but is still not sufficient to allow for a working lasers with the existing electrically injected III-V waveguide designs.

To solve this problem this work proposed a novel III-V waveguide geometry that drastically reduces the optical mode size and reduces its effective index. To accomplish this a 1.5 μm wide stripe is etched in the top layers to push the mode down and the MQW region is under-etched to confine the optical mode horizontally. Full vectorial 3D FDTD simulations show that such a waveguide, combined with a silicon hybrid band-edge/defect grating cavity can yield reflectivities of up to 90%. The threshold current is estimated to be somewhere between 1.54 mA and 11.8 mA.

This work developed a technological process to fabricate these proposed III-V waveguide geometries. The most important challenges were the protection of quaternary III-V layers during the long, wet MQW undercut and to prevent the structure from collapsing. A detailed description of this process can be found in this work.

The fabricated devices were characterised in a pulsed current regime and a threshold current of 4mA was demonstrated. The side-mode suppression ratio reached values up to 47 dB. It was shown that the laser operating wavelength depends solely on the resonance wavelength of the silicon cavity. The thermal properties of the laser were studied and it was found that its thermal constant T_0 is extremely low (16.86K). One possible explanation for this is that the III-V waveguide and silicon cavity become detuned when the laser heats up. It is believed that this low thermal constant prevents the laser from operating at room temperature.

To conclude, the results of this work can be compared to the list of requirements stated in the first chapter. Refer to table 1.1 to compare to state of the art. This work achieves part of its goals:

- High side mode suppression ratio: 48 dB
- Low threshold current: 4mA
- Definition of wavelength in the silicon layer
- High tolerance for III-V patterning
- On 220 nm SOI platform

However, the fact that the laser does not operate in continuous wave is a major drawback that limits its practical usability. The next section will discuss what steps can be taken to reach this target.

6.4 Future work

The next major milestone for this work is continuous wave laser operation. It is believed that the predominant hurdle preventing this are thermal issues due to self-heating. The following paragraphs provide suggestions to tackle these problems.

6.4.1 Reducing thermal resistance

A first option is to reduce the amount of self heating due to power dissipation in the III-V waveguide. The BCB layer and the thick silicon oxide buffer layer prevent efficient extraction of excess heat from the III-V waveguide to the silicon substrate. A simple way to reduce the thermal resistance between the III-V waveguide and the silicon substrate significantly is to increase both the width and the thickness of the gold top p-contact. This way heat is extracted from the III-V waveguide and spread out across a large area where it can propagate to the silicon substrate. It is estimated that this approach can yield a 50% to 70% reduction in thermal resistance.

6.4.2 Tackling low thermal constant T_0

Apart from reducing the temperature increase due to self heating, a second approach is to reduce the dependence of the laser properties with respect to temperature changes (increase T_0). The fact that T_0 is so low indicates that it is not dominated by material properties but rather by design or process aspects. A thorough study should be performed first to investigate how temperature increases and temperature gradients in the device influence the laser operation.

Such a study should include benchmarking the III-V material used and evaluating how the fabrication process influenced the performance. By placing the III-V waveguide in an amplifier configuration the gain characteristics can be measured as a function of for example:

- the width of the active region: this might uncover problems related to surface phenomena such as surface recombination of carriers and scattering due to the active layer roughness (which might be the result of the long 1 hour undercut)
- the width of the wedge in between the p-InP pillars: can reveil problems with optical leakage to the highly absorptive p-InP layers
- the junction temperature: to characterize the material properties

Based on the findings of this study, the fabrication process can and/or design can be adjusted to improve the performance of the laser.

The most concerning aspects of the fabrication process is the condition of the MQW slab after the undercut. At this stage there is no information on how smooth the edge is and how well the surface is passivated. From microscope images of other features on the die the undercut region usually looked relatively rough, which might be a significant optical loss mechanism. It would be useful to investigate the sidewall of the undercut region by SEM. This is not straight forward as this edge is buried under the p-doped layers. One possible way to see the MQW waveguide edge is to following this procedure:

- Undercut MQW
- Fill undercut with BCB
- Remove al dielectrics with long SF_6/O_2 RIE etch
- Perform a series of sulphuric acid based and hydrochloric acid based etch steps to remove the p-doped layers until the MQW layer is reached
- Remove the BCB by SF_6/O_2 RIE etch

- Look at MQW with SEM

A possible alternative route to creating the undercut would be to undercut 80-90% of the necessary length and oxidise the remaining 20-10%. This way the surface might also be better passivated.

One of the reasons for the extremely low thermal constant T_0 might be some sort of phase-mismatch between the silicon cavities and the III-V waveguide due to transversal temperature gradients. Another possibility is that, due to for example the asymmetric injection scheme, the two silicon cavities are detuned and start reflecting at different wavelengths at continuous wave operation. One way to solve such problems is to actively tune the resonance wavelength of the two silicon cavities. Tuning can for example be done thermally or by injection electrical carriers in the cavity.

An example implementation is shown in figure 6.1. Instead of using a fully etched waveguide structure, the grating should be implemented in a 'rib-waveguide' configuration. This means that the cladding of the grating is only etched to the level of the corrugations. The will have implications on the grating strength of the cavity. However, this allows an electrical path between the cavity a pair of metallic N and P contacts. Outside the grating region the silicon slab is P- and N- doped in a pattern according to the figure to create PIN diode structure. This allows injection of electric carriers into the cavity region so the effective index and consequently the resonance wavelength of the silicon cavity can be adjusted to phase-match with the other cavity and phase match with the III-V waveguide. This actively tuned mirror(s) can also be used to modulate the laser's output power. By deliberately tuning and detuning the grating to the III-V waveguide, the laser cavity is Q-switched.

Another interesting configuration would be to put only one resonant mirror in the laser structure and use an evanescent Bragg grating as the other reflector. This way there are no 3 cavities that have to be aligned spectrally. However, due to the relatively thick BCB layer, the evanescent Bragg grating will probably be relatively weak which results in a long interaction length and narrow stop band. Consequently that might cause new problems in therms of aligning the resonant mirror to the evanescent grating's stop band.

Once continuous wave operation is established, it would be interesting to design an array of lasers with 10 or more wavelengths and multiplex them into one single waveguide using for example an AWG. Such a system can be used to perform spectroscopic measurements or as a short length WDM transmitter.

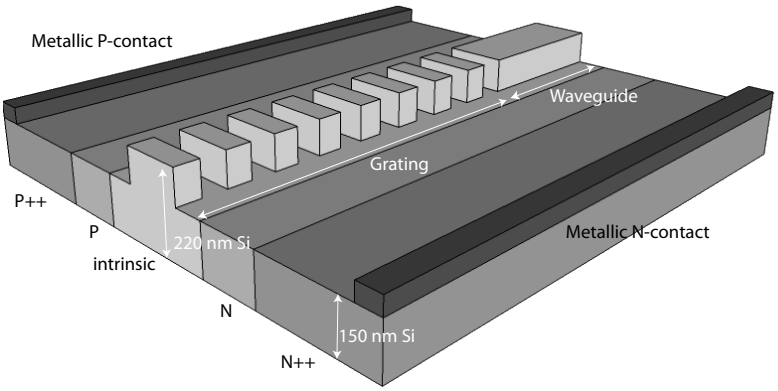

Figure 6.1: Schematic representation of an example of an active tuning mechanism for the silicon cavity resonator

The End